

# Annual Report 2020

Institut für Kernphysik · COSY  
Jül-4427



# Annual Report 2020

## Institut für Kernphysik / COSY

### DIRECTORS AT THE IKP

**Experimental Hadron Structure (IKP-1):**

**Experimental Hadron Dynamics (IKP-2):**

**Theory of the Strong Interactions (IKP-3/IAS-4):**

**Large-Scale Nuclear Physics Equipment (IKP-4):**

**Prof. James Ritman**

**Prof. Hans Ströher**

**Prof. Ulf-G. Meißner**

**Dr. Ralf Gebel (managing director 2020-21)**

### EDITORIAL BOARD

**Dr. Ralf Gebel**

**Prof. Frank Goldenbaum**

**Dr. Dieter Grzonka**

**Prof. Christoph Hanhart**

**Dr. Volker Hejny**

**Dr. Andro Kacharava**

**Prof. Andreas Lehrach**

**Prof. Livia Ludhova**

**Prof. Ulf-G. Meißner**

**Prof. James Ritman**

**Susan Schadmand, Ph.D. habil.**

**Dr. Thomas Sefzick**

**Prof. Hans Ströher**

**Dr. Raimund Tölle**

**Cover picture:** Photo composition of the Sun, the Borexino detector - placed at the Laboratori Nazionali del Gran Sasso (Italy) - and the Earth. Borexino is a 280 ton liquid scintillator detector measuring neutrinos from the Sun and the Earth. The scintillation light is detected by an array of photomultipliers which are shown in the central part of the figure.

In 2020, Borexino experimentally confirmed with high statistical significance the existence of the CNO fusion cycle in the Sun - paving the way towards the solution of the solar metallicity problem - and has also observed geoneutrinos emitted in the decay of long-lived radioactive elements inside the Earth - a new tool to understand the interior of our planet.



# Contents

<b>Preface</b>	<b>vi</b>
<b>1 Experimental Activities for FAIR</b>	<b>1</b>
1.1 The PANDA Experiment at FAIR	1
1.2 KOALA Experiment	6
<b>2 Storage Ring Based EDM Search</b>	<b>7</b>
2.1 Introduction	7
2.2 Preliminary Results from the 1 <sup>st</sup> EDM Run	7
2.3 Bunch-based Feedback System and Improved Matching of the RF Wien Filter	8
2.4 Goals for the 2 <sup>nd</sup> EDM Run	9
2.5 Technical Improvements at COSY Related to the EDM Experiment	10
2.6 Next Steps: Staged Approach	12
2.7 Progress in Search of Oscillating EDMs (Axions/ALPs)	13
<b>3 Neutrino Physics</b>	<b>14</b>
3.1 Borexino	14
3.2 JUNO	16
3.3 OSIRIS	18
<b>4 Accelerator Research</b>	<b>19</b>
4.1 Tools for Beam Diagnostics and Control	19
4.2 Injector	22
4.3 Progress of the HESR	22
<b>5 Further Activities</b>	<b>25</b>
5.1 PAX-project development	25
5.2 Laser-Plasma Acceleration of Polarized Beams	27
5.3 Spectroscopy with a Sona transition unit: Observation of direct transitions between quantum states with energy differences of 10 neV and below	28
<b>6 Theoretical Investigations</b>	<b>30</b>
<b>A Beam Time at COSY in 2020</b>	<b>36</b>
<b>B Committees</b>	<b>38</b>
B.1 CBAC – COSY Beam Time Advisory Committee	38
B.2 Committee Service	38
<b>C Publications</b>	<b>40</b>
C.1 Journal Articles	40
C.2 Books	45
<b>D Talks and Colloquia</b>	<b>46</b>
D.1 Conference and Workshop Contributions	46
D.2 Colloquia	49
<b>E Academic Degrees</b>	<b>51</b>
E.1 Dissertation / PhD Theses	51
E.2 Master Theses	51
E.3 Bachelor Theses	52
<b>F Awards</b>	<b>53</b>
<b>G Third Party Funded Projects</b>	<b>54</b>
<b>H Collaborations</b>	<b>55</b>

<b>I</b>	<b>Conferences and Outreach Activities (Co-)Organized by the IKP</b>	<b>56</b>
I.1	JUNO DFG Research Unit workshop . . . . .	56
I.2	Interviews . . . . .	56
I.3	HHU Düsseldorf - Nobelpreis live - Physik . . . . .	56
I.4	Publication Contributions . . . . .	56
I.5	Georgian-German Science Bridge: Visit of the Ambassador of Georgia to Forschungszentrum Jülich and RWTH Aachen University . . . . .	56
<b>J</b>	<b>Teaching Positions</b>	<b>58</b>
<b>K</b>	<b>Personnel</b>	<b>59</b>
<b>L</b>	<b>Individual Contributions</b>	<b>61</b>
	FAIR Related Experimental Activities . . . . .	62
	Storage Ring Based EDM Search . . . . .	82
	Neutrino Physics . . . . .	89
	Accelerator Research . . . . .	99
	Further Activities . . . . .	113

## Preface

This Annual Report compiles last year's activities of our institute, which have been achieved together with our cooperation partners and further collaborations at COSY, as well as experiments carried out at other laboratories in Germany and abroad (e.g. Gran Sasso, JLab). In 2020, our institute as virtually everything around us, was substantially affected by work and travel restrictions that were imposed by politics and the management of FZJ to mitigate the Covid-19 pandemic. Nevertheless, we have been able to provide COSY beam for experiments and could also hold a CBAC meeting – for the first time in a hybrid-mode and at GSI Darmstadt. The TransFAIR project achieved a significant milestone by signatures of a cooperation contract between Forschungszentrum Jülich and GSI Darmstadt, which transfers the scientific responsibility of IKP, more specifically IKP-1, -2 and -4 as well as the technical/administrative services (IKP-TA), from FZJ to GSI with the start of the new PoF-IV period on January 2021. One of our colleagues (J.R.) has already moved from FZJ to GSI – other staff and IKP personnel will be offered to follow. The theory institute (IKP-3) will remain part of FZJ as IAS-4 (Institute for Advanced Simulation). The present Annual Report thus constitutes the last common IKP report, which has a history of more than 50 years, starting in 1967 with a brief report of the first director Claus Mayer-Boericke (in German) and continuing in English since 1972 on an annual basis. The format has changed over the years, but the intention always was to inform our national and international colleagues and friends about what's going on scientifically in IKP. In retrospect, it obviously also is an excellent source for people that are looking for some historical information. Notable experimental highlights in 2020 include:

- For JEDI (Jülich Electric Dipole moment Investigations), a calorimetric polarimeter based on inorganic LYSO scintillators has been designed for use in a storage ring to search for electric dipole moments (EDM) of charged particles such as the proton and deuteron. Its development and first use was on the Cooler Synchrotron (COSY) at the Forschungszentrum Jülich with 0.97 GeV/c polarized deuterons, a particle and energy suitable for an EDM search.
- First PANDA straw tube modules have been assembled into the Straw Tube Tracker 1 as a FAIR PHASE 0 experiment. The STS1 has been installed at the HADES experiment at GSI and successfully commissioned with a proton-proton beamtime. All channels are working as planned and the system is ready for physics measurements that are scheduled in the upcoming year.
- Polarized HD Molecules have been realized, a polarized atomic beam source to produce nuclear polarized atomic hydrogen (H) or deuterium (D) beams has been used to polarize both isotopes independently at the same time.
- A comprehensive geoneutrino measurement has been performed using the Borexino detector, located at Laboratori Nazionali del Gran Sasso (LNGS) in Italy, resulting in a geoneutrino signal of about 47 TNU (terrestrial neutrino units). This corresponds to a total radiogenic heat of the Earth of about 38 TW (tera watt).
- The Borexino collaboration has also reported the direct observation of neutrinos produced in the CNO fusion cycle in the Sun. This was achieved after advances in the thermal stabilization of the detector and with a method to constrain the rate of radioactive contaminations in the scintillator.

The theory group has been active in a broad range of research fields and some of the highlights are listed below:

- They have developed a new algorithm for nuclear lattice effective field theory, that for the first time allowed to map out the location of the critical point and the liquid-vapor coexistence line for nuclear matter based on an ab initio calculation.
- Based on a coupled-channel approach, they have analyzed the new data from LHCb and could interpret the observed pentaquark states as hadronic molecules and predicted an additional narrow state at 4.38 GeV.
- They have investigated the impact of QCD with a non-vanishing theta-angle on the formation of the elements in the Big Bang and in stars and derived implications for the primordial abundances of the light nuclei and our anthropic view of the universe.

The work of our scientists has been very well supported by all of the infrastructure groups in our institute and by others from the research center. It is a pleasure for us to express sincerest thanks to all of them for the outstanding support. The accomplishments shared in this report would not have been possible without the dedication of our technicians and engineers, the service groups, the colleagues of the infrastructure of the FZJ and the students that have advanced the scientific case with their theses. A key element is the fruitful collaboration with our partners. We express our gratitude for obtained help and advice by our advisory committees and board of directors and also for their commitment.

Jülich, April 2021

Jim Ritman, Hans Ströher, Ulf-G. Meißner, Ralf Gebel

# 1 Experimental Activities for FAIR

## 1.1 The $\bar{\text{P}}\text{ANDA}$ Experiment at FAIR

One of the major open questions in modern hadron physics is the creation of confined, complex hadrons like protons or neutrons based on the interaction of quarks via the exchange of gluons. The well established theory of Quantum Chromo Dynamics (QCD) describes these interactions and works well at high energies but gets more and more complicated if larger objects and lower energies are studied.

The antiProton ANnihilation at DArmstadt ( $\bar{\text{P}}\text{ANDA}$ ) experiment wants to investigate the behavior of QCD by studying the interaction of antiprotons with protons in the energy regime of light, strange and charmed hadrons.  $\bar{\text{P}}\text{ANDA}$  is part of the Facility of Antiproton and Ion Research (FAIR) and will utilize a cooled antiproton beam provided by the High Energy Storage Ring (HESR) with a beam momentum between 1.5 GeV/c and 15 GeV/c.

The luminosity at the beginning of the experiment will be limited to  $\mathcal{L} = 10^{31} \text{ cm}^{-2} \text{ s}^{-1}$  which makes physics channels with large production cross sections like baryons with one or more strange valence quarks, so called hyperons, an ideal case to start with.

An understanding of the excitation pattern of baryons is indispensable for a deeper insight into the mechanism of non-perturbative QCD. A large fraction of the inelastic  $\bar{p}p$  cross section is associated to final states with an antibaryon-baryon pair together with additional mesons. This gives access to excited states both in the baryon and antibaryon channel. The cross section for final states containing an  $\bar{\Xi}^+ \Xi^-$  pair is of the order of  $\mu\text{b}$ , corresponding to a production rate of  $\sim 10^6$  pairs per day at the start-up luminosity. A detailed analysis of the reconstruction and analysis capability of the  $\bar{\text{P}}\text{ANDA}$  experiment for excited  $\Xi$  states have been performed this year.

One key feature for the study of many physics channels with the  $\bar{\text{P}}\text{ANDA}$  detector is its capability to precisely measure the flight path of charged particles. This is especially true for ground state hyperons which have a comparably long decay length of several cm. They can be identified by charged tracks, which do not originate from the primary interaction point of the antiproton beam with the proton target. To identify them both high resolution tracking detectors as well as sophisticated track reconstruction algorithms are needed, which are under development and production in Jülich. The design and the production of the main tracking detector of  $\bar{\text{P}}\text{ANDA}$ , the Straw Tube Tracker (STT), is one of the responsibilities of the IKP. After the in-depth tests of the STT in many beam tests and the development of the reconstruction methods based on the gained data, a first real test of the system will be the usage of one of the  $\bar{\text{P}}\text{ANDA}$  tracking stations made out of STT straw tubes in the HADES experiment, which was prepared in the last year. This is considered a so-called FAIR Phase-0 experiment.

The reconstruction of charged tracks within a complex detector system like  $\bar{\text{P}}\text{ANDA}$  requires the development

of highly specialized tracking algorithms. Here a dedicated tracking algorithm for straw tubes based on a Hough transformation was developed. After the proof-of-principle in the previous year, the focus in this year was to improve its performance both in tracking quality as well as in speed.

### Study of Excited $\Xi$ Baryons

In this study, the focus is on specific excited  $\Xi$  states, i.e.  $\Xi(1530)^-$ ,  $\Xi(1690)^-$  and  $\Xi(1820)^-$  as well as their charge conjugate (c.c.) particles. Various decay modes of the resonances are investigated to study the reconstruction into neutral and charged final state particles. The antiproton momentum is chosen to be  $p_{\bar{p}} = 4.6 \text{ GeV}/c$ . Different decay channels of the  $\Xi$  resonances are investigated:  $\Xi^{*-} \rightarrow \Lambda K^-$ ,  $\Xi^{*-} \rightarrow \Xi^- \pi^0$ , and their c.c. channels. For each production and decay mode an isotropic angular distribution is chosen since there are neither experimental data nor theoretical predictions for the specific reactions. For the ground state production at  $p = 3 \text{ GeV}/c$  beam momentum a cross section of  $\sigma \simeq \mu\text{b}$  has been measured. Based on the comparison of the ground state and excited states of single strange hyperons, the cross section  $\sigma(\bar{p}p \rightarrow \bar{\Xi}^+ \Xi^{*-})$  is assumed to be  $\sim 1 \mu\text{b}$ .

**Reconstruction of  $\bar{p}p \rightarrow \bar{\Xi}^+ \Lambda K^- + \text{c.c.}$**  In this study, in total about 10 million signal events of the reactions  $\bar{p}p \rightarrow \bar{\Xi}^+ \Lambda K^-$  and  $\bar{p}p \rightarrow \Xi^- \bar{\Lambda} K^+$  have been analyzed. Up to now, PandaRoot does not enable the reconstruction of delayed decay vertices. Therefore, in this study an ideal pattern recognition algorithm is used. In addition, candidates with less than four hits in one of the inner tracking detectors are rejected. Furthermore, no PID information is used for the candidate selection. To avoid the reconstruction of incomplete signal events, at least three candidates for each charged sign have to be available.

The candidates selection of  $\bar{\Lambda}$  and  $\Lambda$  starts by combining the daughter particles:  $\bar{p}$  and  $\pi^+$  for  $\bar{\Lambda}$  and  $p$  and  $\pi^-$  for  $\Lambda$ . In the next stage,  $\bar{\Lambda}$  and a  $\pi^+$  are combined to  $\bar{\Xi}^+$  as well as  $\Lambda$  and  $\pi^-$  to  $\Xi^-$  in the c.c. channel. To reduce the number of wrongly combined candidates a coarse mass window selection of  $\pm 0.15 \text{ GeV}/c^2$  around the nominal hyperon mass is applied to the candidate masses.

The final event selection is based on a least-squares fit of the full decay chain. Beside the vertex and momentum constraints, which are necessary for the fit, constraints of the hyperon masses and the overall four-momentum of the initial  $\bar{p}p$  system are implemented. The reconstruction of the full decay tree is done by combining the  $\bar{\Xi}^+ \Lambda K^-$  and  $\Xi^- \bar{\Lambda} K^+$ , respectively. The resulting candidates are fit with the DecayTreeFitter implemented in PandaRoot. The  $\chi^2$  value represents the fit quality and the calculated fit probability is used as selection criterion under the condition that the fit has converged. A threshold of  $P > 10^{-4}$  is applied. The contributing resonances can be investigated by studying the Dalitz plot of the  $\bar{\Xi}^+ \Lambda K^-$  (Fig. 1) and  $\Xi^- \bar{\Lambda} K^+$  three-body state. The mass and width of the

resonances are determined by fitting a function containing two Voigt functions and a polynomial to the corresponding  $\Lambda K$  mass distribution. The fit results as well as the respective reconstruction efficiency are summarized in Tab. 1.

Table 1: Fit results for the mass and width of the  $\Xi$  resonances decaying into  $\Lambda K$ . In addition, the reconstruction efficiency  $\epsilon$  is listed.

	M [MeV/c <sup>2</sup> ]	$\Gamma$ [MeV/c <sup>2</sup> ]	$\epsilon$ [%]
$\Xi(1690)^-$	$1689.0 \pm 0.1$	$30.1 \pm 0.6$	5.4
$\Xi(1690)^+$	$1690.2 \pm 0.1$	$30.2 \pm 0.6$	5.5
$\Xi(1820)^-$	$1823.0 \pm 0.1$	$22.9 \pm 0.4$	5.4
$\Xi(1820)^+$	$1823.1 \pm 0.1$	$22.7 \pm 0.4$	5.5

**Reconstruction of  $\bar{p}p \rightarrow \Xi^+ \Xi^- \pi^0$**  About 9 million signal events have been analyzed containing a continuum contribution and the resonant states  $\Xi(1530)^-$ ,  $\Xi(1690)^-$  and  $\Xi(1820)^-$  as well as their c.c. states.

The reconstruction of the charged final state particles is similar to the previous reconstruction. In addition, the neutral candidate list is filled whenever hits in the EMC cannot be assigned to any charged track. To reduce the large number of combinations, various selection criteria are used as prefilters, i.e. PID information deduced from the reconstructed tracks. For further reduction of combinatorics, the candidates have kinematical constraints on the transversal and longitudinal momentum ( $P_T$  vs.  $P_z$ ) distribution.

Beside the hyperon reconstruction, a  $\pi^0$  has to be reconstructed from two neutral candidates. Each neutral candidate is required to have an energy of at least 15 MeV and a flight time difference  $T - T_{v=c} < 3$  ns. Subsequently, a mass window selection of  $|M_{\text{cand}} - m_{\pi^0}| < 0.05 \text{ GeV}/c^2$  is applied to the remaining candidates. All candidates are subject to a mass constraint fit which requires  $P > 10^{-3}$ . In the last step of the analysis the  $\Xi^+ \Xi^- \pi^0$  system is combined. To reduce the amount of wrongly combined candidates a selection on the momentum in each com-

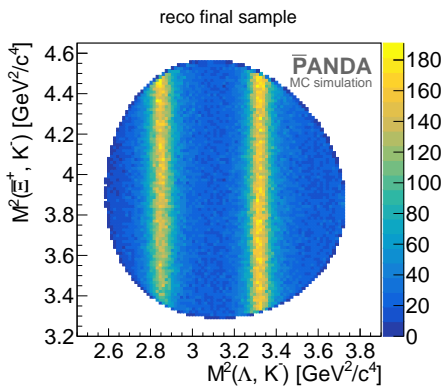


Figure 1: Dalitz plot for the final selected  $\Xi^+ \Lambda K^-$  candidates from  $\bar{p}p \rightarrow \Xi^+ \Lambda K^-$ .

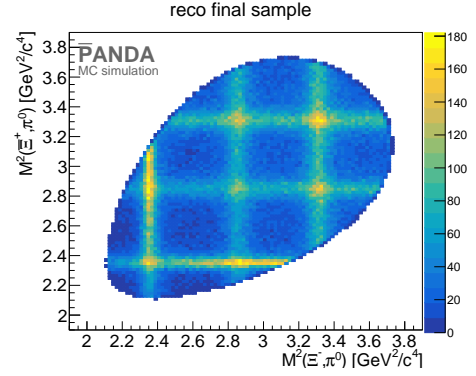


Figure 2: Dalitz plot for the  $\Xi^+ \Xi^- \pi^0$  candidates.

ponent is performed. The remaining candidates are then subject to the full decay tree fit with additional constraints of the hyperon masses and the  $\pi^0$  mass. A fit probability of more than  $10^{-4}$  is required. The reconstruction efficiency is 3.6%. The signal purity of the candidates is 93.5%. Fig. 2 shows the  $\Xi^+ \Xi^- \pi^0$  Dalitz plot. Table 2 summarizes the masses and widths of the contributing resonances by fitting the single peaks of the corresponding  $\Xi \pi^0$  mass distributions.

Table 2: Fit results for the mass and width of the  $\Xi$  resonances decaying into  $\Xi \pi^0$ . In addition the reconstruction efficiency  $\epsilon$  is listed.

	M [MeV/c <sup>2</sup> ]	$\Gamma$ [MeV/c <sup>2</sup> ]	$\epsilon$ [%]
$\Xi(1530)^-$	$1535.9 \pm 0.3$	$10.4 \pm 0.4$	3.6
$\Xi(1530)^+$	$1536.0 \pm 0.3$	$10.4 \pm 0.4$	3.6
$\Xi(1690)^-$	$1690.4 \pm 0.2$	$21.7 \pm 0.5$	3.6
$\Xi(1690)^+$	$1690.7 \pm 0.2$	$21.1 \pm 0.5$	3.6
$\Xi(1820)^-$	$1819.3 \pm 0.3$	$20.1 \pm 0.7$	3.6
$\Xi(1820)^+$	$1820.3 \pm 0.3$	$20.5 \pm 0.7$	3.6

**Background Studies** About 100 million background events were generated with the Dual Parton Model based generator DPM including only inelastic processes. These background events were subject to the same analysis strategies used for the signal events, leading to no surviving event in case of  $\Xi^+ \Lambda K^-$  and 7 remaining events for  $\Xi^+ \Xi^- \pi^0$ . The remaining events can be removed by requiring a separation of more than 1 cm between the  $\Xi^-$  and  $\Xi^+$  decay vertex. This reduced the signal reconstruction efficiency to 3.1%. The non-observation of background events corresponds to a 90% confidence upper limit of 2.3 events, which is used to calculate a lower limit for the signal-to-background ratio  $S/B$  and the signal significance  $S_{\text{sig}}$ . The signal significance is calculated with the expected number of events within 3 days of data taking, which is needed to collect the statistics necessary for a future partial wave analysis. Assuming a luminosity of  $\mathcal{L} = 10^{31} \text{ cm}^{-2} \text{ s}^{-1}$ ,  $\sigma_{\text{sig}} = 1 \mu\text{b}$  for  $\Xi^+ \Lambda K^-$  and  $\sigma_{\text{sig}} = 2 \mu\text{b}$  for  $\Xi^+ \Xi^- \pi^0$ , the expected number of

events is  $N_{\text{sig}} \approx 12 \cdot 10^6$  for  $\bar{\Xi}^+ \Lambda K^-$  and  $N_{\text{sig}} \approx 24 \cdot 10^6$  for  $\bar{\Xi}^+ \Xi^- \pi^0$ . This leads to a signal-to-background ratio and signal significance of  $S/B > 19.1$  and  $S_{\text{sig}} > 361$  for  $\bar{\Xi}^+ \Lambda K^-$  (+c.c.), and  $S/B > 22.0$  and  $S_{\text{sig}} > 392$  for  $\bar{\Xi}^+ \Xi^- \pi^0$ .

**Summary and Outlook** We presented the study of the  $\Lambda K$  and the  $\Xi \pi$  decay of  $\Xi$  resonances with the PANDA detector in the reaction  $\bar{p} p \rightarrow \bar{\Xi}^+ \Xi^{*-}$  and its c.c. channel. By performing a full decay tree fit a reconstruction efficiency of about 5% for  $\bar{\Xi}^+ \Lambda K^-$  and 3.1% for  $\bar{\Xi}^+ \Xi^- \pi^0$  could be achieved. Assuming a luminosity of  $10^{31} \text{ cm}^{-2} \text{ s}^{-1}$  15 days of data taking are sufficient to reconstruct data samples with comparable statistics to the presented MC samples. The analysis of 100 million DPM background events showed that the hadronic background is sufficiently suppressed by the analysis procedure. A major goal of the  $\Xi$  spectroscopy program within the PANDA research program is the determination of the spin and parity quantum numbers of the  $\Xi$  states. For this, a partial wave analysis (PWA) of the reconstructed three-body state has to be performed. First investigations on a PWA tool are ongoing.

### The PANDA Straw Tube Tracker

The PANDA experiment infrastructure, including the installation scheme and requirements for all detection systems in the PANDA target (TS) and forward (FS) spectrometer has been worked out in detail and summarized in a technical design report by the PANDA collaboration. For the Straw Tube Tracker (STT) a gas supply scheme with two gas lines for the drift gas mixture components argon and  $\text{CO}_2$  and an additional gas line for an optional further admixture is included in the infrastructure. The central tracking systems of the Micro-Vertex-Detector (MVD) and the STT are mounted to a Central Systems Frame (CSF), which also holds the beam-target pipe section. The CSF with mounted components is inserted as one unit along top and bottom rail bars into the TS and is part of the experiment infrastructure.

Fig.3 shows a CAD<sup>1</sup> drawing of the TS in its parking position with the installation platform. The platform section in front of the TS can be lowered so that the CSF is at the exact height of the TS opening. As last installation step the backward EMC<sup>2</sup> will be moved in. The installation platform exhibits a clean room for service work, for instance on the STT during the maintenance time of the PANDA experiment.

The data analysis of the in-beam test campaign conducted in 2018 was continued. In this campaign a STT test system was exposed to proton and deuteron beams from COSY, covering a beam momentum range from about 0.6 to 2.5 GeV/c in order to emulate similar particle energy-loss measurements in the PANDA experiment. The data

<sup>1</sup>Computer aided design

<sup>2</sup>Electro-magnetic calorimeter

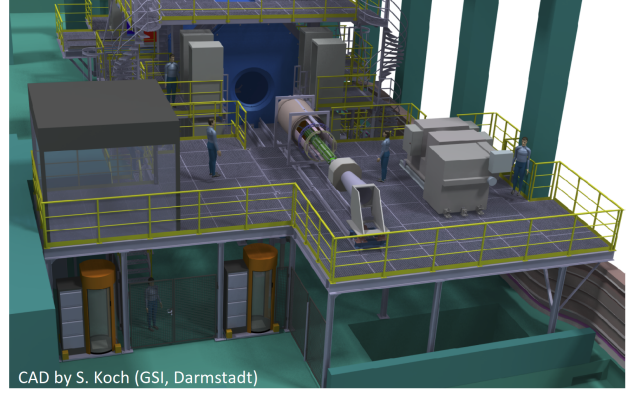


Figure 3: The PANDA target spectrometer (TS) in its parking position with the installation platform and the CSF with mounted detector components, followed by the backward EMC in front of the TS.

was used to develop the algorithms for the space - drift time calibration of the straw hits and the spatial track reconstruction. For the two different particle species and different momenta a resolution ( $\sigma$ ) in the range from about  $110 \mu\text{m}$  to  $125 \mu\text{m}$  was achieved. The spatial resolution showed the expected slight worsening from heavier to minimum ionising particles, the  $125 \mu\text{m}$  resolution corresponds to the data-set of 2.5 GeV/c momentum protons, which still is far better than the design goal of  $150 \mu\text{m}$ .

Reconstructed beam tracks were then used to determine the straw characteristic efficiency of the drift time measurements. For a single straw a high hit detection efficiency of 98% within an active straw radius of 4.95 mm was obtained for the 2.5 GeV/c proton momentum. The sharp drop of the efficiency towards the nominal straw radius of 5.00 mm is explained by the reduced track path length, which produces not enough ionisation electrons for a drift time signal above the electronic readout threshold. The hit time readout window of  $1 \mu\text{s}$  slightly reduced the detection efficiency for signals with very large signal widths above 700-800 ns, which are attributed to the tail of the Landau-distribution for the particle energy-loss. The data sets with lower momentum have higher average energy loss, and thus have lost more hits due to the signal width. Since the PANDA-STT uses a continuous readout these signals will not be lost and thus the measured efficiencies are considered to be lower limits.

The measured distribution of the radial hit detection efficiency of the straws will be implemented as a response function in the simulation of the STT hits. The obtained very high single straw hit detection efficiency of at least 98%, combined with the close-packed geometry of 26 straw layers in radial direction, will improve the hit pattern recognition capability and spatial track resolution of the PANDA-STT. More details are discussed in an individual report.

### The PANDA Phase-0 Straw Tracker Station in the HADES Experiment

HADES will start an early FAIR phase-0 experiment program at the SIS 18 synchrotron at FAIR. The physics program consists of proton scattering on protons or nuclear targets (A). In particular, the study of hyperon structure by measuring radiative hyperon decays ( $p + p(A) \rightarrow Y + X \rightarrow \Lambda e^+ e^- + X$ , with Y=any hyperon, X=rest) is of interest and well connected to the PANDA physics program. For the phase 0 experiment, the HADES spectrometer will be upgraded by a dedicated detection system consisting of two straw tracker stations (STS1 and STS2) and a RPC detector in the forward region, covering the polar angle range from about  $0.5^\circ$  to  $7^\circ$  for particle track reconstruction.

The HADES phase 0 experiment proposal was approved by the GPAC<sup>3</sup> in 2020. A first commissioning proton beam time to test the new detector systems installed in the HADES spectrometer was granted and scheduled for February 2021.

The new Straw Tracker Station STS1 was completed at the IKP in 2020 with a full system test before its transport to GSI and installation in HADES by the end of 2020 (see Fig.4). The STS1 station consists of 704 straws arranged in four vertical double-layers with  $0^\circ$  and  $90^\circ$  azimuthal orientations. A double-layers consists of four modules, each with 32 straws, and one center module with 48 straws and featuring a  $8 \times 8 \text{ cm}^2$  hole for the direct beam. The layout and dimensions of the modules were adjusted to the PANDA Forward Tracker to allow a later use of the straw modules in the PANDA Tracker Stations FT3 and FT4. For setting up and pre-testing the STS1 a data-acquisition system was installed, which is based on TRB3<sup>4</sup> readout boards. The same DAQ system will be also used for the PANDA-STT system.

Before its transport to GSI a dedicated test program of all mounted STS1 system components was carried out to verify the readiness for installation. The STS1 was connected to a gas supply system to provide the Ar/CO<sub>2</sub> gas mixture of 2 bar absolute pressure and the straws were put on high voltage. Then, the STS1 was irradiated by a <sup>90</sup>Sr radioactive source and the signals were recorded by the data-acquisition. The electrons emitted from the <sup>90</sup>Sr  $\beta$ -source have a broad continuous energy spectrum up to 2.2 MeV. The electrons passed through a 2 mm thin scintillator to trigger the readout and provide a reference time for the drift time measurement.

Fig.5 shows the straw signals time and time-over-threshold distribution of the irradiated STS1 in comparison to the same distribution of a PANDA-STT straw test-system, which was illuminated by 2.5 GeV/c momentum proton beam tracks in the 2018 test campaign. Notice the almost identical characteristic correlation of the signal time-over-threshold with the signal leading edge time for both, which proves that the <sup>90</sup>Sr  $\beta$ -source irradiation is ideally suited to test the detector channel functionality.

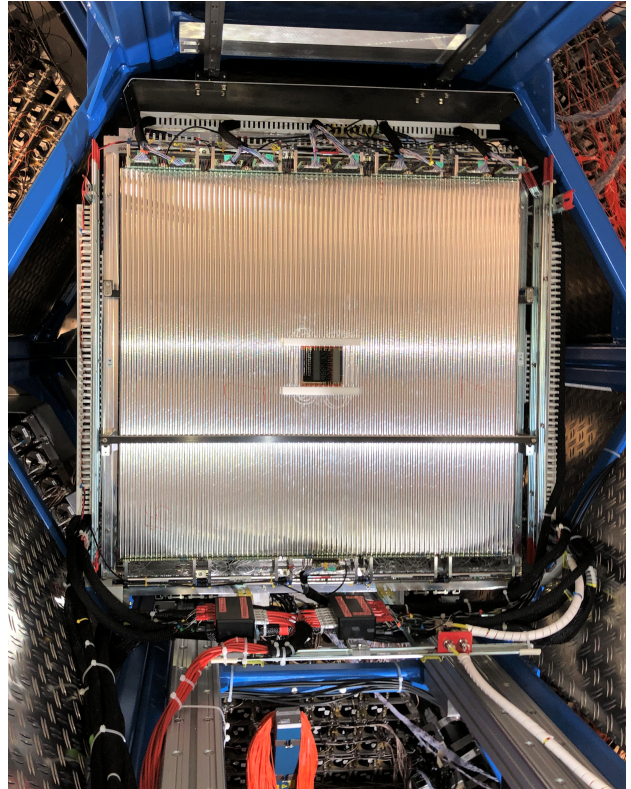


Figure 4: Photograph of the new Straw Tracker Station STS1 installed in the HADES spectrometer.

The weakly visible intensity pattern in the top right distribution in Fig.5 within the TDC time region from about -730 ns to -650 ns is due to the collimated (few mm<sup>2</sup> cross-section) beam, passing through the slightly inclined horizontal straw layers. This leads to a weak radial illumination pattern in the straws and the corresponding drift time region.

The uniformity of the electronic signal amplification and shaping by the front-end mounted PASTTREC<sup>5</sup> ASICs was checked by a measurement of the time-over-threshold (ToT) distribution and determination of the distribution mean for all straws. For channels with deviating ToT the individual baseline in the ASIC, which determines the effective signal threshold, was adjusted accordingly. Fig.6 shows the result for all 704 STS1 channels with a ToT alignment better than 10 ns ( $\sigma$ ) around the 245 ns ToT mean. As can be seen, a few channels could be not better aligned due to a malfunction in the corresponding ASIC on the front-end board. Such front-end boards should be replaced as soon as more spare ASIC boards are available.

Note that no straw failure was observed and the drift time signals from all 704 straws were recorded. Stable and robust high voltage operation of the STS1 during several months was successfully demonstrated. With the completion of these tests the STS1 readiness was achieved

<sup>3</sup>Advisory committee which evaluates all proposed experiment programmes at the GSI accelerator.

<sup>4</sup>Trigger readout board, version 3, design by GSI, Darmstadt.

<sup>5</sup>PANDA Straw Tube Readout Chip, design by AGH Krakow, Poland.

for the detector installation in the HADES spectrometer carried out by the end of 2020.

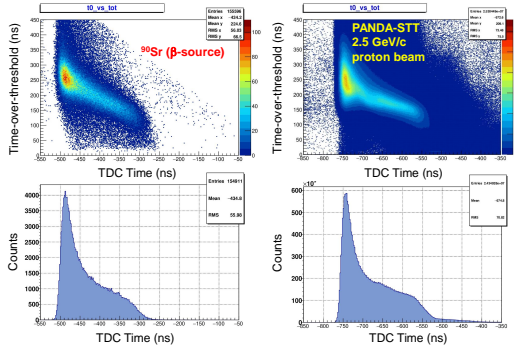


Figure 5: Correlation of the signal time and time-over-threshold distributions for the STS1 irradiated by a  $^{90}\text{Sr}$  radioactive source (left) and comparison with the distribution of straws irradiated by a 2.5 GeV/c momentum proton beam (right). The similar shape is also clearly visible in the projected signal time distributions.

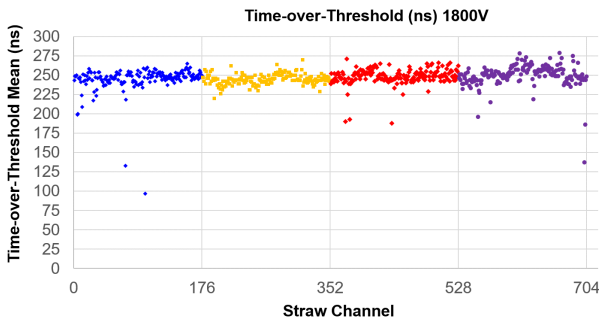


Figure 6: Distribution of the measured mean signal time-over-threshold for all 704 channels of the STS1 illuminated by the  $^{90}\text{Sr}$  source and after optimisation of the front-end electronic parameters.

### Quality and Runtime Optimization of a PANDA Track Finding Algorithm based on Hough Transformations

A track finding algorithm based on Hough transformations for the barrel part of the PANDA detector has been optimized. The track finder is well adapted to the STT by using the hit point information and also taking into account the drift time information measured by the STT. The procedure has been described in more detail in the annual report of last year.

The first implementation of the algorithm in 2019 was not compatible with other algorithms both in quality and in speed. Therefore, the focus in the last year was to optimize the two parameters. The quality is measured by three quantities: the track finding rate of reconstructible primary tracks (possible primaries), the fraction of wrongly found tracks (ghosts) and the fraction of

tracks found more than once (clones). The results of the optimization procedure are shown in fig. 7 and are described in the following.

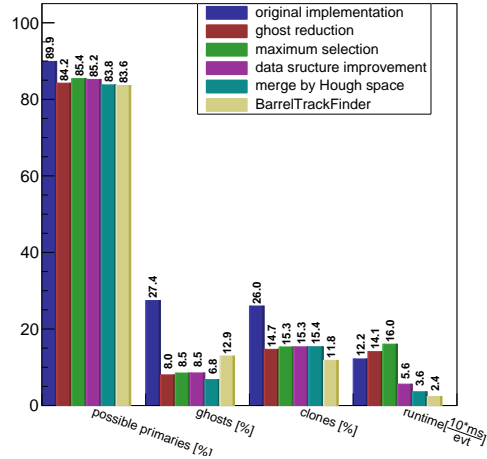


Figure 7: Contribution of each optimization step.

The first optimization step investigated reducing the number of created ghost tracks. The analyzed parameters are the number of neighbors of a hit, the average distance between hits in the x-y-plane and the number of hits per detector type. Based on a receiver operating characteristics (ROC) curve, a threshold for each parameter was chosen with a high accuracy ((true positives + true negatives) / (all data)) and a low number of false negatives.

The second optimization step was to analyze a method to decide which maximum is taken if there are several maxima in the Hough space. Here the sum of the distances of each hit to the track resulting from the corresponding maximum is determined. The maximum with the smallest sum of distances is then chosen. Since the focus in this part of the optimization is on the finding rate of possible primaries the large increase in computing time can be neglected here.

The various additional steps to improve the track finding quality caused an additional increase of the runtime by 31.1 %. To optimize the speed of the algorithm, the used data structure was examined in more detail. Maps were introduced, which links an integer to a region in the Hough space and a fired straw in the STT with the corresponding isochrone radius. This has the advantage to speed up the access to the data and to prevent time consuming type casts.

The last step to optimize the algorithm was to exchange the merging method, which decide if tracklets could belong to the same particle track. This method was exchanged by a simpler merging method based directly on the found maxima of the Hough spaces. It exploits the proximity of maxima from the same track compared to those from different tracks. The new merging method leads to a large improvement in computing time but also to a loss in efficiency, which has to be investigated in

more detail in the future.

The effect of the individual optimization steps on the quality parameters and the runtime are shown in Fig. 7. The ghost ratio could be reduced by a factor of four, the clone ratio by a factor of three. The improvements lead to a small efficiency loss of 8.6 % points. The runtime of the algorithm could be improved by a factor of five. A comparison to the BarrelTrackFinder, which is the currently best track finder in PANDA, shows that this implementation is comparable to the BarrelTrackFinder in terms of quality and speed. The advantage of this algorithm is the possibility to extend the algorithm to find secondary particles, which is not possible for the BarrelTrackFinder. Additionally, the speed of the algorithm still has potential for improvement, since it is easily parallelizable. For this purpose, a parallelization on GPUs is currently under development.

## 1.2 KOALA Experiment

The goal of the KOALA experiment is to measure the differential cross section of antiproton-proton elastic scattering in a wide range of four-momentum transfer squared, *i.e.*,  $|t|=0.0008-0.1$  (GeV/c)<sup>2</sup>, which is down to the Coulomb region. The concept of KOALA is to measure the scattered beam particles at forward angles by fast timing detector and the recoil protons near 90° by energy detectors. The forward arm covers the low *t* range to suppress inelastic background by coincidence with the recoil detector. To validate the experiment proposal as well as the detector concept the KOALA setup was commissioned at COSY by measuring the proton-proton elastic scattering since both reactions have the same kinematics and particles stopped in the recoil detector.

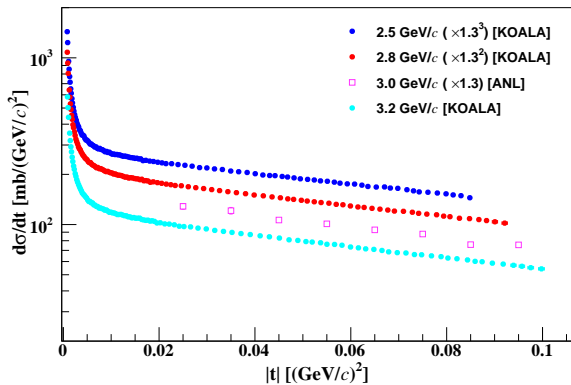


Figure 8: The differential cross section distributions measured by the recoil detector together with a previous measurement. For display purposes factors of 1.3, 1.3<sup>2</sup> and 1.3<sup>3</sup> have been applied to the data points at 3.0, 2.8 and 2.5 GeV/c, respectively.

One recoil detector has been built and commissioned at COSY. The KOALA recoil detector included two

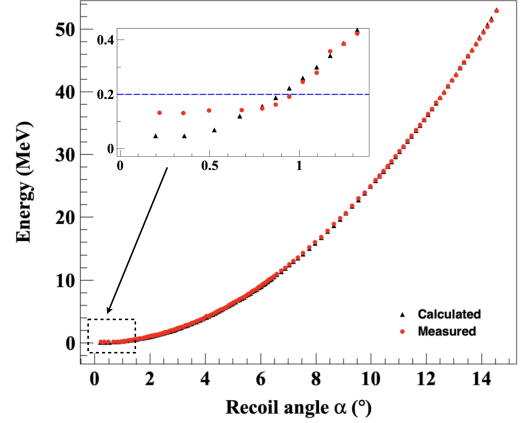


Figure 9: The red and black dots show the measured energy and the calculated energy of recoil protons as a function of the recoil angle, respectively. The inset shows a narrower recoil angle range.

76.8 mm × 50 mm × 1 mm silicon strip sensors that were positioned about 1 m from the target. Each silicon detector has 64 strips with 1.2 mm pitch. In order to measure higher energy protons, two germanium strip detectors with 5 and 11 mm thickness were added. Each has 67 strips and a strip pitch of 1.2 mm. The four solid state strip detectors were installed on a cold plate viewing the intersection region and covering recoil angles from  $\alpha = -1.5^\circ$  to  $13.6^\circ$ .

Differential cross sections at 2.5, 2.8 and 3.2 GeV/c are presented in Figure 8 as solid circles with different colors. Previously measured data at 3.0 GeV/c in a similar *t* range are also shown with open squares. The strong rise for  $|t| < 0.005$  (GeV/c)<sup>2</sup> due to the Coulomb interaction is clearly visible in the KOALA data in contrast, the ANL data do not extend into that kinematic region.

Inelastic background limited the minimum useful *t* to 0.001 (GeV/c)<sup>2</sup>. In order to suppress the background and to gain the full range of *t* desired, the forward detector has been built and installed at COSY. The forward detector is located at *Z* = 4.6 m downstream of the interaction region. The forward detector consists of 4 pairs scintillators which have been symmetrically located at up, down, left and right to the beam axis. Each pair has been sequentially installed along the beam axis with distance of 20 cm relative to each other. The scintillator detector covers polar angles of  $0.37^\circ-1.2^\circ$ .

Benefiting from the coincidence measurement between the recoil and forward detectors, the background events at lower *t* range have been significantly suppressed. The recoil protons can now be measured down to 200 keV, which corresponds to about 0.0004 (GeV/c)<sup>2</sup>. The measured recoil energy as a function of recoil angle at 2.2 GeV/c has been plotted in Fig. 9. The measured energy overlaps the ideal energy calculated based on the recoil angle of the detector strips.

The validation of the coincidence between the recoil and forward detector will enable the measurable  $t$  range to be extended even beyond the design goals. This is very promising for KOALA when it is installed at HESR. For further details see Phys. Lett. B 812 (2021) 136022.

## 2 Storage Ring Based EDM Search

### 2.1 Introduction

The JEDI- and CPEDM-collaborations with their project to search for electric dipole moments of charged particles (both permanent and oscillating) in storage rings (srEDM) have been very active in 2020 in spite of the restrictions imposed by the pandemic. Most importantly, a very positive statement was received in the strategic evaluation of the Programme-oriented-Funding (PoF) of the Helmholtz-Association, which paves the way for the continuation of the srEDM project in the upcoming funding period (2021-2027).

The following experiments were conducted at COSY: February/March:

- Exp. E2.7: 1 week machine development (MD) + 1 week experiment (JEDI polarimeter (JePo) commissioning)
- Exp. A9.1: 1 MD + 2 weeks (Proton Spin Coherence Time (SCT) studies / Snake commissioning)

August/September:

- Exp. E5.6: 1 MD + 1 week (Bunch-based spin phase-lock feedback system)
- Exp. E10.1: 2 MD + 3 weeks (Optimization of the alignment of magnetic elements using spin tune)

The CPEDM activities, to which the JEDI collaboration has contributed substantially, were presented in a number of community-building meetings like, e.g.: (i) the CERN PBC (Physics Beyond Colliders) diversity program, (ii) the European JENAA (Joint ECFA-NuPECC-APPEC Activity) initiative, and (iii) the Snowmass process, which is part of the strategic planning of the US Particle-Physics community.

Two JEDI-collaboration meetings took place (via video conference): (i) No. #16 (June 22-24), (ii) No. #17 (December 14-16), combined with the CPEDM kickoff meeting. The work on the feasibility study „Storage Ring to Search for Electric Dipole Moments of Charged Particles“ has been finalized and is now in the process of being published as a „CERN Yellow Report“ (CERN-PBC-REPORT-2019-002).

### 2.2 Preliminary Results from the 1<sup>st</sup> EDM Run

The EDM related experiments are intrinsically complicated and very difficult to perform. The CBAC granted

for the 1<sup>st</sup> deuteron EDM run two weeks for machine development and four weeks of actual beam time. Perfecting all involved techniques constituted the primary objective and this again proved very time consuming. Setting up the machine, including the adjustment of all relevant beam parameters, orbit corrections, target setup, detector operations, Wien filter setup and tuning, and the chromaticity adjustments and measurements to ensure a long spin-coherence time, took most of the allocated time. To put this into perspective, eventually it was possible to run for about 6 days with the desired machine conditions during the 1<sup>st</sup> EDM precursor run.

According to the generalized Thomas-BMT equation, in the presence of an EDM, the invariant spin axis in an ideal ring would be tilted in radial direction. In reality, however, there are additional magnetic misalignments, so that the invariant spin axis is tilted in both radial and longitudinal directions. The goal achieved during the 1<sup>st</sup> precursor run was to determine the tilt of the invariant spin axis which allows to obtain an experimental access to the EDM. The determination of the EDM then amounts to an accurate spin dynamics calculation using the magnetic imperfections of the machine, and the difference to the measured result.

In order to induce a vertical polarization build-up, the RF Wien filter, was operated on a harmonics of the spin precession frequency ( $\approx 871$  kHz), and the RF phase was locked with the spin-precession phase. In this case, a particle passing through the RF Wien filter gets a spin kick in the same direction every turn. In order to obtain a map of the EDM resonance strength, the measurements were performed for different RF Wien filter rotations around the beam axis and for different settings of a solenoid in the opposite straight section which rotates the invariant spin axis at the RF Wien filter longitudinally. 31 points in total were measured during the run in November - December 2018. The initial slopes of the polarization build-up ( $\dot{\alpha}$ ) were observed for various phases of the RF Wien filter, resulting in sinusoidal dependencies. The map of all data points for the measured  $\dot{\alpha}$ , interpreted as EDM resonance strength  $\varepsilon^{\text{EDM}}$  of deuterons with momenta of 970 MeV/c depending on the RF Wien filter rotation angles and solenoid settings is shown in Fig.10. The fit function<sup>6</sup> reads

$$\varepsilon^{\text{EDM}} = \frac{\chi_{\text{WF}}}{4\pi} \left[ A_{\text{WF}}^2 (\phi^{\text{WF}} - \phi_0^{\text{WF}})^2 + A_{\text{Sol}}^2 \left( \xi_0^{\text{Sol}} + \frac{1}{2 \sin \pi v_s} \xi^{\text{Sol}} \right)^2 \right]^{\frac{1}{2}} + e_0, \quad (1)$$

it represents a square root of an elliptic paraboloid, which means there appear quadratic dependencies of the  $\varepsilon^{\text{EDM}}$  for both the RF Wien filter rotations and the solenoid settings. Here  $\chi_{\text{WF}}$  is a rotation angle in the Wien filter,  $\phi^{\text{WF}}$

<sup>6</sup>An analytic expression for the function describing the surface is derived in Eq. (A5), Spin dynamics investigations for the electric dipole moment experiment Phys. Rev. Accel. Beams 23 (2020) 024601

and  $\xi^{\text{Sol}}$  are Wien filter and solenoid setting respectively. The minimum of the surface, given by

$$\begin{aligned}\phi_0^{\text{WF}} &= -3.80 \pm 0.05 \text{ mrad}, \\ -\xi_0^{\text{Sol}} &= -5.68 \pm 0.05 \text{ mrad}.\end{aligned}\quad (2)$$

corresponds to the orientation of the invariant spin axis at the location of the RF Wien filter. The scaling coefficients amount to

$$\begin{aligned}A_{\text{WF}} &= 0.57 \pm 0.005, \\ A_{\text{Sol}} &= 0.84 \pm 0.008, \text{ and the offset} \\ e_0 &= (-1.1 \pm 0.1) \times 10^{-10}.\end{aligned}\quad (3)$$

The reduced  $\chi^2/\text{ndf}$  of the fit to the data of Fig. 10 using the fit function given in Eq. (1) amounts to

$$\chi^2/\text{ndf} = 459/26 = 17.65.\quad (4)$$

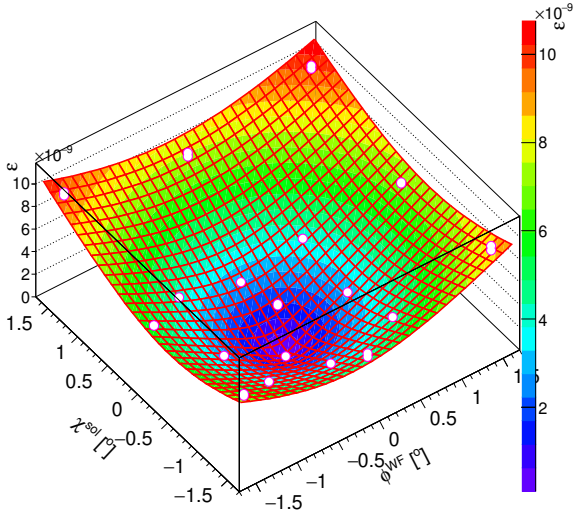


Figure 10: Preliminary experimentally observed parametric resonance strength  $\varepsilon \simeq \dot{\alpha}/\omega_{\text{rev}}$ , plotted in terms of the initial slope  $\dot{\alpha}|_{t=0}$ , for various values of  $\phi_0^{\text{WF}}$  and  $\chi_0^{\text{Sol}}$ . The surface is a fit to the data using the analytic expression of Eq. (1). The minimum of this graph yields the orientation of the invariant spin axis, the parameters are given in Eq. (2).

As discussed above, these data were taken during a relatively short period of about six days. Originally, it was planned to record more data points with a smaller spacing and, also repetitions of each data point of the map  $\varepsilon^{\text{EDM}}(\xi^{\text{Sol}}, \phi^{\text{WF}})$  were foreseen. However, due to the limited running time available, these data could not be recorded. Therefore, the data of Fig. 10 appear not to be consistent, which is evidenced by the rather large  $\chi^2/\text{ndf} = 17.65$ . During the second run (scheduled for the beginning of 2021), we would like to apply a pilot-bunch approach for the spin-tune feedback. Recording

the spin tune of the unperturbed pilot bunch acts as a co-magnetometer during the EDM measurement. This alone constitutes a potentially crucial step to better understand the systematics of the EDM precursor experiment.

### 2.3 Bunch-based Feedback System and Improved Matching of the RF Wien Filter

During the EDM measurement using the RF Wien filter one would like to ensure that the Wien filter is operated on resonance with the spin-precession frequency of the stored deuterons in the machine. The spin tune is actually defined only for a *static* machine, *i.e.*, for a machine where no RF device is affecting the polarization evolution of the beam. In case, there is a time-dependent *running* or *instantaneous* spin tune, the direction of the invariant spin axis  $\vec{n}_s$  also changes as a function of time, *i.e.*,  $\vec{n}_s \equiv \vec{n}_s(t)$ <sup>7</sup>. Thus, operating the RF Wien filter actually modifies the spin tune in the machine, and this is unavoidable. What can be avoided, however, is the use of the running spin tune to provide the input to the spin-tune feedback system. Instead, it was suggested a new scheme, where multiple bunches (typically four) are stored in the machine, and only three of these bunches are used to determine the EDM resonance strengths, while the fourth one, not affected by the RF Wien filter, is used to determine the spin tune as if the machine were static. The latter can be accomplished by implementing a set of four fast RF switches into the input ports to the RF Wien filter.

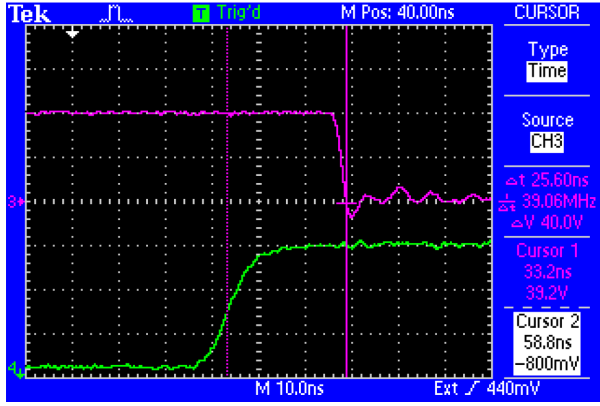
It should be emphasized that the pilot-bunch technique provides a co-magnetometer, because it allows to monitor changes of the experimental setup of the machine with all its imperfections during the EDM measurement, like, *e.g.*, drifts of the magnetic field. The pilot bunch concept has been tested experimentally with beam during the JEDI experiment E5.6.

In order to enable the RF Wien filter to manipulate the spin of individual bunches stored in the machine, the driving circuit was equipped with custom-designed RF switches. These switches are in principle able to handle up to 500 W each, which permits the system to run near a total power of 2 kW in pulsed mode.

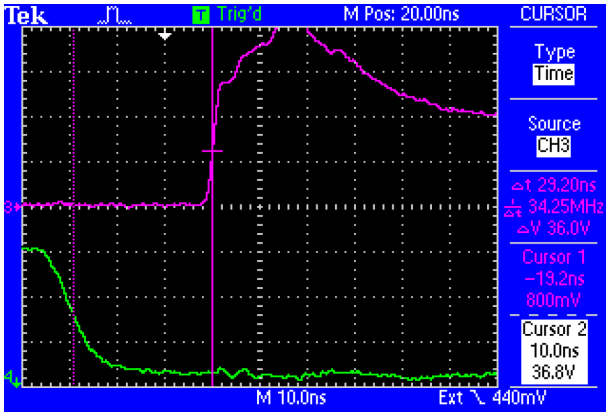
Figure 11 shows offline test results of the switches when they are switched off (panel a) and on (b), respectively. The including the internal delay between the driving circuit and the RF transistors, approximately, the switches need 25 ns to go into the 'low state'. The actual switching-off time is less than 10 ns. On the other hand, the switches exhibit some delay of approximately of 19 ns. In conclusion, the aforementioned numbers should be sufficient to run the RF Wien filter in a way to have a pilot bunch, which will enable to conduct a frequency-based EDM measurement at COSY.

The Wien filter, in principle, should be able to generate RF electric and magnetic fields so that the corresponding Lorentz force exerted on the beam vanishes. The Lorentz

<sup>7</sup>Spin dynamics investigations for the electric dipole moment experiment *Phys. Rev. Accel. Beams* 23 (2020) 024601



(a) Switching RF on



(b) Switching RF off

Figure 11: Offline test of the fast RF switches. The magenta trace shows the response of the switch and the green trace is the trigger signal.

force, in this context, is quantified in terms of the amplitude of the induced beam oscillations, when the forces are mismatched. Figure 12 shows the measured values of the amplitude of these induced beam oscillations as a function of two variable capacitors,  $C_L$  and  $C_T$ . Each combination of these capacitors corresponds to a well-defined case of electric and magnetic forces. We were able to match the RF Wien filter so that the minimum measured amplitude of beam oscillations read  $1 \mu\text{m}$  at a conventional COSY BPM, nearly 70 m away from the RF Wien filter. This value is amplified by the square root of the ratio of the beta-functions at these two locations. This value corresponds to the smallest point that could be measured with the available BPM readout electronics based on lock-in amplifiers. The spin dynamics simulations, however, have shown indeed that an oscillation amplitude that is at least one order of magnitude smaller could be obtained, still within the capabilities of the driving circuit. The effect on the EDM measurements is yet to be investigated in more detail in the future.

The data on RF Wien filter induced oscillations, shown in Fig. 12, are presently evaluated in much more detail,

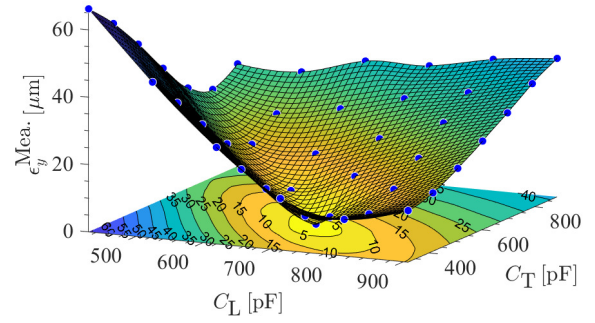


Figure 12: Preliminary data of the measured amplitudes of beam oscillations  $\epsilon_y$  as a function of the variable capacitor values  $C_L$  and  $C_T$ .

with the goal to understand how close we are already to the quantum limit.

## 2.4 Goals for the 2<sup>nd</sup> EDM Run

The map of EDM resonance strengths  $\epsilon^{\text{EDM}}$ , determined from the initial slopes of the polarization buildup and shown in Fig. 10, is not completely understood. From the theoretical point of view, the fitted parameters  $A_{\text{WF}}$  and  $A_{\text{Sol}}$ , given in Eq. (3), should both be equal to unity. In addition, the  $\chi^2/\text{ndf}$  is not good, which indicates that there are not yet understood systematic effects present. In order to improve this situation, a different technique has been proposed for the determination of the EDM resonance strength during the 2<sup>nd</sup> run. The present spin-tune feedback system has another drawback in that it does not allow one to accumulate the polarization build-up beyond the first maximum of the vertical spin component. Using the pilot bunch approach, discussed above, we should be able to determine the unperturbed spin tune in the machine during cycles that extend for as long as the spin-coherence time permits. Thus, we shall be able to stay on resonance for the duration of the full cycle time.

With the pilot bunch spin-tune feedback in place, the oscillation of the vertical polarization component  $p_y$  is expected to proceed as depicted in Fig. 13. These data were obtained from simulations<sup>8</sup>. The upper panel shows the initial slope  $\dot{p}_y|_{t=0}$  as function of the RF phase  $\phi^{\text{RF}}$ . The middle panel shows the oscillation frequency  $\omega$  of  $p_y$  also as function of the RF phase  $\phi^{\text{RF}}$ . Obviously,  $\omega$  is independent of  $\phi^{\text{RF}}$ , and the phases should just be properly fixed, so that the frequencies can be determined with small errors. As a consequence, the number of build-up measurements at different RF phases can be somewhat reduced, which shall lead to an increased duty cycle with respect to the determination of  $\epsilon^{\text{EDM}}$ .

<sup>8</sup>Spin dynamics investigations for the electric dipole moment experiment [Phys. Rev. Accel. Beams 23 \(2020\) 024601](#)

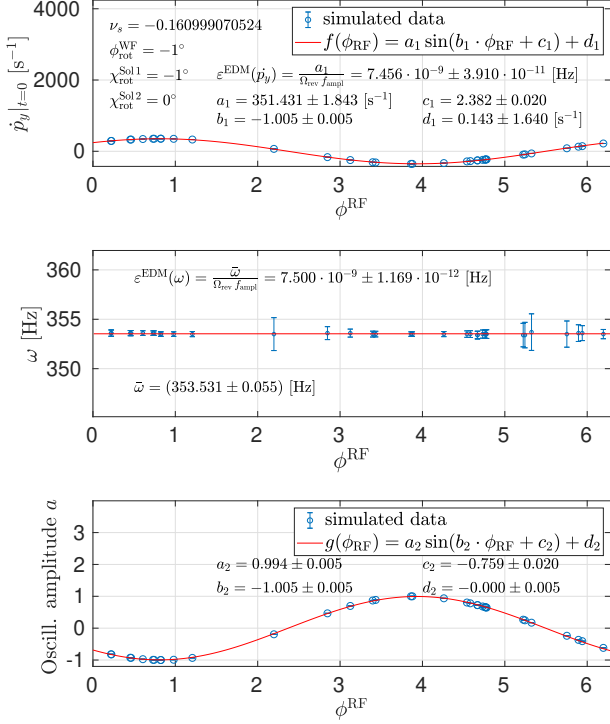


Figure 13: Simulation for one specific combination of the RF Wien filter and solenoid spin rotation angles  $(\phi_{\text{rot}}^{\text{WF}}, \chi_{\text{rot}}^{\text{Sol1}}) = (-1^\circ, -1^\circ)$ . 36 random values of  $\phi_{\text{RF}}$  are used to obtain the resonance strengths  $\epsilon^{\text{EDM}}$  from the sinusoidal oscillation of  $p_y(t)$  (see Fig. 18 of Ref.: Phys. Rev. Accel. Beams 23, 024601, 2020). Depicted here as function of the randomly chosen  $\phi_{\text{RF}}$  are the extracted initial slopes  $\dot{p}_y(t)|_{t=0}$ ,  $\omega = \Omega^{p_y}$ , and the amplitude  $a$  of the  $p_y$  oscillation. The parameters used for the calculation are  $n_{\text{turns}} = 2 \times 10^4$ ,  $n_{\text{points}} = 200$ , and  $d = 10^{-20}$  ecm. The RF Wien filter is operated at harmonic  $K = -1$ .

The approach to determine  $\epsilon^{\text{EDM}}$  based on the oscillation frequency offers two new distinct benefits over the determination based on the initial slope alone. Firstly, it becomes possible to investigate systematic effects that appear *during* the buildup process by inspecting  $\omega$  as function of time in the cycle. Secondly, having available also the amplitudes of the polarization oscillation (lower panel in Fig. 13) from a fit to  $p_y(t)$ , one can provide a direct comparison of  $\epsilon^{\text{EDM}}$  extracted from the two methods.

The spin evolution, *e.g.*, described by Eq. (1), depends on the location of the solenoid in the machine that is used for the measurements. Therefore, making a measurement with the Siberian snake solenoid and the 2 MV electron cooler solenoid, shall allow to independently determine the orientation of the invariant spin axis from the two obtained maps.

## 2.5 Technical Improvements at COSY Related to the EDM Experiment

An ambitious program has been initiated to enhance the beam diagnostics capabilities at COSY with respect to, *e.g.*, beam position, machine tune, and chromaticity. In the subsequent sections, various of these topics are addressed.

### Alignment campaigns of the COSY magnet system

There have been various surveys and alignment campaigns conducted at COSY during the past years. An example of the results of the dipole parameters are presented in JINST 16, P12005, 2020. It should be emphasized that the uncertainties of these parameters are of the order of  $\approx 0.3$  mm and  $\approx 0.3$  mrad. Similar results have been obtained for the translational and rotational parameters of the quadrupole magnets in COSY. Well aligned quadrupoles permit one to absolutely calibrate the Beam Position Monitors (BPMs). The method is based on the fact that a particle beam, which does not pass through the center of a quadrupole, experiences a deflection. The precision reached by the method is approximately  $40 \mu\text{m}$ . As a result of the beam-based alignment, a beam-position monitor calibration could be obtained, which moves the quadrupole centers onto or close to the zero line of the coordinate system. This makes the corrected orbit pass close to the centers of the quadrupoles. The overall improvement of the closed-orbit could be confirmed by the fact that after the beam-based alignment procedure was applied, less steerer correction power is needed to reach the optimal orbit, as one does not have to act against the steering effects from off-center quadrupoles. For the vertical direction, this amounts to about 80% less and for the horizontal direction to about 20% less required steering power.

### Improvements of COSY signals and distribution

A GPS-driven 10 MHz signal is now used to synchronize all frequency-related devices in COSY including the experiment installations. Especially important is the synchronization of the frequency generators for the COSY cavity, the RF solenoid and the RF Wien filter. Both, the RF solenoid and the RF Wien filter have to operate at a harmonic of the COSY revolution frequency  $f = f_{\text{COSY}} |v_s + n|$ , where  $v_s$  is the spin tune and  $n$  an integer number. With individual oscillators for each device, the resonance condition had to be retuned at least once per day by an amount of the order up to some 10 mHz  $10^{-7}$  to  $10^{-8}$  relative), which is 1 to 2 orders of magnitude larger than the typical cycle-by-cycle variation of the spin tune. A change in frequency results in running slightly off-resonance. In case of the RF solenoid, which is used to rotate the spins after injection into the horizontal plane, this means incomplete or too large rotations and, thus, different starting conditions for the EDM measurement. This circumstance adds further systematic

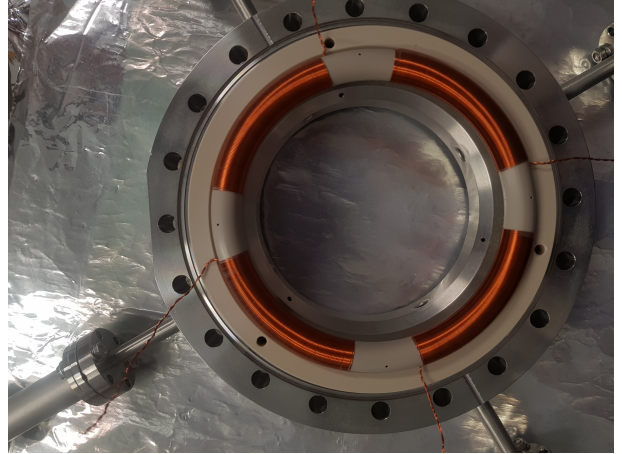
uncertainties. With the new frequency synchronization enabled, no retuning was necessary during the last long-running Axion search experiment.

The Fiber-Optics-based Reference Frequency Distribution System (**FO-RFDS**), recently implemented at COSY, is a system that distributes up to four reference frequencies through fiber optic cables from signal source devices (frequency generator, arbitrary waveform generators) to relevant systems of the EDM experiment, where a clean frequency signal with a low-phase noise and a high signal-to-noise ratio is required. Through fiber-optic cables, signals and data can be transported over short and long distances, as well as with a low and high bandwidth, depending on the application. Fiber optic cables are electromagnetically not radiating and they are immune to interference and grounding issues. With such an optical signal transport and distribution, source generators of TTL (Transistor-Transistor Logic) and/or Sine-wave signals are electrically decoupled from their destination systems. Electrical decoupling prevents noise contamination to the signal and noise propagation through cross-talks, interference, pickups, and ground-loops. Electrical decoupling is insured by optocoupler devices like transmitters and receivers. This approach ensures the cleanliness of the signals during their transport and during arrival at the target destinations. With transceivers, the electrical signal is converted to an optical signal and subsequently transported through optical fibers. Close to the target system, the optical signal is converted back to electrical signal (mainly TTL) to be fed to the destination devices.

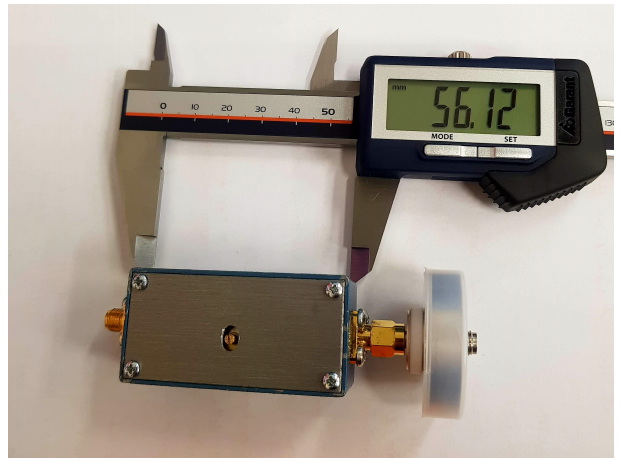
### Optimization of Rogowski BPM system

A new type of Beam-Position Monitor (BPM), based on a Rogowski coil design, has been recently developed at COSY. These pick-ups are presently in a development stage. One of the primary advantages of these BPMs is that they require only a very short beam insertion length of  $\approx 60$  mm and provide an offset-bias free response to counter-circulating beams, which makes these instruments attractive as BPM candidates for EDM storage rings.

The Rogowski BPMs used at the entrance and exit of the RF Wien filter so far in COSY had turn number and self resonance frequency (measured for the complete realistic single-quadrant system, including effects from cabling, as well as pre-amplifiers, for single quadrant coil) of 445 and 1.2 MHz, respectively. With these specifications, the BPMs were well-suited for the operation in single bunch mode at the typical JEDI deuteron beam momentum of 0.97 GeV/c, corresponding to a beam revolution frequency of 750 kHz. For COSY beam in four-bunch mode, a new Rogowski BPM has to be developed, where the operational bandwidth is at least a factor of three higher. One possibility to increase the frequency bandwidth (keeping the geometrical parameters of the torus unchanged) is to use a thicker wire for the windings of the coil which in turn results in decreased number of windings. This can help to decrease overall inductance of the



(a) Winding of Rogowski BPM with higher bandwidth.

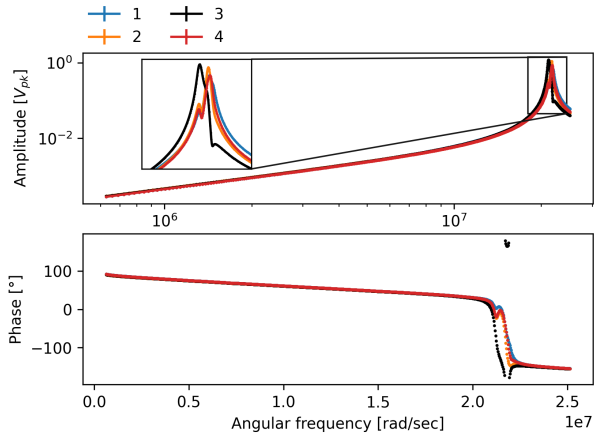


(b) Adjustable capacitor (trimmer) for tuning quadrants.

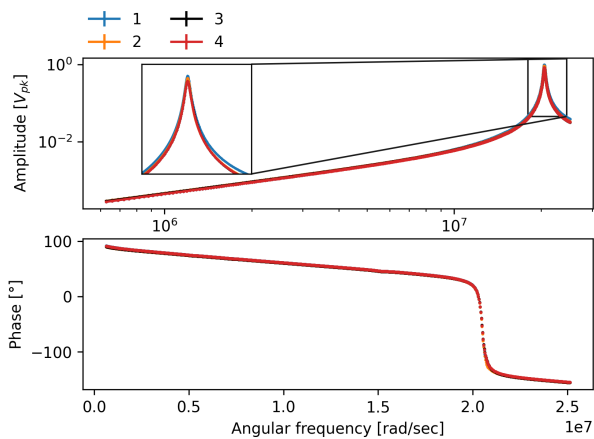
Figure 14: (a) Winding of the Rogowski BPM with higher bandwidth. Each quadrant coil has 132 turns and covers an angular range of around  $60^\circ$ . (b) Adjustable capacitor (trimmer) used in parallel connection with each quadrant coil in order to tune the four-quadrant system at 3.229 MHz.

coil by a factor corresponding to the fractional change introduced in the turn number and hence, to increase the natural frequency of the system by the same factor (the inductance is proportional to the square of the turn number, while the self resonance is inversely proportional to the square root of the inductance).

The wire diameter of the windings was increased from 140 to 400  $\mu\text{m}$ . Thereby, the angular winding coverage was decreased from about  $90^\circ$  to around  $60^\circ$ , which resulted in overall single-quadrant turn number of 132 [see Fig. 14(a)]. Mechanical or human-related imperfections mainly induced during winding of the four quadrants or during the assembly process, where electrical connections are made with the help of twisted-pair wire extensions, can introduce unwanted (non-ideal) effects on the resonance curves of the four quadrants, leading to a situation, where the individual quadrant coils do not resonate at the same frequency. In order to improve this, an ad-



(a) Measured frequency response before tuning.



(b) Measured frequency response after tuning.

Figure 15: Measured frequency response of the four quadrants before (panel a) and after (b) tuning. The inserts in the upper plots show voltage amplitudes in a logarithmic scale. The lower subplots show phase responses in a linear scale. The numbers in the legends indicate the quadrant number.

justable capacitor [see Fig. 14(b)] was connected in parallel with each quadrant coil (just before amplification). In an attempt to get the system of four quadrants resonating at the same frequency, the trimmers were adjusted by introducing capacities of a few pF (each quadrant required a unique capacitance as all quadrants were showing slightly different frequency curves with their original circuits.)

Figure 15 shows the frequency dependence of the four quadrants of the Rogowski BPM before [15(a)] and after [15(b)] tuning the system to resonate at 3.229 MHz. The tuning was successfully accomplished with a phase shift of less than  $1^\circ$  on resonance for all quadrants. Obviously, the distortions in both amplitude and phase response were greatly minimized by the tunable capacitor system.

## 2.6 Next Steps: Staged Approach

In view of the various technical challenges involved in building the final all-electric ring, as e.g., described in [CERN Yellow Report], the CPEDM agreed to adopt a staged approach (see Figs 16 and 17). As a next step the collaboration decided to design and build a demonstrator ring for charged-particle EDM searches. The new

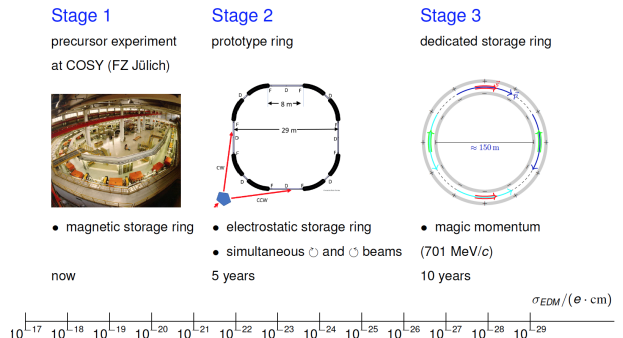


Figure 16: Roadmap for the realization of a full electric storage ring at the magic momentum. After the completion of the precursor experiments at COSY, the Collaboration plans to design and construct a prototype storage ring to address the still unsolved technical challenges, as a necessary milestone for the design of the final ring.

CPEDM collaboration, which evolved out of the success and the achievements of JEDI, brings together scientists from CERN and the JEDI collaboration. The project is part of the Physics Beyond Collider (PBC) process presently carried out at CERN, and the European Strategy for Particle Physics Update. A possible host site for the prototype EDM storage ring is either COSY or CERN. The scope of the project is to provide for protons at a kinetic energy of  $T_p = 30$  MeV an all-electric machine operation with simultaneous clockwise (CW) and counterclockwise (CCW) orbiting beams of the machine. The circumference of the machine is about 100 m. By adopting vertical magnetic fields superimposed on the radial electric fields in the deflector elements, frozen-spin operation for protons shall be possible. Items to be studied with the prototype ring include:

- All-electric ring (high field, field homogeneity and stability)
- Storage time investigations
- CW/CCW operation
- Spin coherence time in electric machine
- Polarimetry (efficient, sampling, non-destructive)
- Optimum orbit control
- Studies of magnetic moment effects due to imperfect shielding and artificially induced magnetic fields

- Multi-bunch approach to co-magnetometry
- Tests of stochastic cooling
- Direct measurement of the EDM of the proton.

The gained experienced and developed technologies result important in perspective of the design and realization of a future dedicated storage ring (stage 3).

1	2	3
Precursor Experiment	Prototype Ring	All-electric Ring
<b>dEDM proof-of-capability</b> (orbit and polarisation control; first direct dEDM measurement)	<b>pEDM proof-of-principle</b> (key technologies, first direct pEDM measurement)	<b>pEDM precision experiment</b> (sensitivity goal: $10^{-29}$ e cm)
<ul style="list-style-type: none"> <li>- Magnetic storage ring</li> <li>- Polarised deuterons</li> <li>- d-Carbon polarimetry</li> <li>- Radiofrequency Wien-filter</li> </ul>	<ul style="list-style-type: none"> <li>- High-current all-electric ring</li> <li>- Simultaneous CW/CCW op.</li> <li>- Frozen spin control (with combined E/B-field ring)</li> <li>- Phase-space beam cooling</li> </ul>	<ul style="list-style-type: none"> <li>- Frozen spin all-electric (at <math>p = 0.7</math> GeV/c)</li> <li>- Simultaneous CW/CCW op.</li> <li>- B-shielding, high E-fields</li> <li>- Design: cryogenic, hybrid, ...</li> </ul>
Ongoing at COSY (Jülich) 2014 → 2021	Ongoing within CPEDM 2017 → 2020 (CDR) → 2022 (TDR) Start construction > 2022	After construction and operation of prototype > 2027

Figure 17: Summary of the important features of the proposed stages in the storage ring EDM strategy.

## 2.7 Progress in Search of Oscillating EDMs (Axions/ALPs)

An experimental analysis nearing completion has demonstrated for the first time the possibility to use a polarized beam in a storage ring to search for QCD axions or similar axion-like particles (ALPs). If present in sufficient quantities, ALPs could be the main component of dark matter, the material whose gravitational effects help hold together star clusters and galaxies. The axion field would add an oscillating part to any intrinsic nuclear electric dipole moment, as  $d = d_0 + d_1 \cos(\omega t + \phi_a)$  where  $\omega_a = 2\pi f_a$  is the frequency associated with the axion mass and  $\phi_a$  is the axion primordial phase.

The experiment used in-plane polarized deuterons to search a region accessible with a 0.97 GeV/c beam centered around  $f_a = 121$  kHz. The beam momentum was ramped in short, overlapping steps while measuring the vertical component of the in-plane polarization. The expected ALP signal is a jump in the vertical component created by a resonance between the axion frequency and the precession of the polarization relative to the radial direction of the particle-frame electric field. Prior to ramping, the beam was electron cooled. The WASA Forward Detector was used to continuously monitor the beam polarization, both vertical and in-plane. Since  $\phi_a$  is unknown, four beam bunches were injected on each fill with different polarization directions (and hence phases) to ensure no ALP would be missed. When the COSY injected polarization is rotated from vertical to horizontal, the  $f = f_{REV}(1 - G\gamma) = 629755$  Hz harmonic was chosen for the rotation solenoid as this yielded four directions spread across two opposite quadrants. This made possible the cancellation of systematic zero offsets in the observation of any resonant polarization jumps. Once in-plane, the horizontal polarization was continuously mon-

itored by observing and unfolding the precession of the up/down asymmetry in the polarimeter. This horizontal component is subject to depolarization by spreading of the individual particle spin directions in the ring plane. Polarization lifetimes were maintained through sextupole field adjustments to be always larger than 300 s and were generally much larger.

To verify that the setup was capable of detecting an axion-like resonance, a test signal was made using an RF Wien filter with a radial magnetic field tuned to  $f = f_{REV}(1 + G\gamma) = 871450$  Hz. When this resonance is crossed, a set of positive and negative jumps are created in the polarization of the four bunches (see Fig. 18 for an example).

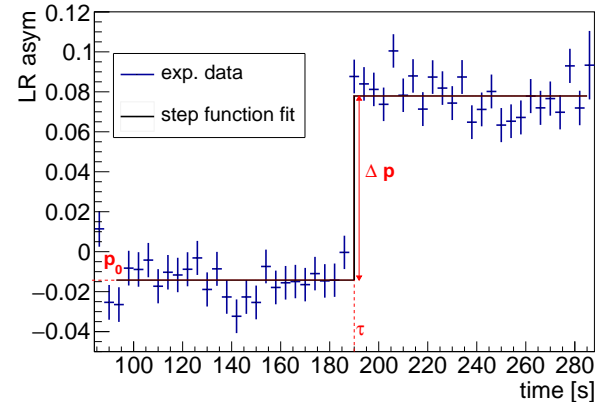


Figure 18: Example of step function fits to the L/R asymmetry histogram versus time from an RF Wien filter scan. The black line is the fit at the resonance crossing.

Figure 18 also illustrates how any data set from a scan may be searched for a resonance crossing by varying the time of the crossing while looking for the largest jump ( $p_2$ ) and the best overall fit. Given the distribution of bunch polarizations, this type of scan is free of systematic errors at the level of sensitivity reported here.

About 100 scans were completed. Most scans operated at a fractional momentum change of  $1.38 \times 10^{-4}$  over 135 s. At the end, the fractional momentum change was reduced to  $1.12 \times 10^{-4}$  to produce slower scans. A single polarized beam state was used throughout. A run consisted of ten fills, eight of which were made with polarization turned on. It was assumed that  $\phi_a$  would be different for each fill. No axion signals were observed. Figure 19 shows an example scan where no signal is observed. The total scanning range is from 120.0 to 121.4 kHz corresponding to an ALP mass range of  $4.96 \times 10^{-9}$  to  $5.02 \times 10^{-9}$  eV. The expected sensitivity is  $\sigma_{d_1} = 10^{-22} e \cdot \text{cm}$  corresponding to an error on the axion-gluon coupling strength  $C_g/f_a$  of  $10^{-3} \text{ GeV}^{-1}$ .

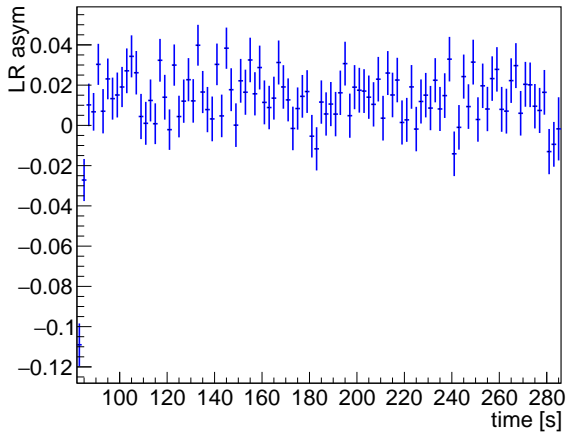


Figure 19: Example of L/R asymmetry histogram where no jump is observed. The frequency is ramped between 120s and 255s.

### 3 Neutrino Physics

The neutrino group is specialized in low-energy neutrino physics with liquid-scintillator (LS) based detectors. Borexino (Sec. 3.1), the world’s radio-purest 280 tons LS detector in the Laboratori Nazionali del Gran Sasso in Italy is taking data since 2007, focused on solar neutrinos, geoneutrinos, and searches for rare processes in coincidence with astrophysical events. JUNO (Sec. 3.2) will be the first multi-kton LS detector currently under construction in Jiangmen, China. German groups are leading the construction of the 20 tons OSIRIS detector (Sec. 3.3) that will monitor the level of radio-purity of the LS during the several months long period of filling the JUNO central detector.

#### 3.1 Borexino

##### 3.1.1 First observation of CNO-cycle solar neutrinos

Solar neutrinos are elementary particles that are copiously produced inside the Sun, by the same nuclear processes that generate the heat. Neutrinos interact rarely after their production and are therefore a direct probe of solar nuclear processes. According to the Standard Solar Model (SSM), which represents the best knowledge available about the Sun, the heat in the Sun’s core is generated by two main series of processes fusing protons to Helium: the primary proton–proton ( $pp$ ) chain, responsible for about 99% of the solar energy production and the sub-dominant Carbon – Nitrogen – Oxygen (CNO) cycle. Neutrinos are detected via their elastic scattering on electrons in a large volume of liquid scintillator.

Borexino has already published a complete spectroscopy of  $pp$  chain neutrinos <sup>9</sup>. In November 2020, Borexino

published the first direct experimental evidence of solar neutrinos produced in the rare CNO nuclear fusion cycle in Nature<sup>10</sup>. The journal has devoted the cover page to this result, that was also listed among the Physics World’s Top 10 breakthroughs in 2020<sup>11</sup>. The main challenges of this analysis were the very low interaction rate of CNO neutrinos and the similarity of its spectral shape to that of  $pep$  solar neutrinos and the intrinsic  $^{210}\text{Bi}$  background. The  $pep$  neutrino rate can be independently determined with 1.4% precision using the constraint on solar luminosity, global analysis with all solar neutrino experiments excluding the latest Borexino data, exploiting theoretically precisely known ratio of  $pep$  and  $pp$  neutrino fluxes, and using the most recent values of the oscillation parameters. The  $^{210}\text{Bi}$  background, the short-living decay product of  $^{210}\text{Pb}$ , can be determined via the counting of  $\alpha$ -decays of  $^{210}\text{Po}$ , daughter of  $^{210}\text{Bi}$ , assuming secular equilibrium of the chain down from  $^{210}\text{Pb}$ , which is a long-living isotope contaminating the liquid scintillator. Alpha particles can be identified on an event-by-event basis via pulse shape discrimination techniques. Until mid-2016, additional  $^{210}\text{Po}$  was brought from peripheral sources to the fiducial volume, a wall-less region in the core of the detector, through the convective motions of the scintillator, triggered by seasonal temperature changes. However, the detector’s thermal stabilisation campaign performed between 2015 and 2016 has minimized the residual convection in the innermost parts of the detector, making it possible to measure  $^{210}\text{Bi}$  via  $^{210}\text{Po}$ . This helped in obtaining a  $^{210}\text{Bi}$  upper limit from the cleanest region of the detector called the Low Polonium Field. A multivariate fit was then performed using the Phase-III data (July 2016 - February 2020), after constraining the rates of  $pep$  and  $^{210}\text{Bi}$ . The best fit value for the CNO neutrino rate is  $7.2^{+2.9}_{-1.7}(\text{stat})$  counts per day(cpd)/100t. The total contribution of systematics was evaluated as  $^{+0.6}_{-0.5}$  cpd/100t using 13.8 million pseudo-datasets with the same exposure as Phase-III. The systematic uncertainties included the  $^{210}\text{Bi}$  spectral shape, the energy scale and resolution of the Monte Carlo model, non-linearity and non-uniformity of the detector’s response, as well as variation in the absolute value of the scintillator light yield. This study excluded the no-CNO signal scenario with a significance greater than  $5.0\sigma$  at 99.0% CL. A simple counting analysis, complementary to the multivariate fit, rejected the null CNO hypothesis at  $3.5\sigma$ . The significance achieved in the data analysis is compatible with the median sensitivity as published in the European Physical Journal C in November 2020<sup>12</sup>. The 68% confidence interval ([5.5 - 10.2] cpd/100t) from the multivariate fit is compatible with both high- and low-metallicity (the abundance of heavy elements in the Sun) predictions of the Standard Solar Model.

<sup>10</sup>Experimental evidence of neutrinos produced in the CNO fusion cycle in the Sun [Nature 587 \(2020\) 577](#)

<sup>11</sup>[Physics Breakthrough Prize 2020 finalists](#)

<sup>12</sup>Sensitivity to neutrinos from the solar CNO cycle in Borexino [Eur. Phys. J. C 80 \(2020\) 1091](#)

<sup>9</sup>Comprehensive measurement of  $pp$ -chain solar neutrinos [Nature 562 \(2018\) 505](#)

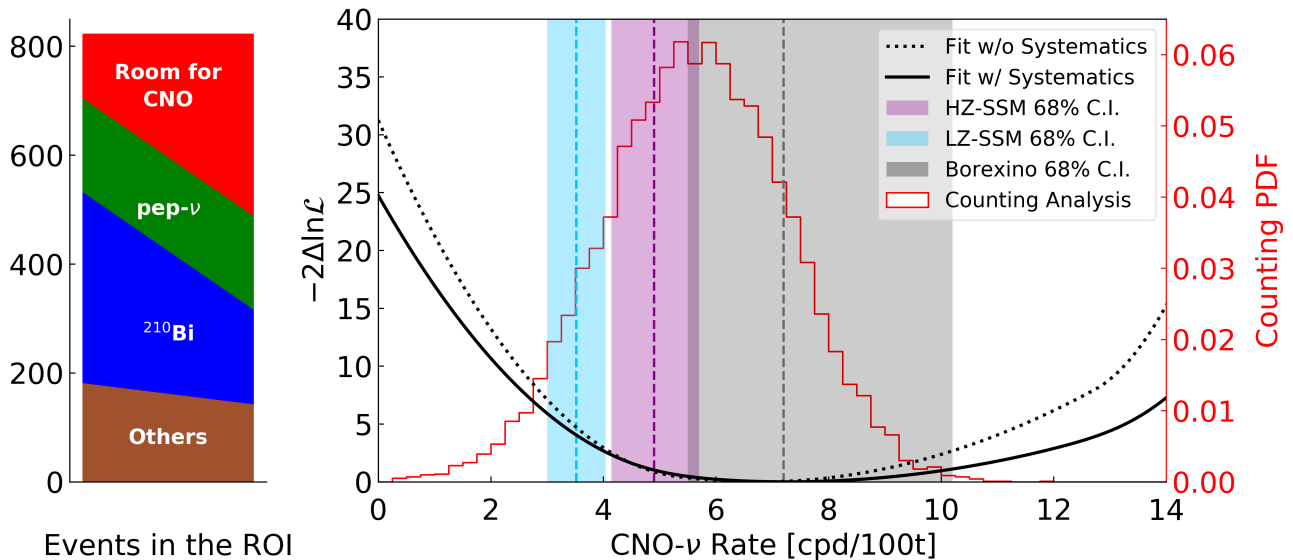


Figure 20: Results of the Borexino CNO analysis. Left: Counting analysis. The vertical axis is the number of events allowed by the data for CNO neutrinos and backgrounds in the Region-Of-Interest (ROI); on the left, the CNO signal is minimum and backgrounds are maximum, while on the right, CNO is maximum and backgrounds are minimum. It is clear from this figure that CNO cannot be zero. Right: CNO neutrino rate negative log-likelihood profile directly from the multivariate fit (dashed black line) and after folding in the systematic uncertainties (black solid line). Histogram in red: CNO neutrino rate obtained from the counting analysis. Finally, the blue, violet, and grey vertical bands show 68% confidence intervals (C.I.) for the LZ and HZ SSM predictions and the Borexino result (corresponding to black solid-line log-likelihood profile), respectively. Taken from<sup>10</sup>.

The observed interaction rate can be converted to a flux of  $7.0^{+3.0}_{-2.0} \times 10^8 \text{cm}^{-2}\text{s}^{-1}$  CNO neutrinos at Earth. The result, demonstrated in Figure 20, paves the way towards the future, more precise measurements, that will be able to solve the so-called "metallicity-puzzle", one of the key issues of the solar physics. This measurements also provides evidence of the primary mechanism for the stellar conversion of Hydrogen into Helium in the Universe.

### 3.1.2 $^8\text{B}$ and *hep* solar neutrinos

Technical details concerning the *pp*-chain solar neutrino analysis in the High Energy Region (Nature 2018<sup>9</sup>) were published in March 2020 in Physical Review D<sup>13</sup>. This analysis regards the improved measurement of the  $^8\text{B}$  solar neutrino interaction. The measured rate of scattered electrons above 3 MeV of energy is  $0.223^{+0.015}_{-0.016}(\text{stat})^{+0.006}_{-0.006}(\text{syst})$  cpd/100 t, which corresponds to an observed solar neutrino flux of  $2.57^{+0.17}_{-0.18}(\text{stat})^{+0.07}_{-0.07}(\text{syst.}) \text{cm}^{-2}\text{s}^{-1}$ , assuming no neutrino flavor conversion. This measurement exploits the active volume of the detector in almost its entirety for the first time, and takes advantage of a reduced radioactive background following the 2011 scintillator purification campaign and of novel analysis tools providing a more precise modeling of the background. Additionally, a new

limit on the interaction rate of solar *hep* neutrinos was set, searched via their elastic scattering on electrons as well as their neutral current-mediated inelastic scattering on carbon  $^{12}\text{C}$ .

### 3.1.3 Geoneutrinos

Geoneutrinos are electron (anti)neutrinos emitted in the radioactive decays of long-lived isotopes such as  $^{235}\text{U}$ ,  $^{238}\text{U}$ ,  $^{232}\text{Th}$ , and  $^{40}\text{K}$  inside the Earth. Electron antineutrinos ( $\bar{\nu}_e$ ) above 1.8 MeV from  $^{238}\text{U}$  and  $^{232}\text{Th}$  chains are detected in an organic liquid scintillator through the inverse beta decay reaction on proton (IBD). Through the measurement of the geoneutrino rate, one can estimate the contribution of radiogenic heat to the overall heat flow on the surface of the Earth. Borexino released a new update on the geoneutrino measurement with improved analysis techniques using the data from December 2007 to April 2019 (3263 days), which was published in Physical Review D in January 2020<sup>14</sup>. The reported exposure represents an increase by a factor of two over a previous Borexino analysis from 2015, thanks to an improved data selection that included an enlarged fiducial volume and sophisticated cosmogenic vetoes. The analysis also requires the evaluation of different backgrounds, especially the most important reactor antineutrino background that comes from man-made nuclear reactors around the world. By observing  $52.6^{+9.4}_{-8.6}(\text{stat})^{+2.7}_{-2.1}(\text{sys})$  geoneutrinos, ob-

<sup>13</sup>Improved measurement of  $^8\text{B}$  solar neutrinos with 1.5 kton · yr of Borexino exposure *Phys. Rev. D* 101 (2020) 062001

<sup>14</sup>Comprehensive geoneutrino analysis with Borexino *Phys. Rev. D* 101 (2020) 012009

tained through the spectral fit of 154 golden candidates, a geoneutrino signal of  $47.0^{+8.4(\text{stat})+2.4(\text{sys})}_{-7.7-1.9}$  TNU<sup>15</sup> with  $^{+18.3}_{-17.2}\%$  total precision was obtained. The null-hypothesis of observing a geoneutrino signal from the mantle was excluded at 99.0% C.L. for the first time, exploiting detailed knowledge of the local crust around the experimental site. The measured mantle signal of  $21.2^{+9.5(\text{stat})+1.1(\text{sys})}_{-9.0-0.9}$  TNU corresponds to the production of a radiogenic heat of  $24.6^{+11.1}_{-10.4}$  TW (68% interval) from <sup>238</sup>U and <sup>232</sup>Th in the mantle. Assuming 18% contribution of <sup>40</sup>K in the mantle and  $8.1^{+1.9}_{-1.4}$  TW of total radiogenic heat of the lithosphere (crust + rigid uppermost mantle), the Borexino estimate of the total radiogenic heat of the Earth is  $38.2^{+13.6}_{-12.7}$  TW, which corresponds to the convective Urey ratio of  $0.78^{+0.41}_{-0.28}$ . The convective Urey ratio quantifies the fraction of radiogenic heat to the overall heat flux. This is compatible with different geological predictions, however there is a  $\sim 2.4\sigma$  tension with those Earth models which predict the lowest concentration of heat-producing elements in the mantle. In addition, the existence of a hypothetical georeactor, i.e. a <sup>238</sup>U powered reactor at the center of the innermost layer of the Earth (core) was verified. After fitting the data with a constraint on the number of expected reactor antineutrino events, the existence of such a hypothetical georeactor at the center of the Earth having a power greater than 2.4 TW was excluded at 95% C.L. Particular attention was given to the description of all analysis details which should be of interest for the next generation geoneutrino measurements using liquid scintillator detectors.

### 3.1.4 Low energy neutrinos from astrophysical sources

The Borexino collaboration reported on the searches for neutrinos and antineutrinos from astrophysical sources which was published in the *Astroparticle Physics* journal in September 2020<sup>16</sup>. Astrophysical neutrinos cover at least 18 orders of magnitude in energy, starting from meV (relic neutrinos) till PeV, the highest energy neutrinos ever detected as of today. Collecting more data on astrophysical neutrinos and discovering their possible new sources will affect the very foundations of our understanding of the Universe. Neutrino detectors indeed start playing a substantial role in multi-messenger astronomy. In this work, model-independent upper limits were set on neutrino fluxes from unknown sources, in the energy range 1.8 to 16.8 MeV, that improve the previous Borexino results by a factor 2.5. Using the same data set, experimental constraints on the diffuse supernova fluxes in the previously unexplored region below 8 MeV were also studied. A search for  $\bar{\nu}_e$  in the solar neutrino flux

<sup>15</sup>1 TNU corresponds to 1 antineutrino event detected via IBD over 1 year by a detector with 100% detection efficiency containing  $10^{32}$  free target protons (roughly 1 kton of liquid scintillator).

<sup>16</sup>Search for low-energy neutrinos from astrophysical sources with Borexino *Astop. Phys.* 125 (2021) 102509

was also presented. The presence of  $\bar{\nu}_e$  would be a manifestation of a non-zero anomalous magnetic moment of the neutrino, making the conversion to antineutrinos possible in the strong magnetic field of the Sun. A limit of  $384 \text{ cm}^{-2}\text{s}^{-1}$  (90% C.L.) for the solar  $\bar{\nu}_e$  flux was obtained, assuming an undistorted energy spectrum of <sup>8</sup>B solar neutrinos. At lower energies, by investigating the spectral shape of elastic scattering events, a new limit on solar <sup>7</sup>Be neutrino to antineutrino conversion was obtained as  $< 0.14$  (90% C.L.) at 0.862 MeV. Finally, solar flares as possible neutrino sources were also investigated and the strongest limits on the fluence of neutrinos of all flavor neutrino below 3–7 MeV were obtained. An intense solar flare as the cause of the observed excess of events in run 117 of the Cl-Ar Homestake experiment (1970-1994) was excluded, assuming the neutrino flux to be proportional to the flare’s intensity.

### 3.1.5 Non-standard neutrino interactions

Borexino measures solar neutrinos via elastic neutrino-electron scattering. The energy spectra due to solar neutrinos in Borexino depend on the solar- $\nu_e$  survival probability  $P_{ee}$  and the chiral couplings of the neutrino and electron. Some theories of physics beyond the Standard Model postulate the existence of Non-Standard Interactions (NSI’s) which modify the chiral couplings and  $P_{ee}$ . A search for such NSI’s, in particular, flavor-diagonal neutral current interactions that modify the  $\nu_e e$  and  $\nu_\tau e$  couplings using Borexino Phase II data was performed and published in January 2020 in the *Journal of High Energy Physics*<sup>17</sup>. Standard Solar Model predictions of the solar neutrino fluxes for both high and low metallicity assumptions were considered. No indication of new physics was found at the level of sensitivity of the detector and constraints on the parameters of the NSI’s were placed. In addition, with the same dataset, the value of  $\sin^2\theta_W$  was obtained with a precision comparable to that achieved in reactor antineutrino experiments.

## 3.2 JUNO

The Jiangmen Underground Neutrino Observatory (JUNO) is a multi-purpose, liquid scintillator-based neutrino experiment, originally proposed in 2008 to determine the Neutrino Mass Ordering (MO) by detecting reactor antineutrinos. The detector site is at an equal distance from two complexes of nuclear reactors and has been chosen in order to achieve the best sensitivity to the MO measurement. The JUNO complex is currently under construction in China, with a rock overburden above the experimental hall of around 700 m, and is located 53 km away from Yangjiang and Taishan nuclear power plants. The first data are expected by the end of 2022. JUNO will contain 20 kton of liquid scintillator and will be the first multi-kton liquid scintillator detector ever con-

<sup>17</sup>Constraints on flavor-diagonal non-standard neutrino interactions from Borexino Phase-II *JHEP* 2 (2020) 38

structured. Its energy resolution must reach unprecedented 3% at 1 MeV. In order to reach the target performance, several challenges have to be faced. The optimal composition of the JUNO scintillator "cocktail" containing LAB scintillator, PPO fluor, and bis-MSB wavelength shifter, has been determined using the 20t detector previously used by the Daya Bay experiment. The results have been published as a collaboration paper in Nuclear Instruments and Methods A<sup>18</sup>. The key to a successful measurement of MO is a precise knowledge of the detector's energy scale and its intrinsic non-linearity and non-homogeneity. To achieve this, a complex calibration strategy has been developed and published as another collaboration paper in Journal of Instrumentation<sup>19</sup>. Future JUNO results about neutrino MO could be further improved by combining them with those from other experiments. A recent paper published on Physical Review D<sup>20</sup> shows that the exclusion of the wrong mass ordering at more than  $5\sigma$  C.L. could be achieved within few years of data-taking, by combining the reactor neutrino results from JUNO and the atmospheric neutrino data from IceCube Upgrade.

Beside the main goal of the neutrino MO identification, JUNO, as a next generation experiment, has a large potential in other areas of neutrino and astroparticle physics. The reactor antineutrino flux can be further exploited for a measurement of the solar oscillation parameters  $\theta_{12}$  and  $\Delta m_{12}^2$  with a sub-percent accuracy, what will represent the most precise measurement in the neutrino solar oscillation sector. Geoneutrinos, antineutrinos generated in the radioactive decays of  $^{238}\text{U}$  and  $^{232}\text{Th}$  chains inside the Earth, represent another class of events accessible to JUNO. Both geoneutrinos and reactor antineutrinos will be detected via the inverse beta-decay (IBD) reaction, where an antineutrino interacts with a proton and generates a prompt signal from a positron plus a delayed one from a neutron. Supernovae neutrinos could also be observed in case of a stellar core-collapse, measuring important parameters from the burst process at the source. Relic supernovae, which exploded in the past and filled the galaxy with a diffuse neutrino flux, are another source which could be accessible to JUNO. The detector performances can also be exploited to observe solar neutrinos, by means of elastic scattering on electrons. The collaboration has recently published in Chinese Physics C a paper about the potential to measure  $^8\text{B}$  solar neutrinos down to unprecedented 2 MeV threshold<sup>21</sup>. The potential to measure low-energy solar neutrinos is currently under study and of particular interest to the IKP-2 neutrino group, thanks to the experience with solar neutrinos physics in Borexino. Also atmospheric neutrinos, pro-

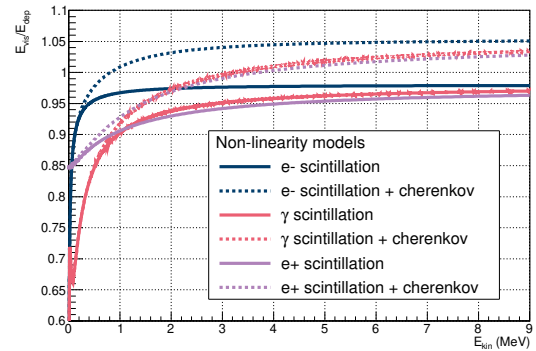


Figure 21: The non-linearity models for positrons (purple), electrons (blue), and gammas (red) as the ratio of the visible energy to the total deposited energy in the detector. The solid curves show the non-linearity curves for scintillation light only, while the dashed curves include also the Cherenkov light. Published in<sup>22</sup>.

duced after Cosmic Rays interactions in the atmosphere, can be observed in JUNO. Since 2020, this topic is of particular interest of the IKP-2 group, in particular on the spectral and oscillation analysis. A paper about the measurement of the atmospheric neutrino energy spectrum is currently in the process of review by the publication committee of JUNO collaboration. JUNO will also search for exotic phenomena, as non-standard interactions, sterile neutrinos, proton decay, and dark matter annihilation signals.

Robust and reliable analysis, event reconstruction, and Monte Carlo simulation is fundamental for all analysis. The IKP-2 neutrino group is involved in the development and testing of the event reconstruction and analysis methods. A substantial requirement to the JUNO experiment is the knowledge of the energy scale with a sub-percent precision. As the light yield of the liquid scintillator is not fully linear with respect to the deposited energy of the measured particle, a model has been developed within the group to describe this so-called non-linearity effect. This model uses the respectively simple non-linearity model of electrons to derive the more complex non-linearity model of gammas and combine both eventually to the required non-linearity model of positrons. The resulting non-linearities are shown in Figure 21 as the ratio of the visible energy to the total deposited energy for the different particle types. Additionally to the scintillation light, solely shown with the solid curves, the smaller contribution of Cherenkov light is considered in the dashed curves.

The conversion uses an algorithm to calculate the secondary electron energies from an initial gamma, which was developed for that purpose and made accessible on the IKP-2 neutrino group webpage. The work has been summarized in a paper, which has been published in

<sup>18</sup>Optimization of the JUNO liquid scintillator composition using a Daya Bay antineutrino detector, *NIM Phys. Res. Sec. A* 988 (2021) 164823

<sup>19</sup>Calibration Strategy of the JUNO Experiment, *arXiv:2011.06405* (2020)

<sup>20</sup>Combined sensitivity to the neutrino mass ordering with JUNO, the IceCube Upgrade, and PINGU, *Phys. Rev. D* 101 (2020) 032006

<sup>21</sup>Feasibility and physics potential of detecting  $^8\text{B}$  solar neutrinos at JUNO, *Chin. Phys. C* 45 (2021) 023004

Journal of Instrumentation in 2020<sup>22</sup>.

Event reconstruction techniques based on machine-learning algorithms are also developed in the group, with the application in waveform, energy, and position reconstructions, as well as in the pulse shape event discrimination. A paper, where the result of the latter application is presented, has been published in Journal of Instrumentation<sup>23</sup>.

The group activity includes also the development of clustering techniques for event reconstruction. JUNO liquid scintillator will indeed contain a non-negligible amount of the radioactive isotope  $^{14}\text{C}$ , which can not be removed due to its chemical similarity to the major isotope  $^{12}\text{C}$ . Pile-up of these events can worsen the sensitivity to the neutrino MO. Clustering algorithms aim to identify multiple events signatures inside one DAQ event and thus to remove the  $^{14}\text{C}$  component. This studies lead to the development of a more precise vertex reconstruction algorithm.

### 3.3 OSIRIS

The main goal of JUNO, the determination of the MO, as well as other measurements in the low-energy region, such as solar neutrinos, could be highly impaired by radioactive contaminations of the liquid scintillator. For the neutrino MO-analysis a concentration of  $^{238}\text{U}$  and  $^{232}\text{Th}$  less than  $10^{-15}$  g/g in the liquid scintillator is required, while for the solar neutrino analysis this requirement is one order of magnitude tighter. To ensure the observance of these limits, the Online Scintillator Internal Radioactivity Investigation System (OSIRIS) is developed. This pre-detector is designed to monitor the radioactivity of the liquid scintillator after its purification during the several months of filling procedure of the large 20 kt JUNO detector. OSIRIS can contain about 18 t of liquid scintillator and samples from each purification batch will be constantly flown through it. The principle of measuring the levels of  $^{238}\text{U}$  and  $^{232}\text{Th}$  contamination's lies in identification of the fast time-coincident decays of the isotope pairs  $^{214}\text{Bi}$ - $^{214}\text{Po}$  and  $^{212}\text{Bi}$ - $^{212}\text{Po}$ , respectively. In addition, OSIRIS will be able to measure the  $^{14}\text{C}$  concentration down to a  $^{14}\text{C}/^{12}\text{C}$  ratio of  $10^{-17}$  at 90% C.L.

The OSIRIS detector design consists of two optically separated vessels. The inner vessel is an acrylic cylinder with a diameter and height of 3 m each. It holds the 18 t of scintillator and is observed by 64 20"-PMTs. These PMTs are held by a steel frame which is fully contained in the outer vessel. Due to the purpose of OSIRIS to constantly monitor the liquid scintillator quality, it has an inlet on the top and an outlet in the bottom of the inner vessel: both equipped with a diffuser to ensure an equal distribution of the scintillator in the vessel. The outer vessel

<sup>22</sup>A semi-analytical energy response model for low-energy events in JUNO, *JINST* 15 (2020) 10007

<sup>23</sup>Particle identification at MeV energies in JUNO, *JINST* 16 (2021) 01016



Figure 22: A photograph of the Automated Calibration Unit, which will be used to lower sources into the scintillator volume of OSIRIS detector. The different pulleys allow the automatic selection and use of different pre-mounted calibration sources.

is a stainless steel cylinder filled with water, which serves as a buffer volume to shield against external radioactivity from the surrounding rock. It is equipped with additional 12 20"-PMTs that will detect the Cherenkov light from cosmogenic muons.

The readout design of the PMT's will use a novel approach. To maximize the quality of the signal, the readout electronics as well as the digitizer is placed directly inside the base of the PMT, which is then powered and read out with a single ethernet cable. This enables better impedance matching of the PMT base and therefore a higher quality of the signal. The analogue-to-digital converter chip was developed in the ZEA-2 institute of FZJ, while the effort in integrating this chip and developing the readout electronics stack is led by RWTH Aachen. IKP-2 neutrino group supports the respective working group from RWTH Aachen in the efforts of testing and preparing the PMT system to be shipped to the experimental site in China. In these efforts, simulation studies on the PMT holding structures were performed, which resulted in a reinforced improved design. A cleaning procedure for the PMT system was developed and prepared to minimize the dust contamination of OSIRIS.

In this novel readout design approach, the PMTs send out digitized waveforms alongside with their corresponding GPS time stamps without the requirement and existence of a conventional hardware trigger system. Instead, the waveforms are sorted according to their time stamps and a software trigger is formed, which is used to construct

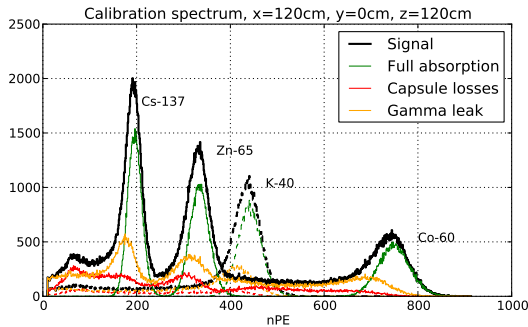


Figure 23: The expected charge spectrum, expressed in number of photoelectrons, of  $\gamma$ 's from the sources placed at the edge of OSIRIS detector. Each black peak represents the spectrum from one isotope labeled next to it. The coloured lines show different contributions to the black spectrum; (green) the full absorption peak of the gammas depositing their total energy in the scintillator; (red) gammas losing parts of their energy in the calibration capsule; (orange) gammas partially depositing energy outside of the scintillator volume due to their long track length. The spectrum of the combined  $^{60}\text{Co}$ - $^{65}\text{Zn}$ - $^{137}\text{Cs}$  source is shown with solid lines, while the spectrum of the  $^{40}\text{K}$  source is shown with dashed lines.

events to be collected for the analysis. This trigger is optimized on the ability to detect low-energy events, namely  $^{14}\text{C}$   $\beta$ -decays with 156 keV end point, while maintaining a reasonable low event rate due to PMTs' dark noise. Furthermore, to give out early warnings in case of a radioactively contaminated batch, the collected data needs to be analyzed in real-time. The IKP-2 neutrino group is highly involved in the development of the trigger, event reconstruction, and online analysis software and algorithms. The responsibility of the IKP-2 neutrino group is the development of the calibration system, which will utilize  $\gamma$  radioactive sources to characterize the detector response in terms of energy and position reconstructions, as well as pulsed LED for PMTs' time and charge calibration. Both radioactive sources and the LED will be deployed in the detector along the off-center vertical axis with the help of the ACU (Automatic Calibration Unit), kindly provided by the Daya Bay collaboration. A photograph of the ACU top can be seen in Figure 22, while the expected spectrum of two radioactive sources at one position on the calibration axis in the OSIRIS detector is shown in Figure 23. A substantial effort has been made to adapt the unit in OSIRIS and to plan the whole calibration procedure with a minimal risk of the contamination of the scintillator.

## 4 Accelerator Research

### 4.1 Tools for Beam Diagnostics and Control

During 2020 the efforts to improve beam diagnostics and control have been continued. Several new tools were de-

veloped and existing ones improved. By continuously migrating our systems to the control system EPICS, we take advantage of its new capabilities. The activities are driven by the needs of the operating crew as well as the requirements of the experiments. Here we give an overview on the recent progress.

### Control System Studio Upgrade

The user interface to the control system is implemented with the Eclipse-based Control System Studio software. The variant used at COSY is encompassing BOY (Best OPI - Operator Interface - Yet) GUI development and operation, Saving and Restoring of various machine and subsystem states and parameters, Data Browser interface to the EPICS Archiver, and the COSY tailored Orbit Correction interface.

The software package was updated to the most recent community version, bringing in more functions and utilities and allowing to keep the control system interface upgradable and expandable.

The Phoebus Architecture is planned to succeed the Eclipse basis and allow stand-alone, slimmer displays as well as compatibility to EPICS V4. The Display Builder will in time replace BOY; due to these functioning in parallel the transition can happen at convenience.

The Save&Restore module was improved to handle complete machine states consisting of multiple subsystems which were stored individually up to now. This modification is preparing an implementation of experiment-to-experiment restoring function.

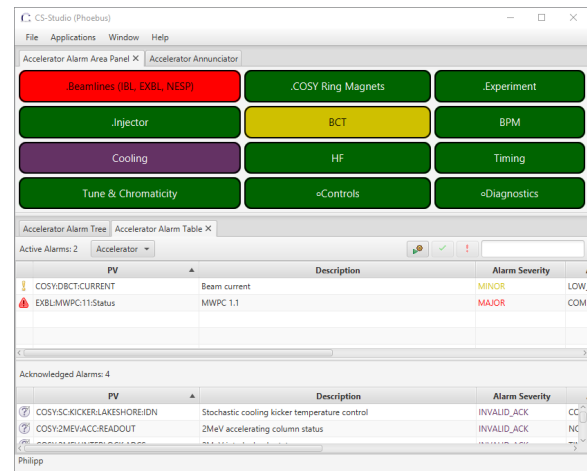


Figure 24: EPICS Alarm Display

### EPICS alarm server and display

A new alarm display is another module of the Phoebus Architecture. It was commissioned together with the alarm server infrastructure. It allows monitoring of EPICS based systems, providing a clear control room display as shown in figure 24. This allows operators to notice and locate issues immediately. The problem can

then be addressed with support contents directly accessible from the alarm message. Conditional filters and acknowledgement ensures that only relevant issues are shown, e.g. by excluding systems under maintenance.

### MAD-X Model Upgrade and Integration

Model calculations are an integral part of accelerator research and operation. The improved and updated MAD-X model of COSY was introduced in 2020 together with a periphery of tools and services. Most notably, the SQL database listing all accelerator components was revised and a MAD-X-Generator was build that converts the parameters from the database into MAD-X compatible input files. The tools were integrated into the control system with the help of a dedicated EPICS IOC and GUI. This enables the operators to calculate and compare essential beam dynamic quantities with different parametrization (figure 25). Some of which – like tune and orbit – can also be compared with the corresponding measured values. The new model development based on MAD-X and tools around it is described in a dedicated article on page 99 of the individual contributions.

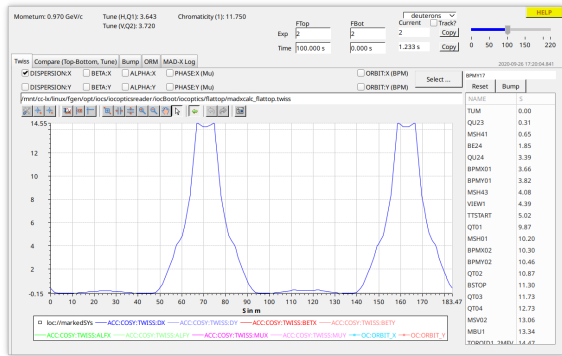


Figure 25: MAD-X Twiss GUI

### Frequency Sweep Tool

The COSY RF is controlled by a set of predefined piecewise polynomials (splines) stored in a so called *fgen* file. Recently a new tool was developed that allows to easily add an arbitrary number of frequency sweeps or jumps to the *fgen* files. These are defined by their amplitude, duration and times. The tool was primarily developed in conjunction with a chromaticity measurement (see below), to induce a slow but steady momentum change on the beam. In the course of this development, a comprehensive python *fgen* library was created. The library allows to easily generate, modify and parse *fgen* files, not only for the frequency but also for the magnetic fields.

### Beam current monitor capturing

The data acquisition of the BCT (beam current transformer) is based on EtherCAT and integrated in EPICS. It has received an update allowing for convenient, detailed

capturing of the beam current during injection and acceleration processes by means of EPICS. This enables an easier setup and optimization of the machine by the operations crew. Figure 26 shows how the new display helped to track down a beam loss during acceleration.

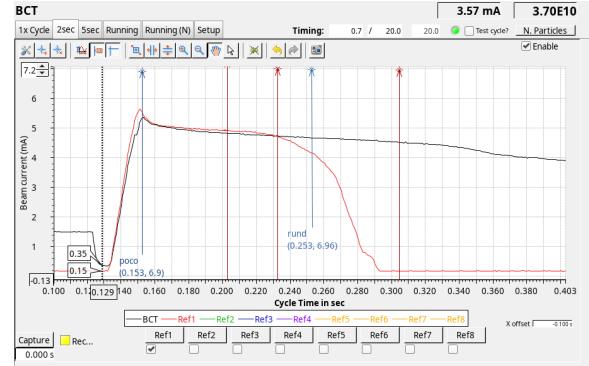


Figure 26: BCT signal captured during rampup

### Chromaticity Measurement

Based on the fast tune measurement system a chromaticity measurement has been developed. It utilizes the classical method of a momentum change induced by an RF frequency change. During a slow frequency sweep the tune is monitored continuously and the chromaticity derived from linear fits to the tune and frequency change given the slip factor. Figure 27 shows an exemplary measurement. The development was driven by the requirements of the JEDI collaboration and successfully used during the JEDI run in September 2020.

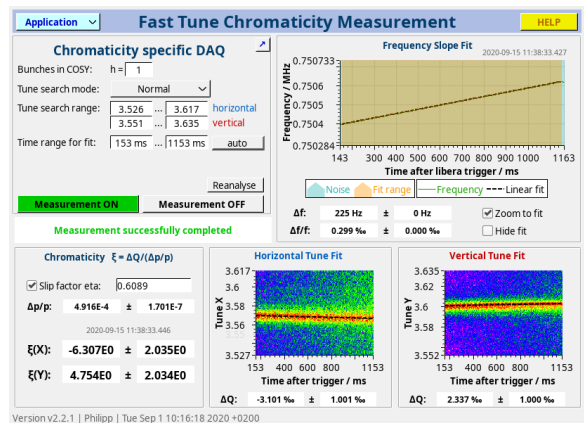


Figure 27: Chromaticity measurement GUI

### Momentum Compaction and Slip Factor Measurement

The method for determination of the momentum compaction factor  $\alpha_p$  and the slip factor  $\eta = \gamma^{-2} - \alpha_p$  has been revised. A measurement of the revolution frequency as a function of the dipole field strength (B-jump) yields

$\alpha_p$ . The established method required manual adjustments of the dipoles over several machine cycles. The frequencies measured by means of a Schottky spectrum had to be entered into a spreadsheet like interface, all of which was an effortful and time-consuming task. The measurement routine was now incorporated into the Schottky spectrum GUI, where the dipole current and RF frequency are automatically read out, displayed and fitted. Furthermore, the dipole strength is now ramped slowly, allowing for a measurement within a single machine cycle and only one set-up step. This improves usability and significantly reduces the time needed for such a measurement.

## Orbit Control

The development of the Orbit Control software continued, including the BPM-IOC (consolidating the Libera-, 2MeV-, and Rogowski-BPM data), the Steerer-IOC (controlling the COSY steerers), the Orbit Correction (OC) IOC (performing the closed orbit feedback), the Optics-IOC mentioned prior (also calculating the Orbit Response Matrix (ORM) from the model), and the ORM measurement software. Apart from multiple small bug fixes and convenience changes, there was a list of notable improvements.

The control over cyclic DC mode, originally developed for the OC, has been incorporated into the Steerer-IOC and was thereby centralized. This allows an easier development and integration of further algorithms, e.g. beam-based alignment, a bump application used during the JEDI beamtime and the ORM measurement. Some of these are already in the process of integration.

To regulate the multitude of algorithms – some of which could potentially erroneously run in concurrence – a soft locking mechanism was implemented in the Steerer- and OC-IOC that inhibits double-usage of COSY-steerers. Additionally, an algorithm template with the soft-lock and exemplary steerer access is being developed for broader usage and further extension.

A new alarming facility was introduced for Steerer magnet currents, comparing the actual and nominal values. It uses the power supply monitoring and acquisition already implemented in EPICS.

Parts of the OC-IOC's functionality were also incorporated into the BPM-IOC. This includes the reconstruction of orbits from individual measurements as well as the detection of BPM malfunctions, which was integrated into the alarming system.

## Generic FPGA-based Integrator for Beam Instrumentation Applications

For several systems like ionization chambers (IC), beam cups (BC) and fast current transformers (FCT) the integral of signal pulses is of interest. For this purpose a custom FPGA firmware for the Red Pitaya SoC platform was written and its embedded EPICS IOC expanded. Here we introduce three modes of operation.

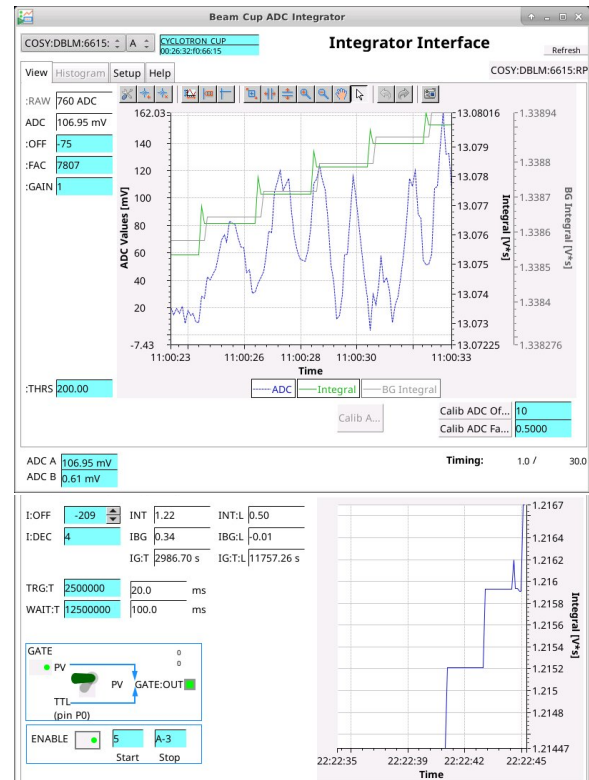


Figure 28: (1) GUI for Beam Cup signal; (2) GUI of Integrator Setup; (3) Concept of background suppression

First mode delivered by the ionization chambers used in diagnostics of beam extracted from the COSY ring. The signals are continuous and rather slow (seconds or minutes). The integrator is using the 14bit ADC sampling of up to 8ns or an adjustable multiple. An arbitrary digital offset can be defined to avoid intrinsic signal offsets. Integration in the FPGA is continuous until a reset signal (manual or automatic e.g. at cycle end) is received, then the value is zeroed. The integral value for the previous extraction cycle as well as continuous intermediate integral are provided via EPICS process variables (PVs).

Second mode is common for beam-cups hit by periodic short bursts of particles with longer intermissions. A threshold for an integration start has to be defined. The duration of integration is up to 34 seconds, with the behaviour similar to the first mode. For effective baseline shift suppression a waiting time can be defined after which another integration window starts with the result being added to a separate background register (c.f. figure 28). Considering the timing parameters and subtracting the register value from the integral allows estimating

integral values even with highly variable background (see figure 28). This integration was also successfully used for conceptual detector studies related to the future High Brilliance Neutron Source (HBS).

The reset facility described above is augmented by a gate signal, delivered either directly via a TTL input or an EPICS PV. These define runs of several machine cycles, writing out separate integral and background values. Additionally the duty time of the integration is counted.

Another integrator mode was prepared in the scope of a bachelor thesis. The FCT delivers a bunch synchronous signal from stored beam directly and the above integration approaches are not suitable: The baseline subtraction is essential for the high signal repetition rate and there is frequently not enough time between the bunches to estimate the baseline as described in the second mode. A dedicated module chain (c.f. figure 29) was implemented performing parametric signal smoothing, bunch detection, baseline estimation, bunch selection and finally integration. Further details are given in the thesis.

Integration of the FCT mode into the control system and its introduction into operation are in preparation.

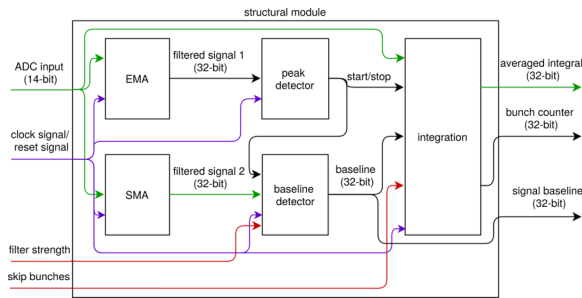


Figure 29: Module design of the FCT integrator

## 4.2 Injector

The JULIC cyclotron serves as injector for the storage ring COSY, accelerating polarised and unpolarised protons and deuterons to the injection energies of 45 and 75 MeV for the protons and deuterons, respectively.

The maximum energies of the extracted JULIC beams are limited by the parameters of the cyclotron RF-system and extraction elements. Although the cyclotron was routinely operational with deuterium beam at 75 MeV, especially the cyclotron extraction electrostatic septum was a subject for permanent monitoring and concern due to the rather high extraction voltage of 34.4 kV. On the other hand, intensity in COSY was never limited by a space charge effect and hence the injection of the higher energy particles was not motivated by the accelerator physics arguments.

In order to reduce high voltage at the cyclotron electrostatic septum a new cyclotron mode of operation with deuteron beam was developed in summer 2020. After a week of the machine development, a 55 MeV deuteron beam was for the first time injected, stored, and accelerated to the 970 MeV in COSY. No major intensity losses

in COSY due to the space charge limit effects at the injection have been observed. At the same time, the number of sparks in the cyclotron septum was significantly reduced, due to decrease of the extraction voltage to 27.7 kV. This step will significantly increase stability of the cyclotron operation and a septum exchange interval. Furthermore, cyclotron RF-system operation at 23.3 MHz is more stable than at 27.3 MHz, allowing to reduce the number of interruptions during the COSY operation due to the cyclotron RF restarts. The COSY injection energy reduction allowed to decrease currents in the Injection Beam Line (IBL) magnets, and hence to improve IBL power supplies operation stability. Polarimetry of the 55 MeV deuterons was done with NEPOL polarimeter in the IBL using detector angles of 55° and agrees well with the results of previous measurements.

Since September 2020 COSY is injecting polarised and unpolarised deuterons accelerated in JULIC cyclotron to the 55 MeV.

## 4.3 Progress of the HESR

### Introduction

IKP is leading the international consortium which is dedicated to build the HESR. It is strongly supported by colleagues from the Central Institutes for Engineering and Analytics (ZEA) of the Research Center Jülich. By the end of 2020 about 79% (previous year: 68%) of the total project investment money has been either spent or bound by contract. All planning is re-adjusted to deliver the pre-assembled HESR hardware components with the available personnel to FAIR as soon as possible to the storage hall or in time for the installation dates. Deliveries are planned to happen significantly before 31-Dec-2024. There is one exception to this date: The site acceptance test of the power supplies for the main dipole magnets can only be done on the installed and wired dipole magnets as no test load is available. Thus this delivery date is depending on the end of installation in the tunnel. Main impacts in 2020 were

- *Corona-induced lockdowns* Hardware work had to be re-organized. Nearly all communication with the relevant partners is now done via video conferences or by email.
- *transfer of IKP personnel to GSI* Starting in the second half of the year each colleague was involved to prepare for a possible change in her / his working contract. Some colleagues are no longer available for the project. Hiring new staff is not possible for IKP.
- *Rebaselining the FAIR schedule* Start of the pit works for the HESR tunnel is now scheduled for Q1/2023. The scheduled dates for start of testing and commissioning are moved beyond Q3/2024. The compliance of the planned installations especially in the PANDA hall with respect to earth-

quake resistance will only be possible after the oscillation modes of the building will become available from the architects (app. 2022/2023).

### Work Package Magnets and Pre-Assembly

The special beam pipes in the 4 dipole magnets in the neighbourhood of the SPARC target places are NEG coated and delivered to Jülich. The pre-assembly of these last 4 dipole magnets is scheduled for early 2021, followed by the delivery to the storage hall.

The pre-assembly of the first quadrupole unit in the arc sections has started, see Figure 30. The sequence of the planned assembly steps is being optimized. The first beam position monitors (BPMs) and the ion clearing chambers (ICCs) have been delivered by their respective manufacturers and are available for assembling the first units. In parallel, the quadrupole magnets are prepared for installation on the girders, i.e. mount 4 additional ancillary fiducials and 1 interlock adaption box.

The delivery of the correction magnets (steerers and sextupoles) by our Romanian partner for magnet fabrication is completed.

### Work Package Power Converters

The specification of the 2 main dipole power converters is approved by all relevant working groups. It will be used for the call for tender once we can add a serious date for delivery, i.e. the HESR buildings must be contracted.

EMC measurements for the power converters contributed by our Romanian partners are now performed on a routine basis. Issues with the ACU system and with details of how and where to store the acquired data are solved now. Checks of the long term stability were done for the first six power converters. The results allow a reduction of the frequency of the long term stability tests.

The power supply for the injection septa has been delivered and passed the site acceptance test. Key parameters are 386 kVA, 2500 A, 110 V. For protection of the septum magnets, a dedicated fast temperature interlock system has been developed. It monitors the current and the voltage at each coil with 1 megasample per second and will trigger the interlock at the power supply in case of dangerous deviations. After a successful test of this system the power converter will be released for storage.

### Work Package RF System

The cavities are being assembled in a clean-room, see Figure 31. Ferrite cores and amplifiers are already on site.

The work on the low level control system has started.

### Work Package Injection

The first two systems (magnet + pulser) have been tested successfully. The tests proved that after assembly into the



Figure 30: chicane Assembly of the quadrupole unit. Top: Beam direction from left to right. Components along the beam: Small pumping chamber 'floating bearing', sextupole magnet, beam position monitor with vacuum chamber extensions, quadrupole magnet, sextupole magnet, large pumping chamber 'fixed bearing'. All vacuum chambers or pipes are equipped with heating jackets. Stand for the laser tracker in the background. Bottom: Snapshot from the other side, beam direction from right to left. Turbomolecular pump attached to the pumping chamber 'fixed bearing' to allow immediate check of the vacuum assembly.

vacuum tank the required rise / fall time of the 3.6 kA current pulse is below 220 ns for each system, see Figure 32. The original coaxial cables that were developed for these systems were used. 4 systems of magnet and pulser are needed to obtain the required 6.4 mrad deflection at the injection beam rigidity of 13 Tm.

### Work Package Beam Diagnostics

The beam position monitor (BPM) fabrication is now on a routine level. Problems with the fabrication of the long types have been analysed and solved. The production encountered technical problems with specific welds. These problems were thoroughly investigated and solved. Now the production is running smoothly. For each BPM the geometry is measured individually on a test stand to de-

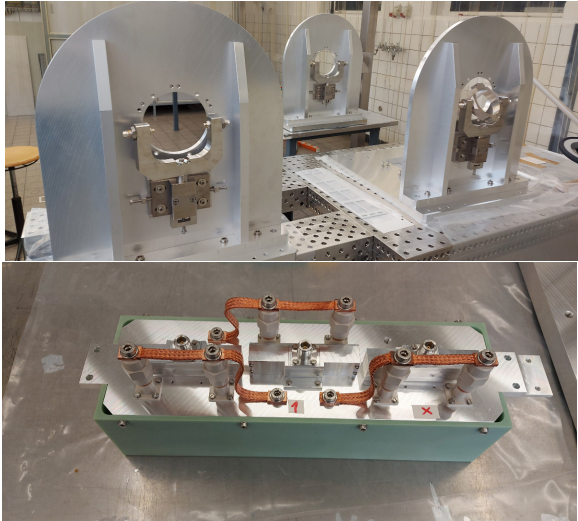


Figure 31: Top: Setting up the assembly bench in the clean room for the cavities. Bottom: The current feedthrough for the coils.

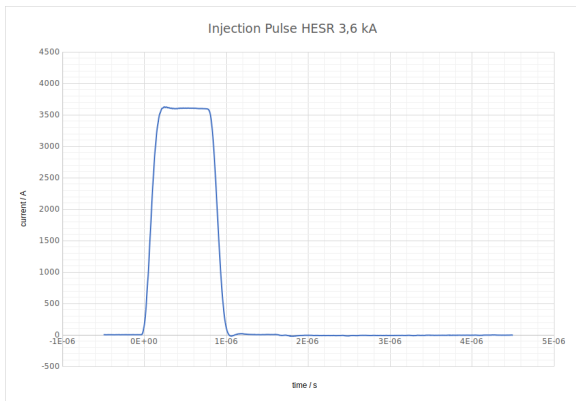


Figure 32: Current pulse for injection into the HESR. The revolution time is about 2000  $\mu$ s. The complete magnet pulse must not be longer than 1000 ns.

termine the calibration factors for a precise beam position measurement in the accelerator.

Two full scraper modules were fabricated, each with 4 jaws i.e. left, right, top, bottom. Figure 33 shows an assembled scraper unit, one flange on the beam axis removed. The heating jackets arrived and will be assembled after software tests.

The first viewer (destructive beam profile measurement) was built. This first one is foreseen to be placed at the end of the high energy beam line (HEBT). Four more ones are planned within the HESR ring, but with an extension: If the screen is moved out of the beam path an RF cage is moved into its position to have a better RF conductivity within the ring.

The mechanical design work for the non-destructive ionization beam profile monitor has been completed. The next step is the design review together with GSI. It is scheduled for 2021. This design will also be used for the about 40 units for HEBT subproject at FAIR as well.

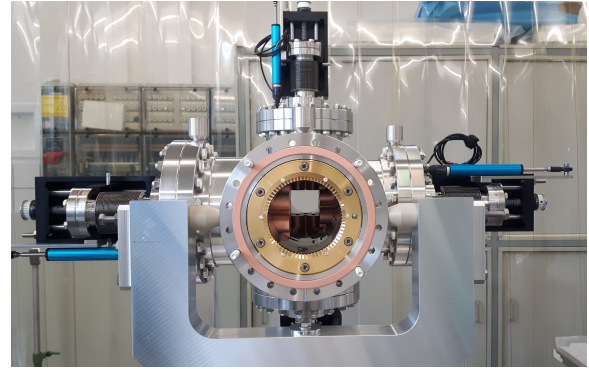


Figure 33: One of the scraper systems in the clean room. The inner 'golden' insert is the circular spring contact for a low impedance connection to the beam pipe.

The BLM system has been designed and first work on the integration into the FAIR control system has started. As for this system in relation to hardware a working setup is already present on site, it was used as a showcase for the integration into the FESA control system of FAIR. The external company Cosylab set up a stand-alone FESA environment in which the BLM system is integrated for learning purposes. In 2021 an training for operators and programmers on the system will follow.

In addition the work on slow controls for the beam instrumentation was started. Mainly the stepper motor drivers and the pneumatic drives for the scrapers and viewers will be controlled with that, but also the camera settings for the viewers a. o. are planned. This task has been started in close cooperation with the GSI BI department and the radiation protection group of IKP, whose members have a deep knowledge of PLC systems because of their work for the personnel protection system of COSY.

### Work Package Vacuum, Girders and Space Management

The mechanical design of the girders for the straight sections is completed and the mechanical properties during transport and operation could be verified in a simulation. The call for tender has been published. Most heating jackets are already ordered. The biggest efforts have been tracking of contracts, finding solutions for problems which are beyond the scope of the selected manufacturers, verifying the quality of delivered components, and space management. A concept for merging the space requests in the tunnel for cabling, connection boxes, installation aids and a mobile crane has been developed, see Figure 34. The girders for the septum magnets and the injection dipole magnet have been produced.

Uploading and updating the documentation of individual components to the electronic data management system is approaching a routine operation.

The interface of the vacuum system of the SPARC experiment to the HESR vacuum control could be defined to guarantee a smooth change between the experiment in-

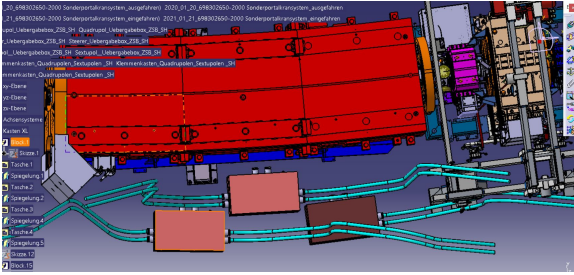


Figure 34: Dipole and quadrupole group with connection boxes. Cables between the connection boxes and the magnets on the girder of the quadrupole group are not shown. Frame of the mobile crane needed for maintenance at the quadrupole group is indicated on the right side of the (red) dipole magnet.

stallation and reverting to the situation without the experiment.

### Work Package Stochastic Cooling

The pre-assembly of each stochastic tank on its own girder with water manifolds, amplifier connections etc. is progressing well (see Fig. 35). Detailed descriptions of the assembly steps are being recorded. The feedback line will be of the optical fiber type. Mode damper beam pipes are being assembled.



Figure 35: Stochastic kicker tank on girder. One half of the water-cooled high power amplifiers is visible, the other half is on the back.

## Work Package Experiment Integration

Girders for the chicane dipole magnets are being designed. The specification of the compensation solenoid is still being prepared. Preparations for the acquisition of the big magnet in the middle of the PANDA chicane are in progress. Details of the interfaces between experiment and HESR are continuously monitored and optimized.

## 5 Further Activities

### 5.1 PAX-project development

#### Introduction

The PAX-project aims to provide a method to produce an intense beam of polarized antiprotons. It was supported by an ERC-Advanced Grant ("POLPBAR") between 2010 and 2016, and it is now in a Joint Research Activity (JRA) of the "STRONG 2020" project. After having successfully performed a spin-filtering test with protons using a transversely polarized hydrogen gas target <sup>24</sup>, the PAX Collaboration plans to complete these studies with a test of longitudinal polarization buildup at COSY. In order to ensure that the beam polarization is oriented in the longitudinal direction in the COSY straight section where the PAX interaction point is located, a superconducting solenoid, a so called "Siberian Snake", has been installed in the opposite straight section of the ring (Fig.36).

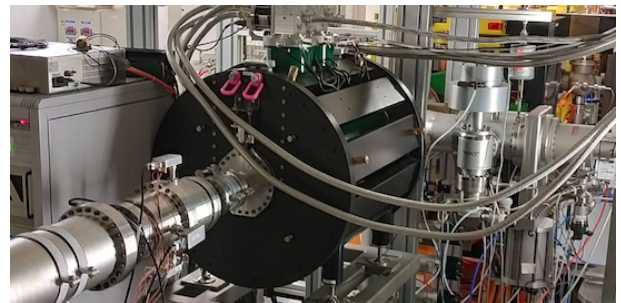


Figure 36: Siberian Snake installed in COSY

The approval by the EU of the STRONG2020 proposal, that includes a work package dedicated to the longitudinal spin-filtering test at COSY ("SPINforFAIR"), offers us the chance to revise the status of these studies and identify a plan for the performance of the measurement. Basically two preliminary steps are required:

- commissioning of the complete PAX detector with four quadrants;
- commissioning of the Siberian snake with protons.

<sup>24</sup>Polarization of a stored beam by spin-filtering *Phys. Lett. B* 718(1) (2012) 64

The completion of the proposed studies is of outmost importance in view of the possible introduction of a polarization in the FAIR facility and puts COSY and its related competence in polarization technology to play a leading role.

### Siberian Snake

In preparation of the longitudinal spin-filtering test, the first snake commissioning beam time took place at COSY in March 2020. For this commissioning, the idea was to inject a vertically polarized proton beam into COSY, electron-cool and accelerate it up to a momentum of 521 MeV/c. By ramping the solenoid from zero to 2.7 Tm, the vertical beam polarization would then be transferred into the horizontal plane<sup>25</sup>. During the ramp-up a shift in the betatron tunes was observed. To counteract it, the Snake ramp was performed step wise and in parallel a slow quadrupole jump was performed. The action of the Snake could be simulated using a MAD-X model of COSY. During operations, it was also found that the chosen tune working point at the start of the snake rump-up could not be reached with the snake on. This happens because, as soon as the solenoid is switched on, it introduces a strong phase space coupling, that creates a tune split around the resonance  $\nu_x - \nu_y = 0$ , thus a region of the tune phase space that cannot be accessed (Fig.37).

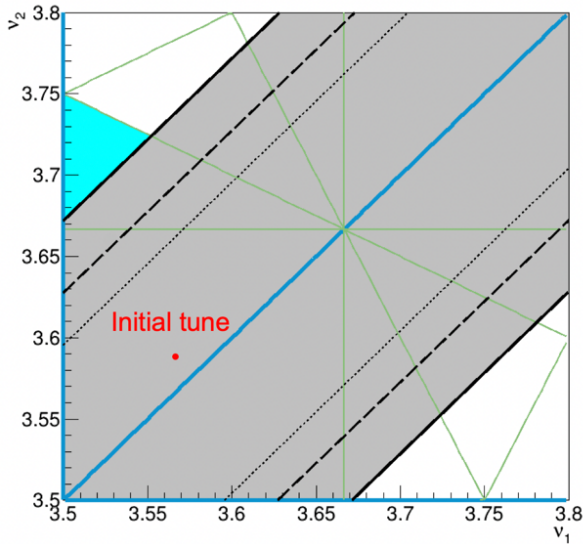


Figure 37: Tune split (preliminary simulation, courtesy of Dr. J. Hetzel): the tunes within the grey-shaded area are not reachable (dotted lines: tune split at 1.5 T, dashed lines: 2.0 T, solid lines: 2.7 T).

The width of such a split can be calculated in dependence of the solenoidal field  $B_{Sol}$  as the following:

$$\Delta\nu_{min} = \frac{gB_{Sol}L}{4|B\rho|} \quad (5)$$

where  $L$  is the effective length of the solenoidal field,  $|B\rho|$  is the magnetic rigidity, and  $g$  is a factor depending on the beta-functions at the solenoid location. Further investigation is required in order to solve this issue.

### PAX Detector

In order to cope with the foreseen experimental activities, a large acceptance silicon vertex detector has been realized in collaboration between the University and INFN of Ferrara (Italy) and the FZJ to serve as a beam and target polarimeter in proton-(anti)proton and proton-deuteron internal gas target experiments in the 30 MeV to 200 MeV beam energy range<sup>26</sup>. It will provide an absolute calibration of the atomic Breit-Rabi polarimeter of the polarized target. At the same time it will serve as a beam position monitor in the beam-target interaction region.

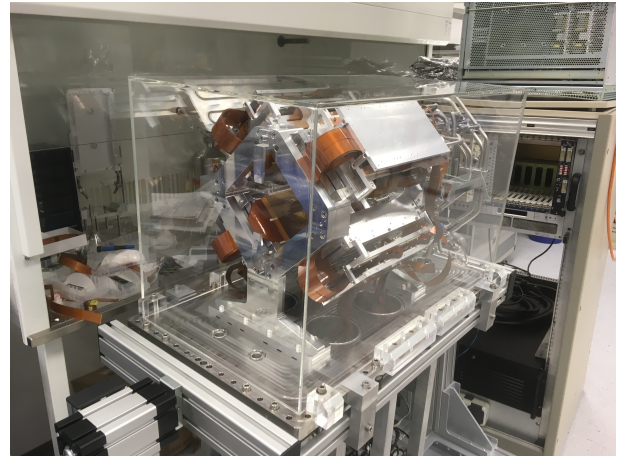


Figure 38: Fully assembled PAX detector.

The detector is composed of four identical quadrants, mounted in a diamond configuration around an openable storage cell. Each quadrant consists of three layers of double-sided silicon-strip sensors, mounted inside an aluminum box, and a front-end readout system. Three kinds of 100 mm x 100 mm silicon sensors are mounted, some of which have been recovered from the HERMES experiment at DESY-HERA. The electronic readout and the silicon sensors are cooled down by two separate cooling circuits. After a first commissioning at COSY in March 2017, with two complete quadrants, the PAX detector has been fully assembled (Fig.38) and is ready for its final commissioning.

<sup>25</sup>Low-energy spin-physics experiments with polarized beams and targets at the COSY storage ring [EPJ Techn Instrum 6 \(2019\) 2](#)

<sup>26</sup>Low-energy spin-physics experiments with polarized beams and targets at the COSY storage ring [EPJ Techn Instrum 6 \(2019\) 2](#)

## 5.2 Laser-Plasma Acceleration of Polarized Beams

### Introduction

Spin-polarized particle beams are of crucial importance for nuclear and particle physics. Strategies that could lead to the generation of polarized electron, proton and ion beams in next generation accelerator facilities based on ultra-intense lasers are under intensive investigations. Recently rapid progress has been made in the development of numerical tools to describe the effect of the huge and rapidly changing laser-plasma magnetic fields on the particle spins. In parallel, first polarized targets, tailored for laser applications, are now in the commissioning phase. The development of laser-plasma accelerated polarized beams relies on several key competences: beam and spin simulation with particle-in-cell codes, production and handling of polarized sources and targets and experience with experiments at conventional storage rings (beam transport and polarimetry) as well as the expertise to operate ultra-intense laser systems. For an in-depth description of this research area, we refer to our recent Review Paper <sup>27</sup>.

### Current Status

One unexplored field of particle acceleration is the precession of particle spins in huge magnetic fields inherently present in relativistic plasmas. Laser-driven generation of polarized proton and <sup>3</sup>He-ion beams in combination with the development of advanced target technologies is being pursued by our group in the framework of the JuSPARC facility <sup>28</sup> and the ATHENA consortium („Accelerator Technology HELmholtz iNfrAstructure”). These novel target technologies will be tested at different laser facilities, e.g. at the 10 Petawatt laser system SULF at SIOM/Shanghai (China) and the PHELIX Petawatt Laser Facility in Darmstadt (Germany) in the near future. A pre-polarized <sup>3</sup>He gas-jet target will be utilized for the experiments at PHELIX. For the experimental realization of a polarized proton beam in the GeV regime at SULF, a pre-polarized target based on an HCl gas jet is under construction at IKP. Finally, these targets can also be utilized in the future stages of JuSPARC with laser intensities from the roughly hundred Terawatt up to the Petawatt level.

After demonstration of laser-accelerated polarized hadron beams, our targets can be modified such that they can also serve as sources of polarized electrons.

<sup>27</sup>Generation of polarized particle beams at relativistic laser intensities, High Power Laser Science and Engineering, 8, E36 (2020); doi:10.1017/hpl.2020.35

<sup>28</sup>JuSPARC - The Jülich Short-Pulsed Particle and Radiation Center, Journal of Large-scale Research Facilities 6, A138; DOI: 10.17815/jlsrf-6-174

### Simulation of Polarized Beam Acceleration

In order to predict the degree of beam polarization from a laser-driven plasma accelerator, particle-in-cell (PIC) simulations including spin effects have been carried out. For this purpose, the Thomas-BMT equation, describing the spin precession in electromagnetic fields, has been implemented into the VLPL (Virtual Laser Plasma Lab) code from the Institut für Theoretische Physik, Heinrich-Heine-Universität (HHU) Düsseldorf. A schematic overview of the interplay between single particle trajectories (blue), spin (red), and radiation (yellow) is shown in Figure 39. The simulations are car-

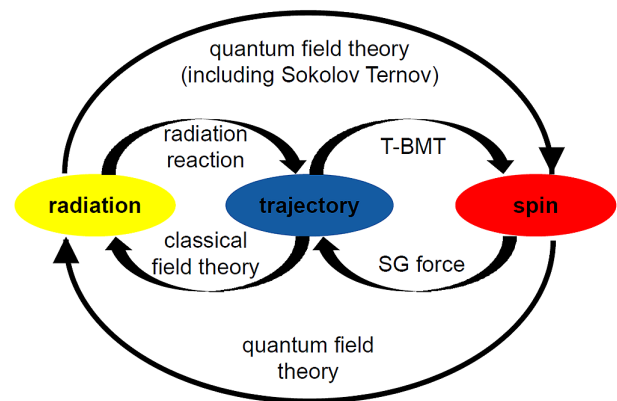


Figure 39: Sketch of the interplay between single particle trajectories (blue), spin (red) and radiation (yellow). Adapted from reference <sup>29</sup>.

ried out on the Jülich supercomputers in close cooperation of IKP-4, PGI-6, JSC and HHU Düsseldorf.

In a series of theoretical papers (see e.g. reference <sup>29</sup> and references therein) we have demonstrated that a crucial prerequisite for producing polarized relativistic particle beams is the availability of targets containing high-density pre-polarized nuclei.

### Polarized Target Development

We have also initiated the development of several polarized targets:

- A polarized HCl gas-jet target is under commissioning at IKP in Forschungszentrum Jülich. Beam energies of up to 100 MeV at high degrees of polarization (up to 82%) are expected from our PIC simulations for the experiments with nuclear polarized H atoms from the HCL jet at SULF.
- We have built a hyperpolarized <sup>3</sup>He gas-jet target for experiments at the PHELIX Petawatt Laser Facility at GSI in Darmstadt for measuring the spin-polarization degree of laser-accelerated <sup>3</sup>He<sup>2+</sup>

<sup>29</sup>Scaling laws for the depolarization time of relativistic particle beams in strong fields, Phys. Rev. Accel. Beams 23 (2020); DOI: 10.1103/PhysRevAccelBeams.23.064401

ions. The particular advantage of  $^3\text{He}$  gas is that it can be polarized, stored and transported at room temperature and can preserve high degrees of polarization over many hours.

- On a long-term scale, it is foreseen to freeze out polarized molecules from an atomic beam source on a cold surface below 10 K to collect the  $\text{D}_2$  or  $\text{HD}$  gas as polarized ice. This ice can be transported and used as targets for laser-acceleration experiments to produce polarized proton/deuteron beams or for laser-induced nuclear fusion with polarized fuel.
- In a collaboration with the Budker Institute for Nuclear Physics, Russia, financed by a joined DFG/RSF grant, another method for the production of polarized  $\text{H}_2$  and  $\text{D}_2$  molecules is on the way. The existing superconducting ABS (Atomic Beam Source) for the polarized target at the VEPP-3 electron-positron storage ring at Budker Institute was modified by the Russian partners to separate different hyperfine states of the molecules by the Stern-Gerlach method.

## Preparatory Experiments

The only experiment measuring the polarization of laser-accelerated protons has been performed by our group at the 100 TW ARCTurus laser facility at HHU Düsseldorf (Germany) almost a decade ago<sup>30</sup>. During these measurements (with an unpolarized foil target) we developed a polarimeter for MeV protons that is the basis for our future studies with polarized targets e.g. at SULF and PHELIX. A proof-of-principle experiment at PHELIX showed that (yet unpolarized)  $^3\text{He}$  ions can be accelerated to energies of a few MeV out of a  $^3\text{He}$  gas-jet target<sup>31</sup>. The measurements with polarized gas will continue in near future.

### 5.3 Spectroscopy with a Sona transition unit: Observation of direct transitions between quantum states with energy differences of 10 neV and below

In atomic and molecular spectroscopy the energy difference  $\Delta E$  between two states is observed through the absorption or (induced) emission of photons with the corresponding energy. The same processes can be described by absorption and emission of an electromagnetic wave with frequency  $f$  according to the Planck-Einstein relation  $\Delta E = h \cdot f$ . Since the velocity of any electromagnetic wave  $c = f \cdot \lambda$  is well known, the wavelength  $\lambda$  of the corresponding wave is defined. Absorption and induced emission of photons occur most likely, if the over-

lap of the atomic and the electromagnetic wave function is at maximum. This is a problem for very small energy differences, because the wavelength is getting large. That is why radio-frequency induced measurements at energies of  $10^{-6}$  eV (Lamb-shift of metastable hydrogen<sup>32</sup>  $\sim 1$  GHz  $\hat{=} \lambda \sim 0.2$  m) and below (Hyperfine-splitting energy of metastable hydrogen<sup>33</sup>  $\sim 177$  MHz  $\hat{=} \lambda \sim 1$  m) are conducted with a beam traveling through a cavity to store a constant radio-frequency inside. Thus, the measurement of smaller energy differences with direct induced transitions, e.g. the energies between hyperfine substates in the Breit-Rabi diagram at low magnetic fields (see Fig. 40), is limited due to increased technical difficulties to build larger cavities with sharp resonances. This problem can be overcome with an alternating static magnetic field along the beam line produced by two solenoids with opposing field directions, i.e. a Sona transition unit. In this case, the through-going atoms experience a non-adiabatic longitudinal zero-crossing and an oscillating radial magnetic field  $B_r$  in their rest frame that is able to induce magnetic dipole (M1) transitions with  $\Delta m_F = +/ - 1$  between the hyperfine substates. The wavelength  $\lambda$  is defined by the distance of the coils and the frequency  $f$  of the second harmonic of the radial oscillation corresponds to their velocity  $v_H$ , i.e.  $v_H = \lambda \cdot f$ . Thus, smaller beam velocities and larger coil distances allow one to decrease the photon energy to much lower energies than observed before for directly induced transitions.

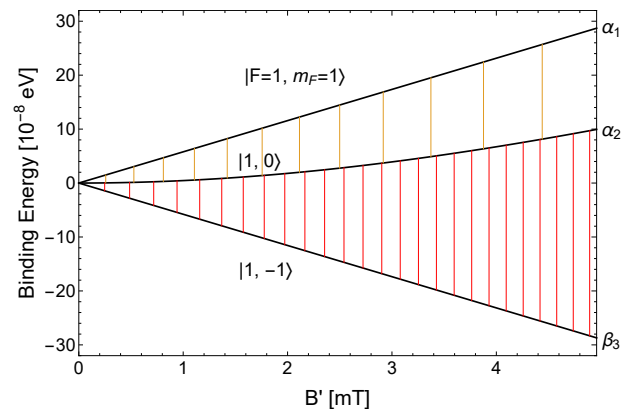


Figure 40: The Breit-Rabi diagram of metastable hydrogen atoms in the  $2S_{1/2}$  state with  $F = 1$  inside a magnetic field of up to 5 mT.

To test this new kind of spectroscopy we started with a beam of metastable hydrogen atoms, because the energy levels of the hyperfine substates and their dependence on an external magnetic field are theoretically fully understood within the Schrödinger equation (Breit-Rabi formula) including QED corrections. Here, the dominating

<sup>30</sup>Polarization measurement of laser-accelerated protons, Physics of Plasmas 21, 023104 (2014); DOI: 10.1063/1.4865096

<sup>31</sup>Laser-induced acceleration of Helium ions from unpolarized gas jets, Plasma Phys. Control. Fusion 61, 115012 (2019); <https://doi.org/10.1088/1361-6587/ab4613>

<sup>32</sup>W.E. Lamb and R.C. Retherford; Phys. Rev. **72** (1947) 241.

<sup>33</sup>N.E. Rothery and E. A. Hessels; Phys. Rev. A **61** (2000) 044501.

longitudinal magnetic field component inside the coils  $B_{max}$  corresponds to a magnetic field  $B' = 0.723 \cdot B_{max}$  that defines the energy distance between the substates within the Breit-Rabi diagram. If the current into the coils is enhanced, the magnetic field  $B'$  is increased, but the frequency seen by the atoms is unchanged. Only the amplitudes of the magnetic fields are raised, i.e. the radio-frequency power, respectively the number of photons is increased too.

For the first observation of these transitions even at very small magnetic fields the components of a Lamb-shift polarimeter, initially used at the polarized target of the ANKE@COSY experiment, were used: A proton beam at a beam energy of 1.28 keV ( $v_H = 4.95 \cdot 10^5$  m/s) is produced with an electron-impact ionizer and a Wien filter is used as velocity filter. By charge exchange with Cesium vapor metastable hydrogen atoms are produced and the different hyperfine substates are selected with a spinfilter to be used as ‘polarizer’. Afterwards, the Sona transition unit induces transitions between the substates, as long as the energy difference  $\Delta E = n \cdot h \cdot f$  is an integer multiple of the basic photon energy. A second spinfilter and a quenching chamber to measure the amount of residual metastable atoms, the ‘analyser’, allows us to observe the corresponding transitions as function of the current in the Sona coils or the magnetic field inside (see Fig. 41). The results of these measurements can be explained in

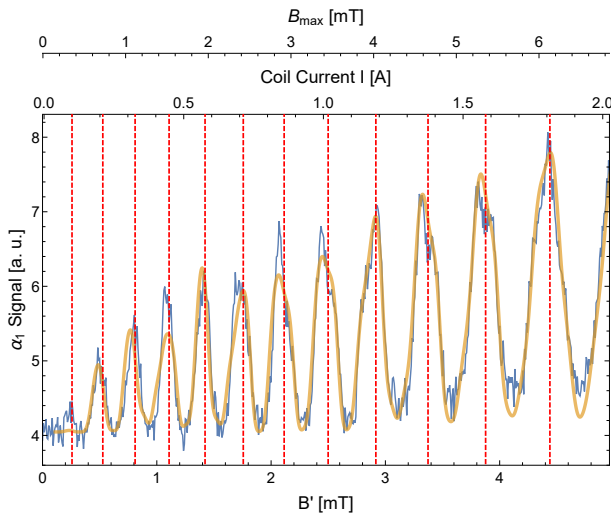


Figure 41: Observed resonances of the transition between the hyperfine substates  $\alpha_1$  and  $\alpha_2$  as function of the magnetic field inside the Sona coils (blue line), the corresponding simulations according to the Schrödinger equation (yellow) and the calibration of the resonances due to the Breit-Rabi diagram (red).

different ways:

- Like mentioned before, the complete process is fully understood and can be simulated within the Schrödinger equation (Breit-Rabi). Even the con-

tribution of further QED corrections are known and used for the predictions shown in Fig. 41 (yellow line). Details are given in Ref.<sup>34</sup>.

- During the measurements that delivers the results shown in Fig. 41 (blue line) the distance between the Sona coils was set to 60 mm. A Fourier analysis of the radial magnetic field between the Sona coils as function of time, when the z-axis is substituted by the known velocity of the beam ( $v_H = 4.95 \cdot 10^5$  m/s), delivers the basic frequency  $f = 3.536 \pm 0.012$  MHz and  $\lambda = 140$  mm with a good precision and, thus,  $\Delta E = (1.462 \pm 0.005) \cdot 10^{-8}$  eV.
- The integer multiples of the basic frequency  $f$  correspond to multi-photon transitions between the hyperfine substates  $\alpha_1$  and  $\alpha_2$  like shown in the example of Fig. 41. Thus, the Breit-Rabi diagram delivers the magnetic fields  $B'$  at which the binding energy differences  $\Delta E = n \cdot h \cdot f$  fits in between (yellow lines in Fig. 40/red lines in Fig. 41). Due to the non-linearity of these energy differences between these substates as function of the magnetic field  $B'$  it is even possible to calculate the basic frequency  $f$  from a calibration to the known Breit-Rabi diagram.

The energy resolution of these first experiments was in the order of  $10^{-11}$  eV/10 kHz. With further improvements, i.e. a better proton source to increase statistics, a more precise and stronger static magnetic field between the Sona coils and a variation of the distances between the solenoids, an absolute uncertainty of  $10^{-13}$  eV/100 Hz should be achievable. Thus, precise tests of the QED corrections of the Schrödinger theory are possible for metastable hydrogen and deuterium atoms. In principle, the beam velocity can be decreased further like in the work of Lamb and Retherford. With a velocity of just  $v_H = 10^3$  m/s the basic frequency is decreased down to  $f = 10$  kHz which would allow the control of energy differences of  $\Delta E = 10^{-10}$  eV between the hyperfine substates.

This method with a static magnetic field to decrease the velocity of electromagnetic waves in the rest frame of the atom or molecule to be explored, is applicable to any kind of beam. Of course, it is necessary to polarize the beam first, i.e. to populate a single quantum state only, and then to analyze the induced transitions afterwards. Here, this method was successfully been applied to induce magnetic dipole transitions between hyperfine substates of metastable hydrogen atoms and the results perfectly fit to the predictions of the Schrödinger equation. Therefore, the wave length  $\lambda$  of such a transition unit can be optimized for other quantum systems, atoms or molecules, where similar energy differences should be investigated and then calibrated to a measurement with metastable hydrogen atoms of given velocity. As long as

<sup>34</sup>Chr. Kannis et al.; contribution to this report.

the distance of the solenoids is kept constant the wavelength  $\lambda$  is preserved and, therefore, the induced photon energy  $\Delta E$ , can be manipulated by tuning the beam velocity. Another option of such a transition unit is the measurement of further Breit-Rabi diagrams, i.e. the hyperfine splitting energy of substates with different  $m_F$ , of different atoms and molecules by ramping the magnetic field amplitudes for a given beam velocity. In principle, the type of induced transitions, e.g. magnetic or electric dipole transitions ( $M1 \leftrightarrow E1$ ) and the polarization of the induced photons ( $\pi \leftrightarrow \sigma$  transitions), can be chosen with dedicated magnetic or even electric field configurations.

## 6 Theoretical Investigations

### Introduction

The IKP theory group studies the strong interactions in their various settings — spanning topics in hadron structure and dynamics, the nuclear many-body problem, symmetry tests in Quantum Chromodynamics (QCD), physics beyond the Standard Model and strongly correlated electronic systems. The first focus of the theory group is the formulation and application of effective field theories for precision hadron and nuclear physics based on the symmetries of QCD. The second focus is related to high performance computing in nuclear, hadronic and condensed matter physics, spear-headed by the work on nuclear lattice simulations. In this year, we added machine learning techniques to our toolbox. Since July 2012, the group is heavily involved in the activities of the collaborative research center “Symmetries and the emergence of structure in QCD” (CRC 110) together with researchers from Bonn University, TU München, Ruhr-Universität Bochum, IHEP/CAS (Beijing, China), ITP/CAS (Beijing, China) and Peking University (China). This CRC is presently finishing its second funding period and just got approved for a third one. Some of the high-lights of these activities are discussed in the following.

### Nuclear physics in a colorful world

QCD is the fundamental theory of the strong interactions. While the physical universe has  $N_c = 3$  colors, it is useful to consider how nuclear physics might appear when  $N_c$  is large. In the large- $N_c$  picture, Kaplan, Savage, and Manohar found that the leading nucleon-nucleon (NN) interaction can be written in the form

$$V_{\text{large-}N_c}^{2N} = V_C + \vec{\sigma}_1 \cdot \vec{\sigma}_2 \vec{\tau}_1 \cdot \vec{\tau}_2 W_S + S_{12} \vec{\tau}_1 \cdot \vec{\tau}_2 W_T + \dots,$$

where the ellipses refer to terms subleading in the large- $N_c$  expansion. Each of the scalar functions  $V_C$ ,  $W_S$  and  $W_T$  are local interactions. The strength of these leading interactions scale linearly with  $N_c$ , while all other terms scale as  $1/N_c$  or smaller. The relative  $1/N_c^2$  suppression of the subleading terms is fairly strong even for

$N_c = 3$ . In the literature, the large- $N_c$  limit is often linked with Wigner’s approximate SU(4) spin-isospin symmetry, where the four spin and isospin nucleon components transform as an SU(4) quartet. In the low-energy limit, NN scattering is dominated by the two S-wave channels. Therefore, if one reduces the abovementioned equation to only the S-wave channels, then the tensor interaction vanishes and one can replace  $\vec{\sigma}_1 \cdot \vec{\sigma}_2 \vec{\tau}_1 \cdot \vec{\tau}_2$  by  $-3$ . One therefore seems to derive the result that the low-energy S-wave interactions satisfy Wigner’s SU(4) symmetry. On the other hand, the deuteron is bound by 2.22 MeV while the spin-singlet channel is unbound. The discrepancy seems larger than the predicted  $1/N_c^2$  relative error of the large- $N_c$  expansion.

In a recent work, we could explain why Wigner’s SU(4) symmetry is not satisfied by the strong nuclear force at the level of  $1/N_c^2$  relative error. The crucial observation is that the large- $N_c$  form of the NN potential is only valid when the momentum resolution scale is not too high or too low, or stated differently, that there is a proper resolution scale so that the large- $N_c$  limit predicts a *spin-isospin exchange symmetry* that is satisfied at the  $1/N_c^2$  level and provides a valuable guide for understanding nuclear interactions and nuclear structure. Indeed, using renormalization group arguments, one can show that the leading large- $N_c$  reduction of the nuclear interaction has error corrections of size  $1/N_c^2$  only when the momentum resolution scale is near an optimal resolution scale called  $\Lambda_{\text{large-}N_c}$ . It is found to be  $\Lambda_{\text{large-}N_c} \sim 500$  MeV. Note that for interactions with a small amount of velocity dependence and therefore nonlocality, there will also be small corrections arising from the velocity dependence of the interactions.

Consider the matrix element between any two-nucleon states  $A$  and  $B$ , both with total intrinsic spin  $S$  and total isospin  $T$ . Let  $H$  be the isospin-invariant part of the nucleon-nucleon Hamiltonian and define the matrix element  $M(S, T)$  as  $1/(2S + 1) \sum_{S_z=-S}^S \langle A; S, S_z; T, T_z | H | B; S, S_z; T, T_z \rangle$ . The statement of spin-isospin exchange symmetry is the constraint  $M(S, T) = M(T, S)$ . As a test of the spin-isospin symmetry, consider seven two-body matrix elements in the 1s-0d shell. One finds that the  $(S, T) = (1, 0)$  and  $(S, T) = (0, 1)$  results are nearly equal at  $\Lambda = 2.5 \text{ fm}^{-1}$  for both AV18 and the  $N^3\text{LO}$  chiral interaction, with a relative error of size  $1/N_c^2$ , as seen for the chiral EFT in Fig. 42.

The large- $N_c$  analysis can also be applied to 3N interactions. At a momentum resolution scale close to  $\Lambda_{\text{large-}N_c}$ , there are 5 leading operators and the subleading central 3N interactions are of size  $1/N_c$ . This simplification should be helpful in constraining the many short-range three-nucleon interactions that appear at higher orders in chiral EFT. The spin-isospin exchange symmetry of the leading interactions also severely limits the isospin-dependent contributions of the 3N interactions to the nuclear equation of state. This fact is relevant for calculations of the nuclear symmetry energy and its density dependence in dense nuclear matter. Spin-isospin exchange

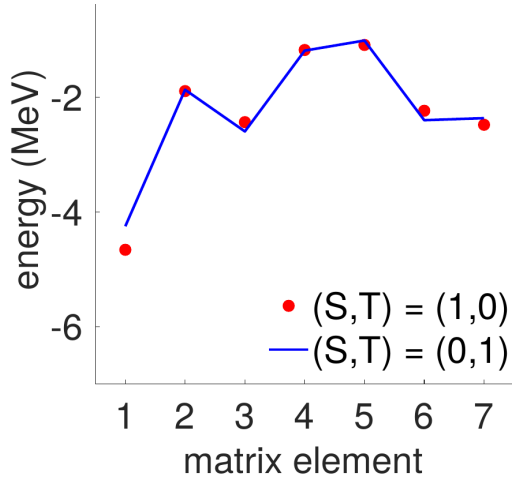


Figure 42: Two-body matrix elements for the 1s-0d shell for the optimal resolution scale. Results for the chiral  $N^3LO$  interaction for  $(S,T) = (1,0)$  with red dots and  $(S,T) = (0,1)$  with blue lines at  $\Lambda = 2.5 \text{ fm}^{-1}$ .

symmetry is also useful for constraining calculations that use local regularization to produce a nonzero interaction range for the 3N contact interaction at  $N^2LO$ . Local regularization produces local interactions with some strength in higher partial waves, and it has been observed that different isospin-dependent structures for the 3N contact interaction produce different behaviors in many-body calculations. Thus, such many-body calculations may be more reliable if one imposes spin-isospin exchange symmetry on the 3N contact interaction for calculations with a momentum cutoff of  $\Lambda_{\text{large-}N_c}$ . Note further that these findings vindicate the Weinberg power counting.

## Impurity lattice Monte Carlo for hypernuclei

The inclusion of  $\Lambda$  hyperons into the *ab initio* framework of nuclear lattice effective field theory (NLEFT) requires the use of specialized Monte Carlo (MC) methods to avoid large sign oscillations. We have made use of the fact that the number of hyperons ( $Y$ ) is typically small compared to the number of nucleons ( $N$ ) in realistic hypernuclei. This has allowed us to use the impurity lattice Monte Carlo (ILMC) method (developed by scientists within the NLEFT collaboration) where the minority species of fermions in the full nuclear Hamiltonian is integrated out and treated as a worldline in Euclidean projection time. The majority fermions (nucleons) are treated in ILMC as explicit degrees of freedom, with their mutual  $NN$  interactions described by auxiliary fields. This is the first application of the ILMC method to systems where the majority particles are interacting, and we have showed how ILMC can be applied to compute the binding energies of the light hypernuclei. See Fig. 43 for a realistic calculation of the  ${}^5_\Lambda\text{He}$  energy using the ILMC method.

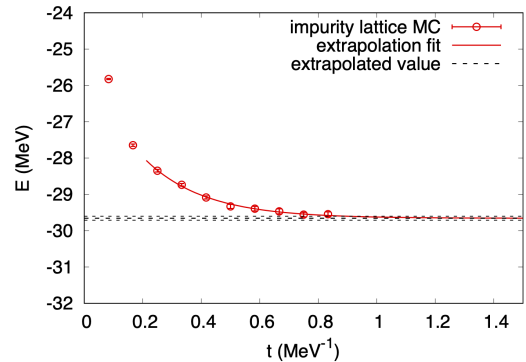


Figure 43: ILMC results for the  ${}^5_\Lambda\text{He}$  energy versus Euclidean time in a periodic box size of  $L = 9.9 \text{ fm}$ . We extract the ground state energy using an exponential *ansatz* for the asymptotic time dependence.

In this exploratory work, we have used spin-independent  $NN$  and hyperon-nucleon ( $YN$ ) interactions to test the computational power of the ILMC method. One of the most promising aspects of this work is the fact that the ILMC simulations scale very favorably with the number of nucleons. We have found that nearly all of the computational effort is consumed in calculating single-nucleon amplitudes as a function of the auxiliary field. As this part of the code scales linearly with the number of nucleons, it should be possible to perform calculations of hypernuclei with up to one hundred or more nucleons. We note also that the particular set of interactions that we have used here can also be directly applied to studying the properties of a bosonic impurity immersed in a superfluid Fermi gas. By modifying the included  $P$ -wave interactions of the impurity, we would also be able to describe the properties of an alpha particle immersed in a gas of superfluid neutrons.

The possible applications of the ILMC method go well beyond hypernuclear structure calculations and have general utility for numerous quantum many-body systems. Work is currently underway to include spin-independent  $NN$  and  $YN$  interactions, as well as the effects of  $\Lambda N$ - $\Sigma N$  transitions. A further extension concerns  $S = -2$  hypernuclei, which on the one hand would involve the  $YY$  interactions and on the other hand a modified ILMC algorithm for two interacting worldlines.

## Light $p$ -shell hypernuclei

The hyperon-nucleon ( $YN$ ) interactions are still to a large extent unknown because there are only a few  $YN$  scattering data at low energy which do not allow one to fully determine the  $YN$  forces. At the same time, knowing these interactions is of very high interest, because hyperons could influence the properties of neutron stars sig-

nificantly. Therefore, several experimental facilities like, e.g., FAIR, J-PARC and JLab are taking new data or are planning new experiments involving hyperons.

Direct scattering experiments are very difficult. Therefore, light hypernuclei are an important additional input for the determination of YN forces. In a new paper, we discuss the extension of the recently developed Jacobi no-core shell model (J-NCSM) to hypernuclei and report the first calculations for  ${}^5_{\Lambda}\text{He}$ ,  ${}^6_{\Lambda}\text{He}$ ,  ${}^6_{\Lambda}\text{Li}$ , and  ${}^7_{\Lambda}\text{Li}$  based on next-to-leading order chiral YN interactions. These are the first predictions for these hypernuclei based on interactions that provide an accurate description of all available YN scattering data.

In order to obtain converged results, we use similarity renormalization group (SRG) evolved nucleon-nucleon (NN) and YN interactions. In this first work, SRG-induced three-baryon forces (3BF) are not taken into account. We therefore find a significant dependence on the YN SRG flow parameter  $\lambda_{YN}$ . In contrast to purely nucleonic systems, the contribution of higher body SRG-induced interactions is much larger than what can be expected from corresponding chiral three-body interactions. At the same time, we observed that the  $\Lambda$ -separation energies of the considered  $A \leq 7$  hypernuclei are strongly linearly correlated with each other. This is exemplified in Fig. 44, for  ${}^5_{\Lambda}\text{He}$  and the ground state of  ${}^7_{\Lambda}\text{Li}$ .

We also observed that for a 'magic' value of  $\lambda_{YN}$  the experimental  $\Lambda$ -separation energy for  ${}^5_{\Lambda}\text{He}$  can be reproduced. It turns out that we then also reproduce our results for the  $\Lambda$ -separation energy of  ${}^3_{\Lambda}\text{H}$  of the non-SRG-evolved interaction. For  ${}^4_{\Lambda}\text{He}$  and  ${}^4_{\Lambda}\text{H}$ , we agree with non-SRG-evolved results within the expected contribution of chiral 3BFs. We can therefore assume that the contribution of SRG-induced and chiral many-body forces can be minimized for the magic  $\lambda_{YN}$ . Also the  $\Lambda$ -separation energies of all considered hypernuclei are in reasonable agreement with experiment. We observe, however, deviations for some of the excitation energies that might point to deficiencies of the YN interactions or significant contributions of 3BFs.

The work shows that reliable results for separations for light hypernuclei up to the  $p$ -shell can be obtained using the J-NCSM. Thereby, most computational resources are required for the preparation of transition coefficients for the application of nuclear and hypernuclear interactions. Once they are prepared, a large number of calculations based on different YN interactions is possible. This will allow us to test YN interactions in future and possibly constrain  $p$ -wave interactions and higher partial waves more stringently. The method is currently extended to also include chiral and SRG-induced 3BFs. Based on this extension, we will be able to identify observables for which 3BFs can be omitted using the magic  $\lambda_{YN}$  allowing for a very efficient improvement of YN interactions. Observables that turn out to be sensitive to such 3BFs will be useful for their determination. Therefore, with the now established J-NCSM for hypernuclei, the available and

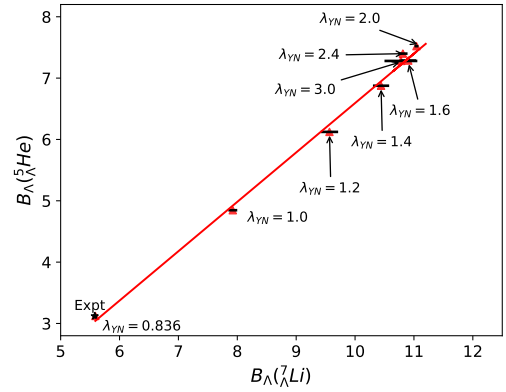


Figure 44: Correlation of  $\Lambda$ -separation energies of  ${}^5_{\Lambda}\text{He}$  and the ground state of  ${}^7_{\Lambda}\text{Li}$ . The error bars indicate the numerical uncertainty, the asterisk indicates the experimental values and the red solid line is a linear fit to the calculates results.

upcoming experimental results can be fully exploited to pin down hypernuclear interactions.

## Predictions for charmed nuclei based on $\Lambda_c N$ forces inferred from lattice QCD simulations

The prospect of an ample production of charmed baryons at modern facilities such as the LHC at CERN, J-PARC and KEK in Japan, or FAIR in Germany has led to a renewed interest in the question whether these baryons, and notably the lightest one, the  $\Lambda_c(2286)$ , could form bound states with ordinary matter.

Indeed, there is a long history of speculations about possible bound systems involving the  $\Lambda_c$  that started soon after the discovery of charmed baryons in 1975. The  $\Lambda_c N$  forces employed in the past investigations were predominantly derived within the meson-exchange framework, often utilizing SU(4) flavor symmetry in one form or the other. In general, the resulting potentials turned out to be fairly attractive and some even supported bound two-body systems. Interestingly, a rather different picture emerged from recent lattice QCD simulations by the HAL QCD collaboration. Those studies, based on unphysical quark masses corresponding to pion masses of  $m_{\pi} = 410 - 700$  MeV, suggest that the  $\Lambda_c N$  interaction could be significantly less attractive than what had been proposed in past phenomenological studies.

We investigated the binding energies of charmed nuclei based on the aforementioned  $\Lambda_c N$  interaction from lattice QCD simulations, after appropriately extrapolating it to the physical point within the framework of chiral effective field theory. The  $\Lambda_c N$  interaction established in this

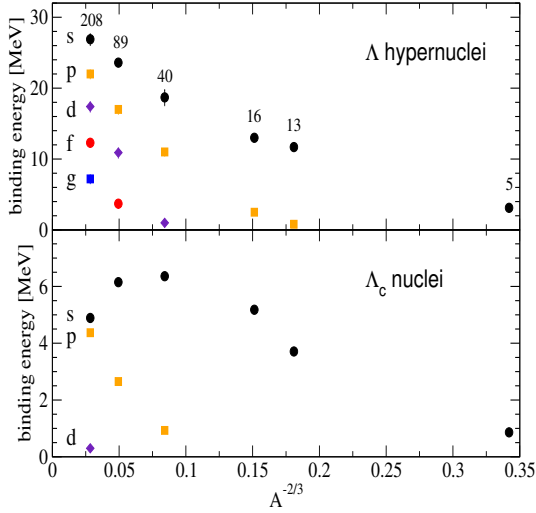


Figure 45: Energy levels of the  $1s$ ,  $1p$ ,  $1d$ ,  $1f$ , and  $1g$  single-particle shells as a function of  $A^{-2/3}$ , where  $A$  is the baryon number. Top: experimental results for  $\Lambda$  hypernuclei; bottom: our predictions for  $\Lambda_c$  nuclei.

way is significantly weaker than what has been employed in most of the studies of charmed nuclei in the literature so far. Bound state calculations for light charmed nuclei were carried out within the Faddeev-Yakubovsky framework. Heavier nuclei were studied within a perturbative many-body approach which allowed us to determine the finite-nuclei  $\Lambda_c$  self-energy from which the energies of the  $\Lambda_c$  single-particle bound states could be obtained.

We found that even for a weak  $\Lambda_c N$  interaction as suggested by the lattice simulations already  $A = 4$  charmed nuclei are likely to exist. Only the lightest nucleus considered, a charmed helium  ${}^3_{\Lambda_c}\text{He}$ , turned out to be unbound. Our results for heavier charmed nuclei are summarized in Fig. 45. For illustration experimental values for  $\Lambda$  hypernuclei are also shown, cf. the upper panel which contains measured binding energies for  $\Lambda$  single-particle states for  ${}^5_{\Lambda}\text{He}$  (right) to  ${}^{208}_{\Lambda}\text{Pb}$  (left). In the lower panel our predictions for the charmed nuclei  ${}^5_{\Lambda_c}\text{Li}$  to  ${}^{209}_{\Lambda_c}\text{Bi}$  are displayed. Obviously, the energies found for the charm sector are roughly a factor 3 smaller. Interesting is also the influence of the charge of the  $\Lambda_c$ . The Coulomb repulsion between the  $\Lambda_c$  and the protons of the nuclear core, together with the kinetic energy of the  $\Lambda_c$ , compensates most of the attraction of the  $\Lambda_c N$  interaction so that the binding energy decreases eventually with increasing baryon number  $A$ .

## Evidence that the LHCb $P_c$ states are hadronic molecules

Amongst the large number of mesons found recently in spectroscopy studies in the heavy quarkonium mass ranges charged states that decay into final states containing a heavy quark and a heavy antiquark are special, since they contain at least 4 quarks. For the analogous reason the three baryons found recently by LHCb in the  $J/\psi p$  channel are explicitly exotic since they contain at least 5 quarks. Since all the three states are located close to the  $\Sigma_c \bar{D}^{(*)}$  thresholds, they appear to be natural candidates for hadronic molecules formed in these channels — in fact, based on phenomenological studies molecules of this kind were predicted to exist already five years before their discovery in 2015.

To deepen our understanding of these states we formulated an effective field theory that allows us to study the system at hand keeping track with all symmetries of QCD, in particular the heavy quark spin symmetry, which is at low orders broken only by the mass splittings within the spin multiplets ( $\Sigma_c, \Sigma_c^*$ ) and ( $\bar{D}, \bar{D}^*$ ), respectively. The symmetry allows for two energy independent contact terms. In analogy to the two-nucleon system in addition the one-pion exchange contributes at leading order. Its inclusion calls for extending the basis to  $D$ -waves, since the tensor force of the one-pion exchange drives large  $S$  to  $D$  transitions. Those appear to be enhanced here as well as in our analogous study of the  $Z_b(10610)$  and  $Z_b(10650)$  compared to the two-nucleon system, since the coupled channels to be included in the heavy quark systems allow for transition momenta of the order of 500 MeV.

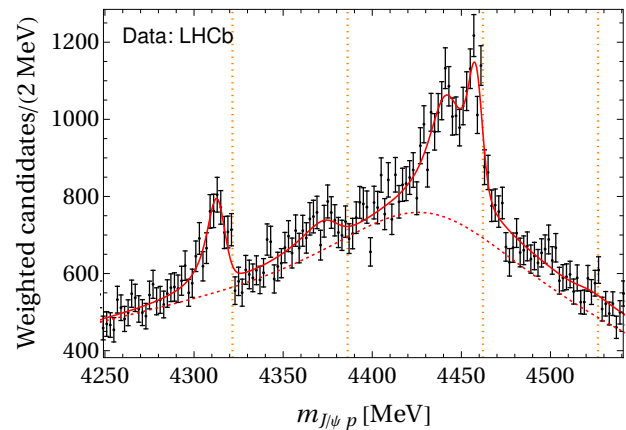


Figure 46: Best fit for the scheme that includes one-pion exchange fully non-perturbatively. The vertical dashed lines in both panels from left to right are the  $\Sigma_c \bar{D}$ ,  $\Sigma_c^* \bar{D}$ ,  $\Sigma_c \bar{D}^*$  and  $\Sigma_c^* \bar{D}^*$  thresholds, respectively.

The results for the full calculation are shown as the solid line in Fig. 46, while the dashed line shows the contribution of an incoherent background. The data are sufficient to fix all parameters and one finds that the system

develops in total seven bound states. Since all states are generated in the  $S$ -wave they share a negative parity. This is one clear prediction from the molecular picture advocated here. Moreover, besides the spin  $1/2$  state near the  $\Sigma_c \bar{D}$  threshold and the two states near the  $\Sigma_c \bar{D}^*$  threshold with spin  $1/2$  and  $3/2$ , respectively, the fit also generates a structure near the  $\Sigma_c^* \bar{D}$  threshold with spin  $3/2$  that was not recognised before our work. On the other hand, the three molecules that are generated in the  $\Sigma_c^* \bar{D}^*$  channels with spin  $1/2$ ,  $3/2$  and  $5/2$ , respectively, do not show up in the data most probably because the production mechanism does not favour the  $\Sigma_c^* \bar{D}^*$  channels. Here a microscopic understanding is still lacking. To establish their existence additional data from different reactions would be very valuable.

Currently we are working on improving our approach by systematic studies of the possible contribution from additional inelastic channels like  $\Lambda_c \bar{D}^{(*)}$  and  $\eta_{c p}$  and higher order operators. The corresponding results will be released soon.

## Machine learning the unitary limit

After neural networks have already been successfully used in experimental applications, such as particle identification, much progress has been made in recent years by applying them to various fields of theoretical physics. One issue that has not been addressed so far was the so-called *unitary limit*, in which the scattering length  $a_0$  tends to infinity and the effective range and all other shape parameters vanish, corresponding to a zero-energy bound state in the two-particle system. To address this question, we have considered attractive, spherically symmetric potentials with a finite range. In a first step, these potentials are discretized, as these can be treated as vectors  $\mathbf{U} \in \Omega \subset \mathbb{R}^d$  and are amenable to machine learning (ML) techniques. As a result of this discretization, the potential space is reduced to the first hyperoctant  $\Omega$  of  $\mathbb{R}^d$ . Counting bound states naturally splits  $\Omega = \bigcup_{i \in \mathbb{N}_0} \Omega_i$  into pairwise disjoint, half-open regions  $\Omega_i$ , with  $\Omega_i$  containing all potentials with exactly  $i$  bound states. All potentials on the  $d - 1$  dimensional hypersurface  $\Sigma_i \equiv \partial\Omega_{i-1} \cap \Omega_i$  between two neighboring regions with  $\Sigma_i \subset \Omega_i$  give rise to a zero-energy bound state, see Fig. 47. Since we observe the unitary limit  $a_0 \rightarrow \infty$  in this scenario, we refer to  $\Sigma_i$  as the  $i^{\text{th}}$  unitary limit surface. Considering the scattering length as a function  $a_0 : \Omega \rightarrow \mathbb{R}$ , this suggests a movable singularity on each unitary limit surface. Consider now the first unitary limit surface  $\Sigma_1$ . Let  $\mathbf{U} \in \Omega$  and  $f \in \mathbb{R}^+$  be a factor satisfying  $f\mathbf{U} \in \Sigma_1$ . This means scaling  $\mathbf{U}$  by the unique factor  $f$  yields a potential on the first unitary limit surface. While potentials with an empty spectrum must be deepened to obtain a zero-energy bound state, potentials whose spectrum already contains a dimer with finite binding energy  $E < 0$  need to be flattened instead.

The factor  $f$  seems to be a powerful quantity for describing the geometry of the unitary limit surface  $\Sigma_1$ . The lat-

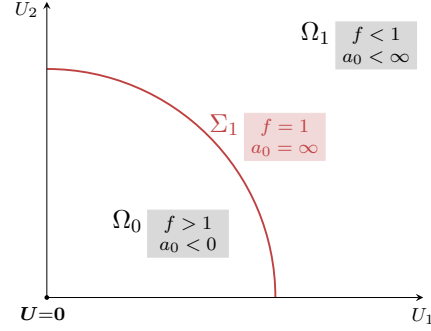


Figure 47: Sketch of the regions  $\Omega_0$  and  $\Omega_1$  and the first unitary limit surface  $\Sigma_1 \subset \Omega_1$  for the degree  $d = 2$  of discretization. In this specific case, the potential space  $\Omega$  is the first quadrant of  $\mathbb{R}^2$  and unitary limit surfaces are one-dimensional manifolds.

ter is merely the contour for  $f = 1$ . It is a simple task to derive  $f$  iteratively by scaling a given potential  $\mathbf{U}$  until the scattering length flips sign. However, an analytic relation between  $\mathbf{U}$  and  $f$  is not known. The remedy for this are neural networks that are trained supervisedly on pairs  $(\mathbf{U}, f) \in T_1$  of potentials (inputs) and corresponding factors (targets) in some training set  $T_1$ . In this case, neural networks can be understood as maps  $\mathcal{F} : \Omega \rightarrow \mathbb{R}$  that additionally depend on numerous internal parameters. The key idea of supervised training is to adapt the internal parameters iteratively such that the outputs  $\mathcal{F}(\mathbf{U})$  approach the targets  $f$  ever closer. As a result of training,  $\mathcal{F}$  approximates the underlying function  $\mathbf{U} \mapsto f$ , such that the factor  $f^* \approx \mathcal{F}(\mathbf{U}^*)$  is predicted with sufficient accuracy even if the potential  $\mathbf{U}^* \in \Omega$  does not appear in  $T_1$ , as long as it resembles the potentials encountered during training. One standard tool are multilayer perceptrons (MLPs). How can we now predict scattering lengths in vicinity of  $\Sigma_1$ ? Being a movable singularity in potential space, the unitary limit itself imposes severe restrictions on MLP architectures and renders training steps unstable. Therefore, one opts for the alternative approach of expressing scattering lengths in terms of regular quantities, that each can be easily predicted by MLPs. Given the factors  $f$  we consider  $b_0 = a_0(1 - f) = a_0 x / \|\mathbf{U}\|$ , where  $x = (1 - f)\|\mathbf{U}\|$  is the distance between the given potential  $\mathbf{U} \in \Omega$  and  $f\mathbf{U} \in \Sigma_1$ . The quantity  $b_0$  provides an equivalent understanding of this distance in terms of  $x = b_0 / a_0 \|\mathbf{U}\|$ , which does not explicitly depend on the factor  $f$ .

Training now separately ensembles  $\mathcal{F}$  and  $\mathcal{B}$  for the scaling factor  $f$  and the quantity  $b_0$ , the quantity  $\mathcal{A}(\mathbf{U}) = \mathcal{B}(\mathbf{U}) / (1 - \mathcal{F}(\mathbf{U}))$  allows one to predict natural as well as unnatural scattering lengths with good precision. It is important to note that both ensembles leave training as “black boxes”. By considering their Taylor approximations, one can obtain an interpretable expression of the predicted scattering lengths  $\mathcal{A}(\mathbf{U})$  in terms of a scalar product. This also provides additional geometric insights like normal vectors on the unitary limit surface. Note

finally that this approach is far more general, than the above analysis of  $\Sigma_1$  suggests and, in fact, is a viable option whenever movable singularities come into play.

## The quantum phase transition of the Hubbard model on the honeycomb lattice

Monte Carlo (MC) simulations of strongly correlated electrons in carbon nanomaterials is an emerging topic in the condensed matter and nuclear physics communities. The basis of such studies is often the Hubbard model, a Hamiltonian approach which reduces, at weak electron-electron coupling, to the tight-binding description of atomic orbitals in a lattice of carbon ions. The properties of the Hubbard model on a honeycomb lattice are thought to resemble those of graphene, as well as those of other carbon allotropes, including nanotubes, nanoribbons, and fullerenes.

In spite of a long history of theoretical studies of the Hubbard model, surprisingly little is known with certainty of its properties in low-dimensional settings, in particular for the 2-dimensional Hubbard model. For example, it is believed that the 2-d Hubbard model undergoes a quantum phase transition (*i.e.* a zero-temperature phase transition), whereby the system (at a critical on-site electron-electron coupling  $U_c$ ), transitions from a conducting semi-metal (SM) state to an anti-ferromagnetic Mott insulating (AFMI) state. Because this transition is interaction-induced, it could be potentially tuned with external magnetic fields and thus manipulated in semiconductor devices. Yet the value of this critical coupling  $U_c$  (along with the associated critical exponents) is not known analytically, and extant numerical determinations have so far failed to agree on these basic observables. This uncertainty has prevented a definitive determination of the electronic phase diagram of the 2-d Hubbard model, which in turn hampers our ability to fully understand the rich phenomena that occurs in low-dimensional systems such as graphene.

We have taken advantage of recent improvements in our grand canonical Hybrid Monte Carlo (HMC) algorithm to perform a precision study of the single-particle gap in the honeycomb Hubbard model. After carefully controlled analyses of the Trotter error, the thermodynamic limit, and finite-size scaling with inverse temperature (this comprehensive analysis represents the first of its kind), we found a critical coupling of  $U_c = 3.834(14)$  (in units of the nearest-neighbor hopping parameter  $\kappa$ ) and a critical exponent  $z\nu = 1.185(43)$  for the transition. Under the assumption that this corresponds to the expected SM-AFMI transition, we were also able to provide a preliminary estimate  $\beta = 1.095(37)$  for the critical exponent of the AFMI order parameter (staggered magnetization). Our findings appear consistent with the view that this system falls in the  $SU(2)$  Gross-Neveu (or chiral Heisenberg) universality class. In Fig. 48, we show our MC results

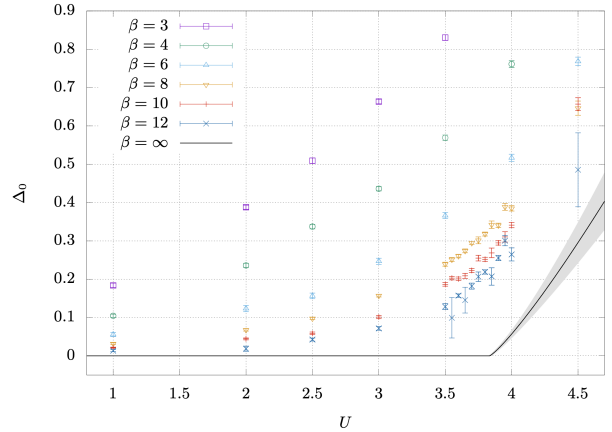


Figure 48: Results for the single-particle gap  $\Delta_0$  (signifying the AFMI phase) as a function of Hubbard on-site coupling  $U$  (in units of the nearest-neighbor hopping parameter  $\kappa$ ) and inverse temperature  $\beta$ . The black line shows the zero-temperature extrapolation determined from a finite-size scaling analysis. The critical coupling where the gap opens up (at zero temperature) corresponds to  $U_c = 3.834(14)$ .

for the single-particle gap as a function of inverse temperature  $\beta$  (colored points) and the zero-temperature extrapolation (black line) determined through a finite-size scaling analysis.

In conclusion, the favorable computational scaling of our HMC algorithm, developed by scientists at IKP-3/IAS-4 and in collaboration with JSC, enables future extensions of our work to carbon nanotubes, fullerenes, and topological insulators.

## A Beam Time at COSY in 2020

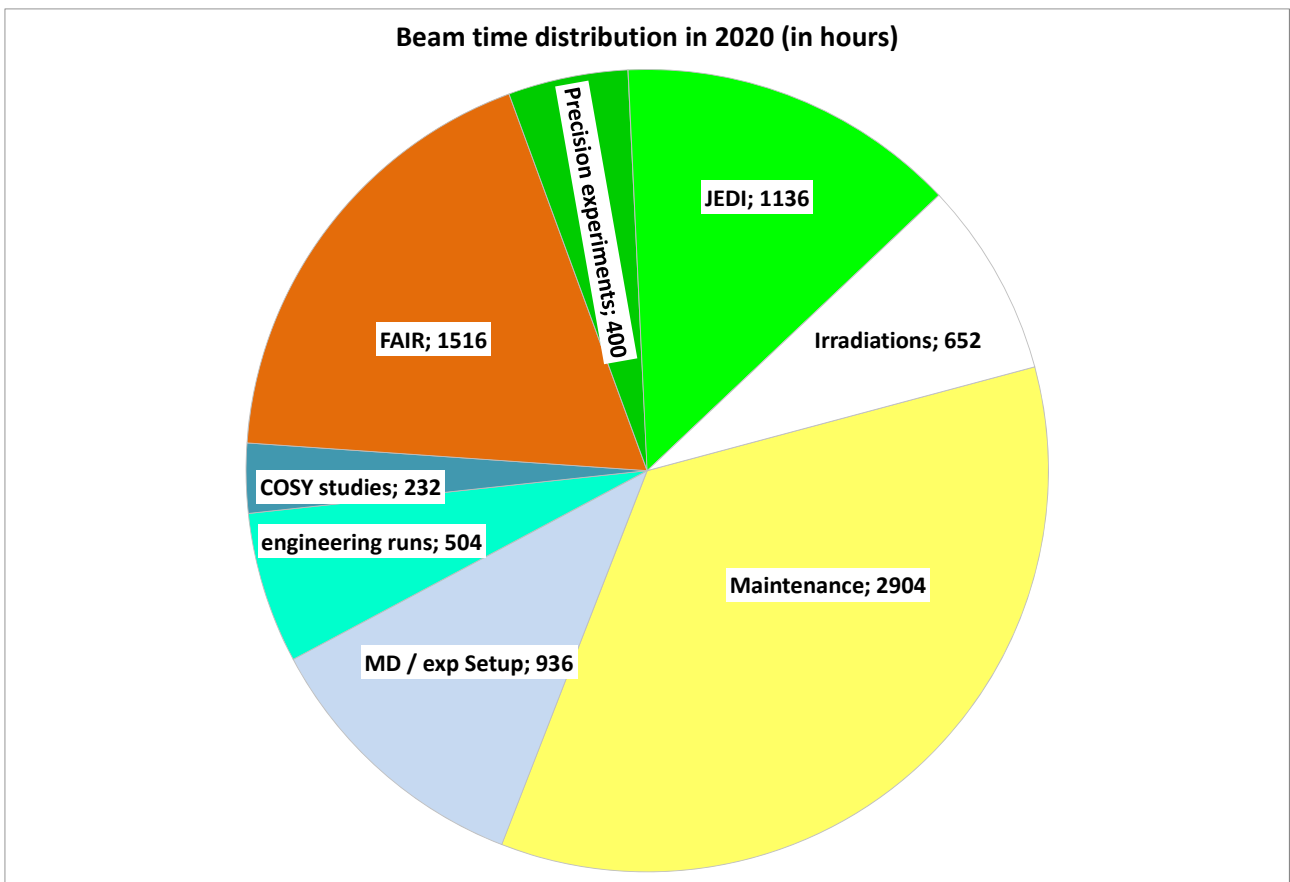


Figure 49: COSY beam-time statistics in 2020.

The distribution of user weeks and maintenance/shutdown periods is listed in Table 3.

Table 3: Overview COSY user beam time and EDM/FAIR weeks in 2020.

Date	Experiment	Duration	Reaction, experiment #
1.01.20.–12.01.20	Maintenance	2 weeks	
13.01.–19.01.	HBS	1 week	High Brilliance Source HBS, Exp. A010.6
27.01.–09.02.	EDM (JEDI)	2 week	EDM Polarimetry, Exp. E002.7
17.02.–23.02.	COSY	1 week	JUSPARC Exp. A016
02.03.–15.03.	COSY	2 week	Siberian Snake Exp. A009
23.03.–29.03.	FAIR (Lumi)	1 week	FAIR Luminosity, Exp. D011.1
30.03.–19.04.	Maintenance	3 weeks	
27.04.–30.04.	COSY	1 week	engineering run
04.05.–05.05.	COSY	2 days	SiPM Radiation hardness measurements, D012.1
11.05.–17.05.	FAIR (CBM)	1 week	CBM measurements COSY Exp. D004.8 (cancelled)
18.05.–27.05.	COSY	1.5 week	stochastic cooling, Exp. A001.10
28.05.–07.06.	COSY	1.5 week	electron cooling, Exp. A002.6
08.06.–14.06.	FAIR (Clust.)	1 week	FAIR Cluster Jet Target, Exp. D009.4 (cancelled)
15.06.–02.08.	Maintenance	7 weeks	
10.08.–16.08.	COSY	1 week	engineering run
17.08.–23.08.	COSY	1 week	Orbit feedback Exp. A014.2
31.08.–20.09.	EDM (JEDI)	3 weeks	JEDI alignment, Exp. E010
21.09.–27.09.	EDM (JEDI)	1 weeks	JEDI Wien Filter Exp. E005.6
28.09.–18.10.	Maintenance	3 weeks	
19.10.–25.10.	COSY	1 week	Loewe-NP, Exp. A017.1
02.11.–08.11.	COSY	1 week	engineering run
09.11.–15.11.	FAIR (CBM)	1 week	CBM measurements COSY Exp. D009.4 (cancelled)
16.11.–19.11.	COSY	3 days	Stable Quadrupole, Exp. A020
24.11.–25.11.	COSY	1 day	HADES Det.-Test Exp. D014
25.11.–13.12.	shutdown	3 weeks	finance driven shutdown
14.12.–31.12.	Maintenance	2 weeks	
<b>user weeks 2020</b>		20 weeks	
maintenance		17 weeks	
finance driven shutdown		3 weeks	

## B Committees

### B.1 CBAC – COSY Beam Time Advisory Committee

Prof. K. Aulenbacher	Universität Mainz, Germany
Prof. O. Kester	TRIUMF, Canada
Prof. C.J. Schmidt	GSI Darmstadt, Germany
Prof. T. Stöhlker	HI-Jena, Jena, Germany
Prof. M. Weber (chair)	KIT, Karlsruhe, Germany

### B.2 Committee Service

O. Felden	- WTR (Scientific and Technical Council), FZ-Jülich GmbH, Germany
F. Goldenbaum	- Chair of the PANDA at FAIR collaboration board
	- WTR (Scientific and Technical Council), FZ-Jülich GmbH, Germany
	- Scientific Secretary of COSY Beam Advisory Committee (CBAC), FZ-Jülich GmbH, Germany
J. Haidenbauer	- Theory advisory Group PANDA
C. Hanhart	- Theory advisory Group PANDA
	- Particle Data Group
	- Task coordinator ( Precision calculations in non-perturbative QCD (I): Effective Field Theories, analyticity and dispersion relations) within STRONG2020
R. Gebel	- International Organising Committee of the International Conference on Cyclotrons and their Applications
V. Hejny	- WTR (Scientific and Technical Council), FZ-Jülich GmbH, Germany
A. Lehrach	- Institutional representative in the European Network for Novel Accelerators (EuroNNAc)
	- Coordination, support and enhancement of training activities for accelerators in Europe in the EU-Projekt ARIES (Accelerator Research and Innovation for European Science and Society)
	- Scientific Advisory Board (SAB) of the 11th International Particle Accelerator Conference (IPAC'20), May 10 - 15, 2020, virtual conference
	- Subtopic Speaker of the HGF Programme "Matter and Technologies", Accelerator Research and Development (ARD), Subtopic 2
	- ARD Management Board, HGF Programme "Matter and Technologies"
	- Member of the JuDocs Council, FZ-Jülich GmbH, Germany
	- Independent Review Committee of the Conceptual Design (CDR) of the Electron Ion Collider (EIC), November 16-18, 2020, Brookhaven National Laboratory, Upton (NY), USA
L. Ludhova	- Institutional Board of Borexino
	- Steering Committee of Borexino
	- Physics Coordinator of Borexino
	- Institutional Board of JUNO
	- Co-Chair of the Speakers Committee of JUNO
	- L2 manager of the OSIRIS calibration
	- Member of the International Advisory Committee of Physics In Collision (PIC) conferences

- U.-G. Meißner - Spokesperson DFG Review Board 309 "Particles, Nuclei and Fields"
- Gründungsmitglied der Kommission für Ethik in der Forschung am Forschungszentrum Jülich
- Scientific Advisory Committee of the Collaborative Research Center (SFB) 1245, "Nuclei: From fundamental interactions to structure and stars", TU Darmstadt
- German/DFG delegate of NuPECC
- Project coordinator, Regional Doctoral Program in Theoretical and Experimental Particle Physics (Bonn, Jülich, Siegen Tiflis, Yerevan), funded by Volkswagen Stiftung
- Spokesperson of the Collaborative Research Center SFB/TR-110 "Symmetries and the Emergence of Structure in QCD"
- Theory advisory Group PANDA
- Particle Data Group
- A. Nogga - WTR (Scientific and Technical Council), FZ-Jülich GmbH, Germany
- D. Prasuhn - International Advisory Committee of the COOL Conferences (Beam Cooling)
- J. Ritman - Deputy speaker HGF-Program Cosmic Matter in the Laboratory
- Scientific Coordinator of COSY
- Co-Chair of the MESON biannual conference series
- Chair of the Scientific Advisory Committee for FAIR-CZ
- Co-Spokesperson of KLF (K-Long Facility at Jefferson Lab)
- S. Schadmand - Jefferson Lab User Organization (JLUO) Board of Directors (until June 2020)
- Workshop Program Committee of the APS Topical Group on Hadronic Physics (GHP)
- R. Stassen - Member of the Machine Advisory Committee for NICA (Nuclotron-based Ion Collider Facility), Joint Institute for Nuclear Research (JINR), Dubna, Russia
- T. Stockmanns - Computing coordinator PANDA
- H. Ströher - IAB KIU (Int. Advisory Board Kutaisi Int. University, Georgia)
- ISPC (Int. Spin Physics Committee)
- NuPECC (Nuclear Physics European Collaboration Committee)
- NuPECC Representative of the JENAA (Joint ECFA-NuPECC-APPEC Activity) EoI (Expression of Interest) Task Force
- PGSB (Palestinian-German Science Bridge) Advisory Committee
- Co-Chair of the Steering Committee of the CNRS/IN2P3-Helmholtz IRL (International Research Laboratory) "DMLab"

## C Publications

### C.1 Journal Articles

1. M.G. Aartsen *et al.*  
**Combined sensitivity to the neutrino mass ordering with JUNO, the IceCube Upgrade, and PINGU**  
Phys. Rev. D **101** 032006 (2020)
2. S. Adhikari *et al.*  
**The GlueX beamline and detector**  
Nucl. Instr. Meth. Phys. Res. A **987** 164807 - (2020)
3. P. Adlarson *et al.*  
**Search for  $\eta$  mesic  $^3\text{He}$  with the WASA-at-COSY facility in the  $pd \rightarrow ^3\text{He}2\gamma$  and  $pd \rightarrow ^3\text{He}6\gamma$  reactions**  
Phys. Lett. B **802** 135205 - (2020)
4. P. Adlarson *et al.*  
**Differential cross sections for neutron-proton scattering in the region of the  $d^*(2380)$  dibaryon resonance**  
Phys. Rev. C **102** 015204 (2020)
5. P. Adlarson *et al.*  
**Corrigendum to “Isoscalar single-pion production in the region of Roper and  $d^*(2380)$  resonances” [Phys. Lett. B **774** (2017) 599]**  
Phys. Lett. B **806** 135555 - (2020)
6. P. Adlarson *et al.*  
**Search for the  $\eta$  mesic He 3 in the  $p d \rightarrow d p \pi^0$  reaction with the WASA-at-COSY facility**  
Phys. Rev. C **102** 044322 (2020)
7. F. Afzal *et al.*  
**Observation of the  $p \eta'$  Cusp in the New Precise Beam Asymmetry  $\Sigma$  Data for  $\gamma p \rightarrow p \eta$**   
Phys. Rev. Lett. **125** 152002 (2020)
8. S.K. Agarwalla *et al.*  
**Constraints on flavor-diagonal non-standard neutrino interactions from Borexino Phase-II**  
J. High Energ. Phys. **2020** 38 (2020)
9. M. Agostini *et al.*  
**Comprehensive geoneutrino analysis with Borexino**  
Phys. Rev. D **101** 012009 (2020)
10. M. Agostini *et al.*  
**Improved measurement of  $^8\text{B}$  solar neutrinos with 1.5 kt · y of Borexino exposure**  
Phys. Rev. D **101** 062001 (2020)
11. M. Agostini *et al.*  
**Sensitivity to neutrinos from the solar CNO cycle in Borexino**  
Eur. Phys. J. C **80** 1091 (2020)
12. M. Agostini *et al.*  
**Experimental evidence of neutrinos produced in the CNO fusion cycle in the Sun**  
Nature <London> **587** 577 - 582 (2020)
13. M. Askins *et al.*  
**Theia: An advanced optical neutrino detector**  
Eur. Phys. J. **C80** 416 (2020)
14. R.W. Assmann *et al.*  
**EuPRAXIA Conceptual Design Report**  
Eur. Phys. J-Spec. Top. **229** 3675 - 4284 (2020)
15. W. Augustyniak *et al.*  
**Three-nucleon dynamics in dp breakup collisions using the WASA detector at COSY-Jülich**  
Phys. Rev. C **101** 044001 (2020)

16. S. Böser *et al.*  
**Status of light sterile neutrino searches**  
Prog. Part. Nucl. Phys. **111** 103736 - (2020)
17. N. Brambilla *et al.*  
**The X Y Z states: Experimental and theoretical status and perspectives**  
Phys. Rep. **873** 1 - 154 (2020)
18. V.D. Burkert *et al.*  
**The CLAS12 Spectrometer at Jefferson Laboratory**  
Nucl. Instr. Meth. Phys. Res. A **959** 163419 - (2020)
19. M. Büscher *et al.*  
**Generation of polarized particle beams at relativistic laser intensities**  
High Power Laser Sci. Eng. **8** e36 (2020)
20. A. Celentano *et al.*  
**First measurement of direct photoproduction of the  $\rho(1320)^0$  meson on the proton**  
Phys. Rev. C **102** 7 / 032201 (2020)
21. Q.B. Chen *et al.*  
**g-factor and static quadrupole moment for the wobbling mode in  $^{133}\text{La}$**   
Phys. Lett. B **807** 135596 - (2020)
22. Q.B. Chen *et al.*  
**Static quadrupole moments of nuclear chiral doublet bands**  
Phys. Lett. B **807** 135568 - (2020)
23. Z.M. Chitgar *et al.*  
**Electron self-injection threshold for the tandem-pulse laser wakefield accelerator**  
Phys. Plasmas **27** 023106 - (2020)
24. M. Du *et al.*  
**Interpretation of the LHCb  $P_c$  States as Hadronic Molecules and Hints of a Narrow  $P_c(4380)$**   
Phys. Rev. Lett. **124** 072001 (2020)
25. M. Du *et al.*  
**Deciphering the mechanism of near-threshold  $J/\psi$  photoproduction**  
Eur. Phys. J. C **80** 1053 (2020)
26. R. Engels *et al.*  
**Production of HD Molecules in Definite Hyperfine Substates**  
Phys. Rev. Lett. **124** 113003 (2020)
27. E. Epelbaum *et al.*  
**How to renormalize integral equations with singular potentials in effective field theory**  
Eur. Phys. J. A **56** 152 (2020)
28. E. Epelbaum *et al.*  
**Towards high-order calculations of three-nucleon scattering in chiral effective field theory**  
Eur. Phys. J. A **56** 92 (2020)
29. K. Föhl *et al.*  
**Muon radiography employing the DIRC principle for density change measurements under volcanoes and fluid reservoirs**  
J. Instrum. **15** C07030 - C07030 (2020)
30. D. Frame *et al.*  
**Impurity lattice Monte Carlo for hypernuclei**  
Eur. Phys. J. A **56** 248 (2020)
31. H.W. Griebhammer *et al.*  
**Scattering Observables from One- and Two-body Densities: Formalism and Application to  $\gamma^3\text{He}$  Scattering**  
Few-body systems **61** 48 (2020)

32. T. Gutberlet *et al.*  
**Sustainable neutrons for today and tomorrow–The Jülich High Brilliance neutron Source project**  
Neutron News **31** 37-43 (2020)
33. J. Haidenbauer, U. Meißner and A. Nogga  
**Hyperon-nucleon interaction within chiral effective field theory revisited**  
Eur. Phys. J. A **56** 91 (2020)
34. J. Haidenbauer, G. Krein and T.C. Peixoto  
**Femtoscopic correlations and the  $\Lambda_c N$  interaction**  
Eur. Phys. J. A **56** 184 (2020)
35. J. Haidenbauer and I. Vidaña  
**Structure of single- $\Lambda$  hypernuclei with chiral hyperon-nucleon potentials**  
Eur. Phys. J. A **56** 55 (2020)
36. J. Haidenbauer and U. Meißner  
**Neutron-antineutron oscillations in the deuteron studied with  $NN$  and  $\bar{N}N$  interactions based on chiral effective field theory**  
Chinese Phys. C **44** 033101 (2020)
37. J. Haidenbauer, A. Nogga and I. Vidaña  
**Predictions for charmed nuclei based on  $Y_c N$  forces inferred from lattice QCD simulations**  
Eur. Phys. J. A **56** 195 (2020)
38. J. Haidenbauer  
**Exploring the  $\Lambda$  -deuteron interaction via correlations in heavy-ion collisions**  
Phys. Rev. C: Nucl. Phys. **102** 034001 (2020)
39. H. Hammer and U. Meißner  
**The proton radius: from a puzzle to precision**  
Sci. Bull. **65** 257 - 258 (2020)
40. C. Hanhart and E. Klempt  
**Are the XYZ states unconventional states or conventional states with unconventional properties?**  
Int. J. Mod. Phys. A **35** 2050019 - (2020)
41. A. Hützen *et al.*  
**Simulation of Polarized Beams from Laser-Plasma Accelerators**  
J. Phys.: Conf. Ser. **1596** 012013 - (2020)
42. C. Kalmahalli Guruswamy, U. Meißner and C. Seng  
**Contraction diagram analysis in pion-kaon scattering**  
Nucl. Phys. B **957** 115091 - (2020)
43. P. Kampmann, Y. Cheng and L. Ludhova  
**A semi-analytical energy response model for low-energy events in JUNO**  
J. Instrum. **15** P10007 - P10007 (2020)
44. H. Krebs, E. Epelbaum and U. Meißner  
**Subleading contributions to the nuclear scalar isoscalar current**  
Eur. Phys. J. A **56** 240 (2020)
45. H. Krebs, E. Epelbaum and U. Meißner  
**Box diagram contribution to the axial two-nucleon current**  
Phys. Rev. C **101** 055502 (2020)
46. S. Kumaran and L. Ludhova  
**A New Journey to the Center of the Earth**  
Nucl. Phys. News **30** 17 - 21 (2020)
47. T.A. Lähde, U. Meißner and E. Epelbaum  
**An update on fine-tunings in the triple-alpha process**  
Eur. Phys. J. A **56** 89 (2020)

48. H. Le *et al.*  
**Implications of an increased  $\Lambda$ -separation energy of the hypertriton**  
Phys. Lett. B **801** 135189 - (2020)
49. H. Le *et al.*  
**Jacobi no-core shell model for p-shell hypernuclei**  
Eur. Phys. J. A **56** 301 (2020)
50. D. Lee *et al.*  
 **$\Theta^-$ -dependence of light nuclei and nucleosynthesis**  
Phys. Rev. Res. **2** 033392 (2020)
51. B. Lu *et al.*  
**Ab Initio Nuclear Thermodynamics**  
Phys. Rev. Lett. **125** 192502 (2020)
52. Z. Lu *et al.*  
**QCD  $\Theta^-$ -vacuum energy and axion properties**  
J. High Energ. Phys. **2020** 1 (2020)
53. T. Luu and U. Meißner  
**Misconceptions on Effective Field Theories and Spontaneous Symmetry Breaking: Response to Ellis' Article**  
Found. Phys. **50** 1140 - 1151 (2020)
54. U. Meißner  
**Two-Pole Structures in QCD: Facts, Not Fantasy!**  
Symmetry **12** 981 - (2020)
55. U. Meißner  
**Precision Predictions**  
Nucl. Phys. News **30** 17 - 20 (2020)
56. U. Meißner  
**Towards a theory of baryon resonances**  
Eur. Phys. J. Web of Conferences **241** 02003 - (2020)
57. F. Müller *et al.*  
**Measurement of deuteron carbon vector analyzing powers in the kinetic energy range 170-380 MeV**  
Eur. Phys. J. A **56** 211 (2020)
58. F. Müller *et al.*  
**A new beam polarimeter at COSY to search for electric dipole moments of charged particles**  
J. Instrum. **15** P12005 - P12005 (2020)
59. N.N. Nikolaev *et al.*  
**New approach to search for parity-even and parity-odd time-reversal violation beyond the Standard Model in a storage ring**  
Phys. Lett. B **811** 135983 - (2020)
60. J. Ostmeyer *et al.*  
**Semimetal-Mott insulator quantum phase transition of the Hubbard model on the honeycomb lattice**  
Phys. Rev. B **102** 245105 (2020)
61. S. Petschauer *et al.*  
**Hyperon-Nuclear Interactions From SU(3) Chiral Effective Field Theory**  
Front. Phys. **8** 12 (2020)
62. J. Pretz  
**Oscillations of a suspended slinky**  
Eur. J. Phys. - **14** (2020)
63. F. Rathmann, N.N. Nikolaev and J. Slim  
**Spin dynamics investigations for the electric dipole moment experiment**  
Phys. Rev. Accel. Beams **23** 024601 (2020)

64. X. Ren *et al.*  
**Meson-baryon scattering in resummed baryon chiral perturbation theory using time-ordered perturbation theory**  
 Eur. Phys. J. C **80** 406 (2020)
65. M. Rimpler *et al.*  
**Determination of the neutron yield of Be, V and Ta targets irradiated with protons (22-42 MeV) by means of prompt gamma neutron activation analysis**  
 Nucl. Instr. Meth. Phys. Res. A **990C** 164989 - (2020)
66. C. Seng *et al.*  
**New method for calculating electromagnetic effects in semileptonic beta-decays of mesons**  
 J. High Energ. Phys. **2020** 179 (2020)
67. C. Seng, D. Galviz and U. Meißner  
**A new theory framework for the electroweak radiative corrections in  $K_{l3}$  decays**  
 J. High Energ. Phys. **2020** 69 (2020)
68. D. Severt and U. Meißner  
**The Roper resonance in a finite volume**  
 Commun. Theor. Phys. **72** 075201 - (2020)
69. Y. Shi *et al.*  
**Towards a heavy diquark effective theory for weak decays of doubly heavy baryons**  
 Eur. Phys. J. C **80** 398 (2020)
70. J. Slim *et al.*  
**The driving circuit of the waveguide RF Wien filter for the deuteron EDM precursor experiment at COSY**  
 J. Instrum. **15** P03021 - P03021 (2020)
71. J. Speth *et al.*  
**Generalized Skyrme random-phase approximation for nuclear resonances: Different trends for electric and magnetic modes**  
 Phys. Rev. C **102** 054332 (2020)
72. J. Stapmanns *et al.*  
**Self-consistent formulations for stochastic nonlinear neuronal dynamics**  
 Phys. Rev. E **101** 042124 (2020)
73. Y.K. Tanaka *et al.*  
**Spectroscopy of  $\eta'$ -mesic Nuclei with WASA at GSI/FAIR**  
 Act. Phys. Pol. B **51** 39 - 44 (2020)
74. E. Tardiff *et al.*  
**Two-symmetry Penning-Ioffe trap for antihydrogen cooling and spectroscopy**  
 Nucl. Instr. Meth. Phys. Res. A **977** 164279 - (2020)
75. J. Thomas *et al.*  
**Scaling laws for the depolarization time of relativistic particle beams in strong fields**  
 Phys. Rev. Accel. Beams **23** 064401 (2020)
76. H. Verhoeven *et al.*  
**Measurement of spallation cross sections for the production of terbium radioisotopes for medical applications from tantalum targets**  
 Nucl. Instr. Meth. Phys. Res. B **463** 327 - 329 (2020)
77. T. Vonk, F. Guo and U. Meißner  
**Precision calculation of the axion-nucleon coupling in chiral perturbation theory**  
 J. High Energ. Phys. **2020** 138 (2020)
78. J. Wu and U. Meißner  
**Towards the continuum coupling in nuclear lattice effective field theory I: A three-particle model**  
 Chinese Phys. C **44** 124109 - (2020)

79. C.W. Xiao, U. Meißner and J.A. Oller  
**Investigation of  $J/\psi \rightarrow \gamma\pi^0\eta(\pi^+\pi^-, \pi^0\pi^0)$  radiative decays including final-state interactions**  
Eur. Phys. J. A **56** 23 (2020)
80. P.A. Zyla *et al.*  
**Review of Particle Physics**  
Prog. Theor. Exp. Phys. **2020** 083C01 (2020)

## C.2 Books

1. C. Hanhart  
**kurz & knapp: Quantenmechanik**, Das Wichtigste auf unter 150 Seiten, DOI: <https://doi.org/10.1007/978-3-662-60702-2>, Springer Spektrum, Berlin, Heidelberg, ISBN: 978-3-662-60702-2 (2020)
2. T.A. Lähde and U. Meißner  
**Nuclear Lattice Effective Field Theory**, An Introduction, DOI: <https://doi.org/10.1007/978-3-030-14189-9>, Part of the Lecture Notes in Physics book series (LNP, volume 957) (2019)

## D Talks and Colloquia

### D.1 Conference and Workshop Contributions

1. M. Agostini *et al.*  
**The study of solar neutrinos and of non-standard neutrino interactions with Borexino**  
16th International Conference on Topics in Astroparticle and Underground physics, Toyama, Japan: 2019-09-09 - 2019-09-13  
J. Phys.: Conf. Ser. 1468 012192
2. Z. Bagdasarian *et al.*  
**Analytical response function for the Borexino solar neutrino analysis**  
15th International Conference on Topics in Astroparticle and Underground Physics, Sudbury, Canada: 2017-07-24 - 2017-07-28  
J. Phys.: Conf. Ser. 1342 012105 -
3. B. Breitkreutz and P. Niedermayer  
**Tune and chromaticity measurement at COSY**  
JEDI Collaboration Meeting #16, Jülich, Germany: 2020-06-22 - 2020-06-24
4. S. Caprioli *et al.*  
**Data selection strategy for solar neutrino analysis with Borexino**  
15th International Conference on Topics in Astroparticle and Underground Physics, Sudbury, Canada: 2017-07-24 - 2017-07-28  
J. Phys.: Conf. Ser. 1342 012110 -
5. D. D'Angelo *et al.*  
**Ten years of cosmic muons observation with Borexino**  
16th International Conference on Topics in Astroparticle and Underground Physics, Toyama, Japan: 2019-09-09 - 2019-09-13
6. X.F. Ding *et al.*  
**Speeding up complex multivariate data analysis in Borexino with parallel computing based on Graphics Processing Unit**  
15th International Conference on Topics in Astroparticle and Underground Physics, Sudbury, Canada: 2017-07-24 - 2017-07-28  
J. Phys.: Conf. Ser. 1342 012115 -
7. M. Du *et al.*  
**Decoding the nature of the pentaquark states from LHCb**  
The 18th International Conference on Hadron Spectroscopy and Structure (HADRON2019), Guilin, China: 2019-08-16 - 2019-08-21
8. T. Gutberlet *et al.*  
**Perspectives for accelerator based neutron sources - The HBS project**  
MLZ User Meeting & German Neutron Scattering Conference 2020, online event, Germany: 2020-12-08 - 2020-12-10
9. J. Haidenbauer  
**Baryon-Baryon Interaction in Chiral Effective Field Theory**  
International Conference on Few-Body Problems in Physics, Caen, France: 2018-07-09 - 2018-07-13
10. J. Haidenbauer  
**Baryon-baryon interactions from correlation functions**  
Mini-workshop on hadron physics with heavy quark, Osaka, Japan: 2020-01-21 - 2020-01-21
11. J. Haidenbauer  
**Hyperon-nucleon interaction in few- and many body systems**  
International symposium on Clustering as a Window on the Hierarchical Structure of Quantum Systems, Beppu, Japan: 2020-01-23 - 2020-01-24

12. J. Haidenbauer  
**Hypernuclei and charmed nuclei**  
 Workshop on Physics programme for the first stage of the NICA SPD experiment, Dubna, Russia: 2020-10-05 - 2020-10-06
13. C. Hanhart  
**Theoretical update on the XYZ states ... and beyond**  
 International Workshops on Hadron Structure and Spectroscopy, Trieste, Italy: 2020-11-15 - 2020-11-20
14. C. Hanhart  
**Amplitude Analysis Theory**  
 Belle II Physics Week, online, Japan: 2020-11-30 - 2020-12-04
15. C. Hanhart  
**Precision calculations in non- perturbative QCD (I): Effective Field Theories (EFT's), analyticity and dispersion relations**  
 Theoretical Aspects of Hadron Spectroscopy and Phenomenology, Valencia, Spain: 2020-12-15 - 2020-12-17
16. L. Hlophe *et al.*  
**Three-Body Approach to Deuteron-Alpha Scattering Using Realistic Forces in a Separable or Non-separable Representation**  
 International Conference on Few-Body Problems in Physics, Caen, France: 2018-02-09 - 2018-02-14
17. S. Kumaran *et al.*  
**Extraction of Bi-210 via Po-210 for CNO neutrino detection with Borexino**  
 Neutrino 2020, Virtual (Chicago), United States: 2020-06-22 - 2020-07-02
18. S. Kumaran *et al.*  
**Analysis strategies for the updated geoneutrino measurement with Borexino**  
 16th International Conference on Topics in Astroparticle and Underground Physics, Toyama, Japan: 2019-09-09 - 2019-09-13
19. C. Lerche *et al.*  
**Design and Simulation of a high-resolution and high-sensitivity BrainPET insert for 7T MRI**  
 NuklearMedizin 2020, Leipzig, Germany: 2020-07-06 - 2020-07-09
20. J. Li *et al.*  
**FLUKA and MCNP simulation benchmark for neutron yield measurement**  
 The Japanese RIKEN Center for Advanced Photonics (RAP) and the Jülich Centre for Neutron Science (JCNS) fourth joint workshop on compact accelerator-driven neutron sources (CANS) special webinar, Forschungszentrum Jülich, Germany: 2020-06-22 - 2020-06-24
21. J. Li *et al.*  
**FLUKA and MCNP simulation benchmark for neutron yield measurement in HBS project**  
 MLZ User Meeting & German Neutron Scattering Conference 2020, online event, Germany: 2020-12-08 - 2020-12-10
22. J. Li *et al.*  
**Monte Carlo simulation of neutron yield measurements for Be, V and Ta targets**  
 The Japanese RIKEN Center for Advanced Photonics (RAP) and the Jülich Centre for Neutron Science (JCNS) fourth joint workshop on compact accelerator-driven neutron sources (CANS) special webinar, Forschungszentrum Jülich, Germany: 2020-06-22 - 2020-06-24
23. L. Ludhova *et al.*  
**Updated geoneutrino measurement with Borexino**  
 16th International Conference on Topics in Astroparticle and Underground Physics, Toyama, Japan: 2019-09-09 - 2019-09-13
24. L. Ludhova  
**Overview on solar, geo, and reactor neutrino experiments**  
 DISCRETE 2018, Vienna, Austria: 2018-11-26 - 2018-11-30  
 J. Phys.: Conf. Ser. 1586 012034

25. L. Ludhova and Borexino collaboration  
**Limiting the effective magnetic moment of solar neutrinos with the Borexino detector**  
 TAUP 2017, Sudbury, Canada: 2017-07-24 - 2017-07-28  
 J. Phys.: Conf. Ser. 1342 012033 -
26. L. Ludhova  
**Borexino: Experimental evidence of neutrinos produced in the CNO fusion cycle in the Sun**  
 7th KAT Strategy meeting, online, Germany: 2020-12-04 - 2020-12-05
27. S. Marcocci *et al.*  
**The Monte Carlo simulation of the Borexino detector**  
 15th International Conference on Topics in Astroparticle and Underground Physics, Sudbury, Canada: 2017-07-24 - 2017-07-28  
 J. Phys.: Conf. Ser. 1342 012035 -
28. U. Meißner  
**Nuclear Lattice Effective Field Theory: Status and Perspectives**  
 NIC Symposium 2020, Jülich, Germany: 2020-02-27 - 2020-02-28
29. U. Meißner  
**Nuclear lattice effective field theory: Status and perspectives**  
 10th NIC Symposium, Jülich, Germany: 2020-02-27 - 2020-02-28
30. U. Meißner  
**Two-pole structures in QCD: Facts, not fantasy!**  
 Workshop on "Theoretical Aspects of Hadron Spectroscopy and Phenomenology", Valencia(online), Spain: 2020-12-15 - 2020-12-17
31. U. Meißner  
**Topics and open issues in hadron physics**  
 Workshop on Future prospects in hadron physics, Bonn(online), Germany: 2020-12-08 - 2020-12-08
32. P. Niedermayer  
**New diagnostic tools & systems at COSY**  
 12th COSY Beamtime Advisory Committee session, Jülich, Germany: 2020-10-08 - 2020-10-09
33. A. Nogga  
**Status of SMS 3NFs and application to 3H, 3He and 4He**  
 5th LENPIC meeting, Cracow(online), Poland: 2020-03-24 - 2020-03-24
34. Ö. Penek and et al. Borexino Collaboration  
**Borexino Sensitivity Studies towards Detection of Solar Neutrinos from the CNO Fusion Cycle**  
 The XXIX International Conference on Neutrino Physics and Astrophysics, Chicago, USA: 2020-06-22 - 2020-07-02
35. J. Pütz *et al.*  
**Study of  $\bar{p}p \rightarrow \bar{\Xi}^+ \Lambda K^-$  with the  $\bar{P}$ ANDA Detector**  
 The 12th International Workshop on the Physics of Excited Nucleons (NSTAR 2019), Jülich, Germany: 2020-09-22 - 2020-09-22
36. F. Rathmann  
**Test of the Standard Model and Search for Physics Beyond\* Opportunities for Fundamental Physics using Small-scale Storage Ring Experiments**  
 Townhall Meeting of the 2021 Rare Processes and Precision Frontier, online, USA: 2020-10-02 - 2020-10-03
37. F. Rathmann  
**Spin physics using storage rings - Spin-physics tools, instruments, opportunities and perspectives**  
 17th SPARC WORKSHOP (collaboration meeting), online, Germany: 2020-09-14 - 2020-09-16
38. M. Redchuk *et al.*  
**Comprehensive measurement of pp-chain solar neutrinos with Borexino**  
 European Physical Society Conference on High Energy Physics, Ghent, Belgium: 2019-07-10 - 2019-07-17

39. M. Rimmler *et al.*  
**Neutron yield measurements for Be, V and Ta targets from 22-42 MeV proton beams**  
 MLZ User Meeting & German Neutron Scattering Conference 2020, online event, online event: 2020-12-08 - 2020-12-10
40. M. Rimmler  
**Proton beam multiplexer developments towards HBS**  
 The Japanese RIKEN Center for Advanced Photonics (RAP) and the Jülich Centre for Neutron Science (JCNS) fourth joint workshop on compact accelerator-driven neutron sources (CANS) special webinar, Forschungszentrum Jülich, Germany: 2020-06-22 - 2020-06-24
41. D. Rönchen  
**Phenomenological determination and status of the light baryon spectrum**  
 Accessing and Understanding the QCD Spectra, online (geplant Seattle, Washington USA), online (geplant USA): 2020-08-17 - 2020-09-04
42. P. Salabura *et al.*  
**Exploring time like tranistions in pp,  $\pi p$  and AA reactions with HADES**  
 The 12th International Workshop on the Physics of Excited Nucleons (NSTAR 2019), Jülich, Germany: 2020-09-22 - 2020-09-22
43. G. Settanta  
**Atmospheric Neutrino Physics with JUNO**  
 LXX International conference "NUCLEUS - 2020, Online, Online: 2020-10-11 - 2020-10-17
44. A. Solovev *et al.*  
**Optimization and first tests of the experimental setup to investigate the double-polarized DD-fusion reactions**  
 The International School for Advanced Studies (SISSA), find out more The International School for Advanced Studies (SISSA), find out more The International Conference Instrumentation for Colliding Beam Physics (INSTR2020), Novosibirsk, Russia: 2020-02-24 - 2020-02-28  
 J. Instrum. 15 C08003 - C08003
45. P. Zakalek *et al.*  
**Big Karl Experimental Area**  
 The Japanese RIKEN Center for Advanced Photonics (RAP) and the Jülich Centre for Neutron Science (JCNS) fourth joint workshop on compact accelerator-driven neutron sources (CANS) special webinar, Forschungszentrum Jülich, Germany: 2020-06-22 - 2020-06-24

## D.2 Colloquia

1. F. Abusaif  
**Development of Compact Beam Position Monitors (Rogowski based)**  
 Physik-Kolloquium at RWTH Aachen University, Aachen, Germany: 2020-01-17 - 2020-01-17
2. Z. Bagdasarian  
**Solar Neutrinos with Borexino: First evidence of CNO fusion cycle**  
 Lawrence Berkeley National Laboratory Research Progress Meeting, Berkeley, USA: 2020-07-16
3. Z. Bagdasarian  
**Solar Neutrinos with Borexino: First evidence of CNO fusion cycle**  
 Sheffield, United Kingdom (UK): 2020-07-06
4. Z. Bagdasarian  
**"Dive into the deep Earth with neutrinos: Borexino latest results**  
 Zeuthen, Germany: 2020-04-17
5. Z. Bagdasarian  
**Borexino. Sun. Earth. Neutrinos**  
 Berkeley, USA: 2020-04-03

6. R.W. Engels  
**The PREFER Collaboration: Status and Perspectives**  
 Joint Meeting with Uni. Ferrara, INFN Catania and PNPI, St. Petersburg 2020-10-26 - 2020-10-26
7. J. Haidenbauer  
**Aspects of the hyperon-nucleon interactions**  
 Uppsala, Sweden: 2020-02-27
8. J. Haidenbauer  
**The hyperon-nucleon and the hyperon-nucleon-nucleon interactions**  
 Kyushu, Japan: 2020-08-06 -
9. C. Hanhart  
**Theoretical insights about the XYZ states ... and beyond**  
 Seminar talk, Valencia, Spain: 2020-11-10 - 2020-11-10
10. L. Ludhova  
**JUNO - the first multi-kton liquid scintillator detector**  
 Seminars of the Institute for Nuclear and Particle Astrophysics, Berkeley National Laboratory, USA: 2020-10-30
11. U. Meißner  
**Hypernuclear Physics from Nuclear Lattice EFT**  
 Joint THEIA-STRONG2020 seminar, Mainz(online), Germany: 2020-10-28 - 2020-10-28
12. Ö. Penek  
**First experimental evidence of neutrinos produced in the CNO fusion cycle in the Sun**  
 IKP Seminar, Jülich, Germany: 2020-11-30 - 2020-11-30
13. J. Pretz  
**Storage Ring Electric Dipole Moment Measurement**  
 Seminar University of Liverpool, Liverpool, UK: 2020-01-30
14. F. Rathmann  
**Electric Dipole Moment Searches using Storage Rings**  
 Colloquium talk at the Landau Institute for Theoretical Physics, Chernogolovka, Russia 2020-01-24 - 2020-01-24
15. G. Settanta  
**First detection of solar neutrinos from the CNO cycle with the Borexino detector**  
 RTG Colloquium, RWTH Aachen: 2020-12-08

## E Academic Degrees

### E.1 Dissertation / PhD Theses

1. P. Kampmann  
**Energy scale non-linearity and event reconstruction for the Neutrino Mass Ordering measurement of the JUNO experiment**  
RWTH Aachen
2. H. Le  
**Jacobi No-Core Shell Model for P-shell Hypernuclei**  
Rheinische Friedrich-Wilhelms-Universität Bonn
3. J. Pütz  
**Study of Excited  $\Xi$  Baryons in Anti-Proton Proton Collisions with the  $\overline{\text{P}}\text{ANDA}$  Detector**  
Rheinische Friedrich-Wilhelms-Universität Bonn
4. M. Redchuk  
**Looking inside the Sun with the Borexino experiment: detection of solar neutrinos from the proton-proton chain and the CNO cycle**  
RWTH Aachen
5. S. Ropertz  
**A formalism for a consistent treatment of two-pion interactions in heavy meson decays**  
Rheinische Friedrich-Wilhelms-Universität Bonn
6. Y. Xu  
**Machine learning application in low energy liquid scintillator neutrino experiment**  
RWTH Aachen
7. J.-L. Wynen  
**Strongly interacting few-body systems from lattice stochastic methods**  
Rheinische Friedrich-Wilhelms-Universität Bonn

### E.2 Master Theses

1. L.v. Detten  
**A new parametrization for scalar  $K\pi$  scattering and production**  
Rheinische Friedrich-Wilhelms-Universität Bonn
2. S. Krug  
**The complete next-to-leading order potential for  $B^{(*)}B^{(*)} \rightarrow B^{(*)}B^{(*)}$  scattering**  
Rheinische Friedrich-Wilhelms-Universität Bonn
3. F. Noel  
**Towards a consistent description of  $K\pi$  scattering**  
Rheinische Friedrich-Wilhelms-Universität Bonn
4. A. Sen  
**Spin Tune Analysis for Electric Dipole Moment Searches**  
RWTH Aachen
5. A. Singhal  
**Observation of CNO solar neutrinos with the Borexino Experiment**  
RWTH Aachen

### **E.3 Bachelor Theses**

1. T. Kehlenbach  
**Real Time Integration of a MHz Signal using a Fast Programmable Gate Array**  
RWTH Aachen
2. S. Pütz  
**Polarization measurement of a pulsed H-/D- ion beam with a Lamb-shift Polarimeter**  
FH Aachen
3. M. Schindler  
**Resonanzen in wenig-Baryon Systemen**  
Rheinische Friedrich-Wilhelms-Universität Bonn
4. V. Verhoeven  
**Production of HD Molecules in Definite Hyperfine Substates**  
Heinrich-Heine Universität Düsseldorf

## F Awards

**Falastine Abusaif** received one of the "Best presentation" prizes in the PGSB (Palestinian-German Science Bridge) Fellows and Alumni Award Competition 2020; video can be viewed at:

[https://www.fz-juelich.de/SharedDocs/Videos/UE/DE/UE-B/pgsb\\_fellow\\_falastine\\_abusaif\\_2020.mp4?\\_\\_blob=videoFile](https://www.fz-juelich.de/SharedDocs/Videos/UE/DE/UE-B/pgsb_fellow_falastine_abusaif_2020.mp4?__blob=videoFile)

**Christoph Genster** was awarded the first "JUNO PhD thesis award" for his contributions to the JUNO Experiment.

**Observation of solar neutrinos from the CNO fusion** by Borexino collaboration was nominated among the Top 10 Physics Breakthroughs of 2020 by Physics World. (<https://physicsworld.com/a/physics-world-announces-its-breakthrough-of-the-year-finalists-for-2020/>)

## G Third Party Funded Projects

Project	Responsible/Contact	Funded by
Untersuchung von exotischen 4-Quark Zuständen	E. Prencipe	DFG
PGSB: Experimental tests of time-reversal	H. Ströher	BMBF
Bestimmung der Neutrino-Massenhierarchie	L. Ludhova	DFG
SFB/TRR 110 Quantenchromodynamik TP A01	J. Haidenbauer	DFG/NSFC
SFB/TRR 110 Quantenchromodynamik TP A05	U.-G. Meißner	DFG/NSFC
SFB/TRR 110 Quantenchromodynamik TP B03	C. Hanhart	DFG/NSFC
SFB/TRR 110 Quantenchromodynamik TP B06	A. Nogga	DFG/NSFC
SFB/TRR 110 Quantenchromodynamik TP B09	T. Luu / U.-G. Meißner	DFG/NSFC
SFB/TRR 110 Quantenchromodynamik TP Z01	U.-G. Meißner	DFG/NSFC
SFB/TRR 110 Quantenchromodynamik TP Z02	C. Hanhart	DFG/NSFC
PANDA/ Straw Tube Tracker	J. Ritman	Industrieprojekt mit der GSI GmbH
PANDA/ Micro Vertex Detector	J. Ritman	Industrieprojekt mit der GSI GmbH
HESR - Dipole und Quadrupole	R. Tölle	Industrieprojekt mit der FAIR GmbH
HESR - sonstige Magnete	J. Böker	Industrieprojekt mit der FAIR GmbH
HESR - Netzgeräte	M. Retzlaff	Industrieprojekt mit der FAIR GmbH
HESR - Hochfrequenz	R. Stassen	Industrieprojekt mit der FAIR GmbH
HESR - Injektion	R. Tölle	Industrieprojekt mit der FAIR GmbH
HESR - Strahldiagnose	V. Kamerzhiev	Industrieprojekt mit der FAIR GmbH
HESR - Vakuum	F. Esser	Industrieprojekt mit der FAIR GmbH
HESR - Stochastische Kühlung	R. Stassen	Industrieprojekt mit der FAIR GmbH
HESR - Panda-Integration	D. Prasuhn	Industrieprojekt mit der FAIR GmbH
HESR - P1SR	R. Tölle	Industrieprojekt mit der GSI GmbH
AVA MSCA ITN	D. Grzonka	EU
Unit Costs TA1	D. Grzonka	EU (STRONG2020)
Travel and Subsistance for Users TA	D. Grzonka	EU (STRONG2020)
Transnational Access to COSY TA1	D. Grzonka	EU (STRONG2020)
JRA2-FTE@LHC:	F. Rathmann	EU (STRONG2020)
Fixed Target Experiments at the LHC		
JRA3-PrecisionSM:	S. Schadmand	EU (STRONG2020)
Precision Tests of the Standard Model		
JRA7-HaSP:	C. Hanhart	EU (STRONG2020)
Light-and heavy-quark hadron spectroscopy		
JRA12-SPINFORFAIR: Spin for FAIR	F. Rathmann	EU (STRONG2020)
srEDM ERC Advanced Grant Management	H. Ströher	EU
srEDM ERC Advanced Grant Research	H. Ströher	EU
ATHENA <sub>h</sub> (Accelerator Technology HELmholtz iN-frAstructure)	A. Lehrach	HGF

## H Collaborations

- ATHENA Accelerator Technology Helmholtz Infrastructure  
([https://www.athena-helmholtz.de/home/index\\_eng.html](https://www.athena-helmholtz.de/home/index_eng.html))
- Belle-II (B(meson) to lepton lepton (v.2) )  
(<https://www.belle2.org>)
- Borexino (Boron solar neutrino experiment, LNGS, Italy)  
(<http://borex.lngs.infn.it>)
- CBM (Compressed Baryonic Matter)  
(<https://www.gsi.de/work/forschung/cbmnqm/cbm.htm>)
- CLAS (CEBAF Large Acceptance Spectrometer, JLab, USA)  
(<https://www.jlab.org/Hall-B/clas-web>)
- CPEDM (Electric Dipole Moments, CERN)  
(<http://pbc.web.cern.ch/edm/edm-org.htm>)
- ELENA (CERN) (Extra Low Energy Antiproton ring)  
(<https://espace.cern.ch/elena-project/SitePages/Home.aspx>)
- GlueX (The GlueX experiment, JLab, USA)  
(<https://www.jlab.org/Hall-D/>)
- HADES (High Acceptance DiElectron Spectrometer)  
(<https://www-hades.gsi.de>)
- HBS (High Brilliance Neutron Source)  
([https://www.fz-juelich.de/jcms/jcms-2/EN/Forschung/High-Brilliance-Neutron-Source/\\_node.html](https://www.fz-juelich.de/jcms/jcms-2/EN/Forschung/High-Brilliance-Neutron-Source/_node.html))
- JEDI (Jülich Electric Dipole moment Investigation, COSY)  
(<http://collaborations.fz-juelich.de/ikp/jedi>)
- JUNO (Jiangmen Underground Neutrino Observatory, Jiangmen, China)  
(<http://juno.ihep.cas.cn>)
- JuSPARC (Jülich Short-Pulsed Particle and Radiation Center)  
(<https://jusparc.fz-juelich.de/>)
- KLF (K-long Facility, Jefferson Lab)  
([https://wiki.jlab.org/klproject/index.php/December,\\_2020](https://wiki.jlab.org/klproject/index.php/December,_2020))
- LENPIC (Low Energy Nuclear Physics International Collaboration)  
(<http://www.lenpic.org/>)
- PANDA (Anti-Proton Annihilation at Darmstadt, FAIR)  
(<https://panda.gsi.de>)
- PAX (Polarized Antiproton eXperiments, COSY)  
(<http://collaborations.fz-juelich.de/ikp/pax>)
- PDG (Particle Data Group)  
([pdg.lbl.gov](http://pdg.lbl.gov))
- PREFER (Polarization Research for Fusion Experiments and Reaktors)
- STRONG-2020 (The strong interaction at the frontier of knowledge: fundamental research and applications)  
([www.strong-2020.eu](http://www.strong-2020.eu))
- WASA (Wide Angle Shower Apparatus, FRS)  
(<https://www-win.gsi.de/frs/index.htm>)
- WASA (Wide Angle Shower Apparatus, WASA-at-COSY)  
(<http://collaborations.fz-juelich.de/ikp/wasa/>)

# I Conferences and Outreach Activities (Co-)Organized by the IKP

## I.1 JUNO DFG Research Unit workshop

October 5 - 7 2020. The yearly meeting of the DFG Research Unit "Determination of the Hierarchy of Neutrino Masses with the JUNO-Experiment" was organized by the neutrino group at the grounds of FZJ with more than 30 participants.

## I.2 Interviews

- Interview with L. Ludhova **Neutrino-Physikerin mit einem Faible für Berge** in [Weltmaschine.de](http://Weltmaschine.de).
- Interview with L. Ludhova **Was die Erde von innen wärmt** in Frankfurter Allgemeiner Zeitung about the latest Borexino geoneutrino measurement.
- Interview with L. Ludhova **Astrophysiker werfen einen tiefen Blick in die Sonne – und werden reich belohnt** with Neue Zürcher Zeitung about the CNO observation by Borexino.

## I.3 HHU Düsseldorf - Nobelpreis live - Physik

Hans Ströher participated in the Event "Nobelpreis live - Physik" at the HHU Düsseldorf. (<https://www.youtube.com/watch?v=JyM5EfYfXJw>)

## I.4 Publication Contributions

Livia Ludhova and Hans Ströher contributed to the publication "Die 42 größten Rätsel der Physik" by Ilja Bohnet, Franckh-Kosmos, 10/2020, ISBN-13: 9783440168820

## I.5 Georgian-German Science Bridge: Visit of the Ambassador of Georgia to Forschungszentrum Jülich and RWTH Aachen University

On September 22, the Chairman of the Board of Directors, Prof. Wolfgang Marquardt, and some Directors of Institutes of Forschungszentrum Jülich, including colleagues from IKP, hosted distinguished Georgian guests, Prof. Levan Izoria (Ambassador of Georgia in Germany) and Mr. Levan Diasamidze (Consul General at the Consulate General of Georgia in Frankfurt), for a discussion of topics of mutual interest within the Georgian-German Science Bridge (see Fig. 50). Besides summing up the well-established scientific exchange, the talks focused on the further GGSB development (under the name GGSB PLUS) along the theme „Health as a Global Challenge“, support of the newly founded Kutaisi International University (KIU) and plans for further SMARTILabs in the fields of Neuroscience, Engineering and Data Science in



(a) Visit in IKP



(b) Visit in JuLAB.

Figure 50: (a) Visit in IKP: (from left to right ) L. Diasamidze, H. Ströher, Prof. L. Izoria. (b) Visit in JuLab: (from left to right) A. Kacharava, L. Diasamidze, L. Izoria, A. Fuchs-Döll, I. Keutmann.

Georgia. Prof. Izoria was also briefed on the joint research at the Cooler Synchrotron COSY of the Institute of Nuclear Physics as well as on the activities of the Jülich student laboratory (JuLab) by Ina Keutmann, head of JuLab. Together with Anne Fuchs-Döll, they provided an overview of their work and a review of the first advanced training event in Georgia at TSU, which took place in 2019. A short meeting with Georgian PhD students and guest scientists concluded the visit of the distinguished guests to Forschungszentrum Jülich. The Georgian delegation also visited RWTH (organized by Achim Stahl), where the delegation was welcomed by RWTH Rector Ulrich Rüdiger.

During November 12 – 20, 2020, 30 students from four Georgian universities (AUG, GTU, ISU and TSU) attended the online "Science Lectures" within our Autumn School, during which they were giving presentations (available from: <http://collaborations.fz-juelich.de/ikp/cgswhp/cgswhp20/program/program.shtml>). Originally, the School was planned during GGSWBS'20 in Tbilisi, which had to be postponed to Autumn 2021 due to the pandemic. The participants had been preselected earlier in personal

interviews at Georgian universities. The lectures were organized by Institutes of Forschungszentrum (IBG, IEK, INM, IKP, and ZEA). During the lectures, the students were also introduced to the research at the institutes. As part of the event, 10 excellent students from various scientific fields – Physics, Mathematics, Chemistry, Biology and Engineering Technology – were selected and granted internships of one month each at FZJ. For IKP a total of 3 students were identified, which will visit the institute in March/April 2021.

## J Teaching Positions

Institute	Name	University
IKP-1	PD. Dr. A. Gillitzer Prof. Dr. F. Goldenbaum Prof. J. Ritman Ph.D. Dr. T. Stockmanns	Rheinische Friedrich-Wilhelms-Univ. Bonn Bergische Univ. Wuppertal Ruhr-Univ. Bochum Ruhr-Univ. Bochum
IKP-2	PD Dr. F. Rathmann Prof. Dr. L. Ludhova Prof. Dr. Dr. h.c. mult. H. Ströher Prof. Dr. J. Pretz	RWTH Aachen RWTH Aachen Univ. zu Köln RWTH Aachen
IKP-3/IAS-4	Univ. Doz. Dr. J. Haidenbauer Prof. Dr. C. Hanhart Prof. Dr. T. Luu Prof. Dr. Dr. h.c. U.-G. Meißner Dr. A. Nogga PD Dr. A. Wirzba	Univ. Graz Rheinische Friedrich-Wilhelms-Univ. Bonn Rheinische Friedrich-Wilhelms-Univ. Bonn Rheinische Friedrich-Wilhelms-Univ. Bonn Rheinische Friedrich-Wilhelms-Univ. Bonn Rheinische Friedrich-Wilhelms-Univ. Bonn
IKP-4	Dr. O. Felden Prof. Dr. A. Lehrach	FH Aachen RWTH Aachen

## K Personnel

MSc. F. Abusaif (IKP-2)  
MSc. D. Alfs (IKP-1)  
MSc. A. Alicke (IKP-1)  
BSc. A. Andres (IKP-2)  
Dr. M. Anwar (IKP-3/IAS-4)  
BSc. A. Asokan (IKP-3/IAS-4) (since 23<sup>rd</sup> Nov. 2020)  
Dr. Z. Bagdasarian (IKP-2) (until 31<sup>st</sup> Jan. 2020)  
Dr. I. Bekman (IKP-4)  
C. Berchem (IKP-TA)  
Dr. C. Böhme (IKP-4)  
M. Böhnke (IKP-4)  
Dr. J. Böker (IKP-4)  
DI N. Bongers (IKP-4)  
Dr. B. Breitzkreutz (IKP-4)  
P. Brittner (IKP-4)  
J. But (IKP-TA)  
W. Classen (IKP-4)  
M. Comuth-Werner (IKP-TA)  
DI F. U. Dahmen (IKP-4)  
DI N. Demary (IKP-TA)  
MBA A. Derichs (IKP-1)  
C. Deliege (IKP-4)  
G. D'Orsaneo (IKP-2)  
R. Dosdall (IKP-1)  
C. Ehrlich (IKP-4)  
Dr. R. Engels (IKP-2)  
B. Erkes (IKP-4)  
MSc. W. Esmail (IKP-1)  
DI F. –J. Etkorn (IKP-4)  
Dr. O. Felden (IKP-TA)  
H. - W. Firmenich (IKP-TA)  
Dr. D. Frame (IKP-3/IAS-4)  
F. Frenzel (IKP-4)  
N. Fröhlich (IKP-4)  
BSc. C. Gäntgen (IKP-3/IAS-4) (since 1<sup>st</sup> July 2020)  
Dr. R. Gebel (IKP-4)  
Dr. C. Genster (IKP-2) (until 29<sup>th</sup> Feb. 2020)  
PD Dr. A. Gillitzer (IKP-1) (until 31<sup>st</sup> March 2020)  
J. Göbbels (IKP-TA)  
Prof. Dr. F. Goldenbaum (IKP-1)  
N. Goertz (IKP-TA) (until 30<sup>th</sup> November 2020)  
MSc. A. Göttel (IKP-2)  
Dr. K. Grigoryev (IKP-4)  
Dr. D. Grzonka (IKP-1)  
M. Gülpen (IKP-TA)  
MSc. Y. Guo (IKP-2) (until 29<sup>th</sup> September 2020)  
PD Dr. J. Haidenbauer (IKP-3/IAS-4)  
A. Halama (IKP-4)  
E. Hall-Brunton (IKP-TA)  
DI S. Hamzic (IKP-4)  
Prof. Dr. C. Hanhart (IKP-3/IAS-4)  
T. Hahnrahts-von der Gracht (IKP-TA)  
Dr. M. Hartmann (IKP-2)  
DI R. Hecker (IKP-TA)  
Dr. V. Hejny (IKP-2)  
Dr. J. - H. Hetzel (IKP-4)  
M. Holona (IKP-1)  
MSc. O. Javakhishvili (IKP-2)  
Dr. A. Kacharava (IKP-2)  
Dr. V. Kamerdzhev (IKP-4)  
MSc. P. Kampmann (IKP-2)  
MSc. J. Kannika (IKP-1)  
MSc. C. Kannis (IKP-4)  
A. Kelleners (IKP-TA)  
Dr. I. Keshelashvili (IKP-2)  
A. Kieven (IKP-4)  
S. Kistemann (IKP-TA)  
B. Klimczok (IKP-TA)  
BSc. A. Koushik (IKP-2)  
M. Kremer (IKP-TA)  
DI T. Krings (IKP-TA)  
M. Küven (IKP-4)  
Dr. P. Kulesa (IKP-1)  
MSc. S. Kumaran (IKP-2)  
Dr. T. Lähde (IKP-3/IAS-4)  
K. - G. Langenberg (IKP-4)  
Prof. Dr. A. Lehrach (IKP-4)  
MSc. H. Le Thi (IKP-3/IAS-4)  
MSc. S. Liebert (IKP-4)  
R. Liu (IKP-2)  
MSc. K. Luckas (IKP-1)  
Prof. Dr. L. Ludhova (IKP-2)

Prof. T. Luu (IKP-3/IAS-4)  
 M. Maubach (IKP-TA)  
 MSc. I. Matuschek (IKP-3/IAS-4)  
 J. Meisenberg (IKP-TA) (until 31<sup>th</sup> July 2020)  
 Prof. Dr. Dr. h. c. U.-G. Meißner (IKP-3/IAS-4)  
 Dr. S. Merzliakov (IKP-4) (until 31<sup>st</sup> Aug. 2020)  
 DI A. Messaaf (IKP-4)  
 Dr. A. Naß (IKP-2)  
 P. Niedermayer (IKP-4)  
 Dr. A. Nogga (IKP-3/IAS-4)  
 L. Pelicci (IKP-2) (since 23<sup>th</sup> Nov. 2020)  
 MSc. Ö. Penek (IKP-2)  
 MSc. G. Perez-Andrade (IKP-1)  
 Dr. A. Pesce (IKP-2) (since 1<sup>st</sup> March 2020)  
 BSc J. T. Peters (IKP-4)  
 MSc. V. Poncza (IKP-4) (until 1<sup>st</sup> Aug. 2020)  
 C. Poulwey (IKP-4)  
 Dr. D. Prasuhn (IKP-4)  
 Prof. Dr. J. Pretz (IKP-2)  
 D. Prothmann (IKP-TA)  
 DP J. Pütz (IKP-1)  
 S. Pütz (IKP-4)  
 PD Dr. F. Rathmann (IKP-2)  
 BSc. L. Razmadze (IKP-3/IAS-4) (since 2<sup>nd</sup> Nov. 2020)  
 MSc. M. Redchuk (IKP-2) (until 31<sup>st</sup> May 2020)  
 DI K. Reimers (IKP-4)  
 DI M. Retzlaff (IKP-4)  
 M. Rifai (IKP-2) (since 1<sup>st</sup> Sep. 2020)  
 MSc. M. Rimmler (IKP-4)  
 Prof. J. Ritman (IKP-1)  
 Dr. D. Rönchen (IKP-3/IAS-4) (since 1<sup>st</sup> July 2020)  
 G. Roes (IKP-TA)  
 D. Ruhrig (IKP-4)  
 G. Rupsch (IKP-4) (since 1<sup>st</sup> March 2020)  
 Dr. A. Saleev (IKP-2) (until 31<sup>st</sup> Oct. 2020)  
 Ph.D. habil. S. Schadmand (IKP-1)  
 Dr. R. Schleichert (IKP-2)  
 F. Scheiba (IKP-4)  
 H. Schiffer (IKP-TA)  
 M. Schmühl (IKP-4)  
 M. Schubert (IKP-4)

Dr. Th. Sefzick (IKP-TA)  
 BSc. A. Sen (IKP-2) (until 30<sup>th</sup> Jun. 2020)  
 Dr. V. Serdyuk (IKP-1)  
 Dr. G. Settanta (IKP-2)  
 Dr. S. Shen (IKP-3/IAS-4) (since 15<sup>th</sup> September 2020)  
 Dr. V. Shmakova (IKP-2)  
 MSc. N. Shurkhno (IKP-4)  
 R. Similon (IKP-4)  
 DI M. Simon (IKP-4)  
 MSc. A. Singhal (IKP-2)  
 H. Smitmanns (IKP-2) (since 1<sup>st</sup> Oct. 2020)  
 J. Spelthann (IKP-TA)  
 D. Spölgen (IKP-2)  
 Dr. R. Stassen (IKP-4)  
 G. Sterzenbach (IKP-1)  
 Dr. T. Stockmanns (IKP-1)  
 Prof. Dr. Dr. h. c. mult. H. Ströher (IKP-2)  
 MSc. A. Thampi (IKP-1)  
 MSc. M. Thelen (IKP-4)  
 Dr. R. Tölle (IKP-4)  
 Dr. Y. Valdau (IKP-4)  
 DI T. Vashegyi (IKP-4)  
 V. Verhoeven (IKP-2) (until 30<sup>th</sup> Apr. 2020)  
 MSc. M. Vitz (IKP-4)  
 MSc. C. Vollbrecht (IKP-2)  
 MSc. T. Wagner (IKP-2)  
 L. Werth (IKP-TA)  
 M. Westphal (IKP-2) (since 9<sup>th</sup> Nov. 2020)  
 V. Wettig (IKP-TA)  
 Dr. P. Wintz (IKP-1)  
 PD Dr. A. Wirzba (IKP-3/IAS-4)  
 K. Wolff (IKP-TA) (until 15<sup>th</sup> June 2020)  
 Dr. J. - L. Wynen (IKP-3/IAS-4) (until 31<sup>st</sup> August 2020)  
 Dr. H. Xu (IKP-1)  
 MSc. Y. Xu (IKP-2) (until 15<sup>th</sup> Jul. 2020)  
 H. Zens (IKP-4)  
 Dr. Y. Zhou (IKP-1)

IKP-1 = Experimental Hadron Structure  
 IKP-2 = Experimental Hadron Dynamics  
 IKP-3/IAS-4 = Theory of the Strong Interactions  
 IKP-4 = Large-Scale Nuclear Physics Equipment  
 IKP-TA = Technical Services and Administration

# L Individual Contributions

## Contents

FAIR Related Experimental Activities	62
Production of the $\Sigma^0$ Baryon in proton-proton collisions at $\sqrt{s} = 3.176$ GeV	62
Extraction of Elastic Scattering Events in KOALA	63
Determination of the Cluster Target Density Profile in KOALA	65
Prospects to use PAWIAN for a Partial Wave Analysis of the $\bar{\Xi}^+ \Lambda K^-$ Final State with Data from PANDA	67
Thermal Test of a Mock-up of the Readout Volume for the PANDA STT	69
Quality and Runtime Optimization of a PANDA Track Finding Algorithm based on Hough Transformations	70
Improving Noise Tolerance in the Track Finding Process by Using Correlations between Multiple Language Models	71
Progress of the Sampling ADC based Front End Free Readout System for Straw Tube Tracker	72
Preparatory Studies for the Application of the PASTTREC ASIC at HADES	74
TRB3 DAQ System for HADES Straw Tubes Station Test	76
InnerTOF - a Trigger Scintillator for HADES	77
Pre-commissioning of the STS1 Detector for the FAIR Phase-0 Experiments with HADES	78
In-beam Straw Tests Measurements for the PANDA-STT	80
Storage Ring Based EDM Search	82
Progress toward a direct measurement of the deuteron Electric Dipole Moment at COSY	82
Automatized dedicated measurement setup for SiPM array characterization	83
Spin tune mapping with three-steerer vertical orbit bumps	84
Simulation and Optimization of the SCT of Protons in a Prototype EDM Ring	85
Pellet target development for the JePo polarimeter	86
Chromaticity measurements together with spin coherence time	87
Search for axion-like particles at COSY	88
Neutrino Physics	89
Systematic corrections of $^{210}\text{Bi}$ constraint and $^{11}\text{C}$ energy scale for CNO solar neutrinos analysis with the Borexino Experiment	89
Reduction of the $^{14}\text{C}$ impact on the Neutrino Mass Ordering measurement of JUNO	90
Mechanics and cleaning of iPMTs in OSIRIS	91
Trigger Condition Optimization of Event Builder for OSIRIS	92
Poster: Borexino Sensitivity Studies towards Detection of Solar Neutrinos from the CNO Fusion Cycle	93
Poster: Extraction of $^{210}\text{Bi}$ via $^{210}\text{Po}$ for CNO neutrino detection with Borexino	94
Poster: Spectral Fit of Borexino Phase-III Data for the Detection of CNO Solar Neutrinos	95
Prospects for Proton Decay Searches in JUNO	96
Poster: OSIRIS - A 20 ton liquid scintillator detector as a radioactivity monitor for JUNO	97
Poster: Atmospheric Neutrino Physics in JUNO	98
Accelerator Research	99
Model-Related Applications	99
Calibration of COSY Steerers for Advanced Orbit Feedback	101
Longitudinal beam instability due to simultaneous electron and stochastic cooling	103
Numerical simulation of Sona transitions	105
Status of the ExB Deflector Development	106
Preparation for Single Bunch Extraction from the Cyclotron JULIC	107
Tests with multiplexed proton beam from JULIC	109
Poster: Automatic Position Shift of the Magnet 3MDBE32	112
Further Activities	113
Redetermination of the strong-interaction width in pionic hydrogen	113
Measurement of the Radiative Decay $\Sigma(1385) \rightarrow \Lambda\gamma$ in the Reaction $\gamma p \rightarrow K^+ \Lambda\gamma$ at GlueX	114
Search for $c\bar{c}s\bar{s}$ States in the $J/\Psi \Phi$ Invariant Mass Distribution	115
P349 Antiproton Polarization Experiment: Results and Monte Carlo Simulations of Elastic $\bar{p}p$ -Scattering	116
Study of SiPM Irradiation with COSY Beam	117
Cold moderator tests with liquid hydrogen at Big Karl	118

# Production of the $\Sigma^0$ Baryon in Proton-Proton Collisions at $\sqrt{s} = 3.176$ GeV

Waleed Esmail and James Ritman

The production of  $\Sigma^0$  baryons in the  $p(3.5\text{GeV}) + p \rightarrow p + K^+ + \Sigma^0$  ( $\sqrt{s} = 3.176$  GeV) exclusive reaction is studied with the detector setup HADES at GSI, Darmstadt. While several experimental results exist for  $\Lambda$  hyperons in  $p+p$  and  $p+A$  reactions, measurements of  $\Sigma^0$  production are rare.  $\Sigma^0$ s were identified via the decay  $\Sigma^0 \rightarrow \Lambda\gamma$  (BR  $\approx 100\%$ ) with the subsequent  $\Lambda \rightarrow p\pi^-$  (BR = 63.9%), where photons are identified as missing particles. In the following we summarize the procedure followed to reconstruct the  $\Sigma^0$  signal.

## Time of flight reconstruction

During the data taking, the HADES setup was not equipped with a start detector, therefore the time of flight (tof) of particles was not directly accessible. To reconstruct the tof we select negatively charged tracks that are not geometrically correlated to a ring in the RICH detector and assume they are  $\pi^-$ . The start time  $t_0$  for each event is calculated as follows:

$$t_0 = t_1 - \left( \frac{d}{c} \times \sqrt{1 + \frac{1}{m_\pi/p}} \right)$$

where  $t_1$  is the stop time,  $d$  is the distance to the TOF or TOFino systems,  $m_\pi = 139.57$  MeV/ $c^2$ ,  $p$  is momentum of the  $\pi^-$  and  $c$  is the velocity of light. The tof of the other particles in the event is given by  $\text{tof} = t_1 - t_0$ .

## Charged particle identification (PID)

To perform the PID an Artificial Neural Network (ANN) is used. The network is trained on both simulated and real events in order to avoid domain shift. The output layer has three nodes corresponding to  $p$ ,  $\pi^+$  and  $K^+$  respectively, as mentioned in the previous sections  $\pi^-$ s are identified as negative charged tracks that are not correlated to the RICH detector.

## Lambda hyperon reconstruction

After PID two different data-sets have been identified. The first one is the HADES data-set, where we require exactly 2  $p$ , 1  $\pi^-$  and 1  $K^+$  to be within the acceptance of the HADES detector. The second is the Wall data-set, where we require exactly 1  $p$ , 1  $\pi^-$  and 1  $K^+$  within the HADES acceptance and in addition at least one hit in the forward wall (FW), assuming that this hit is due to the secondary proton (from  $\Lambda \rightarrow p\pi^-$ ). A primary vertex is defined for both data-sets as the Point of Closest Approach (PCA) between the tracks of the primary proton and the kaon. For the HADES data-set the  $\Lambda$  hyperon is reconstructed from its decay products in combination with topological cuts. The Minimum Track Distance (MTD) between the  $p$ , and the  $\pi^-$  tracks is required to be less than 10 mm. In addition the Distance of Closest Approach (DCA) between the  $p$  track and the primary vertex  $d_{p,pvtx}$  is required to be smaller than the DCA between the  $\pi$  track and the primary vertex  $d_{\pi,pvtx}$ . Finally, the Pointing Angle Vector (PVA), the angle between the spatial vector, pointing from the primary to

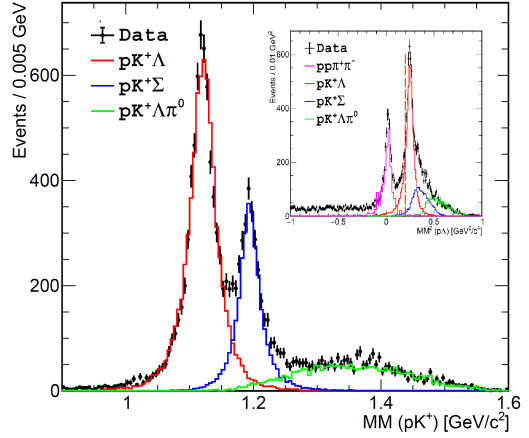


Figure 1: The missing mass of  $p_{\text{primary}}$  and  $K^+$ . Two peaks are visible due to the exclusive  $pK^+\Lambda$  and  $pK^+\Sigma$  final states as denoted by the red and the blue histograms. The green histogram is the simulation of  $p + p \rightarrow pK^+\Lambda\pi^0$ . The inset shows the missing mass squared of  $p_{\text{primary}}\Lambda$  and the red line is indicating the cut value  $MM^2(p_{\text{primary}}\Lambda) > 0.2$  GeV $^2/c^4$ .

the secondary vertex, and the momentum vector of the reconstructed  $\Lambda$  is required to be smaller than 1 rad. To further purify the Lambda signal, the background underneath the signal peak should be removed. In order to achieve this the missing mass squared of protons and Lambdas  $MM^2(pp_{\text{HADES}}\pi^-)$  is required to be greater than 0.2 GeV $^2/c^4$  as marked by the red line in the inset of figure 1.

For the FW data-set, the proton was reconstructed as a straight line from the primary vertex to the hit point in the FW. In order to select a relatively pure  $\Lambda$  sample we select events in the kinematic production range of the  $p + p \rightarrow pK^+\Lambda$  and  $p + p \rightarrow pK^+\Sigma$  reactions by applying the following cuts: (1)  $MM^2(pp_{\text{wall}}\pi^-) > 0.2$  GeV $^2/c^4$  and (2)  $-0.02 < MM^2(pK^+p_{\text{wall}}\pi^-) < 0.02$  GeV $^2/c^4$ .

## Sigma hyperon reconstruction

For the combined data-set of HADES and the FW, we apply a kinematic refit by constraining the intermediate Lambda mass ( $M_\Lambda = 1.11568$  GeV/ $c^2$ ) and the missing mass of all particles ( $MM(pK^+\Lambda) = M_\gamma = 0$ ). We select events satisfying a 1% confidence level cut  $P(\chi^2) > 0.01$ . The missing mass spectrum of  $p_p$  and  $K^+$  after the kinematic fitting is shown in figure 1. As can be seen most of the background is rejected. The remaining background is described by the  $p + p \rightarrow pK^+\Lambda$  as indicated by the red histogram and  $p + p \rightarrow pK^+\Lambda\pi^0$  reaction as indicated by the green histogram. A total number of 3145  $\Sigma^0$  events was reconstructed, which corresponds to a production cross section of  $18 \pm 0.5$  (stat)  $\pm 1.3$  (sys)  $\mu\text{b}$ .

Precise extraction of the elastic scattering event rate is critical for the determination of the differential cross section in KOALA. The reconstructed energy spectrum of the recoil detector shows a clear pattern of elastic scattering in the distribution of the deposited energy versus the position along the beam axis, as shown in Fig. 1. The elastically scattered events are well separated from the low-energy background at large recoil angles, while they are hard to distinguish at small recoil angles. Thus, different techniques are needed to separate the elastic events from the background for strips at different recoil angles. Three methods are presented in this report and the consistency of these methods is discussed.

For all strips of Ge#1, Ge#2 and most strips of Si#2, a combined fit with a three-component background model and an elastic peak model is used to extract the number of elastic events. The elastic peak is described by the so-called Crystal-Ball function[1], which is composed of a Gaussian core and a power-law tail on each side of the core. The three components in the background model are: 1) a fast-decreasing exponential component, which has very high yield at low energy; 2) a slow-decreasing exponential component, which extends to very high energy; 3) a minimum-ionizing-particle (MIP) component, which is described by a Landau distribution. A typical result using this fit model is shown in Fig. 2. The MIP events are mainly generated by the pions from inelastic interactions, which have a most probable energy deposit of 0.37 MeV in Si#1 and Si#2, 2.2 MeV in Ge#1 and 7.0 MeV in Ge#2. The accuracy of this method deteriorates when the elastic peak is close to the MIP peak, and both peaks are embedded among the large low-energy background. In this case, it's hard to estimate the parameters of each component separately and thus a large error exists in determining the fraction of each background component.

For recoil strips at small recoil angles ( $\alpha$ ), the low-energy background can be selectively suppressed by using the

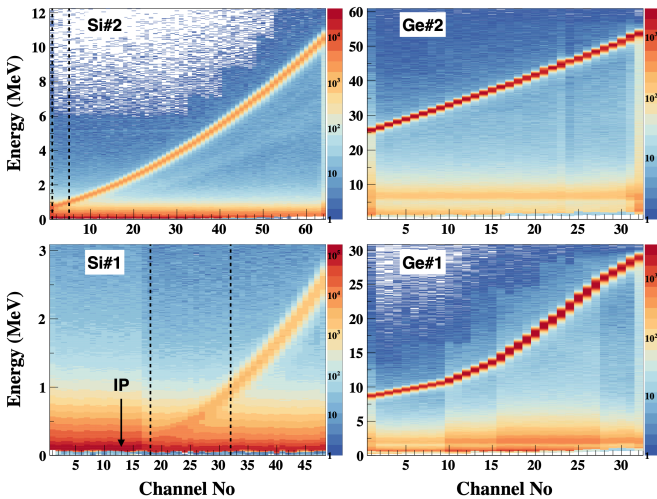


Fig. 1: Energy spectra of all strips of the recoil detector obtained at  $P_{beam} = 2.2 \text{ GeV}/c$ .

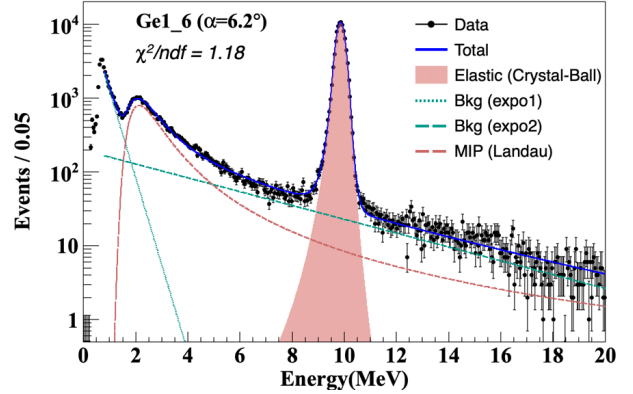


Fig. 2: An example of the combined fit of the total energy spectrum for a strip at large recoil angle.

TOF-E relation of the recoil proton in coincidence with the forward scattered particle. The energy spectra from three strips at different recoil angles are shown in Fig. 3, before and after the TOF-E selection. The remaining background after this selection comes from elastic scattering off the residual gas. The shape of this background is well described by the Coulomb elastic scattering cross section, due to the uniform distribution of the residual gas [2] and the rapid decrease of the elastic scattering cross section beyond the Coulomb region. Thus, the extraction of the yield of elastic events from the target body is carried out using a combined fit of a Coulomb elastic scattering formula and the Crystal-Ball function. The results of this fit for the three strips are also shown in Fig. 3. However, this method is constrained by the limited acceptance of the forward detector: 1) below the lower limit, the full target body isn't covered as shown in Fig. 3 (a); 2) beyond the upper limit, the full beam profile isn't covered as shown in Fig. 3 (c). Only a few strips on Si#1 and Si#2 can use this method to extract all elastic scattering events from the beam-target interaction, see Fig. 3 (b).

A third method is used to extract the rate of elastic events on those strips of Si#1 and Si#2 that are not fully covered by the forward detector or the elastic peak is not well separated from the MIP peak or low-energy background. First, a background model is determined from the strips which are fully covered by the forward detector. The elastic peak in these strips is already subtracted using the second method, thus generating pure inelastic background spectra, which are used as the background model for the other strips in the same sensor. This background model is combined with the Crystal-Ball function to fit the full energy spectrum and extract the yield of elastic events. An example of the fit result for the same channel in Fig. 3 (c) is shown in Fig. 4, in which the fitted background component is subtracted. Comparing to the TOF-E selected elastic peak, the full elastic peak can now be extracted. This method can be applied on all strips on Si1/Si2. However, the systematic error becomes larger for strips located at very

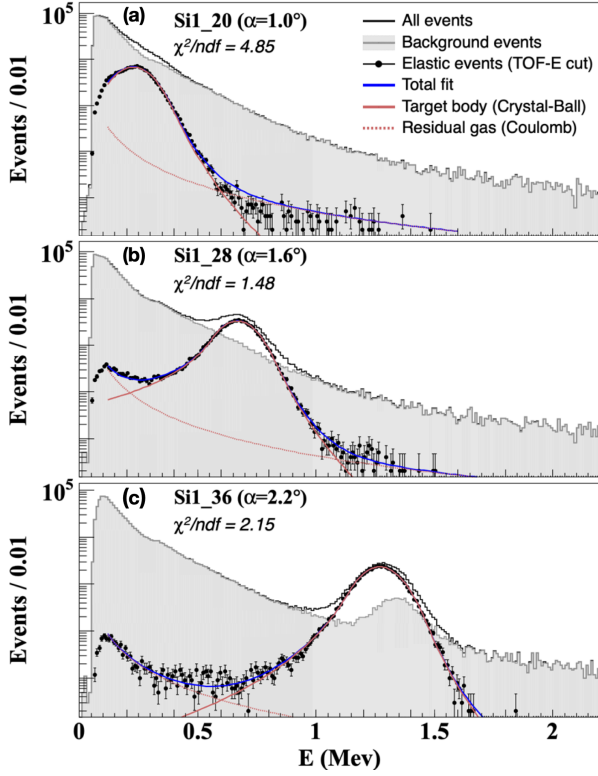


Fig. 3: The energy spectra of TOF-E selected events (black dots) from strips at three recoil angles. The black lines are from all events and the grey areas are the suppressed background events.

small recoil angle and far away from the strips, which are used for the extraction of the background model.

The consistency of the different extraction methods is checked by comparing the ratio of the number of events under the extracted elastic peak of the same recoil strip. Two groups of strips from Si#1 and Si#2 respectively are selected for the comparison between method 2 and 3, and one group of strips from Si#2 are selected for the comparison between method 1 and 3. The results are

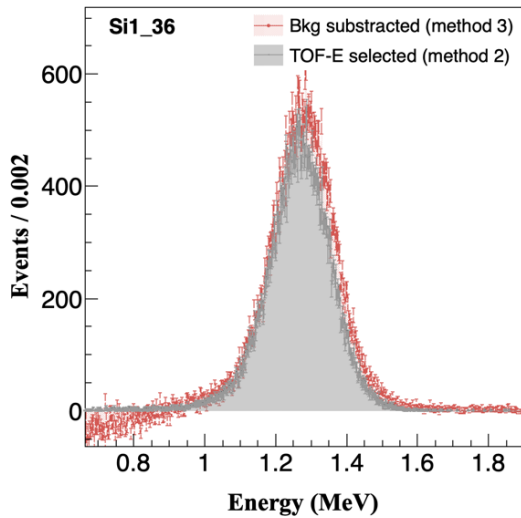


Fig. 4: Comparison of the elastic peak extracted using method 3 (red) and the TOF-E selected elastic peak using method 2 (grey).

summarized in Fig. 5. For all studied strips, the relative difference in yield between the methods is less than 0.6 %, indicating excellent consistency. The increasing discrepancy at low and high recoil energies between method 2 and method 3 on Fig. 5 (a) is due to the limited acceptance of the forward detector. The fully-covered strips on Si#1 and Si#2 can also be identified based on this comparison.

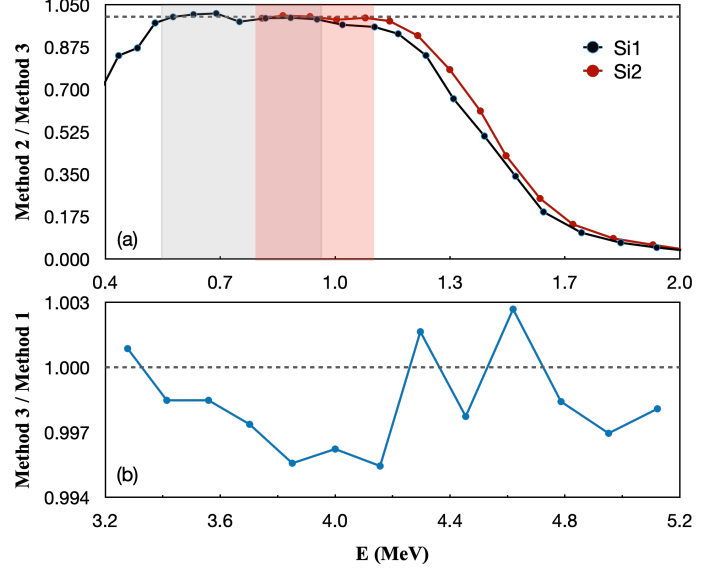


Fig. 5: Comparison between the different extraction methods: a) the ratio of elastic scattering event yield between method 2 and method 3, the shaded regions show the fully-covered strips on Si#1 (black) and Si#2 (red), respectively; b) the ratio of the elastic yield for method 3 to method 1 in the higher energy range.

Three methods of extracting the yield of elastic scattering from the total energy spectrum are studied and compared. The Crystal-Ball function is adopted as the response function of a single recoil strip to the elastic scattering events from the target body. The three methods differ by processing the background components differently. Although these methods are consistent with each other, it's found that they are best suited for processing strips located at different recoil angles, to achieve the best accuracy and smallest error. No single method is suitable for processing all recoil strips. The extracted yield of elastic events from these methods can be used as the essential input data set for the determination of the differential cross-section in the further analysis.

References:

- [1] J. E. Gaiser, Appendix-F Charmonium Spectroscopy from Radiative Decays of the J/Psi and Psi-Prime, Ph.D. Thesis, SLAC-R-255 (1982).
- [2] Y. Zhou, Determination of the cluster target density profile in KOALA, IKP Annual Report 2021.

Yong Zhou

KOALA aims to measure the differential cross section of (anti)proton-proton elastic scattering over a wide  $|t|$  range from 0.0008 to 0.1 (GeV/c)<sup>2</sup>. In the initial setup, in which only the recoil detector was in operation, the high yield of low-energy background deteriorates the elastic peak identification at small recoil angles and limits the lower measurement range of KOALA. The forward detector, which consists of fast scintillators, has been commissioned in 2019 to help suppress the low energy background based on the TOF-E relation of the recoil protons. The design of the forward detector has been verified in the following test runs and energy spectra from pure elastic scattering events can now be obtained after the TOF-E selection. Due to the lower limit of the acceptance of the forward detector, the spectra of strips at very small recoil angles start to lose events from the target volume below a threshold angle. However, it is found that this phenomenon already appears at a larger recoil angle than the design goal. More accurate information about the target profile is needed to clarify this phenomenon. In this report, a new method of determining the density profile of the cluster target is described, and the result from the 2019 test is presented. Implications of the measured target profile on the lower limit of KOALA measurement range is also discussed.

Three scenerios are depicted in Fig. 1 to show the variation of the TOF-E selected energy spectra from strips at decreasing recoil angles. The acceptance of the forward detector are represented by the recoil angle as  $[\alpha_{min}, \alpha_{max}]$ , which in turn can be converted to a region before the strip as indicated by blue bars in Fig. 1. Elastic scattering events from this region will hit both the recoil detector and the forward detector and generate coincidences. Starting from a strip which covers the full

target volume (Fig. 1 (1)), part of the target volume gradually fall out of the acceptance region as approaching to the interaction point (Fig. 1 (2)), then the peak, and finally only the tail of the target is covered (Fig. 1 (3)). Strips further upstream no longer have a coincidence with the forward detector for events in the beam-target overlap volume. Instead only events occurring in the rest-gas within the beam pipe generate coincidences.

The number of TOF-E selected elastic scattering events  $N_{elastic}$  recorded on a single recoil strip has the following relation with other experiment parameters,

$$N_{elastic} = \epsilon_{DAQ} \cdot l_{beam} \cdot \rho_{target} \cdot \sigma_{elastic} \cdot \epsilon_{acceptance}. \quad (1)$$

where  $\epsilon_{DAQ}$  is the DAQ efficiency,  $l_{beam}$  is the beam intensity,  $\rho_{target}$  is the target density,  $\sigma_{elastic}$  is the cross section of elastic scattering and  $\epsilon_{acceptance}$  is the acceptance of the forward detector.  $l_{beam}$  and  $\epsilon_{DAQ}$  are constant in the same run. To determine  $\rho_{target}$ , the last two items  $\sigma_{elastic}$  and  $\epsilon_{acceptance}$  need to be fixed.  $\sigma_{elastic}$  is determined by the energy of the recoil proton, thus can be fixed by choosing the same energy value as reference.  $\epsilon_{acceptance}$  varies with the recoil angle as well as the beam size. Simulation shows that strips at the lower range of the forward coverage are guaranteed to be fully covered as long as the width of the beam profile is smaller than 10 mm, see Fig. 2. The estimated width of the beam profile of COSY is about 7 mm. Since each strip corresponds to a specific recoil angle which in turn can be converted to an energy value, this indicates that the elastic events with energy near the edge the TOF-E selected energy spectrum are guaranteed to be fully covered and have  $\epsilon_{acceptance} \approx 1$ . Thus, the number of events in these energy bins provides a direct measurement of the target density.

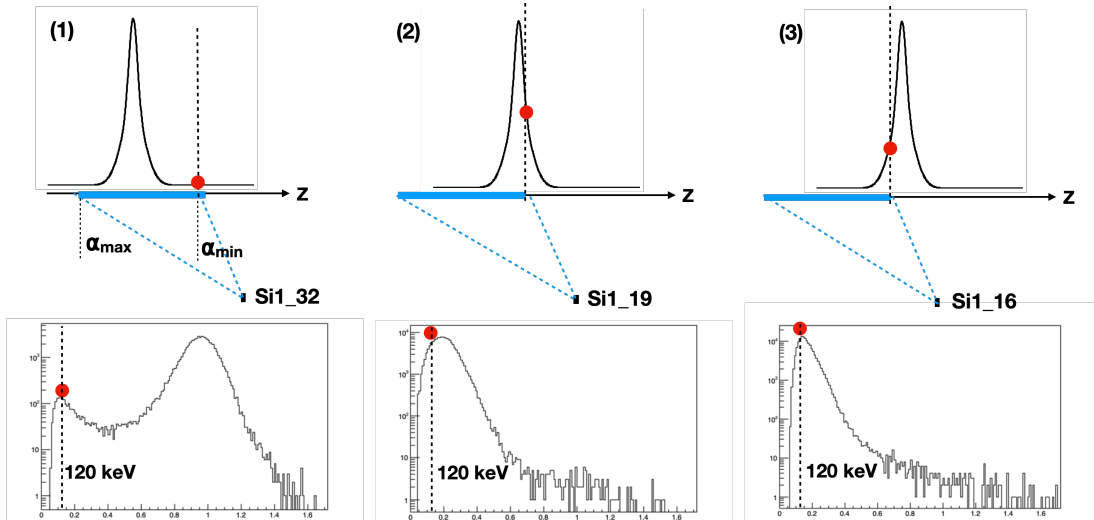


Fig. 1: Elastic energy spectra measured by three strips at different recoil angles: (1) the full target volume is within the Forward Detector acceptance; (2) part of the target volume is not within the acceptance, but the center of the target volume is still within the acceptance; (3) the target center is outside of the acceptance, only the tail of the target profile is recorded. The first row shows the target profile shape and the second row shows the energy spectrum. The red dot indicates the reference energy bin and its corresponding position in the target profile.

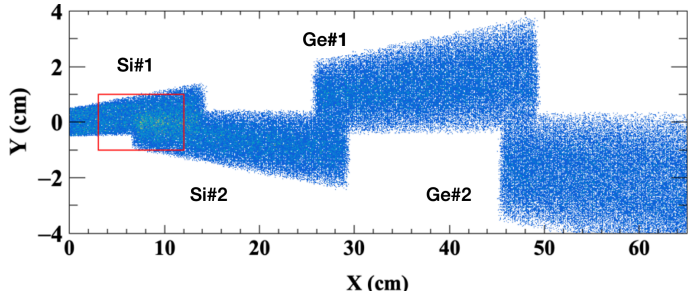


Fig. 2: Hit positions of the forward scattered particle on a plane at  $z = 4.6\text{m}$  that are coincident with a recoil particle hitting one of the four recoil sensors. The beam is assumed to have a width of 10 mm. The red square indicates the fiducial volume of the forward scintillators.

The observed lower limit of the forward acceptance is about 100 keV for the data collected with  $P_{beam} = 2.2\text{GeV}$ , as shown in Fig. 3. The value is consistent with the calculated range of the forward detector's acceptance with ideal beam condition, which is from 0.096 to 1.56 MeV. Thus, 120 keV with a bin width of 10 keV is selected as the measurement reference. The target density distribution along the beam axis is obtained by recording the number of events at a given energy bin in all strips. The reference energy is then converted back to a position before the strip center (at  $2.2\text{GeV}/c$  beam momentum, 120 keV corresponds to  $z = 10\text{mm}$ ).

Two independent methods are used to deduce the position distribution of the density profile. The first method is based on the strip position in the ideal geometry model. This method gives the distribution in the laboratory reference frame. The second method is based on the energy difference of the reference energy and the peak energy. The elastic energy peak corresponds to the target density center. Thus, the energy difference can be converted to a position relative to the target center. This method gives the distribution in the reference frame where the target center is at the origin. However, it is limited by the requirement of the coverage of the target center and only gives the first half of the density

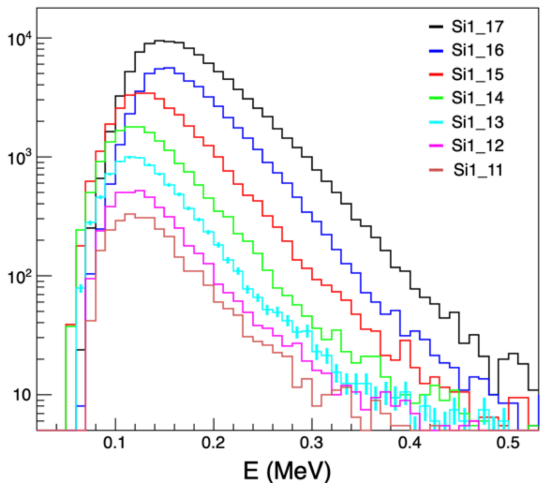


Fig. 3: TOF-E selected energy spectra from several strips that only cover the tail of the target volume. The lower limit can be clearly identified.

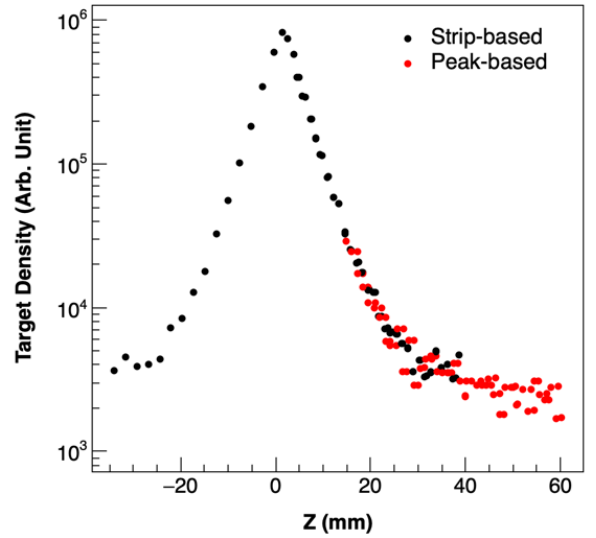


Fig. 4: Target density profile measured at  $2.2\text{GeV}/c$ . The black data points are from the first method, the red data points are from the second method. They are aligned with each other after a 1.8 mm shift of the recoil sensors along the beam axis.

distribution. The comparison between the results from the two methods can be used to align the the recoil detector to the target center.

Fig. 4 shows the target density profile measured at  $2.2\text{GeV}/c$ . The distribution is almost symmetric with respect to the target center. The main target volume lies above a wide spread of residual gas. The main volume can be described by a double-gaussian model, with 43 % and 57 % contribution from the narrow and wide component, respectively. The narrow component has  $\sigma = 2\text{mm}$  and the wide one has  $\sigma = 5.6\text{mm}$ . The overall FWHM of the target profile is about 6.9 mm. The residual gas has a relatively uniform distribution over a wide region, even beyond the recoil sensor's coverage. The density of the residual gas is about a factor 260 lower than the peak density of the target.

The measured target density distribution is much wider than the design value of 2 mm FWHM. However, the deduced density is an integrated value over the X-Y plane, thus may be affected by the finite angular dispersion of the beam. Consequently, the TOF-E selection method reaches its lower limit at larger recoil angle than the design goal. At  $P_{beam} = 2.2\text{GeV}/c$ , the target volume is not fully covered by the forward detector starting from the strip Si1\_26. This corresponds to the recoil energy of 500 keV and  $|t| \approx 0.001 (\text{GeV}/c)^2$ . The background subtraction method using the background model from strips which are fully covered by the forward detector can extend the lower limit to  $|t| \approx 0.0006 (\text{GeV}/c)^2$ . However, this method has larger systematic error than the TOF-E selection method. Finally, to reach even lower  $|t|$ , new methods need to be developed to unfold the actual event rate from the partially-recorded energy spectrum.

References:

[1] Y. Zhou, Extraction of elastic scattering events in KOALA, IKP Annual Report 2021.

# Prospects to use PAWIAN for a Partial Wave Analysis of the $\Xi^+ \Lambda K^-$ Final State with Data from PANDA

J. Pütz and J. Ritman

## Introduction

For a deeper insight into the mechanisms of QCD in the non-perturbative regime it is necessary to understand the excitation spectrum of baryons. So far, experimental studies focused on the nucleon excitation spectrum, while the knowledge on the excitation spectra of double and triple strange baryons is poor. An example is the lack of information on the quantum numbers of the excited  $\Xi$  states. A partial wave analysis (PWA), which is a tool to extract the complex amplitudes of certain processes, allows the determination of the mass and width of the  $\Xi$  resonances as well as their spin and parity quantum numbers.

Here, prospects to use the Partial Wave Interactive Analysis Software (PAWIAN) [1] for the extraction of the quantum number for specific  $\Xi$  resonances measured with the future PANDA detector are presented.

## Event Generation and Reconstruction

PAWIAN provides an internal event generator based on a user-defined decay model. Different data samples for the  $\Xi(1690)^-$  and  $\Xi(1820)^-$  have been generated with a beam momentum of 4.6 GeV/c: a data sets for each single resonance, a data set for each  $\Xi$  resonance including also the process  $\bar{p}p \rightarrow \bar{\Lambda}(1890)\Lambda \rightarrow \bar{\Xi}\Lambda K^-$  with  $J^P(\bar{\Lambda}(1890)) = 3/2^+[2]$ , called crossed channel in the following, and a data set for each  $\Xi$  resonance event passing the full simulation and reconstruction chain of the PANDA software framework PandaRoot as well as an analysis based on a full decay tree fit. Based on the study presented in [3], for the first two cases 30,000 and for the latter case about 600,000 signal events were generated. The normalization of the fit is done by Monte-Carlo integration, which requires reference data sets containing 90,000 and 1.8 million phase-space distributed events of the reaction  $\bar{p}p \rightarrow \Xi\Lambda K^-$ , respectively.

## Determination of the $J^P$ Quantum Numbers

The data sets just described have been generated with different quantum numbers:  $1/2^+$ ,  $1/2^-$ ,  $3/2^+$ , and  $3/2^-$  motivated by the values given in [2]. Each generated sample has been successively fit with all hypotheses using a multi-dimensional fit. The number of free fit parameters in the fit depends upon the spin-parity hypothesis. The selection of the preferred hypothesis is based on the Aikake Information Criterion (AIC) [4]. In general, there is no relation

Table 1:  $\Delta AIC$  values determined from the multi-dimensional fit for the  $\Xi(1690)^-$  sample including the crossed channel. The green cells indicate the hypotheses preferred by the fit.

Gen.↓ Fit→	$1/2^+$	$1/2^-$	$3/2^+$	$3/2^-$
$1/2^+$	0.0	42.6	35.6	103.2
$1/2^-$	84.2	0.0	102.8	378.4
$3/2^+$	1,598.6	3,195.4	0.0	175.8
$3/2^-$	1,908.5	2,132.6	840.1	0.0

between the AIC value and the conventional significance. Therefore,  $\Delta AIC$  is used as a measure for the significance:  $\Delta AIC < 2$  means the hypothesis is suitable, whereas hypotheses with  $\Delta AIC > 10$  are excluded. The study of the single resonances showed for both resonances and for all tested cases that always the true hypothesis is preferred by the multi-dimensional fit with  $\Delta AIC \gg 10$ . Table 1 summarizes the resulting  $\Delta AIC$  for  $\Xi(1690)^-$  including the crossed channel. The fit prefers the true hypothesis in each tested case. Figure 1 shows the Dalitz plot for the generated and fitted  $J^P = 1/2^+$  sample. The  $\Xi(1690)^-$  resonance as well as  $\bar{\Lambda}(1890)$  in the crossed channel are identifiable. Similar results could also be achieved for  $\Xi(1820)^-$  including the crossed channel. In the last step, the data samples passing the full PandaRoot simulation and reconstruction chain are tested. About 5% of the gener-

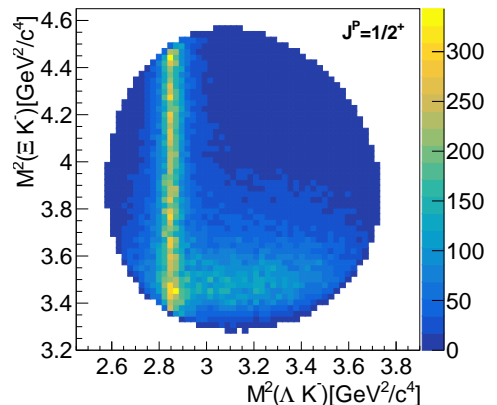


Figure 1: Dalitz plot for  $\Xi(1690)^-$  with generated and fitted  $J^P = 1/2^+$  hypothesis. The  $\Xi$  resonance appears as vertical structure while the  $\bar{\Lambda}(1890)$  in the crossed channel is visible as horizontal structure.

ated signal events passed the reconstruction and the analysis procedure, which were then used as input for

Table 2:  $\Delta AIC$  values for the  $\Xi(1820)^-$  sample passing a full PandaRoot simulation and reconstruction chain. The green cells indicate the hypotheses preferred by the fit.

Gen.↓	Fit→	$1/2^+$	$1/2^-$	$3/2^+$	$3/2^-$
$1/2^+$		0.0	1,235.2	583.9	900.8
$1/2^-$		316.4	0.0	329.8	2,332.0
$3/2^+$		4,974.9	5,227.9	0.0	586.1
$3/2^-$		5,346.1	6,617.5	833.3	0.0

the multi-dimensional fit. The results for  $\Xi(1690)^-$  are summarized in Table 2. In case of  $\Xi(1820)^-$  the multi-dimensional fit prefers always the true hypothesis. However, the corresponding Dalitz plots show entries outside the kinematically allowed region, which are caused by wrongly selected events in the phase-space distributed sample. Since the fraction of about  $2 \cdot 10^{-4}$  is small, a strong influence on the fit results is not expected. Nevertheless, tests to confirm this are ongoing.

### Summary and Outlook

In this study, several tests have been performed to show that the determination of the spin and parity quantum numbers of the specific  $\Xi$  resonances with PAWIAN is in general possible. In the future, a data set containing both resonances will be studied first without and then with passing the full PandaRoot simulation and reconstruction chain. The first part of this study is currently under investigation.

### References

- [1] B. Kopf and M. Albrecht, Online: <https://www.ep1.ruhr-uni-bochum.de/en/research/partial-wave-analysis>
- [2] M. Tanabashi *et al.*, Phys. Rev. D **98** (2018) 030001.
- [3] J. Pütz, PhD Thesis, Rheinische Friedrich-Wilhelms-Universität Bonn (2020), <https://bonndoc.ulb.uni-bonn.de/xmlui/handle/20.500.11811/8281>.
- [4] K. P. Burnham and D. R. Anderson, Sociological methods & research **33.2** (2004).

## Thermal Test of a Mock-up of the Readout Volume for the PANDA STT

A. Derichs

Within the Panda experiment, the Straw Tube Tracker (STT) is one of the inner detectors around the interaction point and is the main system responsible to measure the momentum of charged particles. In order to record as much data as possible in high quality, the maximum density of individual straws is required. This leads to the minimum packing space for the required electronic hardware in the STT setup. One aspect in the overall design is the thermal load due to the power consumption, internally as well as from the adjoining detectors. In order to investigate methods to extract the produced heat from this volume, a mock-up of the experimental setup with similar geometric dimensions was produced.

The basic frame structure of the setup consists of aluminum elements arranged into three sectors per semi-detector (figure 1). The frame is used to support forces, cable routing and card positioning. To represent the internal thermal power dissipation, 29 layers have been installed within each of the three sectors. Each layer was equipped with the appropriate number of resistors to represent the 131 front-end cards with 16 channels each [1]. In order to determine the influence of the various factors, the experimental setup was sequentially installed (figure 1 and figure 2). The experimental setup was divided into three phases:

- I. Open system
- II. Closed system
  - a. Excluding External Influence
  - b. With additional MVD radiation heat
- III. Closed system with air cooling
  - a. Basic air cooling
  - b. Homogeneous air distribution



Fig 1: Phase I: Open Setup



Fig 2: Phase II.b: Closed setup with additional radiation load

Table 1: Temperature in each sector for the open system

Sector	VI	VII	VIII
Phase-I temp [ $^{\circ}$ C]	38	34	35

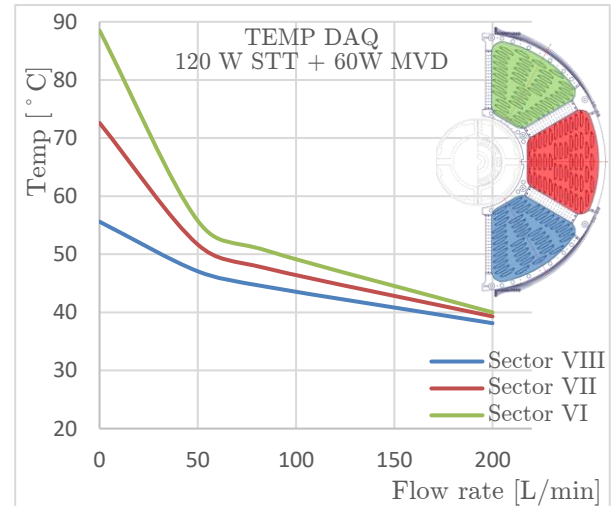


Fig. 3: Temperature as a function of gas flow rate for the setup phase III.b.

The three phases showed a need for external cooling in the encapsulated area of the front-end electronics. For the power consumption of a STT half-barrel with 120 Watt (51mW per channel [2]) and an estimated 60 Watt radiation heat from the inner MVD detector, a cooling flow of 200L/min with an input temperature  $22^{\circ}$ C is needed. The figure 3 shows the average temperature that is characteristic for each sector as a function of the flow rate. For stable operation, temperatures below  $40^{\circ}$ C are required [3].

The mock-up was suitable to provide estimates of the thermal properties of the readout volume, and was operated under various conditions. It turned out that air-cooling is very helpful, but not sufficient. For this reason, the next step is to further refine the mock-up by using individual front-end cards, optimize the cooling flow with improved inlet conditions, and test the card connection to the straw modules.

- [1] PANDA Collaboration et al., Eur. Phys. J. A 25 (2013), pp.22-59. DOI: 10.1140/epja/i2013-13025-8.
- [2] P.Wintz, private communication, (23.02.2021).
- [3] D. Przyborowski et al., Jour. of Instrum. 11.08 (2016), P08009–P08009. DOI: 10.1088/1748-0221/11/08/p08009.

# Quality and Runtime Optimization of a PANDA Track Finding Algorithm based on Hough Transformations

A. Aliche, T. Stockmanns, J. Ritman

A track finding algorithm based on Hough transformations for the barrel part of the PANDA detector has been optimized. The track finder is well adapted to the STT by using the hit point information and also taking into account the drift time information measured by the STT. The procedure has been described in more detail previously [1].

The first implementation of the algorithm in 2019 was not compatible with other algorithms both in quality and in speed. Therefore, the focus in the last year was to optimize the two parameters. The quality is measured by three quantities: the track finding rate of reconstructible primary tracks (possible primaries), the fraction of wrongly found tracks (ghosts) and the fraction of tracks found more than once (clones). The results of the optimization procedure are shown in fig. 1 and are described in the following.

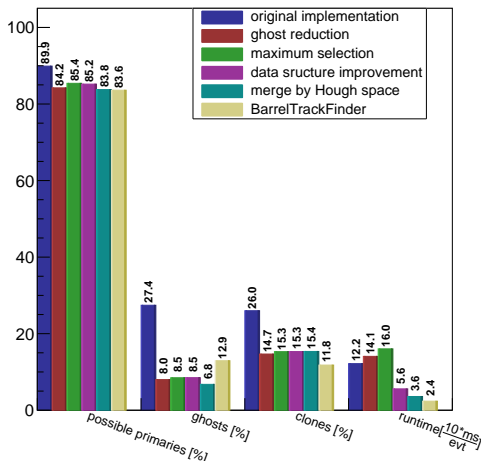


Figure 1: Contribution of each optimization step.

The first optimization step investigated reducing the number of created ghost tracks. The analyzed parameters are the number of neighbors of a hit, the average distance between hits in the x-y-plane and the number of hits per detector type. Based on a receiver operating characteristics (ROC) curve, a threshold for each parameter was chosen with a high accuracy ((true positives + true negatives) / (all data)) and a low number of false negatives. The second optimization step was to analyze a method to decide which maximum is taken if there are several maxima in the Hough space. Here the sum of the distances of each hit to the track resulting from the corresponding maximum is determined. The maximum with the smallest sum of distances

is then chosen. Since the focus in this part of the optimization is on the finding rate of possible primaries the large increase in computing time can be neglected here.

The various additional steps to improve the track finding quality caused an additional increase of the runtime by 31.1%. To optimize the speed of the algorithm, the used data structure was examined in more detail. Maps were introduced, which links an integer to a region in the Hough space and a fired straw in the STT with the corresponding isochrone radius. This has the advantage to speed up the access to the data and to prevent time consuming type casts.

The last step to optimize the algorithm was to exchange the merging method, which decide if tracklets could belong to the same particle track. This method was exchanged by a simpler merging method based directly on the found maxima of the Hough spaces. It exploits the proximity of maxima from the same track compared to those from different tracks. The new merging method leads to an improvement in computing time and ghost ratio and a small loss in efficiency.

The effect of the individual optimization steps on the quality parameters and the runtime are shown in fig. 1. The ghost ratio could be reduced by a factor of four, the clone ratio by a factor of 1.5. The improvements lead to a small efficiency loss of 6.1% points. The runtime of the algorithm could be improved by a factor of three. A comparison to the BarrelTrackFinder, which is the currently best track finder in PANDA, shows that this implementation is comparable to the BarrelTrackFinder in terms of quality and speed. The advantage of this algorithm is the possibility to extend the algorithm to find secondary particles, which is not possible for the BarrelTrackFinder. Additionally, the speed of the algorithm still has potential for improvement, since it is easily parallelizable. For this purpose, a parallelization on GPUs is currently under development.

## References

- [1] A. Scholl, T. Stockmanns and J. Ritman, A PANDA Track Finding Algorithm Based on Hough Transformations, in Annual Report 2019 - Institut für Kernphysik, Forschungszentrum Jülich, pp. 63-64

# Improving Noise Tolerance in the Track Finding Process by Using Correlations between Multiple Language Models

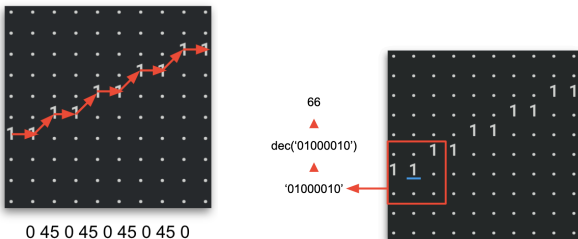
J. Kannika, T. Stockmanns and J. Ritman

When particles travel through detectors in particle physics experiments, they leave tracks of hit signals. In addition to those signals, there are also some noise hits. We are developing a machine learning based track finding algorithm that is robust in the presence of noise hits. The method we are developing uses language models to recognize sequences of hits and uses a multilayer perceptron (MLP) to correlate output predictions between different language models. The language model is a probability distribution calculated from word frequencies that count from the target text corpus. The language model is commonly used in natural language processing. Applications such as the next word predictions also use the language models for making predictions. Assume that we have a text “When I am happy, I smile.”, and we want to know which words could follow the word “I”? We can train the models such as 2-gram or 3-gram language models to recognize sequences of words of the text above. The trained models can give us probabilities of words that could appear after the word “I”:

$$\begin{aligned} \text{2-gram model:} & & \text{3-gram model:} \\ P(\text{am} | \text{I}) = 0.5 & & P(\text{am} | \text{When I}) = 1.0 \\ P(\text{smile} | \text{I}) = 0.5 & & P(\text{smile} | \text{happy I}) = 1.0 \end{aligned}$$

With the 2-gram model, the word after “I” could be either “am” or “smile”, each with a 50% probability. Meanwhile, the 3-gram model gives both “am” and “smile” a 100% chance. This is because the 3-gram model requires two histories of words as the inputs for the model. Thus, higher-gram models can produce less ambiguous output predictions compared to the lower ones.

In this work, we use moving directions and neighbor patterns as tracking features (see Fig. 1a and 1b). These two features can be extracted directly from the hit data, and they can be treated similar to sequences of words. We train a couple of language



(a) Moving directions are the angles from one hit to another hit. (b) Neighbor pattern is calculated from states of the neighbor cells.

Figure 1: Moving directions and neighbor patterns can be treated as sequences of words and recognized using the language models.

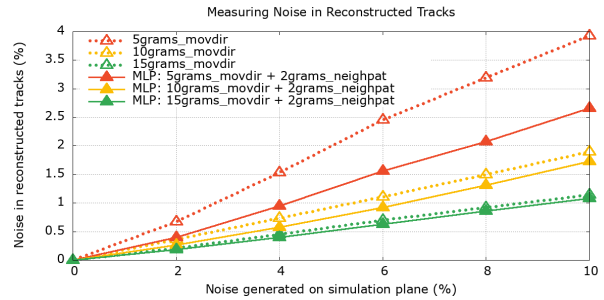


Figure 2: Comparison of fraction of noise hits in a reconstructed track (less is better) between single feature trackings and the multiple features trackings.

models to recognize them. The trained models can work as next hit predictors which are similar to the next word predictor. The models can guide a walking from one point to another point on the tracks. They also learned how to avoid noise. Fig. 2 shows results from a benchmarking that measures how well each tracking model can avoid noise. The first group of models uses moving direction’s language models to find hits, while the second group uses MLPs that can correlate two language models for making predictions. From the figure, we can conclude that:

- MLP can learn correlations between multiple tracking features,
- The neighbor pattern feature can improve noise tolerance in the track finding tasks, especially in short track history cases.

Currently, we are testing our algorithm with tracks that have a non-zero curvature on a new geometry. With the new geometry, the detectors are aligned in a hexagonal lattice instead of the square lattice see (Fig. 3). All these changes make generating data more realistic and similar to the data from the Straw Tube Tracker (STT) in the PANDA experiment. In the next step, we are going to develop and improve the tracking model to work effectively with the STT geometry.

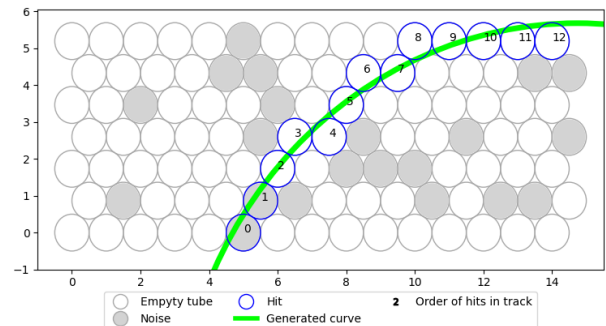


Figure 3: Toy data generator generates data similar to the data from STT in the PANDA experiment.

## Progress of the Sampling ADC based Front End Free Readout System for Straw Tube Tracker

P. Kulesa<sup>1,3</sup>, T. Hahnraaths von der Gracht<sup>1</sup>, L. Jokhovets<sup>2</sup>, H. Ohm<sup>1</sup>,  
K. Pysz<sup>5</sup>, J. Ritman<sup>3,1,4</sup>, T. Sefzick<sup>1</sup>, V. Serdyuk<sup>1</sup>, S. van Waasen<sup>2</sup>, P. Wintz<sup>1</sup>

<sup>1</sup>IKP, Forschungszentrum Jülich, D-52425 Jülich, Germany

<sup>2</sup>ZEA2, Forschungszentrum Jülich, D-52425 Jülich, Germany

<sup>3</sup>GSI, D-64291 Darmstadt, Germany

<sup>4</sup>RUB, D-44801 Bochum, Germany

<sup>5</sup>H. Niewodniczański Institute of Nuclear Physics, PL-31342 Cracow, Poland

Two readout concepts are available for the Straw Tube Tracker (STT), which are now in a rather advanced stage of development. The first one is based on the PASTTREC ASIC, which is placed inside the detector and contains amplifiers and discriminators. Logical (LVDS) signals are fed to FPGA based TDCs (TRB3) placed several meters away from the detector. The second readout system has no active components inside the detector. The readout system including signal decoupling from the high voltage as well as signal processing is placed outside the detector. In this report the recent progress of the sampling ADC based front end free (FEF) system is described regarding hardware and FPGA firmware for digital signal processing.

The FEF system is designed to fully satisfy the requirements of the PANDA DAQ concept: It is free-running and delivers time-stamped readout using the SODANET system for time references. Time information for particle tracking as well as energy-loss information for particle identification is delivered at hit rates up to 1 MHz per channel. At maximum luminosity the system is capable of recognizing signal pileup and synchronous noise events.

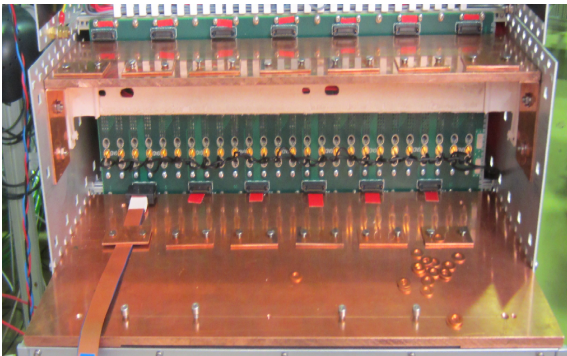


Figure 1: The HV decoupling crate with additional copper plates for better cable grounding and SAMTEC connector mounting and fixing.

The crucial part of the system are long ( $> 10$  m) and thin (approx. 1 mm diameter) coaxial cables which simultaneously carry the operating high voltage for the straw tubes and the superimposed straw signal. They connect the straw tubes with the HV decoupling crate (Fig. 1) from where high density

coaxial cables (SAMTEC) (Fig. 2) guide the signals to boards with amplifiers and shapers. These boards are housed in a modified OpenVPX crate which also contains boards with the sampling ADCs (HMCAD1520) and VIRTEX7 FPGA for digital signal processing (Fig. 3). Each crate provides 14x 160 channel payload plus 2 controller boards.

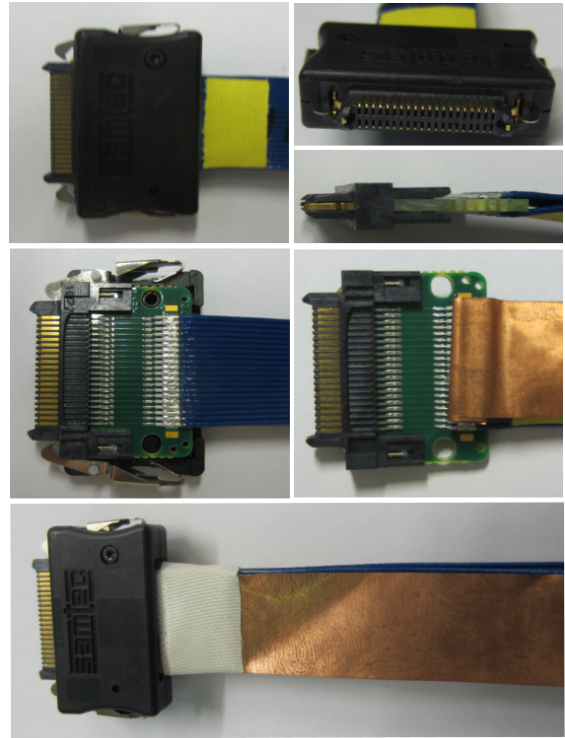


Figure 2: The SAMTEC connector for 40 coaxial cables before and after modifications made for better grounding. Original SAMTEC cables connector before modifications: side view (top left), front view with small grounding pins and fixing clips on both sides (upper part top right). Disassembled SAMTEC connector: side view with small grounding pin visible (lower top right), top view (middle left). Attaching of the additional copper grounding foil (middle right). SAMTEC connector after reassembling with additional copper foil (bottom).

The main advantage of the FEF system is that it easily satisfies the tight boundary conditions inside compact detector systems like PANDA. The only space occupied is needed for cables and connectors. The

electronic components are mounted with some meter distance to the detector, thus no heat is dissipated to the detector and the DAQ is rather insensitive to radiation. The mechanical design of the interior of the detector is made easier, electrical independence of all straw, access to all electronic parts, possibility to adjust feature extraction and shaping without of dismantling the detector.



Figure 3: The rear view of the OpenVPX crate with one amplifier board (bottom part) connected with the HV decoupling crate (upper part) with modified SAMTEC cables.

A particular challenge for the FEF system is to keep the noise level in the analog part low. While the intrinsic noise of the detector–amplifier system is almost unaffected by the long signal cables there is an enhanced sensitivity for electromagnetic interference in the frequency range from 10 MHz to 100 MHz. In most cases the sources are unknown but they are always present in the laboratory environment. The effect can be largely suppressed with a careful electrical shielding of the whole system from the detector via the signal cables up to the amplifiers. This shielding has to be the common ground for all electrical components of the detector system. There must be good conductivity so that no significant high–frequency voltage drop happens for currents induced in the shielding. Good ground connections have to be taken care of in particular around

the signal decoupling board and the amplifiers. Good signal quality was achieved by using Cu mounting plates in the HV crate and by improving ground connection of the SAMTEC cables with additional Cu foils. Fig. 1 shows the improvements done to the HV decoupling crate and Fig. 2 shows the SAMTEC cables modification.

Fig. 3 shows the rear view of the system: modified HV decoupling crate with modified SAMTEC cables connected to the amplifier board in OpenVPX crate.

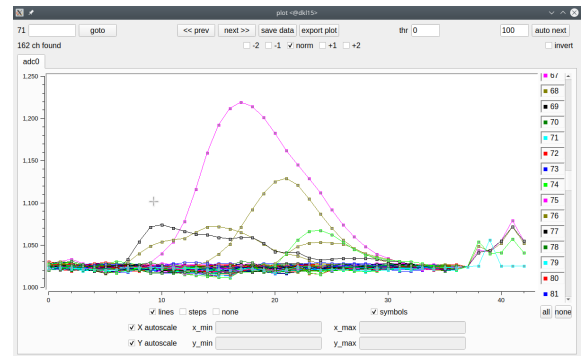


Figure 4: Signals from the straw detectors. At the end (channel > 36) the results of the FPGA processing are visible.

Fig. 4 shows an example of data collected with the recent version of the system. From channel 1 to 36 raw signals are shown and from channel 37 to the end different information from the feature extraction algorithm are included. The signals from several individual straws are visible with low noise ( $\sim 5$  mV). Now 160 data channels are available, which are connected to 6+ layers with 24 straws each. System tests are being performed with cosmic radiation, with Sr-90 and Fe-55 sources or with proton beam from COSY. One of the channels is dedicated to be used as the trigger.

Different versions of the FPGA firmware are currently under test. In all tested versions both raw data and processed data are accumulated (see Fig. 4) which allows the signal processing performed by the FPGA firmware to be cross checked. Different firmware versions allow to collect data with different sampling frequency, and are used to optimize the arrival time extraction, charge accumulation and pileup detection algorithms.

The next tasks in the system development will be testing the FPGA firmware under real beam condition and tests of data output using the dedicated SFP connector. The system is ready for the first task, for the second task the add on has to be designed and produced (needed connections on processing board exists). Test of the SFP connector is needed to close the prototype stage of the processing board, this is the only part of board which is not checked.

## Preparatory Studies for the Application of the PASTTREC ASIC at HADES

P. Kulesa<sup>1,2</sup>, T. Hahnraaths von der Gracht<sup>1</sup>, J. Ritman<sup>2,1,3</sup>, T. Sefzick<sup>1</sup>, P. Wintz<sup>1</sup>

<sup>1</sup>IKP, Forschungszentrum Jülich, D-52425 Jülich, Germany

<sup>2</sup> GSI, D-64291 Darmstadt, Germany

<sup>3</sup> RUB, D-44801 Bochum, Germany

This report describes the baseline correction determination and quality assurance (QA) tests of the PASTTREC ASICs foreseen to be used at the HADES straw tube station (STS1).

The PASTTREC was developed for the readout of the straw tube detectors and each chip contains 8 channels with signal amplification, shaping and discrimination circuitry. The settings of signal shaping, amplification factor (0.67, 1, 2, 4 mV/fC) and threshold are common for all channels. The signal baseline however can be adjusted separately for each channel. The schematic view of the PASTTREC layout is shown in the top part of Fig. 1.

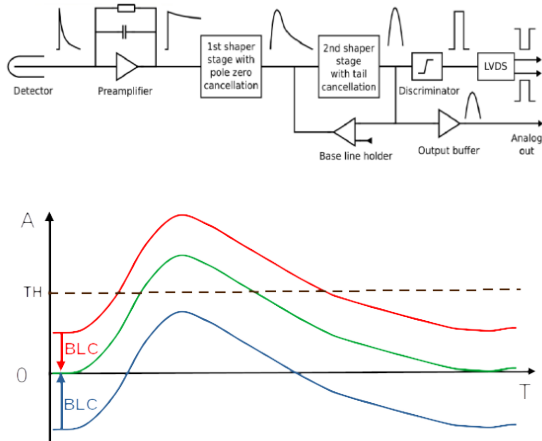


Figure 1: Top: Schematic view of the signal processing in the PASTTREC ASIC (developed by AGH Cracow). Each amplification stage is followed by two shaping stages, baseline correction and a discriminator stage. Bottom: The effect of uncorrected channel baseline values when using a common threshold value (TH). A baseline correction has to be applied for the blue and red signals, otherwise the specific channel will behave as if it has a different threshold.

The fixed global threshold setting of the PASTTREC ASIC requires that the baseline of each individual channel is shifted properly, see the bottom part of Fig. 1. In this way it can be made sure that the effective threshold for all channels is the same. The magnitude of the baseline correction can be found by scanning at zero threshold the baseline correction voltages within an accessible range of 64 mV and then identify the position with the highest count rate. In the upper part of Fig. 2 the expected count rate distribution for white noise is indicated schemat-

ically. Baseline scans with ASIC boards connected to the STS1 HADES tracking station, however, did not provide the expected count rate distribution. The noise level was so low that even at the highest gain setting of the ASIC no continuous count rate distribution could be obtained. Instead, only single points with increased noise counting rate appeared. These result of "on detector" scans are presented in the top part of Fig. 3. Therefore a modified technique based on an external noise generator was applied. This signal was fed into the common test input of the PASTTREC ASIC from where it was capacitively coupled to each channel. With this method the PASTTREC board functional QA tests and baseline determination can be done prior to installation at the detector.

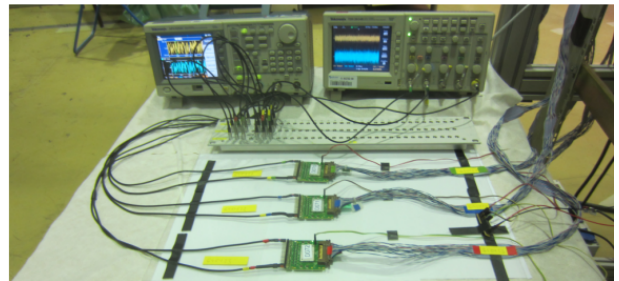
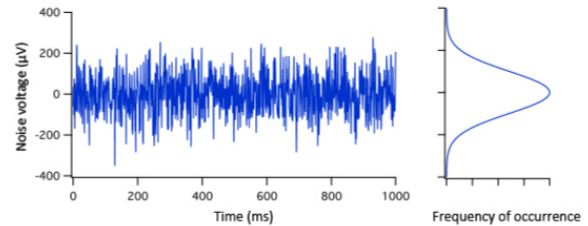


Figure 2: Top: (left) White noise used for test. (Right) Frequency of the amplitude occurrence with is similar to the expected count rate distribution as a function of the applied baseline correction. Bottom: Setup with signal generator, oscilloscope, signal splitter and three PASTTREC boards during the test procedure.

The setup is show in the bottom part of Fig. 2. The measured distributions are displayed in the center and at the bottom of Fig. 3. They have the expected symmetric shape with a well defined maximum which defines the optimum baseline setting. In these tests all available PASTTREC channels were investigated. The results were also used for quality checks, see Fig. 3. Some of the distributions deviate from the regular behavior which indicate a malfunction in the ASIC or front-end board.

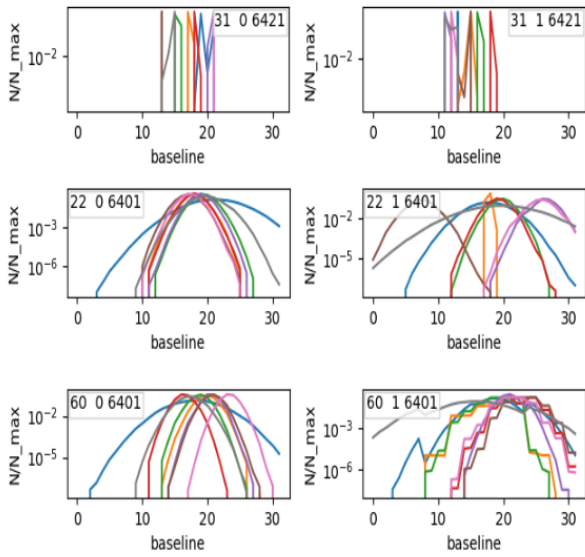


Figure 3: Noise count rate vs. baseline correction value. Different colors represents different PASTTREC channels Top: PASTTREC at its highest gain setting connected to the HADES STS1. Center and bottom: Two examples of PASTTREC board scans obtained on a test stand in the laboratory. The left diagrams show the expected count rate distributions, whereas the distributions on the right indicate that the boards have certain problems like failure of channels (center) and wrong bit settings (bottom).

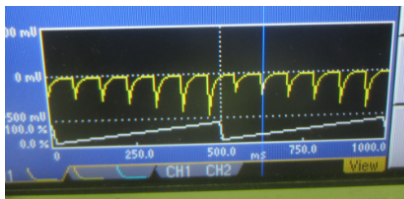
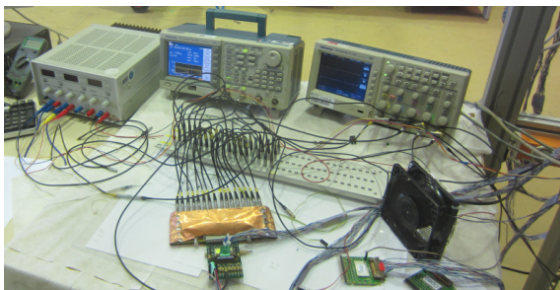


Figure 4: Top: The setup for optimizing baseline corrections. The signal generator, signal splitter and adapter board are shown together with the PASTTREC board. Bottom: Linear amplitude modulated signals (AM) used for this work.

For the STS1 tracking station the best boards were selected. In scans with different PASTTREC shaping and amplification settings it is seen that no readjustment of baseline settings is needed.

The quality of the baseline correction was tested in direct measurements using the setup shown in Fig. 4. Analog signals from a pulse generator were distributed via a multi fold passive splitter and coupled with equal amplitudes and shapes into the PASTTREC inputs.

The critical components are shielded and grounded with copper foil to reduce external noise from electromagnetic interference. The shape of the test signal is linearly AM as can be seen in the bottom part of Fig.4. This type of signal is expected to result in a linear count rate dependence as a function of the global threshold setting.

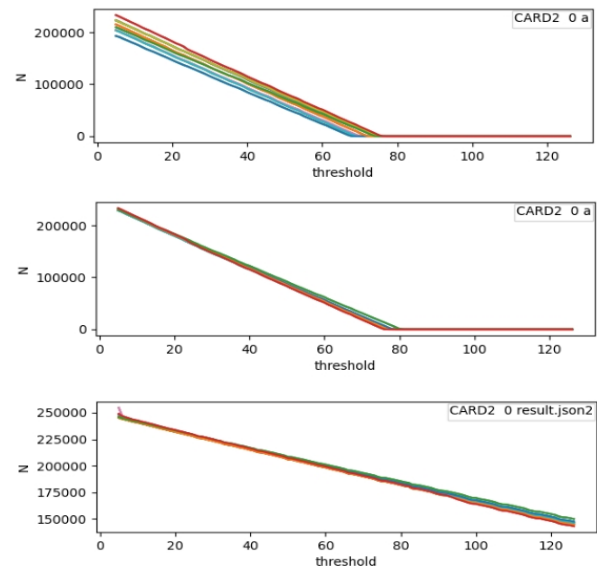


Figure 5: Count rates for amplitude modulated pulser signals as a function of the threshold values. Top: No baseline corrections applied. Center: Effective thresholds are unified through baseline corrections. Bottom: The same as in the center but for the higher gain of the ASIC.

The top part of Fig. 5 shows how the count rate of linearly AM signals changes with the threshold value when no baseline correction is applied. The differences between the channels reflect the differences between the effective threshold values. In the center of Fig. 5 the same data after the application of the baseline correction are shown. In particular at low threshold values, which are usually favored in experiment the count rates are much more uniform than before the application of baseline corrections. At the bottom of Fig. 5 count rate distributions for a higher gain of the amplification stage are shown, as expected the threshold value with still visible count rates is shifted to higher values.

The QA and baseline correction determination method presented in this report are foreseen to be used for the new production run of the PASTTREC ASIC boards for PANDA and HADES.

## TRB3 DAQ System for HADES Straw Tubes Station Test

P. Kulesa<sup>1,2</sup>

<sup>1</sup>IKP, Forschungszentrum Jülich, D-52425 Jülich, Germany

<sup>2</sup> GSI, D-64291 Darmstadt, Germany

The Straw Tube Station (STS1) was built for the HADES detector. This report describes a TRB3<sup>1</sup> readout system setup at FZJ for tests of the STS1. The front and back view of the readout system is presented in the top part of Fig. 1.

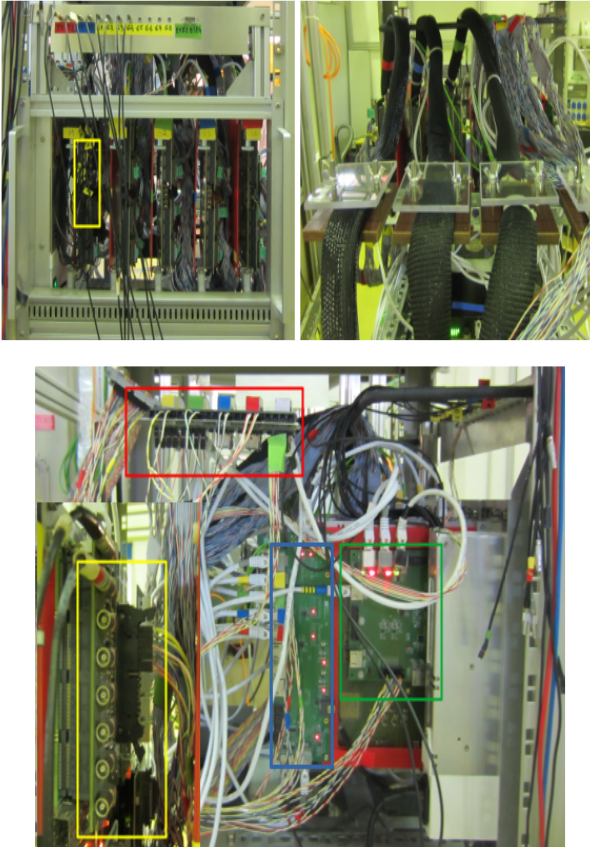


Figure 1: Top: Front and back side of the TRB3 based readout system. Bottom: Side view of the TRB3 board on which the CTS add-on is mounted (green box) it is used to provide eight trigger signals to the CTS. Left side: The trigger distribution board (blue box) it is used to extract two trigger from each TRB3 board and to distribute the main trigger from the CTS to all TRB3 boards. In the left top corner the distribution for another two triggers were placed (red box). The second eight triggers were connected to the GPIN add-on (yellow box).

The setup consists of five TRB3 boards. Four of them were used as TDCs for the readout of the PASTTREC ASIC for one STS1 plane 176 straw

tubes (each plane is equipped with 11 boards on which two 8 channel PASTTREC ASIC are placed). The remaining TRB3 board is used as a Central Trigger System (CTS). On this TRB3 board two add-ons (CTS and GPIN add-on) are mounted to provide additional trigger inputs to the CTS from the other four TRB3 boards or other sources. The whole system is operated via a PC that also stores the data.

The bottom part of Fig. 1 shows a side view on the TRB3 board with the CTS system and all additional equipment needed.

The system allows to implement different triggers at the same time: OR from all straws in layers (each plane consists of two layers), multiplicity per TDC and the coincidence trigger between the first and last straws in a plane. For this trigger setup four independent trigger outputs from each TRB3 board were used: two for the OR trigger, one for multiplicity and one for an in-plane coincidence trigger. On the board with the CTS the trigger connections were chosen in the following way. For the OR trigger all eight layer inputs were connected to the GPIN on which the OR between the plane layers were setup, after this four individual plane ORs were available in the CTS. The four individual in-plane coincidences and four multiplicity trigger were connected to the CTS add-on and were also available in the CTS. For the multiplicity and in-plane coincidence triggers the standard trigger logic of the TRB3 TDC and central FPGA were modified to allow longer time windows needed for the STS1 straw detectors. Time windows of up to 630 ns can be selected. The same modifications were made for the GPIN add-on and the CTS.

The possibility to include all straws into an OR trigger was very useful when testing the STS1 with cosmics. The low rate of the TDC multiplicity trigger indicated that the noise of the system is very low. The in-plane coincidence trigger was implemented to collect tracks hitting many straws.

Tests with beta particles from a Sr-90 source were made in order to measure the drift time distributions. The discriminated signal from an additional scintillator was used as the start time. This signal was connected to one of the GPIN NIM input and used in the different trigger conditions: from the scintillator alone or in a coincidence with of the STS1 planes.

The experience gained with setting up the TRB3 system for the STS1 tests was used for operation of the small TRB3 system for tests of the iTOF detector for HADES or for the bigger TRB3 system consisted of seven TRB3 boards for testing the P349 CERN experimental setup.

<sup>1</sup>More information about the TRB3 system, GPIN and CTS add-ons can be found at [trb.gsi.de](http://trb.gsi.de).

## InnerTOF - a Trigger Scintillator for HADES

D. Grzonka, P. Kulesa, J. Ritman, T. Sefzick

In order to reduce the trigger rate originating from background in proton induced reaction studies at the HADES experiment an additional trigger scintillator will be built. This detector called InnerTOF will be placed in front of the first MDC layer of HADES, see Fig. 1. It will consist of 6 modules with a trapezoidal shape (height  $\approx 730\text{mm}$ , long side  $\approx 700\text{mm}$ , short side  $\approx 90\text{mm}$ ) covering the 6 MDC sectors and each module includes three separate plastic scintillator plates (BC408<sup>1</sup>) with a nominal thickness of 6.4 mm, that are read out by SiPMs.

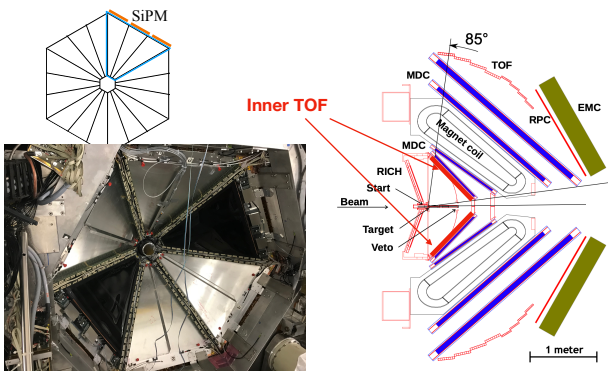


Figure 1: Sketch of the HADES detector cross section with the indicated position of the InnerTOF and its structure consisting of six modules with three separate scintillators read out by SiPMs. The photo shows two InnerTOF modules mounted at the HADES MDC (black triangles).

As SiPM the type MFC-30035<sup>2</sup> ( $3\times 3\text{ mm}^2$ ) is used. The SiPMs are soldered to a printed circuit board with amplifiers on the backside, see Fig. 2. At each scintillator, 3 boards with 4 SiPMs each are attached coupled via silicon pads resulting in 12 separately amplified signals. A particle passage will be detected by a certain multiplicity of SiPM signals which will be included in the trigger signal generation. For the detailed design the photon distribution has been simulated for various scintillator thicknesses and SiPM configurations using GEANT4. In Fig.3 simulation

<sup>1</sup><https://www.crystals.saint-gobain.com>

<sup>2</sup><https://www.onsemi.com>

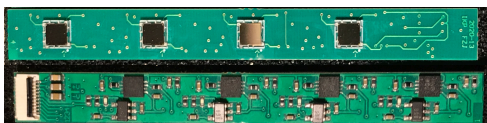


Figure 2: SiPM board with 4 SiPMs on the frontside (at top) and amplifiers on the backside (at the bottom). Three boards are attached to each scintillator.

results for a middle scintillator (6.4mm thick) with 12 SiPMs ( $3\times 3\text{ mm}^2$ ) at the edge are shown. For all hit positions all 12 SiPMs detect photons and at least one SiPM detects more than 5 photons. Therefore a reasonable setting of threshold and SiPM multiplicity for a trigger signal will result in a high efficiency at a low background rate. Test measurements with

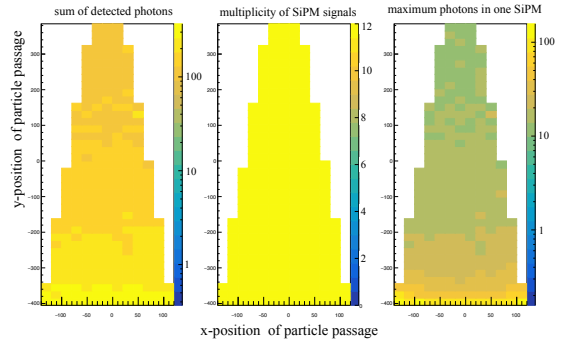


Figure 3: MC studies of photon detection generated by the passage of a charged 3.5 GeV/c pion through the middle scintillator at a certain x,y-position. Shown is the total sum of detected photons (left), the multiplicity of SiPMs with a photon detected (middle) and the maximum number of photons in a single SiPM (right).

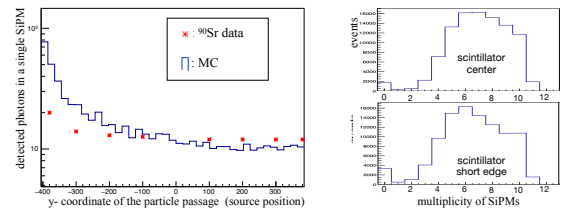


Figure 4: Comparison of source data to MC (left) and multiplicity distribution measured with COSY beam for a particle passage in the center and in a region close to the short edge (right).

one scintillator element have been performed with a <sup>90</sup>Sr source which show a flatter position dependence of the measured light yield compared to the simulations but sufficient photon numbers over the whole area. Furthermore data with COSY beam at 2.74 GeV/c have been taken resulting in efficiencies above 95% dependent on threshold setting and multiplicity selection, see the right frames in Fig.4. The multiplicities are lower compared to MC with a maximum at 11 because one SiPM was not working during the tests. Two prototype InnerTOF modules have been prepared and installed at HADES (see Fig.1) for a test beamtime in which the performance concerning the detection efficiency and trigger selectivity will be studied before the complete detector will be produced.

# Pre-commissioning of the STS1 Detector for the FAIR Phase-0 Experiments with HADES

G. Perez-Andrade, P. Wintz, P. Kulesa, A. Derichs, M. Holona and J. Ritman

The High Acceptance Di-Electron Spectrometer (HADES) is a magnetic spectrometer operating at the SIS18 accelerator at the GSI in Darmstadt (Germany). HADES explores a wide range of physics topics focusing in hadronic matter produced in pion, proton and heavy-ion-induced collisions [1]. HADES will begin its operation at the Facility for Antiprotons and Ion Research (FAIR), in the upcoming years. At FAIR, proton beams with energies up to 29 GeV will be available, enabling hadron production at a poorly explored energy region. The new experimental challenges led to an upgrade of the HADES spectrometer with new detectors and data-acquisition systems. This includes the installation of a Forward Detector system (FD) composed of two new Straw Tracking Stations (STS1 and STS2) and a Forward Resistive Plate Chamber (FRPC) detector for time-of-flight measurements. The new FD System extends the polar angle acceptance of the HADES spectrometer to the region between  $\theta = 0.5$  and  $7^\circ$  (Figure 1, left). The hardware upgrade is crucial for the PANDA/HADES phase-0 hyperon physics program at SIS18, which includes the investigation of hyperon radiative decays and multi-strangeness production [2].

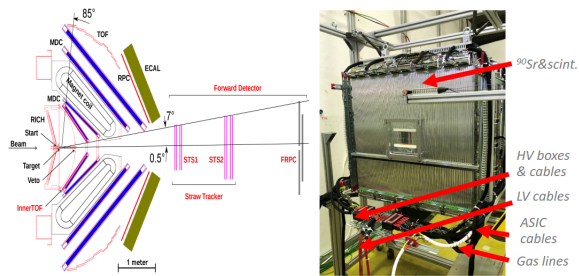


Figure 1: Left) Schematic overview of the HADES spectrometer, including the newly added FD components. Right) Photograph of the STS1 fully cabled for the pre-commissioning tests.

The STS1 was built at IKP in FZ Jülich. It comprises 704 gas-filled straws arranged in four double layers. The azimuthal orientation of the first and last double layers is  $\phi = 90^\circ$  and the second and third double layers are aligned along  $\phi = 0^\circ$  (Figure 1 right). Pre-commissioning tests of the STS1 were carried out at IKP before its installation at GSI. The aim was to evaluate the performance of the straws and corresponding readout electronics, by performing a series of measurements with the system fully connected to the supply and electronic readout.

The straw charge signals are amplified and shaped by the PASTTREC-ASICs [3] on front-end mounted

electronic boards (FEBv3). The STS1 has in total 44 FEBv3 and 88 PASTTREC-ASICs. The leading edge time  $t_{LE}$  and trailing edge time  $t_{TE}$  are measured in multi-hit TDCs implemented in the Trigger Readout Board version 3 (TRB3) [4]. A single TRB3 is used for each double layer *i.e.* there are 4 TRB3. The ASIC parameters can be programmed through the slow control via the TRBv3 board. In particular, a global threshold per chip can be assigned and the baseline (BL) can be adjusted for each single channel in 2 mV steps over a range of  $\pm 32$  mV. The data quality depends largely on the readout electronics settings. Therefore, tests to determine such settings are important. The effective threshold is determined by the global threshold and the individual channel BL. Both  $t_{LE}$  and  $t_{TE}$  are recorded when the signal crosses the threshold. Therefore, the Time over Threshold (ToT) is an observable that can be used to adjust the BL values of the individual channels: the closer the baseline is below the threshold, the higher the measured ToT and vice versa. An initial BL value was determined for each channel with a first tune based on the noise scalar rate. This method was developed by the STS group at the JU Krakow (Poland). A second precise tune *i.e.* fine-tune, based on ToT measurements was performed using signals from a  $^{90}\text{Sr}$  source.

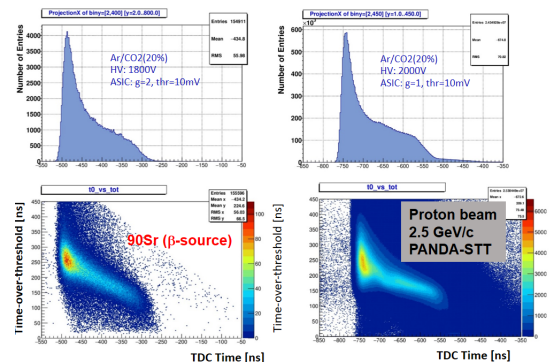


Figure 2: Left) Time over threshold versus drift-time distribution determined by electrons emitted from a  $^{90}\text{Sr}$  source. Right) Same information from a proton beam at  $p_{beam} = 2.5$  GeV/c

The  $^{90}\text{Sr}$  is a  $\beta$ -source decaying into  $^{90}\text{Y}$ , which in turn undergoes  $\beta^-$  decay. All together, the  $^{90}\text{Sr}/\text{Y}$  provides a broad continuous electron energy spectrum up to  $E = 2.2$  MeV [5]. Figure 2 shows a comparison between the time spectra obtained from the  $^{90}\text{Sr}$  on the left and a proton beam at 2.5 GeV/c (*i.e.* minimum ionizing protons) on the right. The projections on the x-axis *i.e.* drift-time spectra are also shown. Even though the  $dE/dx$  range is differ-

ent for  $\beta$  particles and minimum ionising protons and a one-to-one comparison is not exact, the described shape is very similar making it a very suitable and good option to perform complete system tests of the characteristic straw charge signals.

The fine-tune was performed for all 704 straws. With a removable holder as shown in Figure 1 (left), the  $^{90}\text{Sr}$  source together with a trigger scintillator were placed in front of the detector areas to be illuminated. The ASIC parameters were: gain = 2 mV/fC, peaking time = 20 ns and threshold = 10 mV. The gas mixture was Ar/CO<sub>2</sub>:80/20. In Figure 3, the data from a group of 144 straws (*i.e.* 9 ASICs) is shown in Figure 3. In this case, 4 ASICs were connected to the third double layer (STS1.3) and 5 to the fourth (STS1.4). Channels 48 and 98 are not connected reference channels. The straws were at HV = 1800 V, meaning that the expected average ToT is  $\langle\text{ToT}\rangle \sim 250$  ns. Already with the initial BL, the  $\langle\text{ToT}\rangle$  is well aligned. However, certain single channels had to be adjusted. An example is channel 134, whose ToT distribution before and after the fine-tune is shown at the far right of Figure 3. A larger than expected  $\langle\text{ToT}\rangle$  is seen with the initial BL but is then corrected after the fine-tune.

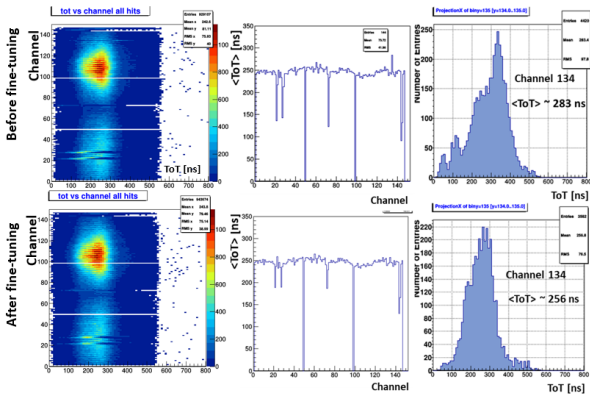


Figure 3: Top) ToT information for the channels in STS1.3 and STS1.4 at HV = 1800V before fine-tuning. Bottom) ToT information of same group of straws after the fine-tune.

The final  $\langle\text{ToT}\rangle$  values for all channels at HV = 1800 V are shown in Figure 4 (Top), where each double layer is represented with a different color. The  $\langle\text{ToT}\rangle$  values are mostly well aligned around the expected value and no dead straws were found. About 26 channels (out of 704) could not be perfectly tuned. Most of those channels show a lower  $\langle\text{ToT}\rangle$  than expected, yet when the baseline was increased, the presence of after-pulses in their drift-time distribution was spotted. The latter is undesired given that the STS1 main task is to perform track reconstruction and therefore clean drift-time spectra are needed. The specific channels showing after-pulses are currently under investigation to iden-

tify *e.g.* malfunctions in an ASIC or FEBv3. The front-end boards with identified bad electronic channels will be replaced as soon as more spare boards become available.

A comparison between the straws  $\langle\text{ToT}\rangle$  at a different HV is shown in Figure 3 (Bottom) where the same 9 ASICs and straws were connected (*i.e.* 144 channels). Higher  $\langle\text{ToT}\rangle$  is seen at higher HV values because the amplification grows with increasing voltage. In general the values and variations are consistent for all HV values thus it can be concluded that there is no BL tune dependence on the signal dynamical range.

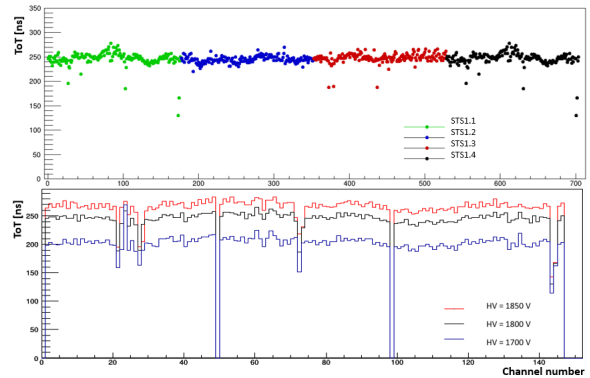


Figure 4: Top) Average ToT values for all 704 straws. Bottom) Average ToT values for 144 straws at three different HV values.

With the performed tests it was demonstrated that all components of the STS1 are working, the electronic parameters were optimised and the system had several months of stable detector operation in Jülich. The STS1 was then transported and successfully installed at HADES in November 2020 and it is ready for the commissioning beamtime scheduled on February 2021. Measurements with the upgraded HADES are planned for early 2022.

## References

- [1] The HADES Collaboration., Agakichiev, G., Agodi, C. *et al.* The high-acceptance dielectron spectrometer HADES. *Eur. Phys. J. A* 41, 243–277 (2009).
- [2] HADES and PANDA Collaborations., J. Adamczewski-Musch *et al.* Production and electromagnetic decay of hyperons: a feasibility study with HADES as a Phase-0 experiment at FAIR arXiv:2010.06961 [nucl-ex] (2020)
- [3] D. Przyborowski *et al.*, *Jour. of Instrum.* 11.08 (2016), 1236 P08009–P08009.
- [4] M. Traxler *et al.*, *Jour. of Instrum.* 6.12 (2011-12), pp. C12004–1239 C12004.
- [5] Abmel, X. C., *et al.* "Therapeutic Radionuclide Generators:  $^{90}\text{Sr}/^{90}\text{Y}$  and  $^{188}\text{W}/^{188}\text{Re}$  Generators." International Atomic Energy Agency: Vienna, Austria (2009): 235.

## In-beam Straw Tests Measurements for the PANDA-STT

G. Perez-Andrade, P. Wintz and J. Ritman

The PANDA Straw Tube Tracker (STT) consists of 4,224 close-packed straws arranged in up to 19 axial and 8 stereo layers surrounding the interaction point. Its location within the solenoidal magnetic field of the target spectrometer will enable charged particle momentum reconstruction after its precise trajectory reconstruction. In addition, measurement of the specific energy-loss (dE/dx) in the straw drift gas for particle identification (PID) in the momentum region below 0.8 GeV/c will be possible [1].

A STT prototype system was tested during in-beam measurements at COSY, which delivered proton and deuteron beams in a momentum range from 0.5 to 2.5 GeV/c. The prototype system consisted of six close-packed layers of 24 straws each. Therefore, about 24 hits per track were registered, which is similar to the PANDA-STT case where a maximum of 27 layers will be available.

A series of studies have been carried out using data collected during the in-beam measurements, including the development and optimization of a self-calibration and tracking method [2],[3] as well as a determination of the straw hit efficiency. The results of these studies for three proton datasets at different beam momenta are summarized in this report.

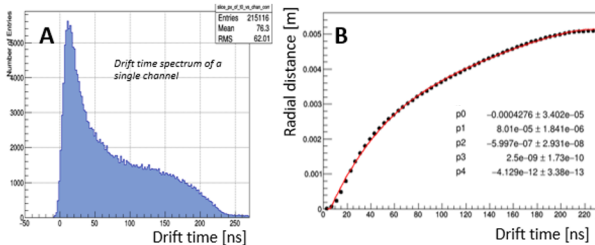


Figure 1: A) Typical single channel drift time spectrum, obtained from all registered  $t_{LE}$  for a specific channel. B) Isochrone radius [m] versus electron drift time [ns]. The red curve shows the polynomial fit to the data points (black points).

The straw raw data consist of the time information associated with each hit, *i.e.* fired channel ID, leading edge time  $t_{LE}$  and trailing edge time  $t_{TE}$ . From this the signal pulse width at the threshold height is calculated and is called the Time over Threshold (ToT =  $t_{TE} - t_{LE}$ ). A so called *self-calibration* procedure starts with the extraction of each single straw drift time spectrum (Figure 1, A) and the straws center position calculation. Based on a uniform illumination assumption, a running integral is made of the ionization electrons drift time  $t_i$  distribution, and this is related to the radial distance of the track from the wire. This distribution has been fit with a

fourth order polynomial  $r(t_i) = \sum P_i \times t^i$  (Figure 1, B).

The  $r(t_i)$  relation is used to calculate the isochrone circle radius from the measured drift time. The track through the prototype system was found by fitting a line tangent to all of the isochrones. The best fit is found through a  $\chi^2$  minimization and is chosen as the reconstructed track. The distances between the reconstructed track and the event isochrones are defined as track residuals ( $r_{track}$ ), and the spatial resolution is given by the RMS width of the  $r_{track}$  distribution. The latter would be centered around zero in the absence of systematic errors. However, a slight wire displacement from the straw center (due to *e.g.* gravitational sag) causes a shift of the  $r_{track}$  distribution mean by up to  $r_0 = 200 \mu\text{m}$ . Such small deviation allows a simple channel-dependent correction to  $r(t_i)$  by adding a constant shift ( $r_0$ ), and performing a re-fit using  $r_{new}(t_i) = r(t_i) \pm r_0$ .  $r_0$  is positive or negative depending upon whether the track has passed above or below the wire, respectively. The track reconstruction is iterated until changes to  $r_0$  become negligible. Single outliers (*e.g.* delta electrons) are identified and rejected in the method.

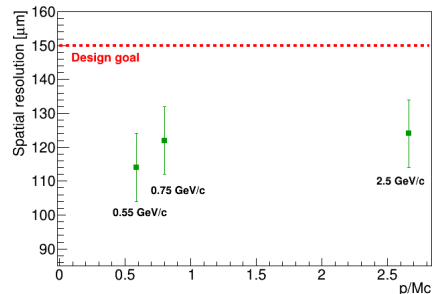


Figure 2: Spatial resolution for the three datasets at different proton beam momenta.

The results from the self-calibration for the three proton datasets at different beam momenta are shown in Figure 2. It was found that the PANDA-STT design goal of a spatial resolution of  $\sigma = 150 \mu\text{m}$  is already achieved after the second iteration. The best resolution is achieved with eight iterations, where a value of  $\sigma < 130 \mu\text{m}$  is obtained.

The average active straw radius can be determined from the final track distance distribution, defined as the calculated minimal distance of the reconstructed tracks from the corresponding straw centers. The information given by the analyzed proton datasets yielded an average active straw radius of  $r_{below} = 4.962 \text{ mm}$  and  $r_{above} = 5.013 \text{ mm}$ , determined with particles crossing below and above the wire respectively. The calculated diameter of  $d = 9.975 \text{ mm}$

is very close to the nominal value of  $d_{nom} = 10.000$  mm. After the self-calibration, track reconstruction and straw radius calculation, the straw efficiency was studied. The straw radial efficiency  $\epsilon$  is defined as:

$$\epsilon = \frac{N_{registered\ hits}}{N_{expected\ hits}}, \quad (1)$$

where  $N_{registered\ hits}$  is the number of raw hits with a drift time within a 250 ns window, whereas  $N_{expected\ hits}$  is the number of hits expected within  $r_{below}$  and  $r_{above}$ .

The obtained straw efficiencies for the different beam momenta are shown in Figure 3, where  $\epsilon$  has been plotted as a function of the complete straw diameter *i.e.* negative track distances correspond to the straw region below the wire. The average efficiency values within  $r_{below}$  and  $r_{above}$  with corresponding beam momenta are shown in Table 1. As the aim is to determine the typical characteristic straw efficiency, seven faulty straws (out of 150 in total) were identified and removed from this study. Such straws showed improper drift time spectra (*e.g.* after-pulses), which has been attributed to an incorrect ASIC parameter setting.

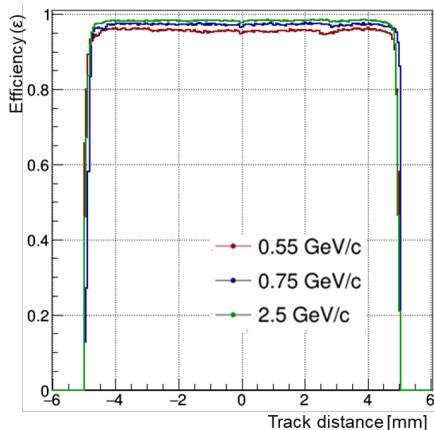


Figure 3: Radial efficiency ( $\epsilon$ ) as a function of the minimal distance between a track and the tube center for the different beam momenta.

Proton datasets	
Momentum [GeV/c]	$\epsilon$ [%]
2.5	98
0.75	97
0.55	95

Table 1: Average radial efficiency ( $\epsilon$ ) for the different beam momenta.

Figure 3 shows that the efficiency stays approximately constant across the straw diameter for all momenta, and it drops strongly near to the straw tube wall. Such behaviour is expected and is attributed to the smaller number of primary ionisation electrons in that straw region (*i.e.* shorter track

length inside the fiducial volume). The figure also shows that the maximum active/efficient straw radius is about 4.95 mm for minimum ionizing protons ( $p_{beam} = 2.5$  GeV/c).

Even though higher efficiency is expected at lower beam momentum, the opposite effect is shown in Table 1. This effect was caused by a time window cut-off: a hit is registered only if both  $t_{LE}$  and  $t_{TE}$  are within the readout time window. Consequently, hits with long  $t_{TE}$  surpassing the read out time window are lost. As shown in Figure 4, the signal widths (*i.e.* ToT) are on average broader for the lowest of beam momentum  $p_{beam} = 0.55$  GeV/c, hence the hit loss is bigger in this case. Inefficiency due to this read out cutoff is estimated to be about (2-4)%, depending upon the beam momentum, with a larger inefficiency for the lower beam momentum. The latter will not represent a problem for the PANDA-STT, which will have a considerably larger read out time window.

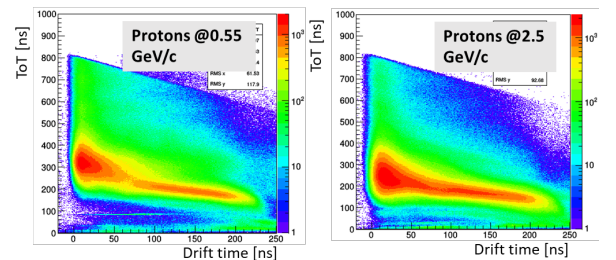


Figure 4: Time over Threshold vs drift time for protons at 0.55 GeV/c (left) and at 2.5 GeV/c. A clear cutoff at high  $t_{TE}$  values can be seen.

The described tests with the prototype PANDA-STT system show that a spatial resolution of  $\sigma < 130$   $\mu\text{m}$ , better than the PANDA design goal of  $\sigma = 150$   $\mu\text{m}$  has been achieved. Moreover, the straw diameter determined from the reconstructed tracks is  $d = 9.975$  mm ( $d_{nom} = 10.000$  mm) with an active/effective radius of 4.95 mm for minimum ionizing protons. Finally, from the measurements a high hit efficiency of at least 98% for a single straw can be expected for the PANDA-STT.

## References

- [1] PANDA COLLABORATION, Technical Design Report for the PANDA Straw Tube Tracker (2012) <https://arxiv.org/abs/1205.5441>.
- [2] G. Perez-Andrade *et al.*, Self-calibration Method for the In-Beam Test of the PANDA STT, Annual Report 2019 Institut für Kernphysik/COSY (2020).
- [3] G. Perez-Andrade *et al.*, Preliminary Results of a Global Calibration for the PANDA STT Annual Report 2019 Institut für Kernphysik/COSY (2020).

# Progress toward a direct measurement of the deuteron Electric Dipole Moment at COSY

A. Andres for the JEDI Collaboration

This report covers the current progress of the analysis of the November 2018 Precursor I Run at COSY. The matter-antimatter asymmetry in the universe cannot be explained by the Standard Model of elementary particle physics. According to A. Sakharov additional CP violating phenomena are needed in order to understand the matter-antimatter asymmetry. Permanent Electric Dipole Moments (EDMs) of subatomic elementary particles violate both time reversal and parity asymmetries and therefore also violate CP if the CPT-theorem holds.

The spin motion inside a storage ring can be characterized by the so-called invariant spin axis  $\vec{n}$ . It is defined by the rotation axis around which the spin precesses. An existing EDM would tilt the invariant spin axis in radial direction inside an ideal storage ring. The goal of the experiment is to measure the direction of the invariant spin axis. However, magnetic misalignments lead to additional tilts in longitudinal and radial direction. Therefore, the results need to be compared to a full simulation model of COSY in order to disentangle the true EDM signal from misalignments. The main observable is  $\alpha$ , which denotes the angle between vertical and horizontal polarization of the deuteron beam. An RF Wien Filter is operated on one of the harmonics of the spin precession frequency (871 kHz) and its phase is locked with the spin precession phase. Therefore, a particle passing through the device gets a spin kick in the same direction every turn which induces a build up of the vertical polarization. The vertical polarization

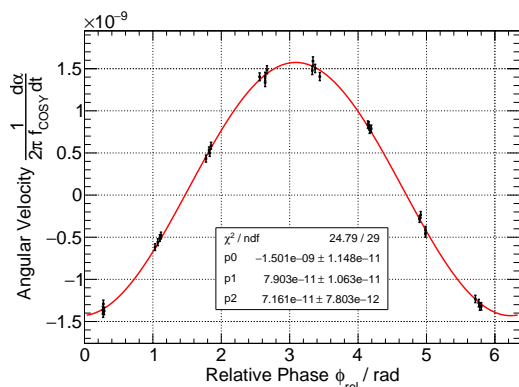


Figure 1: Polarization Build-Up  $\dot{\alpha}$  scaled by the revolution frequency  $2\pi f_{\text{COSY}}$  for a Wien Filter Rotation Angle of 0.945 mrad and a Snake Rotation of 0 mrad. The data points are fitted with Eq. (1).

build-up rate as a function of relative phase is shown in Figure 1. The data points are fitted with

$$\dot{\alpha} = p0 \sin \phi_{\text{rel}} + p1 \sin \phi_{\text{rel}} + p2. \quad (1)$$

The EDM resonance strength  $\epsilon^{\text{EDM}}$  is obtained by calculating

$$\epsilon^{\text{EDM}} = \sqrt{p0^2 + p1^2}. \quad (2)$$

The variable  $p2 \neq 0$  is an unexpected positive offset not understood. The EDM resonance strength  $\epsilon^{\text{EDM}}$  plotted as a function of Wien Filter Rotation Angle and Siberian Snake Angle is shown in Figure 2 along with a paraboloid fit [1]. The minimum of the surface denotes the orientation of the invariant spin axis. The current results are

$$\phi_0^{\text{WF}} / \text{mrad} = -2.91 \pm 0.08, \quad (3)$$

$$\xi_0^{\text{SOL}} / \text{mrad} = -5.22 \pm 0.07. \quad (4)$$

However, the residuals of the fit show for all measurements a systematic behaviour. This could indicate that additional systematic effects are not yet taken into account in the fit formula.

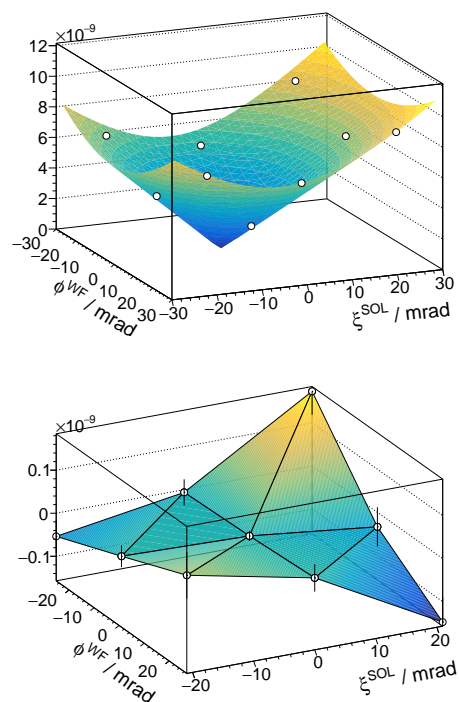


Figure 2: Results 2<sup>nd</sup> Map. **Top:** EDM Resonance Strength  $\epsilon_{\text{EDM}}$  as a function of Wien Filter Rotation Angle  $\phi^{\text{WF}}$  and Siberian Snake  $\xi^{\text{SOL}}$ . **Bottom:** Systematic Residuals.

## References

- [1] F. Rathmann, N. Nikolaev, and J. Slim, *Spin dynamics investigations for the electric dipole moment experiment*, Physical Review Accelerators and Beams, 23 (2020).

# Automatized dedicated measurement setup for SiPM array characterization

A. Koushik and I. Keshelashvili for the JEDI collaboration

## 1 Motivation and objective

The Jülich Electric Dipole moment Investigation polarimeter (JePo) is equipped with 52 Silicon-photomultiplier (SiPM)  $8 \times 8$  array for scintillating light detection and measurement. During beam based alignment in 2019, an accidental irradiation of these SiPMs took place. This made characterization of the SiPMs a requisite for determining their integrity before installation for the upcoming experiments.

The objective of the instrument was a standalone characterization all the SiPM in the SiPM array without any human intervention and to provide a detailed report on the various aspects of the SiPM such as dark current and responsivity. An irradiation experiment was also conducted with 40 MeV protons using the JULIC cyclotron. The sample SiPM array was gradually irradiated up to 11 Gy to study the radiation hardness and annealing effects.

## 2 Instrumentation

The characterization of the SiPM needs to be performed in two parts. Dark current measurement and responsivity measurement were required. Though both the instruments characterize the same SiPM, they express a specific character of the SiPM, hence, they were retained as independent instruments[1].

### 2.1 Dark current characterization

Dark current provides information about the noise of the device in absences of photons (false positive triggers) and the resolution of the readings. The DAQ software and analysis script was written in Python 3 with PyROOT modules running on Raspberry Pi. The SensL evaluation board with the SiPM in a black painted box, the remote controlled modified supply voltage circuit, the Raspberry Pi together with the pico-ammeter and voltmeter, completes the instrument to perform measurements and to generate a report[1].

### 2.2 Responsivity characterization

Responsivity is the average photocurrent produced per unit optical power, usually in a relative scale[1]. A reference SiPM was used along with two stepper motors along with the motor drivers provided the required movements in the xy plane. Decoupled single axis movements for the illuminating module and the SiPM was found to be best suited[1]. 3D design and

simulation of the instrument was performed on Autodesk Fusion 360. The design was then 3D printed and was assembled[1]. The DAQ software was written in Python 3 and an analysis was performed after the completion of the measurement.

## 3 Results

Both instruments produce a detailed report of the SiPM in PDF format.

**Dark current characterization** reports for the SiPM contains its dark current map as matrix, dark current for each SiPM and a concise table with total, average, RMS, minimum and maximum dark current. Higher dark current indicated greater damage to the SiPM.

**Responsivity characterization report** produced for the relative charge of array SiPM to reference SiPM. Values close to unity or greater, show better responsivity than the lower ones.

The reports from both instruments and the interpretation can be found in [1]

A sample map of the dark current matrix from the SiPM array is attached, see Figure: 1.

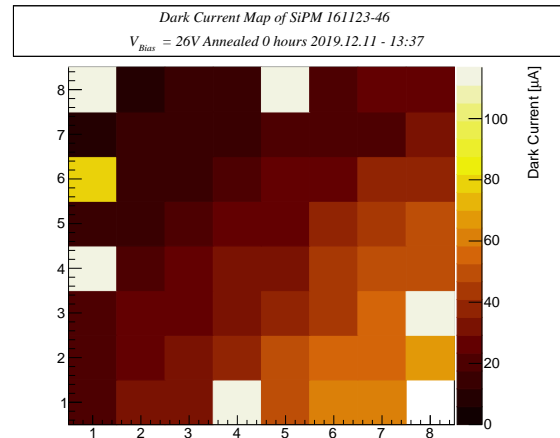


Figure 1: Sample dark current map of the SiPM array which was irradiated

## References

- [1] A. Koushik. Characterization of the SiPM arrays for the JEDI polarimeter using a dedicated measurement setup. *Master thesis* 2020, Institute of Nuclear Physics (IKP), Forschungszentrum Jülich and III. Physikalisches Institut B, RWTH Aachen

# Spin tune mapping with three-steerer vertical orbit bumps

A. Saleev for the JEDI Collaboration

JEDI Collaboration aims at first direct measurement of deuteron electric dipole moment (EDM) at COSY. Accentuation of the EDM signal, which is spin rotation in the electric field, is not feasible in pure magnetic ring such as COSY where the large background comes from magnetic dipole moment (MDM). Nevertheless a major reduction of the unwanted spin rotations by MDM in horizontal magnetic fields can be achieved by decreasing the vertical orbit RMS displacement and alignment campaign that corrects the angular orientation of a dipoles. Conventional accelerator physics method, beam-based alignment, can also be used to improve the positioning of the beam relative to the quadrupole centers and reduce both vertical and horizontal steerer power needed for certain orbit RMS. But the influence of all of those actions, which were already performed at COSY, on the reduction of spin rotation in the horizontal fields, is still not quantified. For that reason, in order to set the limit on the EDM in the JEDI Precursor Experiment with RF Wien filter, precise model of COSY is required, such that it would be reinforced with observation of the effects induced by the variation of the horizontal fields on the spin dynamics.

Using the spin tune mapping with three-steerer vertical orbit bumps allows to restrict the number of model parameters under the question and apply perturbation theory to spin dynamics[1]. Such measurement took place at the JEDI beamtime in August-September 2020. The measurements of spin tune at certain bump setting against a solenoid field allows to validate the model prediction for non-commuting spin rotations in the horizontal fields of the bump steerers and vertical fields of the dipoles located within the bump. This effect is determined independently from any spin rotations produced by other horizontal magnetic fields in the ring. Two solenoids, a superconducting snake solenoid and main solenoid of 2MeV e-cooler were used for this purpose with local bump created by vertical steerers SV18, SV20 and SV22. Several spin tune maps were recorded (see example in Fig. 1) and the non-commuting property, which leads to the tilt of the invariant spin axis at the place of either solenoid, and therefore to the linear dependance of spin tune on the solenoid field, was observed (see Fig. 2). Data analysis is ongoing.

## References

- [1] Optimization of the alignment of magnetic elements using the spin tune response to three-steerer bumps (JEDI Proposal, 2019) [http://collaborations.fz-juelich.de/ikp/jedi/public\\_files/proposals/Optimization-alignments-vs-bumps\\_v1.pdf](http://collaborations.fz-juelich.de/ikp/jedi/public_files/proposals/Optimization-alignments-vs-bumps_v1.pdf)

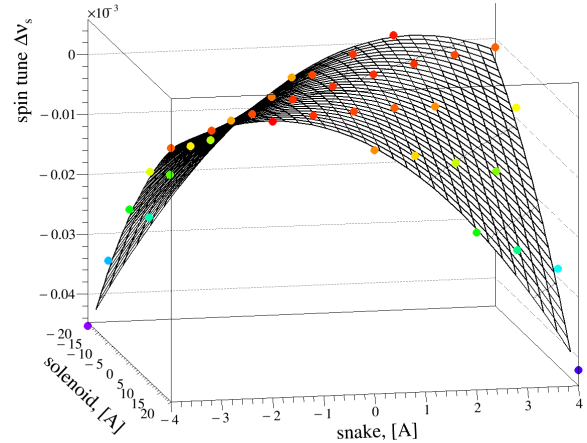


Figure 1: A spin tune map for the bump SV18 - SV20 - SV22 setting at SV20=10% with respect to the current in the Siberian snake and 2MeV e-cooler solenoid.

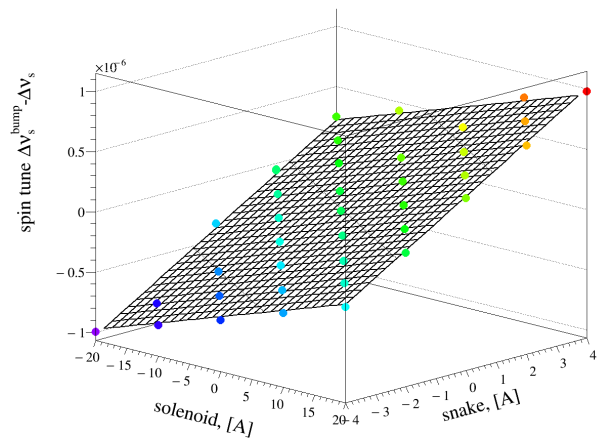


Figure 2: A difference of spin tune maps for the bump SV18 - SV20 - SV22 settings at SV20=10% and SV20=0%.

# Simulation and Optimization of the SCT of Protons in a Prototype EDM Ring

M. Vitz for the JEDI collaboration

This report covers the simulation of protons in the prototype EDM ring [1]. The design of the prototype EDM ring used in the simulations corresponds to a lattice version from February 2020. This lattice version consists of four unit cells. In between the unit cells the quadrupole family QSS is placed to add additional tuning possibilities. The four electromagnetic dipoles in each unit cell provide a total of  $90^\circ$  bending and kept spin and momentum of the reference particle aligned. Each unit cells also contains three additional quadrupoles which belong to the two different quadrupole families QF and QD. Sextupoles placed on each quadrupole in the lattice can be used to manipulate chromaticity. For the simulations an idealized lattice was considered which assumes electric and magnetic box fields and includes no misalignments in between the magnets. A floor plan of this lattice version is shown in figure 1.

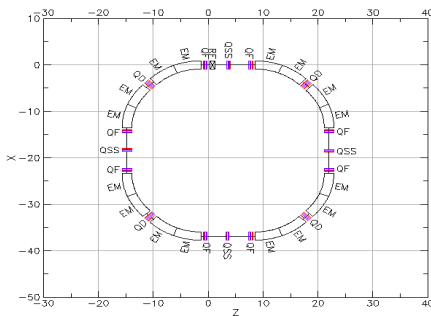


Figure 1: Floor Plan of Prototype EDM Ring.

A scan of possible betatron tunes was performed which recorded betatron tunes while varying the strength of the two quadrupole families QF and QD. During this scan the quadrupole family QSS and the sextupoles were turned off. The results are presented in figure 2 and figure 3.

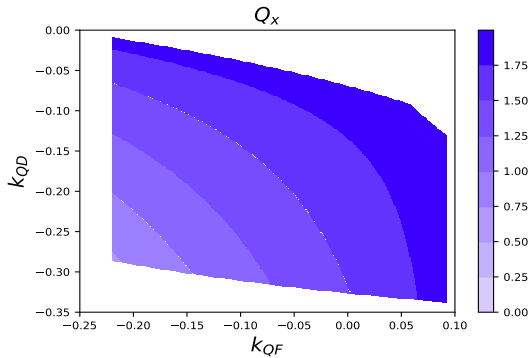


Figure 2: Horizontal betatron tune in dependency of the strength of two quadrupole families QF and QD.

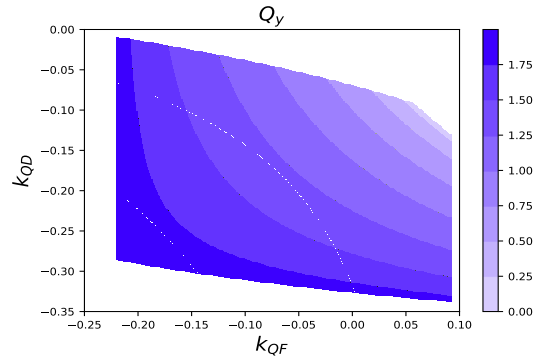


Figure 3: Vertical betatron tunes in dependency of the strength of two quadrupole families QF and QD.

This investigation shows that stable operation is possible with specific configurations of the quadrupole strengths. In the area of stable operation the horizontal and vertical betatron tune is able to vary in between zero and two.

In addition the dependency of the SCT on the vertical chromaticity at an arbitrary chosen working point ( $Q_x = 1.823$ ,  $Q_y = 1.123$ ) was simulated by using one bunch consisting of 1000 particles. While varying the vertical chromaticity, the horizontal chromaticity was kept at a constant value of zero. Figure 4 displays the outcome of the simulations.

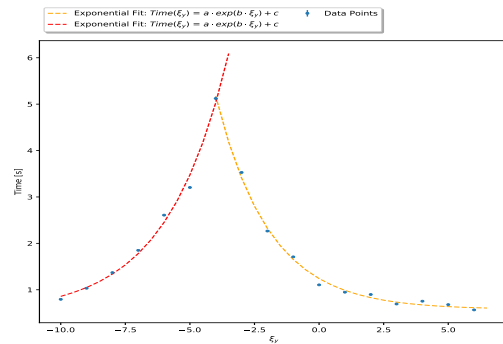


Figure 4: SCT in dependency of the vertical chromaticity.

The simulation results indicate that the maximal SCT is not at zero chromaticity for an arbitrary chosen working point. This observation is not understood so far. It will be further investigated using an already better understood lattice, namely the COSY lattice.

## References

- [1] A. Lehrach, S. Martin and R. Talman, *Design of a Prototype EDM Storage Ring*, Proceedings of Science, PoS SPIN2018, 144, 2018.

## Pellet target development for the JePo polarimeter

O. Javakhishvili and I. Keshelashvili for the JEDI collaboration

One of the key elements of the JEDI experiment at COSY is the new polarimeter (JePo)[1]. The JePo consists of a modular inorganic LYSO crystals and  $\Delta E$  scintillators. The main requirements are simplicity, interchangeability, long term stability and high resolution[2]. One crucial part of the polarimeter is the target system. In storage ring EDM (srEDM) measurements the requirements for the target are minimal influence on beam particles and vacuum system. Most of the traditional target systems are not suitable for srEDM experiments. Considering all the drawbacks of different types of targets we developed new concept of the ballistic carbon pellet target[2]. The idea is to shoot a small (tens of micron) carbon pellet through the beam (see Figure 1). The shooter and catcher mechanisms will oscillate the pellet and make it to cross the beam. By controlling the move-

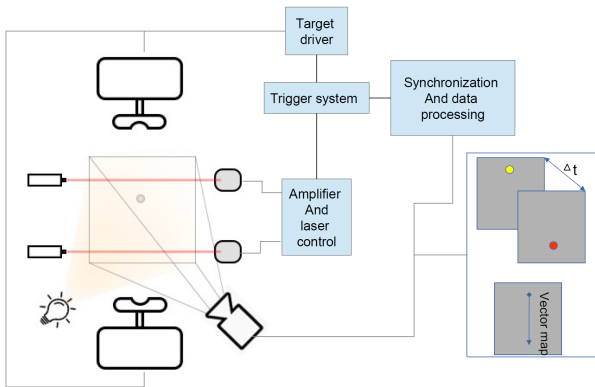


Figure 1: Block diagram of pellet target system

ment of the pellet it will be possible to even scan the beam profile at desired position if the DAQ will be synchronized with the pellet movement. Anything using electrical and magnetic fields must be avoided not to disturb the beam. Frequency and speed of the oscillation must be variable to achieve the desired effective target density. The proper monitoring system must be developed.

The system is controlled by FPGA, so far we have developed a TOF (time of flight) system which consists of lasers and photo diodes. The output of the diodes are amplified and converted to a digital signal which is fed into the FPGA (see Figure 2). To get pellet tracking information, camera signals are fed in to the FPGA, which performs image processing and object extraction algorithms. We tested different algorithms (see Figure 3), for edge detection the CANNY Edge Detect algorithm is used, for object extraction COG (Center of Gravity) method is used. In general, before the COG there is the CCL (Connected Component Labeling) algorithm, but in our

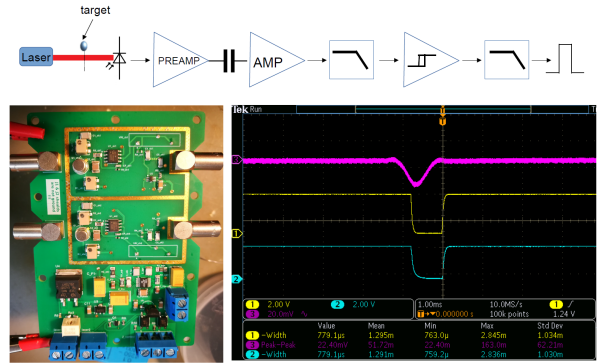


Figure 2: The TOF unit, diagram (top), physical board (left), test figure (right): purple - amplified analog signal, yellow and blue - digital outputs

case, only moving object in the frame is pellet, so we excluded CCL step. For faster performance image processing algorithms are only working on pre-defined ROI. All image processing and triggering is done in FPGA and controlled from CPU side using AXI interface.



Figure 3: The results of different image processing algorithms, left - Sobel filter with color invert, middle - Prewitt filter, right - Canny

The triggering system has been developed. It was tested, the output signal is very clean as it is shown on Figure 2. The image processing part is also finished, now we are working on tracking algorithms, combining these different systems into one, integrating it with detector signals and making a user friendly control interface.

This project was supported by Shota Rustaveli National Foundation of Georgia (SRNSFG) JFZ\_18\_01

## References

- [1] F. Müller, O. Javakhishvili, D. Shergelashvili, I. Keshelashvili, D. Mchedlishvili et al., "A new beam polarimeter at COSY to search for electric dipole moments of charged particles", JINST 15, P12005 (2020)
- [2] I. Keshelashvili et al., "A new approach: LYSO based polarimetry for the EDM measurements", J. Phys. Conf. Ser. 1162, 012029 (2019)

## Chromaticity measurements together with spin coherence time

V. Shmakova on behalf of the JEDI collaboration

In 2020, a new chromaticity tool was developed at COSY that is based on the fast tune measurement. The working principle is to measure the machine tune during a one second long sweep of the RF-excitation of a stripline unit over a span of about 100 Hz. The tool was used for the first time during the JEDI September 2020 run, along with the measurements of the horizontal polarization lifetime, also called spin coherence time (SCT) of a deuteron beam [1]. The SCT itself is very sensitive to even small changes in the ring optics. With the new chromaticity tool, it is now possible to investigate the relation between SCT and chromaticity [2] in a consistent way.

The SCT is optimized by adjusting the arc sextupoles families MXG, MXS, MXL. During the run, the chromaticity was measured in every cycle at a time in the cycle when the beam extraction was switched off.

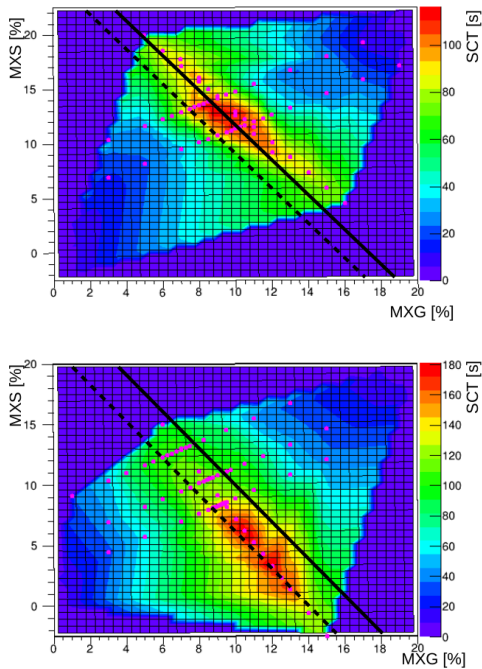


Figure 1: Measured spin coherence time as function of the settings of the sextupoles MXG and MXS. During the measurements shown in the bottom panel, the beam profile monitor was switched on.

There were two large sets of the SCT recorded, which are shown in the two panels of Fig.1. During the measurement of the second set, the beam profile monitor was switched on (bottom panel in Fig.1). This clearly had a visible effect on the location of the region of highest SCTs.

The intersections of the lines where the measured chromaticities are zero, are shown as solid (horizontal  $\chi_x$ ) and dashed (vertical chromaticity  $\chi_y$ ) lines in Fig. 1. It seems that the relation between the chromaticities and the SCT differ in the two panels. The line of maximal SCTs found in the first case and the line of zero horizontal chromaticity are very close, whereas in the second case, the line of zero vertical chromaticity appears to have a dominant effect on the polarisation decoherence.

In Fig. 2, four maps of  $\chi_x$  and  $\chi_y$  are shown, depending on the settings of the sextupole families MXG and MXS. The data were taken for stable conditions, where the MXL was fixed at  $-1\%$ ,  $-0.5\%$ ,  $0.5\%$ , and  $1\%$ . That way all the data could be analysed as one large 4D map. Since the MXL sextupoles are located in the arcs, where  $\beta_x$  function is small,  $\chi_x$  is hardly changing for different values of MXL, and the vertical chromaticity plane is mostly shifted in vertical direction from map to map, moving the general intersecting point of all three planes, point where both  $\chi_x$  and  $\chi_y$  turn to zero. Thus, this allows us to calculate the configuration of the sextupoles needed to reach zero chromaticity.

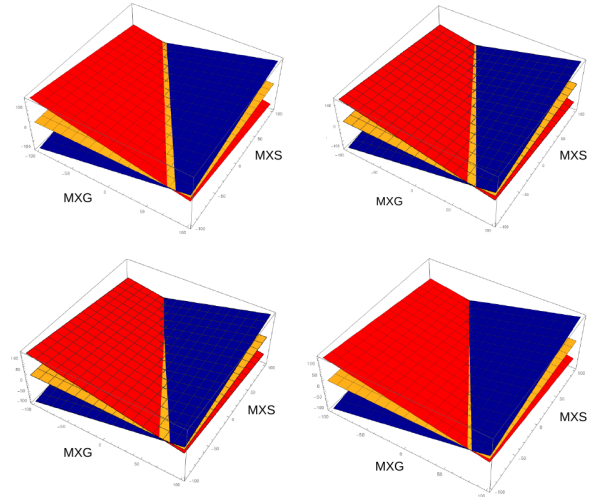


Figure 2: Horizontal (blue) and vertical (red) chromaticity fit planes, depending on the settings of sextupoles MXG and MXS, and the crossing zero planes (yellow). Each plot correspond to the different  $MXL = -1\%$ ,  $-0.5\%$ ,  $0.5\%$ , and  $1\%$ .

## References

- [1] G. Guidoboni *et al.*, Phys. Rev. Lett. 117 (2016) 054801.
- [2] G. Guidoboni *et al.*, Phys. Rev. Accelerators and Beams 22 (2018) 024201.

# Search for axion-like particles at COSY

S. Karanth<sup>a</sup>, E. Stephenson<sup>b</sup>, and A. Wrońska<sup>a</sup> for the JEDI collaboration

Originally, the axion was introduced to resolve the strong CP problem in QCD. Axions or Axion-like Particles (ALPs), when coupled with gluons, induce oscillations in the nuclear electric dipole moment  $d_n$  [1] that can be described as  $d_n(t) = d_0 + d_1 \cos(\omega_a t + \phi_a)$  where  $\omega_a$ , the oscillation frequency, is related to the axion mass  $m_a$  by  $\omega_a = m_a c^2 / \hbar$  and  $\phi_a$  is the oscillation phase.

In spring 2019, the JEDI Collaboration conducted a proof of principle experiment at COSY using a 0.97 GeV/c in-plane polarized deuteron beam. At the resonance between the spin precession frequency and the EDM oscillation frequency, a vertical polarization build-up is expected. The phase  $\phi_a$  that relates these two frequencies is unknown and modulates the size of the effect. To overcome this, four beam bunches with different polarization directions were stored simultaneously in the ring. The machine frequency was slowly ramped to find the resonance between the spin precession frequency and the EDM oscillation frequency, as the latter is unknown. A jump in vertical polarization is expected when the resonance is crossed. A detailed explanation of the experiment is given in the previous annual report [2]. As a test of our experimental method, an RF Wien filter with a sideways magnetic field was set to a fixed frequency. The machine frequency was scanned to cross this resonance and a polarization jump was observed. Such a ‘test’ was helpful for the calibration of jumps from the axion search [2].

The size of the jump as the resonance is crossed will be different for the four bunches because of their relative phase. To find the the magnitude of the jump and to accurately determine the time of the jump, a step function (1) was fit to the asymmetry histogram of each bunch obtained from the polarimeter.

$$f(t) = \begin{cases} p_0 & \text{if } t < p_2, \\ p_0 + p_1 & \text{if } t \geq p_2 \end{cases} \quad (1)$$

Here,  $p_0$  is the asymmetry before the step,  $p_1$  is the step size and  $p_2$  is the time when the step occurs. The parameter  $p_2$  is a fixed parameter of the fit and is changed as the fit is repeated for each time bin in the ramp ( $120 \text{ s} < p_2 < 256 \text{ s}$ ). For each fit, the  $\chi^2/\text{d.o.f}$  is noted down along with the other parameters. Figure 1 shows examples of three such fits to the asymmetry histogram from the Wien filter scan. At the resonance crossing, a significant minimum in the value of  $\chi^2/\text{d.o.f}$  is seen when plotted against time in cycle. At this bin, the step size  $p_1$  for each bunch is plotted as a function of the relative polarization distribution between the bunches. A sinusoidal fit to  $p_1$  would provide us the amplitude of the jump

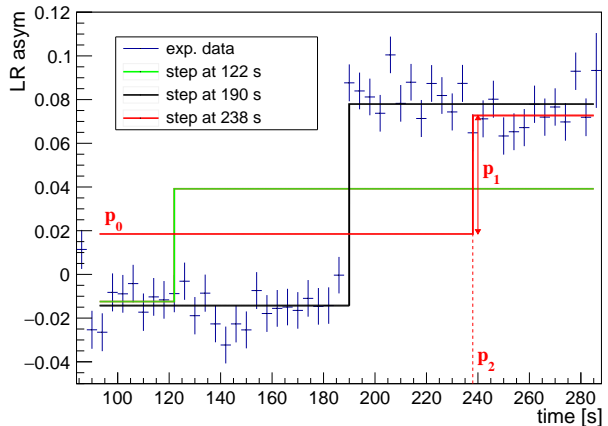


Figure 1: Examples of step function fits to the asymmetry histogram from a Wien filter scan. The black line is fit at the resonance crossing. The step size  $p_1$  will be largest and the  $\chi^2/\text{d.o.f}$  the smallest when compared to the other two fits shown, green and red, whose step occurs away from the resonance.

caused by the ALPs and from the corresponding time bin the resonance frequency, thus the value  $d_1$  of the oscillating EDM can be calculated.

If there is no clear minimum of  $\chi^2/\text{d.o.f}$ , as is the case in this experiment, then the analysis procedure is adjusted to obtain an upper limit of the oscillating EDM value. Instead of performing the sinusoidal fit to the step size ( $p_1$ ) values of just one time bin, this is repeated for each time bin in the ramp. Once the amplitude is obtained, we can calculate the sensitivity of the experiment for all the scanned frequency values.

To summarize, an experiment to search for ALPs was demonstrated at COSY by scanning the machine frequency for a resonance between an axion-induced oscillating EDM and the spin precession frequency. This report explains the analysis procedure to obtain an upper limit of the oscillating EDM.

## References

- [1] P.W. Graham, S. Rajendran, Phys. Rev. D **84**, 055013 (2011)
- [2] IKP annual report 2019, p.12, URL [https://www.fz-juelich.de/ikp/EN/Service/Download/Downloads/jahresbericht\\_2019.pdf](https://www.fz-juelich.de/ikp/EN/Service/Download/Downloads/jahresbericht_2019.pdf)

<sup>a</sup> Marian Smoluchowski Institute of Physics, Jagiellonian university, Kraków, Poland

<sup>b</sup> Indiana University Center for Spacetime Symmetries, Department of Physics, Bloomington, IN, USA

# Systematic corrections of $^{210}\text{Bi}$ constraint and $^{11}\text{C}$ energy scale for CNO solar neutrinos analysis with the Borexino Experiment

A. Singhal<sup>1</sup>

The neutrinos emitted from thermonuclear reactions in the Sun help to unravel the processes occurring in its core. According to the Standard Solar Model predictions, the two processes:  $pp$  (proton-proton) chain and CNO (carbon-nitrogen-oxygen) cycle reactions power the Sun. The  $pp$ -chain processes are the primary source of solar energy while the CNO cycle is assumed to contribute less than 1% to the solar energy. All  $pp$ -chain neutrinos ( $pp-\nu$ ,  $pep-\nu$ ,  $^7\text{Be}-\nu$ , and  $^8\text{B}-\nu$ ) have already been detected before. The observation of solar neutrinos from CNO cycle, which is the dominant source of energy in heavier stars, give a complete picture about the sources of energy in the Sun and provide an insight into the longstanding problem of the metallicity of the Sun.

The Borexino Detector, an ultra-pure liquid scintillator detector located at LNGS lab in Italy, has detected the neutrinos from CNO cycle in the Sun for the first time in history with a confidence level better than  $5\sigma$  [1]. The challenges faced in this analysis are the low rate of CNO  $\nu$ s and degeneracy of the spectral shape of CNO  $\nu$ s to that of  $^{210}\text{Bi}$  background and  $pep$  solar  $\nu$ s and hence, constraints to their rates are applied. My contribution to the analysis concentrates towards systematic corrections of  $^{210}\text{Bi}$  constraint and the correction of  $e^+$  energy scale needed for cosmogenic  $^{11}\text{C}$  background.

The imprecision of the model that determines the energy of  $e^+$  (energy scale of  $e^+$  and  $e^-$  is different) results in the difference of the energy scale of  $^{11}\text{C}$  in data and MC as only  $^{11}\text{C}$  decays to  $e^+$ . Hence, a shift to  $^{11}\text{C}$  Monte Carlo (MC) PDF is applied to match the peak of  $^{11}\text{C}$  energy spectrum in data and in MC. The evaluation of the shift is performed on  $^{11}\text{C}$  events selected by Three Fold Coincidence (TFC) method using strict conditions. The fitting of these data events is performed using MC PDFs for different values of shifts in order to obtain a likelihood profile. Using this likelihood profile, the best value of shift is determined (Fig. 1).

In order to determine the constraint on  $^{210}\text{Bi}$ ,  $^{210}\text{Po}$  data is fitted using a paraboloidal function [2].  $^{210}\text{Po}$  is the daughter of  $^{210}\text{Bi}$  decay which in turn decays via emitting  $\alpha$  particle. The  $^{210}\text{Po}$  events are selected from data using an energy cut and a MLP (It stands for Multi Layer Perceptron, which is a neural network algorithm which distinguishes between  $\beta$  and  $\alpha$  particles) cut to select  $\alpha$  particles. The paraboloidal function makes use of  $\beta_{leak}$  parameter that refers to the leakage of  $\beta$  events in data due to MLP selection and is determined using 2 methods whose results are compatible to each other:

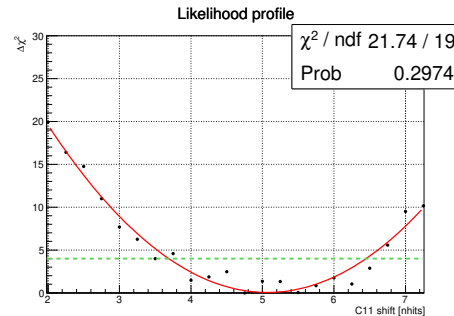


Figure 1: The likelihood distribution for  $^{11}\text{C}$  shift values in nhits (number of hits detected by the PMTs) as an energy estimator. The best value corresponds to a correction of 1% to energy scale for positrons.

- **Gaussian and Exponential fit** - This method uses Gaussian model to fit  $^{210}\text{Po}$  data and an exponential function to determine contribution of  $\beta$  events in  $^{210}\text{Po}$  data as tagging of  $\beta$  events as  $\alpha$  events by MLP has exponential dependency with respect to energy. From this fit (with p-value of 0.11), the value of  $\beta_{leak}$  parameter is  $2.1 \pm 0.4$  cpd/100 ton including systematic uncertainty.
- **Fit using MC PDF** - This method makes use of PDFs for  $^{210}\text{Po}$  and other species lying in the energy region of  $^{210}\text{Po}$ . Further the PDFs of other species are summed together which represents  $\beta$  spectrum and an exponential damping is applied to this spectrum to simulate MLP dependence on energy. At last, the produced PDFs are used to fit  $^{210}\text{Po}$  data. Here, a better p-value of 0.64 is obtained. From this fit, the value of  $\beta_{leak}$  parameter is  $2.6 \pm 0.3$  cpd/100 ton including systematic uncertainty.

Also, I worked towards optimisation of MC simulation in order to prepare simulated  $^{210}\text{Po}$  data for analysis and participated in performing fit of data to extract CNO- $\nu$  signal [3].

## References

- [1] M. Agostini et al. (Borexino Collaboration), "Experimental evidence of neutrinos produced in the CNO fusion cycle in the Sun", Nature 587, p 577–582(2020)
- [2] S. Kumaran, "Extraction of  $^{210}\text{Bi}$  via  $^{210}\text{Po}$  for CNO neutrino detection with Borexino", Poster in Neutrino Conference 2020.
- [3] A. Singhal, Master Thesis, "Observation of CNO solar neutrinos with the Borexino experiment".

# Reduction of the $^{14}\text{C}$ impact on the Neutrino Mass Ordering measurement of JUNO

Philipp Kampmann

The JUNO experiment is a next-generation neutrino experiment under construction in vicinity of the Pearl River Delta in Southern China. It aims to address the determination of the Neutrino Mass Ordering (MO) with  $3\text{-}4\sigma$  sensitivity in about 6 years as its main goal using reactor electron anti-neutrinos from two adjacent nuclear power plants. The reactor electron anti-neutrinos will be selected with the coincident signal of Inverse Beta Decay (IBD) reaction, which consists of a prompt positron and a delayed neutron capture signal. The JUNO detector consists of a large 20 kton liquid scintillator detector, which is instrumented with a dense PMT array consisting of about 18,000 large  $20''$ -PMT's and 25,000 small  $3''$ -PMT's.

Besides the detector design, a meticulous data analysis is needed to ensure, that the JUNO experiment can meet the strict requirement on the energy resolution, which needs to be better than 3% at 1 MeV for the determination of the MO. Due to the large volume of the JUNO detector, the seemingly small expected concentration of  $10^{-17}$   $^{14}\text{C}$  atoms per  $^{12}\text{C}$  atom causes a large total activity of 40 kBq. The low endpoint energy of  $Q = 0.156$  MeV of these beta-decays allows the effective rejection with an appropriate detector threshold. Nevertheless, under the assumption of a readout window of  $1.25 \mu\text{s}$ , about 5% of the IBD prompt event readout windows are expected to be contaminated by additional PMT hits from such  $^{14}\text{C}$  decays. The reconstructed energy of such a so-called pile-up event is expected to be biased as it largely depends on the amount of detected PMT hits. This bias would then spoil the sensitivity to the MO due to the worsened energy resolution.

A fast and simple approach to identify and remove a fraction of these  $^{14}\text{C}$  decay energy depositions from the readout windows is the so-called clusterization algorithm. This algorithm searches for peaks, called clusters, in the time distribution of PMT hits. Although the algorithm can be very effective on these, it is limited to energy depositions, which are sufficiently separated in time minimizing their overlap. The current implementation of the clusterization algorithm reaches its maximal efficiency for finding a  $^{14}\text{C}$  decay following a positron for a time separation of more than about 600 ns between the first hits of the positron and the  $^{14}\text{C}$  decay respectively. The parameters of the clusterization algorithm were optimized to yield the best MO sensitivity with respect to the pile-up effect introduced by  $^{14}\text{C}$  decays. Figure 1 shows the expected gain in the MO discriminator  $\Delta\chi^2$  for rejecting the false MO in dependency of the  $^{14}\text{C}$  concentration in the scintillator. With the optimized clusterization, an improvement of 0.17

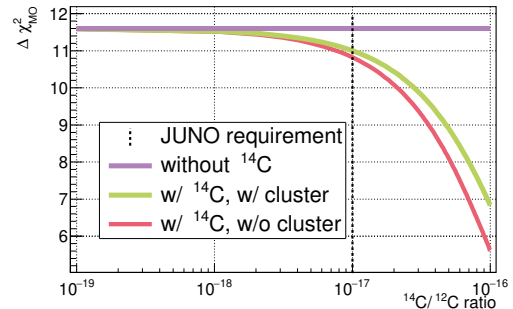


Figure 1: The discriminator  $\Delta\chi^2$  for rejecting the false MO as used in the JUNO experiment in dependency of the  $^{14}\text{C}$  to  $^{12}\text{C}$  ratio. The purple line represents the situation without any  $^{14}\text{C}$  in the scintillator, while the red line includes the estimated effect of the  $^{14}\text{C}$  pile-up on the  $\Delta\chi^2$ . The green line shows the estimated improved  $\Delta\chi^2$  after clusterization effects are applied. The nominal expected  $^{14}\text{C}$  concentration is shown with a vertical dashed line. For the estimation of the  $\Delta\chi^2$  with the presented effects, the GNA-tool [1] was used.

from  $\Delta\chi^2 = 10.83$  to  $\Delta\chi^2 = 11.00$  could be achieved for the nominal concentration of  $10^{-17}$   $^{14}\text{C}$  atoms per  $^{12}\text{C}$  atom. To effectively further identify pile-up events, which can not be separated in time via the clusterization algorithm, a likelihood test was developed, which is based on the charges and times of PMT hits. For the prediction of PMT hit times and charges in the likelihood function, a large Geant4 simulation of electrons was used. This likelihood function, comparing the measured PMT hit time and charge distribution to this prediction, is minimized then with the total deposited signal charge, the event time and the light emission vertex as free parameters. As single point-like events were used for prediction, it is expected, that the likelihood function can not be minimized accordingly for non-point-like events, yielding higher function values. Choosing an discriminator value for the minimized likelihood values, 13.74% of pile-up events, which could not be identified by the clusterization, could be identified by this likelihood test while misidentifying only 0.11% of pure positron events as pile-up. After its application, this identification of the remaining pile-up events would further improve the sensitivity.

## References

- [1] Fatkina, A. et al (2019). GNA: new framework for statistical data analysis, *EPJ Web of Conferences*, 214, 05024.

## Mechanics and cleaning of iPMTs in OSIRIS

Moritz Cornelius Vollbrecht

The neutrino group of IKP-2 is participating in the JUNO collaboration (Jiangmen Underground Neutrino Observatory) and working on the OSIRIS detector (Online Scintillator Internal Radioactivity Investigation System). This cylindrical detector (Fig. 1) will be used to screen the scintillator radiopurity during filling of the 20 kton JUNO detector for any issues that might affect the sensitivity of JUNO, for example contaminations with Uranium or Thorium.

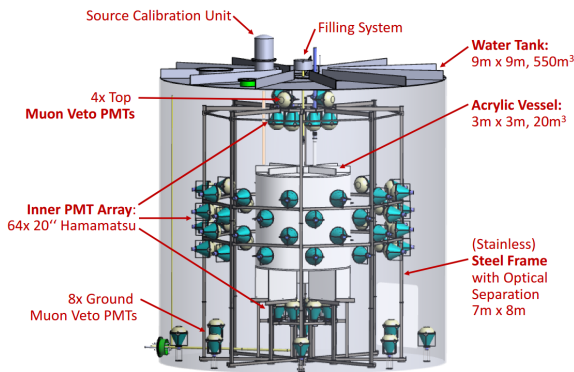


Figure 1: Overview of the OSIRIS detector, Figure by: M. Wurm.

OSIRIS will feature in total 76 20-inch iPMTs (intelligent PhotoMultiplierTubes) to analyse signals originating from the scintillator and the water buffer around it. The newly developed design of the iPMTs combines a PMT together with all needed readout and control devices in such a way that only one Ethernet cable is sufficient to power and operate the whole device. Furthermore, it is possible to implement algorithms working on waveform level on the hardware itself, hence the term "intelligent".

As the PMTs have to be sealed permanently after the assembly, an intensive testing of the complete system beforehand is mandatory. Many tests and procedures have been already developed, two personal contributions will be given in the following paragraphs:

1. Within OSIRIS, the iPMTs will be mounted on a stainless steel frame. The individual iPMTs as well as a magnetic shielding will be held by a stainless steel construction (holder) in place, which is then mounted on the frame. A prototype of the holder was built and measurements testing the mechanical stability under simulated realistic circumstances were carried out. The measurements showed that the resulting deformations could possibly damage

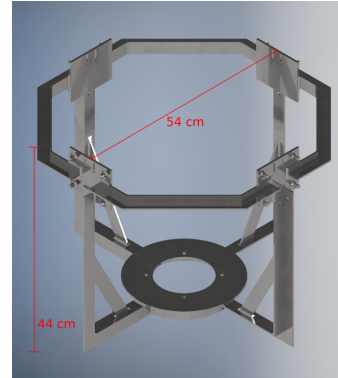


Figure 2: Reinforced design of the PMT holder.

the PMT. In order to increase the strength of the holder, FEM-simulations were performed to analyse the influence of different reinforcement approaches. The chosen configuration, taking the tradeoff between stiffness maximisation and weight increase into account, focuses on T- and L-profiles. The reinforced design can be seen in Fig. 2.

2. In order to achieve the best sensitivity for radiopurity measurements with OSIRIS, the detector components have to be cleaned thoroughly before installation. To address this issue for the German contributions, a cleaning facility was developed at RWTH Aachen University and is currently under construction. It includes different washing steps, ranging from degreasing with industrial detergent and tap water to rinsing with ultra pure water in a clean room. The effects of the final cleaning step will be assessed with water conductivity sensors sampling ion concentrations in the used water. Additionally, optical checks of the cleaned surfaces can be performed with a microscope. It is planned to support the work group at RWTH during production with members of IKP-2 at FZJ Jülich as well as other German universities contributing to OSIRIS.

As the installation of the iPMTs is supposed to take place late summer 2021, the shipment of the German contributions to OSIRIS is consequently expected to be on its way to China in late spring 2021. Until then, many more studies probing other aspects of the system will be undertaken. These include further tests of the iPMT electronics and the evaluation of the iPMT sealing procedures. Other points are test runs of the cleaning facility or general lab preparations for the production phase which is planned to start beginning of 2021.

# Trigger Condition Optimization of Event Builder for OSIRIS

Runxuan Liu

JUNO is a 20 kt liquid scintillator detector under construction in Jiangmen, China, whose goal is to determine the neutrino mass hierarchy. In order to meet the stringent requirements on the radiopurity of the liquid scintillator, the OSIRIS pre-detector is being designed to monitor the liquid scintillator during the several months of filling the large volume of JUNO. The OSIRIS (Online Scintillation Internal Radioactivity Investigation System) pre-detector of JUNO will be equipped with 76 20-inch PMTs. There are 64 of them observing the inner detector, which contains the 18 tons liquid scintillator target, surrounded by water. The remaining 12 PMTs are installed in the water Cherenkov veto detector, which surrounds the inner detector that is optically separated. The DAQ (data acquisition) system will have no global hardware trigger: instead, each PMT will provide a data-stream composed of the digitized PMT pulses, each containing a time stamp. We have readout windows of 240 ns with 120 samples. Based on the latter, the event builder software will organize these data streams into events by sorting the time stamps and apply trigger logics. Then the built events will be sent to disk and online-monitoring analysis framework.

The event builder has been implemented with several modes that aiming on different kinds of testing, operating or calibration purposes. For optimizing the detector threshold, it is needed to determine the optimal trigger conditions for the coincidence mode: multiplicities of  $\mathbf{n}$  hits within sliding trigger window time  $\mathbf{t}$ . Each trigger event will contain PMT pulses that lay in between a defined pre-time to a defined post-time around the trigger time.

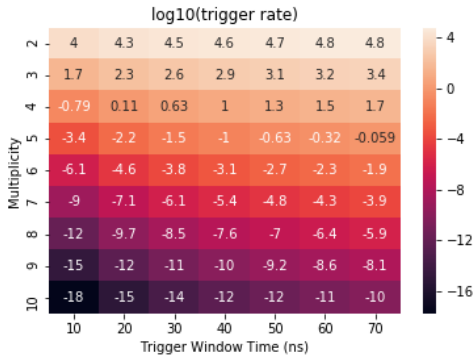


Figure 1: Trigger rate (Bq) as a function of trigger window time (x-axis) and multiplicity (y-axis). Here only dark noise is considered.

To avoid high frequency of noise triggers, the trigger rate by dark noise pulses needs to be considered. An analytical calculation based on binomial distribution was applied for 64 inner PMTs with dark rates of 15,900 Bq each according to PMT testing results.

According to the dark-noise-only trigger rates (shown in Figure 1), for less than 10 dark noise triggered events per second, we need the multiplicity  $\mathbf{n} \leq 4$ . These trigger rates were crossed checked by two other methods, a toy Monte Carlo simulation and the generation of fake dark noise sent to the event builder trigger software. The results agree well.

For physics signals, the Geant4-based OSIRIS simulation software is used to simulate electrons with user-defined energies and positions. The outputs are photon hits on all PMTs. Then a DAQ simulation program is applied to get the original hits packaged and to output PMT pulse time stamps. Dark counts are also simulated at this stage. After that, the output root files can be sent to the event builder.

One of the goals of the OSIRIS detector is to determine the  $^{14}\text{C}$  concentration of the JUNO liquid scintillator. Therefore we need to determine trigger conditions which allow us to measure low energetic  $^{14}\text{C}$   $\beta$ -decays ( $Q=156$  keV). The event rate for the whole detector is assumed to be 30.0 Bq.  $^{14}\text{C}$  simulation of one day exposure in OSIRIS (26 million events, uniformly distributed positions) was produced. In order to have a lower energy threshold, we need lower multiplicity and longer trigger window. According to Figure 2, for a fixed  $\mathbf{n}$ , changing of  $\mathbf{t}$  does not contribute much to our trigger efficiency. For  $(\mathbf{t}, \mathbf{n}) = (70$  ns, 5), we get trigger efficiency at 90% with an energy threshold of 36.0 keV. This yields event rates of 22.5 Bq for  $^{14}\text{C}$  and 2.9 Bq for dark noise in the event builder. In conclusion, we will use  $(\mathbf{t}, \mathbf{n}) = (70$  ns, 5) as our trigger conditions in the experiment, as the optimal trade-off of maintaining a low dark noise event rate with a low energy threshold for detecting  $^{14}\text{C}$  events.

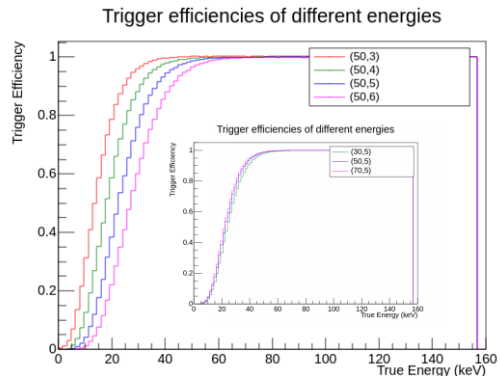


Figure 2: Trigger Efficiencies versus true energies. Different curves represent different pairs of trigger window times and multiplicities:  $(\mathbf{t}$  (ns),  $\mathbf{n}$ ). The simulation was done with flat energy of electrons and then scaled with  $^{14}\text{C}$   $\beta$ -decay energy spectrum shape.

# Borexino Sensitivity Studies towards Detection of Solar Neutrinos from the CNO Fusion Cycle



Ömer Penek<sup>1,2</sup>

on behalf of the Borexino collaboration

Poster Abstract – ID 235



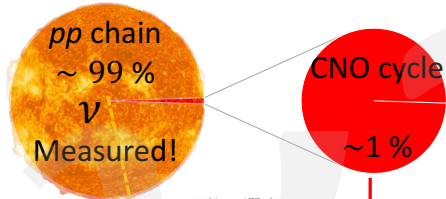
## Motivation ⇔ CNO Cycle Solar Neutrinos

### The Sun ⇔ Nuclear Fusion Processes

Solar Core ⇔ Neutrino Production

*pp* chain and CNO cycle solar  $\nu$ s

Energy Production Mechanisms = *pp* + CNO



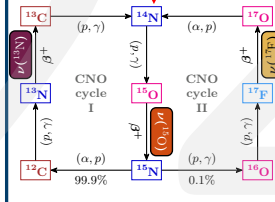
CNO ⇔ Why?

### Proof of new Fusion Process

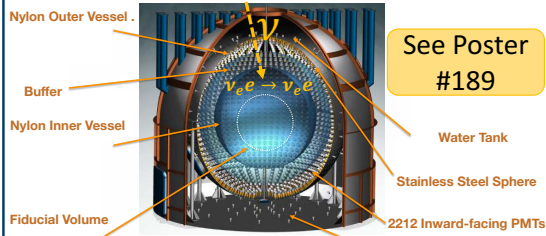
Main Energy Production Mechanism in Heavier Stars

Solar Metallicity Problem (High (HZ) or Low (LZ)?)

Standard Solar Model (SSM)



### BOREXINO Detector (@ LNGS, Italy)



See Poster #189

### Additional Properties

High Light Yield = 551±1 p.e. / MeV

High Radiopurity (<sup>238</sup>U + <sup>232</sup>Th) < 10<sup>-18</sup> g/g

The Borexino detector, located at the Laboratori Nazionali del Gran Sasso in Italy, is a liquid scintillator detector with a primary goal to measure solar neutrinos. The *pp* fusion chain has been measured in Borexino with an outstanding precision through the detection of *pp*, *pep*, <sup>7</sup>Be, and <sup>8</sup>B neutrinos. It is well motivated by standard solar models that around 1 per cent of the solar energy is fueled by the so-called Carbon-Nitrogen-Oxygen (CNO) cycle. A direct measurement of the CNO cycle is difficult due to the low rate and the high spectral correlation with the background isotope <sup>210</sup>Bi and *pep* neutrinos. The sensitivity to CNO neutrinos was evaluated through a likelihood-ratio test, based on thousands of pseudo-experiments analyzed with a counting analysis as well as a spectral fit. This poster presents the resulting discovery potential of Borexino towards the CNO cycle in the Sun.

## Sensitivity Studies ⇔ Toy Monte Carlo ⇔ Methodology

**Borexino Data** See Poster #238

Threefold Coincidence (TFC)

$$\beta^+ \text{-decay of } ^{11}\text{C} + \beta^- \text{'s}$$

$$\rightarrow \beta^- / \beta^+ \text{ Pulse Shape}$$

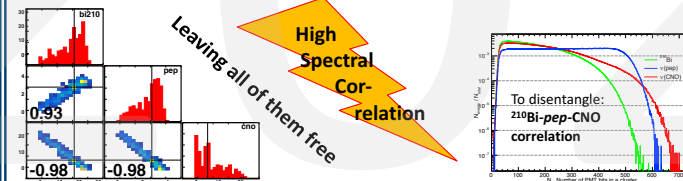
$$1 \mu + ^{12}\text{C} \rightarrow 2 \mu + ^{11}\text{C} + \mu$$

$$29.4 \text{ min } ^{11}\text{C} \rightarrow ^{11}\text{B} + e^+ + \nu_e$$

$$236 \mu\text{s} \rightarrow n + p \rightarrow D + \gamma (2.2 \text{ MeV})$$

- Split data in TFC-subtracted and TFC-tagged energy Spectra → Likelihood  $L_{\text{sub}}(\theta) L_{\text{tag}}(\theta)$
- Radial Distribution → Likelihood  $L_{\text{rad}}(\theta)$
- $e^+ / e^-$  Pulse Shape Parameter → Likelihood  $L_{\text{ps}}(\theta)$

### Challenges ⇔ <sup>210</sup>Bi and *pep*



### Analysis of Model Based Pseudo Datasets

See Poster #93

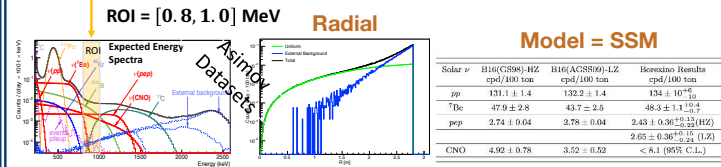
See Poster #238

### Counting

{ Count the number of Events in the region of interest (ROI), dominated by CNO, *pep*, and <sup>210</sup>Bi species }

### Fitting

{ Perform a binned likelihood fit using the relevant PDFs (energy and radial) }

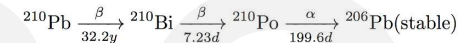


## Results ⇔ Discovery Potential ⇔ Sensitivity

### Constraining <sup>210</sup>Bi and *pep* (through Solar Luminosity)

Global Analysis of all Solar  $\nu$  Experiments

### <sup>210</sup>Bi (through Decay Product <sup>210</sup>Po)



<sup>210</sup>Po- $\alpha$  can be identified event-by-event with almost 100 % efficiency

Realistic Scenario @ Borexino:  
Determine <sup>210</sup>Bi Upper Limit  
 $R_{\text{Bi}}^{\text{UL}} = 11.5 \pm 1.3 \text{ cpd}/100\text{t}$

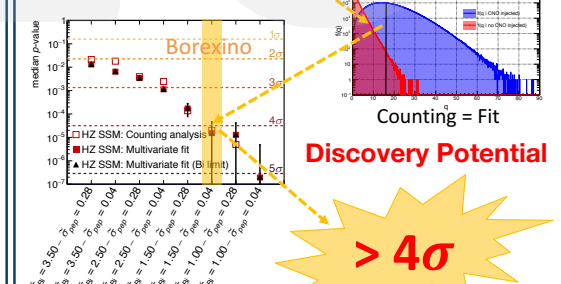
See Posters #212 + #297

### Sensitivity Results

- Fit Pseudo Datasets w/ CNO injected and w/o CNO injected twice: 1. CNO leaving free and 2. CNO fixed to 0
- Define test statistics  $q(\theta) = -2 \times \log \frac{L(\theta=CNO=free)}{L(CNO=0)}$  (log-likelihood-ratio)
- Evaluate *p*-value:  $p = \int_{q_{\text{med}}}^{\infty} f(q|\text{no CNO injected}) dq$  ( $q_{\text{med}}$ : Median of *q*)

### Exposure (Borexino Phase-III)

~ 1000 days × 70 ton



References:  
[1] Sensitivity to neutrinos from the solar CNO cycle in Borexino, arXiv:2005.12829  
[2] M. Agostini et al. (Borexino Collaboration), Comprehensive measurement of *pp*-chain solar neutrinos, Nature, 562, 505-510 (2018)  
[3] M. Agostini et al. (Borexino Collaboration), Simultaneous precision spectroscopy of *pp*, <sup>7</sup>Be, and *pep* solar neutrinos with Borexino Phase-II, Phys. Rev. D 100, 082004 (2019)



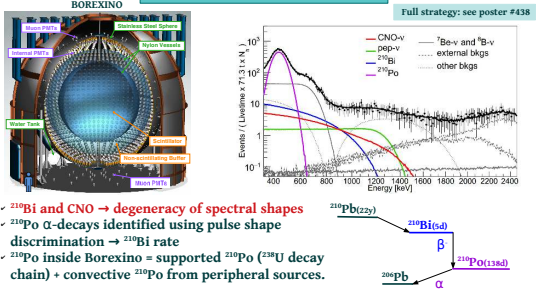
Member of the Helmholtz Association

# Extraction of $^{210}\text{Bi}$ via $^{210}\text{Po}$ for CNO neutrino detection with Borexino

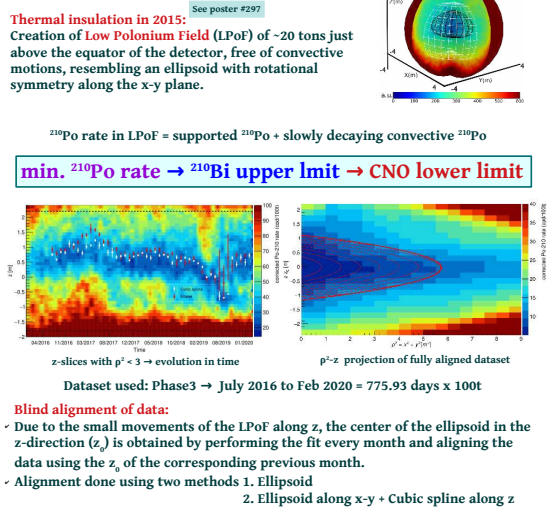
Davide Basilico<sup>1</sup>, Xuefeng Ding<sup>2</sup>, Alexandre Göttel<sup>3,4</sup>, **Sindhujha Kumaran<sup>3,4</sup>**  
on behalf of the Borexino collaboration

# $^{210}\text{Po}$ homogeneity in Borexino gives a $^{210}\text{Bi}$ upper limit for CNO neutrino detection

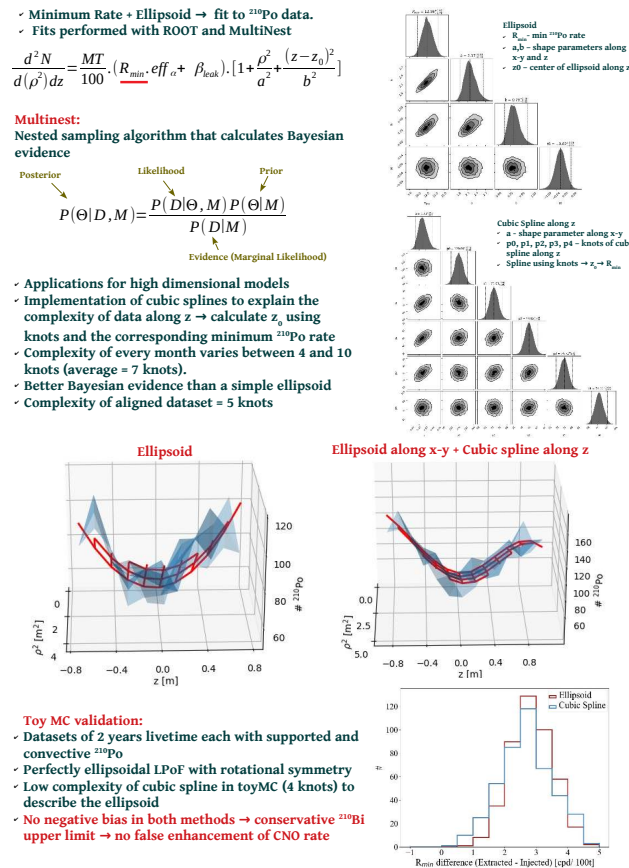
## MOTIVATION



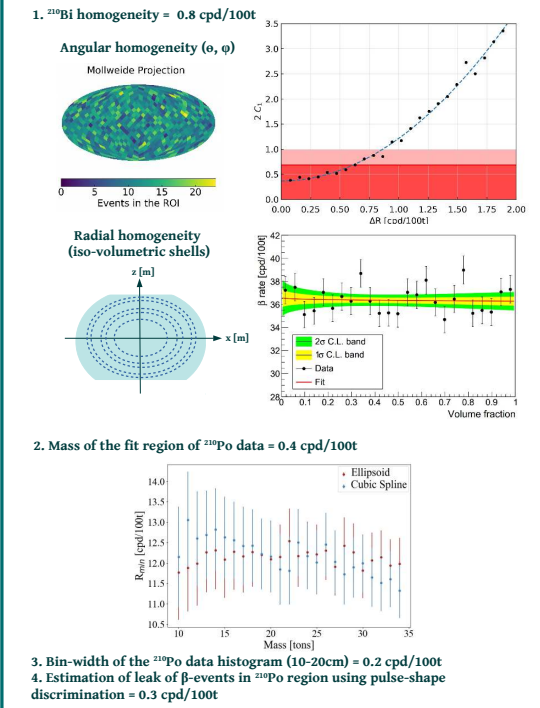
## STRATEGY



## METHODS



## SYSTEMATIC SOURCES



## CONCLUSION

The final  $^{210}\text{Bi}$  upper limit used in the spectral fit for the CNO detection with Borexino is  
See poster #238  **$11.5 \pm 0.8$  (stat.)  $\pm 1.0$  (syst.) cpd/100t**



# Spectral fit of Borexino Phase-III data for the detection of CNO solar neutrinos

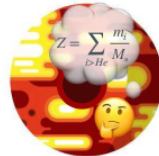
Zara Bagdasarian<sup>1,2</sup>, Davide Basilico<sup>3</sup>, Giulio Settanta<sup>3</sup> for the Borexino collaboration  
<sup>1</sup>University of California Berkeley, <sup>2</sup>Forschungszentrum Jülich, <sup>3</sup>Università degli Studi di Milano and INFN



## Why CNO solar neutrinos?

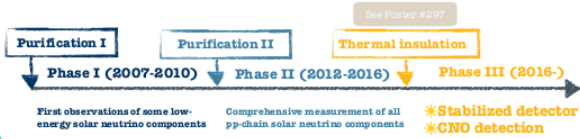
- \* **Proof of principle** of star energy production via carbon - nitrogen - oxygen (CNO) cycle
- \* Important for astrophysics studies of the Sun and heavier stars where the process is expected to be dominant
- \* Sensitive to **Sun core metallicity (Z) problem**: almost 30% difference in predictions from high (HZ) vs low (LZ) Standard Solar Models [1]
- \* Two-fold dependence on Z: Indirectly through core temperature and opacity (as for the pp-chain solar neutrinos) + directly dependent on the amount of carbon and nitrogen.

Solar $\nu$	Expected Flux (HZ)	Expected Flux (LZ)	Difference (HZ LZ)/HZ
pp [ $10^{10} \text{cm}^{-2} \text{s}^{-1}$ ]	5.98 (1±0.006)	6.03 (1±0.005)	-0.8%
pep [ $10^9 \text{cm}^{-2} \text{s}^{-1}$ ]	1.44 (1±0.01)	1.46 (1±0.009)	-1.4%
<sup>7</sup> Be [ $10^9 \text{cm}^{-2} \text{s}^{-1}$ ]	4.93 (1±0.06)	4.50 (1±0.08)	8.7%
<sup>9</sup> B [ $10^9 \text{cm}^{-2} \text{s}^{-1}$ ]	5.46 (1±0.12)	4.50 (1±0.12)	17.6%
<b>CNO [<math>10^9 \text{cm}^{-2} \text{s}^{-1}</math>]</b>	4.88 (1±0.11)	5.51 (1±0.11)	<b>28.1%</b>



## Borexino experiment

- \* **Laboratori Nazionali del Gran Sasso (LNGS) location**:  $10^6$  fold reduction of the cosmogenic background
- \* **Purity**: the most radiopure liquid scintillator
  - \* Low-energy threshold
  - \* High light yield
  - \* Good energy and position resolution

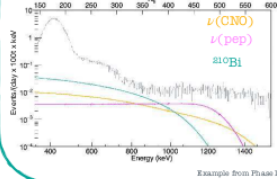


## Signals and Backgrounds

**Detection channel**: neutrino electron elastic scattering  
**Internal backgrounds**:  
 After purifications: <sup>232</sup>Th and <sup>235</sup>U negligible ( $\sim 10^{-19}$  g/g), <sup>85</sup>Kr reduced by factor  $\sim 4.6$ ; <sup>210</sup>Bi reduced by  $\sim 2.3$ , <sup>210</sup>Po - the only  $\alpha$ -decay background, key to its parent, <sup>210</sup>Bi, constraint

**Cosmogenic background**  
 Calculate for each event the likelihood to be <sup>12</sup>C through the three fold coincidence:  
 $\mu + ^{12}\text{C} \rightarrow \mu + ^{11}\text{C} + n$   
 $n + p \rightarrow D + \gamma(2.2 \text{ MeV})$  (250  $\mu\text{s}$ )  
 $^{11}\text{C} \rightarrow ^{11}\text{B} + e^+ + \nu_e$  ( $\sim 30$  min)

**External backgrounds**  
 $\gamma$ s from <sup>208</sup>Tl, <sup>214</sup>Pb, <sup>40</sup>K - efficient reduction by fiducial volume selection + radial dependence



**Solar neutrinos**  
 Yesterday's signal = today's background:  
 pp-chain neutrinos:  $\nu(\text{pp})$ ,  $\nu(^7\text{Be})$ , and  $\nu(\text{pep})$

- Challenges of CNO neutrinos detection**
- \* Low rate of  $\nu(\text{CNO})$
  - \* Shape similar to <sup>210</sup>Bi and  $\nu(\text{pep})$
  - \* Strong correlations  $\rightarrow$  need independent constraints:
    - \* <sup>210</sup>Bi link with <sup>210</sup>Po
    - \*  $\nu(\text{pep})$ : solar luminosity constraint

## Data Selection and Creation of PDFs

\* **Dataset**: July 2016 - February 2020  
 \* **Exposure**: 1071,96 days x 71.3 tons

Data selection main steps:

- All data
- muon and muon daughter cuts: 300 ms after crossing muons
- Fiducial volume (FV) cut:  $R < 8.8 \text{ m}$ ;  $-1.8 \text{ m} < z < 8.2 \text{ m}$
- Three fold coincidence tag (<sup>12</sup>C veto)  $\rightarrow$  <sup>11</sup>C depleted energy spectrum

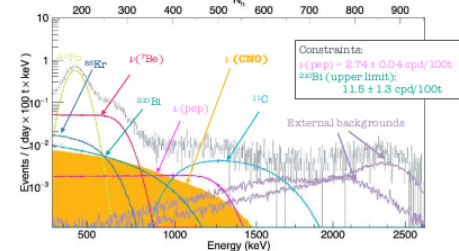
Creation of Probability Density Functions (PDFs):

Generating all species + uniform electrons (flat in energy) in the full Borexino Monte Carlo  
 Applying cuts on uniform electron sample  $\rightarrow$  PDFs for uniform (MC) and external backgrounds radial distributions  
 Applying cuts on all components  $\rightarrow$  PDFs for all neutrinos and backgrounds energy spectra  
 Normalised with the fraction of events passing the cuts to the number of events generated in FV  
 \* All set for the spectral fit!

## Spectral Fit of Phase-III data

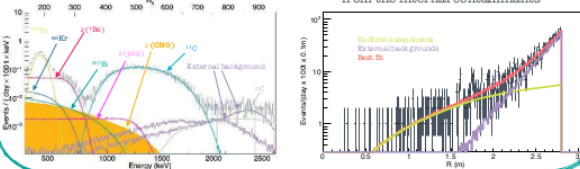
A multivariate fit with the likelihood  $\mathcal{L}_{MV}(\theta) = \mathcal{L}_{\text{sig}}(\theta) \cdot \mathcal{L}_{\text{em}}(\theta) \cdot \mathcal{L}_{\text{rad}}(\theta)$

\* **<sup>11</sup>C depleted energy spectrum**: 63.6% of exposure with 5.5% of <sup>11</sup>C



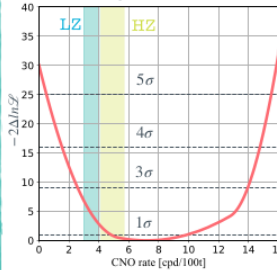
\* **<sup>11</sup>C enriched spectrum**

36.4% of exposure with 94.5% of <sup>11</sup>C



## Conclusions

\* **WITHOUT systematics**



\* **First detection of CNO neutrinos**

- \* Building likelihood profile by performing multivariate spectral fits:
  - \* Best fit value: CNO = 7.2 cpd/100t
  - \* Significance without systematics: 5.48  $\sigma$
  - \* Significance with systematics: see the talk and [2]
- \* Systematics include: light yield, non-uniformity, non-linearity of detector response, <sup>210</sup>Bi shape, <sup>11</sup>C peak position, event selection criteria
- \* Counting analysis - compatible results
- \* Discrimination between HZ and LZ not yet possible

## References

- [1] A New Generation of Standard Solar Models - *Astrophys. J.* 835, 2, 202 (2017)
- [2] new Borexino arXiv submission
- [3] Sensitivity to neutrinos from the solar CNO cycle in Borexino. arXiv:2005.12829
- [4] Comprehensive measurement of pp-chain solar neutrinos *Nature* 562, p 496
- [5] Simultaneous precision spectroscopy of pp, Be7, and pep solar neutrinos with Borexino PhaseII. *Review D 100 p. 08200*
- [6] The Monte Carlo simulation of the Borexino detector *Astroparticle Physics* 97, p136



# Prospects for Proton Decay Searches in JUNO

Yuhang Guo \*, Livia Ludhova, Wanlei Guo, Qingmin Zhang (On Behalf of JUNO Collaboration)

\*guoyuhang@stu.xjtu.edu.cn

## 1. Introduction

Strength vs Energy plot showing EM, Weak, and Strong forces. JUNO detector components: Calibration house, Outer water tank, Steel support structure, Water buffer, Acrylic sphere, Liquid scintillator.

- Proton Decay (PD) is an apparent prediction of Grand Unification Theories (GUTs). The baryon number violation is one of three basic ingredients for an explanation to the asymmetry of Matter and Anti-matter in Universe.
- So many predicted decay modes, among which  $p \rightarrow \nu K^+$  has large branching ratio in Super Symmetry (SUSY) GUTs.
- Many experiments have contributed on this mode to explore new physics, including Super-K and KamLAND.
- The Jiangmen Underground Neutrino Observatory (JUNO), which will be constructed at Jiangmen in South China. It is a 20 kton Liquid Scintillator (LS) detector equipped with ~ 17600 20 inch photomultiplier tubes (PMTs) and ~25000 3 inch PMT.
- The energy resolution is expected to achieve  $3\%/\sqrt{E}$  (MeV), which is very beneficial to low energy delay signal discrimination.

## 2. Simulation

A MC study is undergoing to estimate JUNO's sensitivity to p2vK. The tool is SNIPER, a Geant4 based MC software developed by JUNO collaboration.

- The generator is produced by GENIE, in which the binding effect, the Fermi motion, the N-N correlations of C12 nucleus and the Final State Interaction (FSI) have been included.
- In order to describe correctly the initial proton and K+ FSI, we have modified the codes based on the Spectral Function.

$m_{inv} = m_N - E_B$

The dominant backgrounds are the Atmospheric neutrinos (AN) and Cosmic Muons.

	Kaon Production	Pion Production	Quasi-elastic Scattering	Nucleon Recoil	Total
Neutral current	0.30%	9.74%	---	20.23%	30.27%
Charge current	0.81%	23.75%	45.16%	---	69.73%

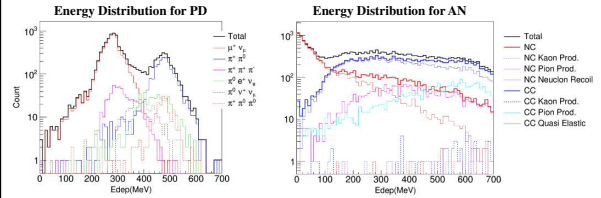
$\nu_\mu + n \rightarrow \mu^- + K^+ + A^0$   
 $\nu_\mu + n \rightarrow \mu^- + K^+ + A^0 + \pi^0$   
 $\nu_\mu + p \rightarrow \mu^- + n^+ + p$   
 $\nu_\mu + p \rightarrow \mu^- + n^+ + \pi^+$   
 $\bar{\nu}_\mu + p \rightarrow n^+ + l^+$   
 $\bar{\nu}_\mu + n \rightarrow p^+ + l^+$   
 $\nu + N \rightarrow N^+ + p + \pi$

## 3. Analysis

- We totally simulated 10 k p2vK and 120 k atmos.  $\nu$  events as candidate sample in SNIPER. The background data volume is equivalent to data volume of 36 years.
- Based on the MC simulation, a set of criteria have been proposed in order to find the rarely seen p2vK from the huge amount of background.
- The criteria can be divided to 3 classes:

## 1. Primary Selection

- 200 MeV <  $E_{vis}$  < 600 MeV
- $R < 17.5m$

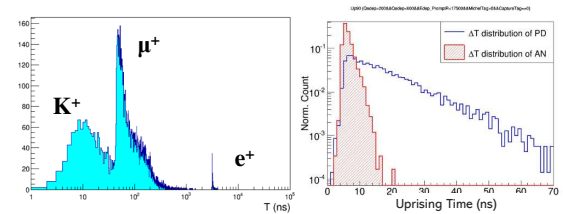


## 2. Delayed Signal Selection

- Michel Electron  $K^\pm \rightarrow \pi^\pm, \mu^\pm \xrightarrow{220ns} e^\pm$
  - Neutron Capture  $n + H \xrightarrow{200\mu s} \gamma + d$
- $\gamma - 2.2 MeV$

- To tag a delayed signal:
1. Correlated AT
  2. Correlated  $E_{dep}$
  3. Correlated Position

## 3. Time Analysis Selection



- Double pulse pile-up in Time spectrum is a feature of p2vK in LS
- Uprising time is defined the time period from 10% Max to 90% Max.
- p2vK is expected to have a larger uprising time.
- Reconstruction of the both signals can also help to distinguish

From BLUE to RED and GREEN, we can know:

1. Tendency to be Double/Single pulse event ( $\chi^2$  of fitting);
2. Correlated AT (K+ lifetime);
3. Correlated Edep (kinetic of K+ and  $\mu^+$ );

The hit time spectrum will be fitted with:

$$\phi_k(x) = \varepsilon_k \cdot f_k(x) + \varepsilon_v \cdot f_v(x - \Delta T_k)$$

$$\phi_b(x) = \varepsilon_b \cdot f_b(x)$$

Energy of each component is:  $E_i = \frac{\varepsilon_i \cdot E_{ref}}{\sum_i \varepsilon_i \cdot E_{ref}} \cdot E_{total}$

The  $\chi^2$  is calculated as:

$$\chi^2 = \sum_i \frac{(\phi(x) - \phi_i(x))^2}{\sigma^2(\phi(x))}$$

$$\chi^2_{ratio} = \frac{\chi^2_A}{\chi^2_B}$$

$\chi^2$  ratio of PD is required to be >3 for a much stricter selection.

The reconstructed correlated time difference  $\Delta T$  and energy deposition of sub pulses ( $E_1$  and  $E_2$ ) are compared for further selection.

## 4. Conclusion

- With 36 years data volume, the p2vK detection efficiency is estimated as 32.48% with 3 Atmos.  $\nu$  remained in 36 years.
- This is a preliminary result and expecting further detailed study and improvement.



40<sup>th</sup> International Conference on High Energy Physics, Jul. 28 - Aug. 6, 2020, Online



PRESENTER:  
Alexandre Göttel  
for the JUNO collaboration

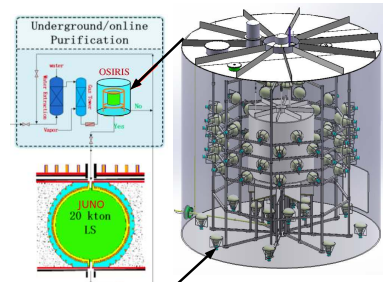
### Motivation

JUNO's requirements on **LS contamination**:  
-  $10^{-15}$  for JUNO reactor neutrinos (IBD)  
-  $10^{-17}$  to  $10^{-16}$  for JUNO solar neutrinos

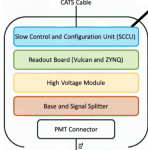
Provide LS radioactivity data during **commissioning of purification systems**

### Detector

Radioactivity levels are too low for "standard" detectors  
→ **20 tons of LS** surrounded by **64 iPMTs**.  
Enclosed in a 9\*9 meter cylinder of **ultra-pure water**.  
LS **flows through** OSIRIS in batches.



### iPMTs



"Intelligent PMT"  
**Digitization in PMT base**  
→ Same cable for power & readout  
→ **High signal quality**  
→ Trigger-less readout scheme

OSIRIS is equipped with 64 iPMTs + 12 veto iPMTs

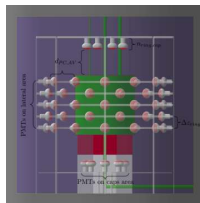
### Simulation

Standalone C++ **software** framework based on **Geant4** (10.02.p03). Full detector simulation with all relevant geometry and physical processes.

Deployed via git & cmake  
→ **Fast simulation**  
→ Parallel development

**Optical photon** simulation  
→ In line with JUNO  
→ Quenching  
→ Cherenkov light  
→ Wavelength dependent

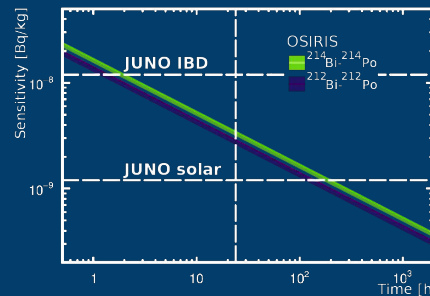
**Biasing** external gammas



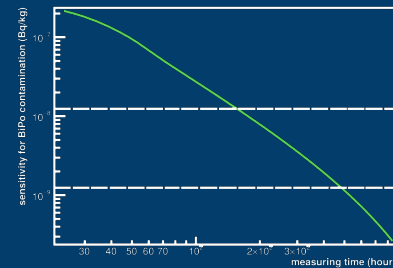
# OSIRIS - A 20 ton liquid scintillator detector as a radioactivity monitor for JUNO

## Results

On a pure LS sample:



Preliminary additional radon contamination estimation:



Assuming 100 counts/day of radon on day one:  
**Reactor requirements met in < 1 week**  
**Solar sensitivity region reached in ~ 20 days**  
**Additional limits on background for JUNO**

### Calibration

#### Laser calibration

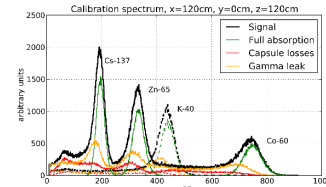
An external laser will send ps pulses with a wavelength of 420 nm. 20 diffusors, controlled with fiber switches, can distribute the light over all PMTs.

Charge  
s.p.e.  
Timing  
Energy

What is being calibrated?

#### Source calibration

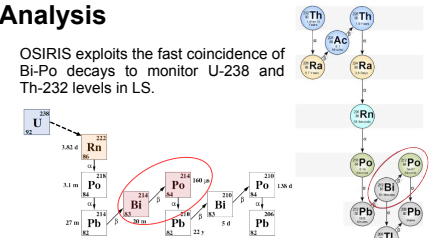
Two capsules containing radioactive isotopes will be lowered into the LS volume. They will be used to calibrate the energy scale and monitor long-term changes in the detector response.



An additional capsule will contain a LED for additional timing calibration.

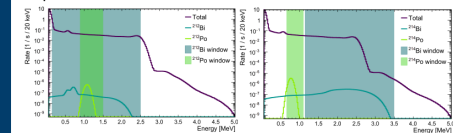
### Analysis

OSIRIS exploits the fast coincidence of Bi-Po decays to monitor U-238 and Th-232 levels in LS.



The analysis is very sensitive to radon contamination in the liquid scintillator, as radon events are indistinguishable from Uranium and Thorium events. After the low-level data analyses and the position/energy reconstructions are performed, a series of cuts are applied.

One obtains the following energy spectra (here from simulations). The signal events are obtained through time-coincidences from events in the energy windows in the plots below.



# Atmospheric Neutrino Physics in JUNO

Giulio Settanta<sup>1</sup>, on behalf of the JUNO Collaboration.

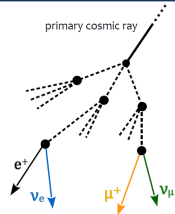
<sup>1</sup>Forschungszentrum Jülich GmbH, Nuclear Physics Institute IKP-2



98

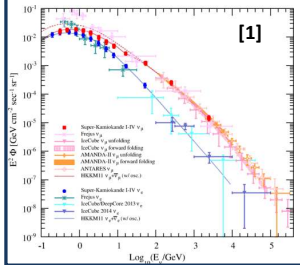
## 1. Atmospheric neutrinos

Produced in extensive air showers, initiated by primary cosmic rays which hit the atmosphere. Almost entirely composed of  $\nu_e$  and  $\nu_\mu$ .



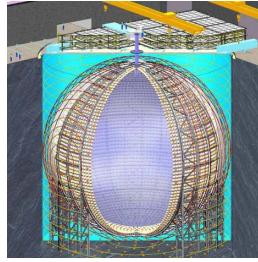
Main sources:  
 $\nu_\mu$  :  $\pi$  and K decays  
 $\nu_e$  : subsequent  $\mu$  decays  
 $\nu_\mu/\nu_e \sim 2$ , decreases as the  $\mu$  energy gets larger.  
 Flux from  $\pi \rightarrow \mu \rightarrow \nu$  :  $\frac{dN_\nu}{dE_\nu}$   

$$\propto \frac{N_0(E_\nu)}{1 - Z_{NN}} \left\{ \frac{A_{\pi\nu}}{1 + B_{\pi\nu} \cos\theta E_\nu/\epsilon_\pi} + 0,635 \frac{A_{K\nu}}{1 + B_{K\nu} \cos\theta E_\nu/\epsilon_K} \right\}$$
 [2]

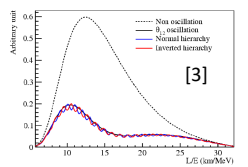


## 2. JUNO detector

JUNO main goal: determine **neutrino Mass Hierarchy (MH)** from reactor  $\bar{\nu}$  spectrum analysis. End of construction: **2021**



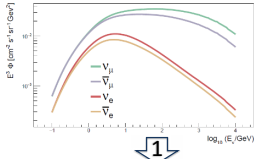
- Central Detector (CD): 20 kt liquid scintillator  
35,4 m diameter acrylic sphere
- Double PMT system  
18.000 x 20" PMTs  
25.000 x 3" PMTs
- Outer water pool (WP)  
Cherenkov veto, 2.400 x 20" PMTs
- Top Tracker  
plastic scintillator strips



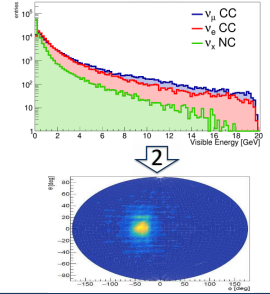
## 3. MC simulation

**Step 1:** Neutrino interaction generation in the detector:

- Flux model: HKKM14 [4]
- Max energy: 20 GeV
- Total events: ~400y  $\nu_e$  +  $\nu_\mu$  (and antineutrinos)
- Software: GENIE  
Neutrino Monte Carlo Generator [5]



**Step 2:** Propagation of secondary particles by a GEANT4 – based simulation inside JUNO, up to the collected charge on PMTs [6]

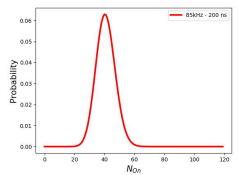


## 4. Atmospheric $\mu$ rejection

- Atm.  $\mu$  can mimic the atm.  $\nu$  topology
- High amount of light both in WP and in CD.  
→ atm.  $\mu$  MC simulation with detector geometry to test impact on the analysis

In WP the dark noise has a relevant impact → dark hits in WP simulated with statistical argument:

$$P(m) = C_N^m (f\tau)^m (1 - f\tau)^{N-m}$$



Selection cuts:  
 • NHITS in WP < 50  
 • NPE20" in CD > 10<sup>5</sup>  
 90% CL atm.  $\mu$  rejection efficiency:  
 $R_\mu < 2.3 \times 10^{-5}$

PDF of fired WP PMTs, assuming single rate  $f = 85$  kHz and a time window  $\tau = 200$  ns

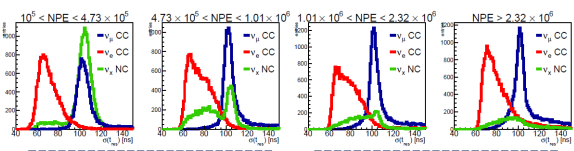
## 5. $\nu_e - \nu_\mu$ discrimination

A time residual variable is defined for each hit on the 3" PMT system [7]

$$t_{res}^i = t_{hit}^i - \left( \frac{R_V^i \cdot n}{c} \right)$$

**Fiducial cuts:**  
 $R_{VERTEX} < 16$  m + NHITS (WP) < 50 (see box 4).

The  $t_{res}$  RMS ( $\sigma(t_{res})$ ) is strongly flavor – dependent:



**$\nu_e$  selection:**  $\sigma(t_{res}) < 75$  ns  
 +  $5.0 < \log(NPE_{20"}) < 7.2$   
**EFF:** 25% **CONT:** 5%

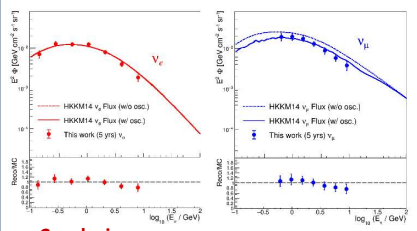
**$\nu_\mu$  selection:**  $\sigma(t_{res}) > 95$  ns  
 +  $5.7 < \log(NPE_{20"}) < 7.2$   
**EFF:** 32% **CONT:** 20%

- 3 classes of events:**
- $\nu_\mu$  CC interaction
  - $\nu_e$  CC interaction
  - NC interaction

## 6. Spectrum reconstruction

Probabilistic unfolding method to extract the energy spectrum from detector observables [8,9]

$$P(E)^{\nu\alpha} = P(E|NPE)^{\nu\alpha} \cdot \frac{P(NPE)^{\nu\alpha}}{\text{Detector observable}} \quad \alpha = e, \mu$$



- ~5 years of MC events as real data
- Uncertainties contributions:
  - statistics
  - unfolding procedure
  - selection process
  - flavor oscillations
  - cross sections

**Conclusions:**

- JUNO has the potential to explore an interesting region of the atmospheric neutrino spectrum.
- Competitive measurement accessible in the first years of data – taking!

## References

[1] Phys. Rev. D 94, 052001 (2016)  
 [2] T. Gaisser, *Cosmic Rays and Particle Physics* (1990)  
 [3] J. Phys. G 43 030401 (2016)  
 [4] Phys. Rev. D 92, 023004 (2015)  
 [5] Nucl. Instrum. Meth. A614 87-104 (2010)  
 [6] J. Phys. Conf. Ser. 664 072053 (2015)  
 [7] EPJ Web Conf. 209 01011 (2019)  
 [8] Nucl. Instrum. Meth. A 362 (1995) 487-498  
 [9] arXiv:1010.0632

## Model-Related Applications

I. Bekman, J. Hetzel

Successful operation of a particle accelerator requires accompanying model calculations. The model helps in understanding the machine and predicts the impact of a change in the settings. For COSY the accelerator simulation software MAD is used to model the accelerator. Recently the official model was updated to use MAD-X[1] instead of the former version MAD-8. To back that up an automated generation of the lattice from our component database has been implemented. Additionally the model was integrated into our EPICS infrastructure [2] and further applications using the modeled parameters have been implemented. This contribution gives an overview over all model-related applications.

### Database

The automatically generated model is derived from the COSY Component Database which was already in 2016 by G. Farren under the supervision of R. Tölle. It is an extensive MySQL database containing not only the elements within the ring and its beam lines but as well their connection to e.g. power supplies. Thus the information which magnets are grouped to a so-called family is already contained in the database. Additionally positions of elements as well as their misalignments are stored in the database.

In 2020 we extended the database by the calibration data of all elements which was formerly stored in an additional database. This enables us to directly connect the calibration data to the corresponding elements. In addition we modified the database to reflect recent changes at COSY. As another new feature the database is monitored by the CI/CD functionality of gitlab and regular backups are created.

The original development already included a web interface to display, insert, and modify elements[3]. It also contains an interactive graphical overview of COSY. The interface was updated such that the mentioned modifications to the database are integrated as well.

### MAD-X Generator

To generate the necessary input files for MAD-X from the database the MAD-X generator[4] is used. It consists of two independent C++ programs to create the necessary files: The static generator and the dynamic generator.

The **Static generator** is used to generate the lattice files, i.e. what elements exist and where they

are located in the ring. To create the files the generator exclusively uses information from the database. This way the model stays up-to-date as long as the database is updated. The generation can be issued by a user, but usually this step is not necessary as the lattice files are as well created each time a change in the database is recognized by the CI/CD of gitlab. The corresponding files can be downloaded at <https://gitlab.cce.kfa-juelich.de/0ps/cosymodel/db-reader#static-lattice-files>.

The **Dynamic generator** writes all information that contain the current status of cosy, e.g. the momentum of the particle beam or the current strengths of all magnets. Therefore it uses not only data from the database but additionally reads the current status of COSY from Fgen-files. It as well needs some information from the user, such as the selected experiment or the time in the cycle at which the model should be evaluated. Other information e.g. the strength of elements that are not controlled with Fgen-files can be parametrized as well.

Both programs are console applications, a GUI has been implemented as part of the EPICS integration. To run the generated files in MAD-X additional information needs to be provided by the user, examples can be found online.

As it was necessary to provide information from various sources to the generators three C++-libraries (so-called readers) have been written:

- The **DB-Reader** [5] queries structured information from the database.
- The **Fgen-Reader** [6] evaluates the polynomials within the Fgen files.
- The **Twiss-Reader** [7] reads the output of a MAD-X run, which is stored in so-called twiss-files.

The development follows a test-driven approach, automatic generated source code documentations exist, as well as contribution guides. So contribution to the readers as well as usage beyond the generators is welcome.

### EPICS Integration

Optics (reader) IOC [10] was designed to read text files related to optics - Armadillo-formatted [12] [13] Orbit Response Matrix (ORM) and MAD-8 [14] Twiss - which were originally implemented in Orbit Correction and Steerer software by Cosylab d.d.

The IOC was expanded to deal with more machine optics related tasks:

**MAD-X calculation wrapper** calls the MAD-X Generator described above. It uses parameter PVs set by user as options and after running ‘madx’ binary yields the Twiss files for currently running experiment setup.

Generation is run periodically such that changes of COSY configuration are reflected in the model quickly.

**Twiss parser module** uses the Twiss-reader library described above and distributes the contained optics quantities to respective PVs, calculating several auxiliary ones. It is possible to process any provided Twiss file, per default the generated above is used.

**Closed orbit bumps calculation** is implemented with 3 and 4 steerers using standard formula and derivatives [15]. Offset and angle independently for 4-bump and offset only for 3-bump at a target element or marker in the ring can be specified. The DB-Reader module is used to retrieve the calibration constants to convert to magnet currents. The resulting bump can be used again in the model calculation, and also directly applied to corresponding steerers.

Based on twiss quantities available online an up-to-date **calculated ORM** [16] can be directly used for the Orbit Correction. The Armadillo-formatted file is generated as well as a PV. Calibration is used as above as well.

### Further Applications

The infrastructure that was created to generate the model and transfer it to EPICS can be further exploited to implement programs that rely on the model. In the following three further applications are presented.

As an alternative approach to calculating and measuring the ORM can also be simulated using the model. This approach is followed by the **ORM Simulator**[8].

To calculate the necessary COSY setting to reach a targeted tune based on the current settings, the **Tune Calculator**[9] can be used. It is currently revised based on experiences from the last tests.

As every model the COSY model can be subject of improvements. A possible approach to achieve these improvements is to use artificial intelligence (AI) methods. For the project COSY Machine-Model Optimization (**COSYMMopt**) an application to the Helmholtz AI Consulting programme[11] has been submitted to optimize the agreement between measured and calculated ORMs.

### References

- [1] MADX, CERN Accelerator Beam Physics Group. Methodical Accelerator Design (MAD). <http://mad.home.cern.ch/mad>. online.
- [2] EPICS, Experimental Physics and Industrial Control System. <http://www.aps.anl.gov/epics>. online.
- [3] IKP, AcceleratorDB. [http://acceleratordb.cce.kfa-juelich.de/accelerator\\_DB/COSY\\_DB/](http://acceleratordb.cce.kfa-juelich.de/accelerator_DB/COSY_DB/). online.
- [4] IKP, MAD-X Generator. <https://gitlab.cce.kfa-juelich.de/0ps/cosymodel/db-reader>. online.
- [5] IKP, Database-Reader. <https://gitlab.cce.kfa-juelich.de/Controls/db/database-reader>. online.
- [6] IKP, Fgen-Reader Cpp. <https://gitlab.cce.kfa-juelich.de/Controls/UTILS/fgen-reader-cpp>. online.
- [7] IKP, TwissReader. <https://gitlab.cce.kfa-juelich.de/AccPhys/simulation/twiss-reader>. online.
- [8] IKP, ORM-Simulator. [https://gitlab.cce.kfa-juelich.de/0ps/orm/orm\\_simulator](https://gitlab.cce.kfa-juelich.de/0ps/orm/orm_simulator). online.
- [9] IKP, Tune Calculator. <https://gitlab.cce.kfa-juelich.de/AccPhys/tune-calculator>. online.
- [10] IKP, Optics IOC. [https://gitlab.cce.kfa-juelich.de/Controls/UTILS/optics\\_reader](https://gitlab.cce.kfa-juelich.de/Controls/UTILS/optics_reader). online.
- [11] Helmholtz Artificial Intelligence Cooperation Unit, Helmholtz AI Consulting. <https://voucher-system.helmholtz.ai>. online.
- [12] Conrad Sanderson and Ryan Curtin. "Armadillo: a template-based C++ library for linear algebra.", Journal of Open Source Software, Vol. 1, pp. 26, 2016.
- [13] Conrad Sanderson and Ryan Curtin. "A User-Friendly Hybrid Sparse Matrix Class in C++.", Lecture Notes in Computer Science (LNCS), Vol. 10931, pp. 422-430, 2018.
- [14] Grote, Hans, and F. Christoph Iselin. "The MAD program (methodical accelerator design): version 8.10; user's reference manual.", No. CERN-SL-90-13-AP-rev-3. CM-P00049316, 1993.
- [15] Wille K. (1996) "Physik der Teilchenbeschleuniger und Synchrotronstrahlungsquellen", Vieweg+Teubner Verlag, Wiesbaden. [https://doi.org/10.1007/978-3-663-11039-2\\_3](https://doi.org/10.1007/978-3-663-11039-2_3)
- [16] M. Simon et al., "COSY Slow Orbit Feedback System", in Proc. 8th Int. Particle Accelerator Conf. (IPAC'17), Copenhagen, Denmark, May 2017, pp. 1802-1805.

# Calibration of COSY Steerers for Advanced Orbit Feedback

I. Bekman, J. Hetzel

**Motivation** Orbit control is an essential part of COSY operation. The Orbit Correction software (OC) was conceived at IKP and integrated in the EPICS control system in collaboration with Cosylab d.d. and has allowed COSY to deliver required orbit parameters to multiple experiments.

The performance of the orbit correction relies on several components, such as ring steerer control, steerer calibration, Beam Position Monitor (BPM) measurements, BPM calibration, Orbit Response Matrix (ORM) modeling and thus COSY optics modeling and ORM measurement. Apart from operative considerations the COSY model and ORMs are used for JEDI studies so that an improvement of the model will be beneficial for various physics analyses overall. IKP-4 is tasked with commissioning of the future High Energy Storage Ring (HESR) at FAIR. Due to similarities in beam physics between HESR and COSY, experiences with model and orbit control will be beneficial for this task.

**Calibration** The objective of the calibration of the steerers is to find a coefficient  $C$  for each steerer that relates its current  $I\%$ , which is given in percentage of its maximal current, to the angle  $\theta$  that the beam is kicked while passing the steerer. As this angle depends on the momentum of the beam the calibration coefficients are normalised by the rigidity  $B\rho$ ,

$$C = \frac{I\%}{\theta \cdot B\rho}. \quad (1)$$

To find this calibration factor two methods have been applied: the 4-bump method and the ORM-method.

**4-Bump Method** One way to calibrate the steerer magnets is to use a calculated closed orbit bump. These bumps consist of three steerers with known calibration factors and a fourth steerer with unknown calibration factor. For the three known steerers the current is set according to the calculated bump, the current of the fourth steerer is varied. To find the calibration factor an observable  $A^*$  is optimized. This observable is a measure for the closure of the bump. Prior to the calibration the lattice was set up such that the dispersion function  $D_T$  in both straight telescope sections of COSY is  $D_T = 0$ . In each telescope section a pair of steerers has been identified with a phase difference of  $\Delta\varphi \approx \pi/2$ . For the measured signal  $u(s)$  outside the four bump and in the dispersion free region it holds:

$$u(s) = A\sqrt{\beta(s)} \cos(\varphi + \phi_0) + u_0(s),$$

where  $u_0(s)$  is the measured orbit without bump and  $\phi_0$  is a fixed phase.  $A$  is the amplitude of the orbit

deviation around COSY which is caused by the non-closure of the bump. If the difference signals  $\Delta u(s) = u(s) - u_0(s)$  of one of the identified steerer pairs<sup>1</sup> are normalized by their beta functions and added quadratically one obtains

$$\begin{aligned} A^* &= \Delta u^2(s_1)/\beta(s_1) + \Delta u^2(s_2)/\beta(s_2) \\ &= (A \cos(\varphi + \phi_0))^2 + (A \sin(\varphi + \phi_0))^2 \\ &\equiv A^2. \end{aligned}$$

Therefore the minimum of  $A^*$  gives the best achiev-

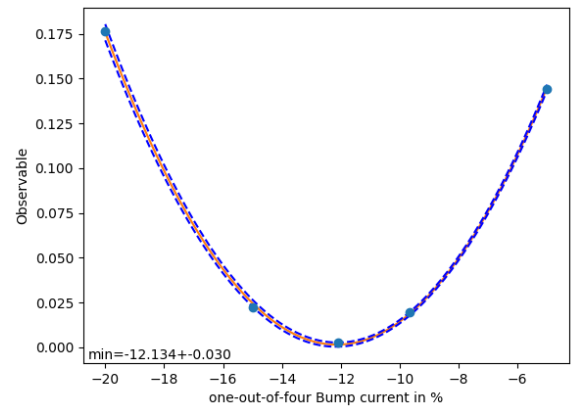


Figure 1: Example of a fit for steerer SVBLW01. The blue dots represent measurements of the observable  $A^*$  in dependency of the steerer current  $I\%$ . The purple line is the fit result, whereas the blue dashed line represents the error band.

able closure of the bump, it can be estimated with a fit to the measured data as Fig. 1 shows. As the rigidity and the necessary angle for a closed bump are known, the calibration factor can be calculated from the corresponding current  $I\%$  and Eq. 1.

**ORM Method** Another way to calibrate the steerers is to extract the coefficients from the measurement of an ORM. The ORM can either relate the change in the orbit at every BPM to the change of the current of a steerer (technical ORM,  $m$ ) or relate the change in the BPMs to the kick angle of a steerer (physical ORM  $M$ ). Usually the lines  $j$  of the matrix represent the BPMs, whereas the columns  $i$  represent the steerers. The physical ORM is given by [1]

$$M_{i,j} = \frac{\sqrt{\beta_i \beta_j}}{2 \sin \nu \pi} \cos(\Delta\varphi_{i,j} - \nu\pi) - \frac{D_i D_j}{\eta L}. \quad (2)$$

<sup>1</sup>The pair which is not within the range of the bump has to be chosen.

Here  $\beta_k$  is the beta-function at the position of element  $k$ ,  $\nu$  is the tune,  $D_k$  is the dispersion at element  $k$ ,  $\eta$  is the phase slip factor,  $L$  is the circumference of COSY, and  $\Delta\varphi_{i,j}$  is the phase difference between the elements  $i$  and  $j$ . As long as the calibration factors are not known, only the technical ORM can be measured as the relation between technical ORM  $m$  and physical ORM  $M$  includes the calibration factor  $C_i$  of steerer  $i$ :

$$m_{i,j} = M_{i,j} \cdot \frac{1}{C_i \cdot B\rho}.$$

The last summand of Eq. 2 depends on the dispersion and hence vanishes in the vertical plane of the accelerator. Thus in this plane the analysis can be simplified by dividing each entry of the ORM by  $\frac{\sqrt{\beta_i\beta_j}}{2\sin\nu\pi}$ , the corresponding values can be extracted from the model. In this case

$$m_{i,j} \cdot \frac{2\sin\nu\pi}{\sqrt{\beta_i\beta_j}} = A_i \cdot \cos(\Delta\varphi_{i,j} - \nu\pi)$$

holds, where the amplitude  $A_i$  is related to the calibration factor  $C_i$  via  $C_i = (A_i B\rho)^{-1}$ . Therefore the

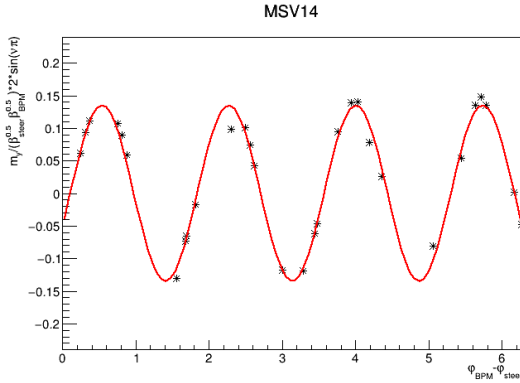


Figure 2: Fit for steerer  $i$ =MSV14, the stars represent measured entries of the ORM  $m_{i,j}$ , the red line shows the fit result.

calibration factors can be extracted from an ORM measurement for all vertical steerers  $i$  by plotting  $m_{i,j} \cdot \frac{2\sin\nu\pi}{\sqrt{\beta_i\beta_j}}$  as a function of the phase difference  $\Delta\varphi_{i,j}$  and fitting the amplitude  $A_i$ . One exemplary fit is shown in Fig. 2.

This method cannot be used to determine the calibration factors of the horizontal steerers, since here the last summand does not vanish. Instead, the amplitude  $A_i$  is found by minimizing the quantity

$$q(A_i) = \sum_j (A_i M_{i,j} - m_{i,j}),$$

again the relation  $C_i = (A_i B\rho)^{-1}$  holds. For the minimization the missing quantities from Eq. 2 are extracted from the model.

**Results and Discussion** The four-bump method was applied to selected steerers only, whereas the ORM method gives the calibration components of all steerers and has been applied at two different energies. The resulting factors are shown in Fig.

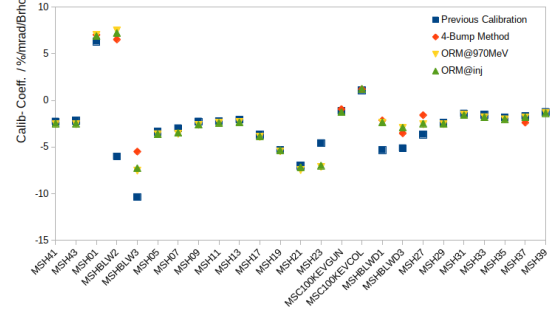


Figure 3: Resulting calibration factors for horizontal steerers. The factors resulting from the different methods are compared to the previously used factors.

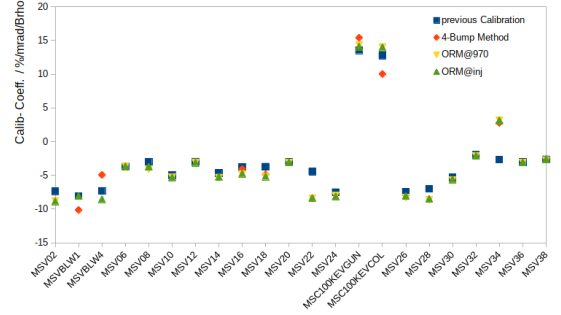


Figure 4: Resulting calibration factors for vertical steerers.

3 and Fig. 4. Some major deviations to the previously used calibration factors have been identified and could be corrected. On the other hand – especially in the vertical plane – deviations in the results of the two calibration methods are observed. These should be subject to further investigations. One possible explanation is that one relies on a set of steerers for the 4-bump method. As the ORM method has shown, even for steerers where we were confident in, that they may have incorrect calibration factors. We plan to redo the measurement with 3-bumps instead of 4-bumps, to reduce the number of steerers where we have to rely on the calibration. In addition only steerers with good agreement in their calibration factor throughout all methods will be used as partners in the three-bump method.

## References

- [1] F. Hinder, B. Lorentz, M. Rosenthal, and M. Simon, IKP Annual Report (2015), "Automation of the orbit response matrix measurement at COSY".

# Longitudinal beam instability due to simultaneous electron and stochastic cooling

A. Halama, V. Kamerdzhev, P. Niedermayer, N. Shurkhno, R. Stassen

## Introduction

An unexpected beam instability was observed during the first joint stochastic and electron cooling beamtime in October 2018 [1]. The longitudinal instability appeared when electron and transverse stochastic cooling systems worked simultaneously. Besides general scientific interest, further studies of the phenomenon could be useful for the future work of HESR, where different regimes of electron and stochastic cooling systems are planned. The detailed study of the phenomenon was scheduled for 2020, but due to technical issues with the electron cooler the study time was reduced to about 1.5 days. The new measurement data allowed to study some features of the instability, but not to understand its nature. The report presents an overview of the instability measurements and proposes possible future studies.

## Features of the instability

Both, electron and stochastic cooling systems function properly when operated independently, gradually shaping the beam without any sudden beam blow-ups. The instability appears in longitudinal phase-space only during simultaneous work of electron and transverse stochastic cooling systems (horizontal, vertical or both). The electron cooling in combination with only *longitudinal* stochastic cooling does not produce the instability, though tests with different stochastic cooling settings (gain and delay) were performed.

The longitudinal Schottky noise was previously mea-

sured with the same pick-up, that was used for the stochastic cooling systems itself. It is known that during simultaneous operation and measurement within the same bandwidth of the stochastic cooling system there could arise measurement errors due to feedback effect. In order to exclude these possible errors, the measurements were now repeated with an old pick-up of the former COSY stochastic cooling system working in the lower frequency range of 1 to 1.8 GHz, non-overlapping with the actual stochastic cooling pickups. Additionally, a Schottky monitor connected to a beam-position monitor was used. All measurements produce similar results.

The instability happens abruptly as can be seen in figure 1. This is not typical neither for electron nor for stochastic cooling. The longitudinal beam changes due to the instability are also very fast in comparison with the typically slow and gradual transient behaviour of the cooling systems. However, it does not lead to beam losses – at least for the measured instability’s intensities. The instantaneous Schottky scan shows that the instability consists of random peaks of different widths and heights (figure 2). The peaks are either located at higher or lower frequencies than the main distribution, but not on both sides at the same time.

It was also found that the instability’s intensity (beam blow-up width) increases with the electronic gain of the stochastic cooling system (see figure 3). The effect is similar for horizontal and vertical cooling.

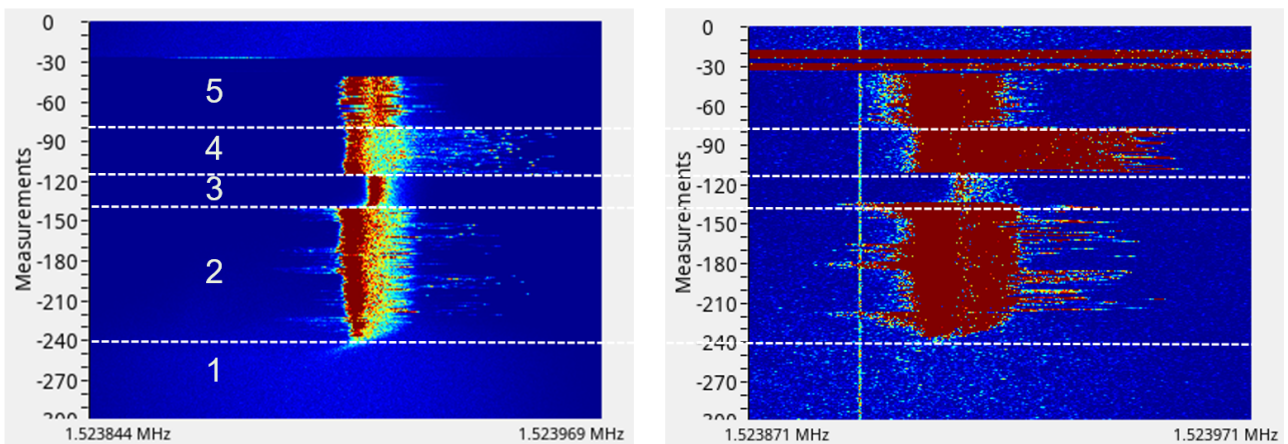


Figure 1: Observed longitudinal beam instability, measured with the HESR pick-ups (left) and a beam-position monitor (right) for different cooling regimes: 1) Vertical and horizontal stochastic cooling, no electron cooling; 2) Electron cooling turned on; 3) Stochastic cooling turned off; 4) Electron cooling and horizontal stochastic cooling; 5) Electron cooling and vertical stochastic cooling

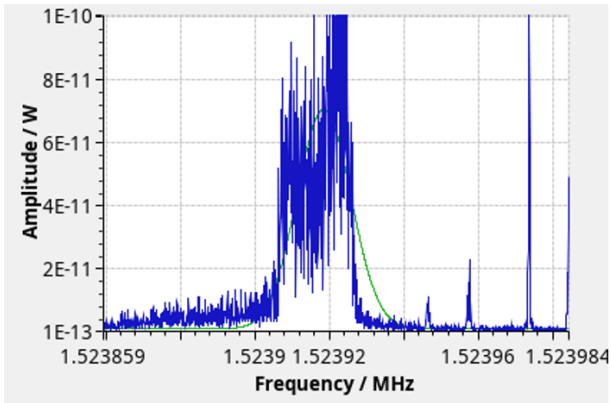


Figure 2: Schottky band with instabilities

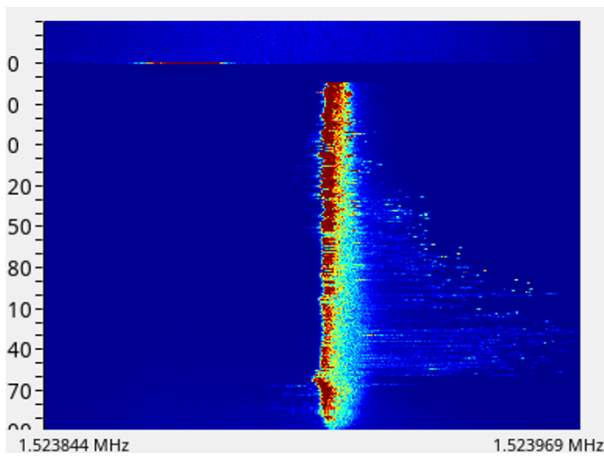


Figure 3: Instability for different gain settings of the horizontal stochastic cooling system. The gain was reducing by 2 dB approximately every 30 s from 0 dB to  $-25$  dB.

### Plans for future studies

The nature of the instability is currently not understood. Therefore, a beamtime is planned for further studies in April 2021. The following steps are proposed for better understanding of the nature of the instability and conditions when and how it appears:

- Vary energy of electron beam, vary electron beam current and alignment to prevent "over-cooling"
- Change tune and orbit to check if the particles' positions have an influence on the instability, especially at the kicker
- Apply noise to the beam to introduce a change in the betatron side-bands
- Change the delay of the stochastic cooling systems to check the influence of de-tuned transverse cooling (or heating) on the instability
- Try to re-adjust the stochastic cooling during electron cooling operation, since the e-cooler

changes beam parameters and the stochastic cooling systems can be de-tuned

- Use a notch-filter in the transverse stochastic cooling system in order to check the influence of a small parasitic longitudinal signal in the transverse loop

### Conclusion

The described effect was observed for the first time in October 2018 at COSY with a unique accelerator set-up, when both electron and stochastic cooling was applied simultaneously. In the recent beam time in 2020, the instability was reproduced independently of the pick-up used for the measurement. The nature of the instability is yet unclear and needs further studies. These will be helpful for refining cooling strategies during future HESR operation and for deeper understanding of beam behaviour when both electron and stochastic cooling are used.

### References

- [1] P.J. Niedermayer *et al.*, "Recent Developments and Experimental Results From Electron Cooling of a 2.4 GeV/c Proton Beam at COSY", in *Proc. COOL'19*, Novosibirsk, Russia, Sep. 2019, pp. 72–76, [doi:10.18429/JACoW-COOL2019-FRX01](https://doi.org/10.18429/JACoW-COOL2019-FRX01)

## Numerical simulation of Sona transitions

C. S. Kannis<sup>a,b</sup>, M. Büscher<sup>c,d</sup>, R. Engels<sup>a</sup>, K. Grigoryev<sup>a</sup>, C. Hanhart<sup>a</sup>  
L. Huxold<sup>d</sup>, A. Lehrach<sup>a,b</sup>, H. Soltner<sup>e</sup>, and V. Verhoeven<sup>a,d</sup>

In 1967 P. G. Sona [1] proposed a method to increase the polarization in polarized metastable hydrogen and deuterium ion sources. For this purpose he designed a device (“Sona transition unit”) that provides a static magnetic field with field direction reversal along the polarization axis. If non-adiabaticity requirements [1] are fulfilled, the transfer of atoms from the hyperfine state  $\alpha_1$  (i.e. electron and proton spins parallel to the external magnetic field/quantization axis) to the state  $\beta_3$  (or  $\beta_4$  for deuterium, i.e. electron and proton spins antiparallel to the quantization axis) is possible.

A Sona transition unit consists of two concentric solenoids [2] with opposed field directions. An additional quadruple-layer magnetic field shielding [3] is constructed, in order to reduce the influence of stray fields that have a disturbing effect on the zero-crossing between the solenoids. The distance between these coils inside the shielding can be adjusted according to the experimental requirements. Figure 1 shows the longitudinal and the radial magnetic flux density components along the axis for a typical setting.

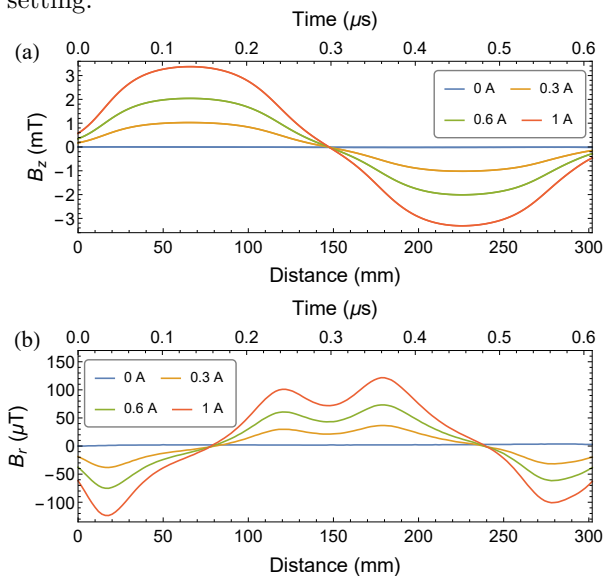


Figure 1: Measured longitudinal (a) and radial (b) magnetic flux density components  $B_z$  and  $B_r$  at a distance  $r = 3$  mm from the beam axis  $z$  for different currents in the coils of the Sona transition unit. The distance between the coils is 60 mm.

Here we report a study of metastable hydrogen, but the following analysis has been expanded to metastable deuterium as well. The atoms are prepared in the  $\alpha_1$  state and move along the  $z$  axis with a constant velocity of 495 km/s ( $E_k = 1.28$  keV). In their rest frame experience a time-dependent magnetic field (see the upper horizontal axis of Fig. 1).

This can therefore be described by a hamiltonian  $H(t) = H_0 + V(t) = A\mathbf{I} \cdot \mathbf{J} - (g_J \mu_B \mathbf{J} + g_I \mu_N \mathbf{I}) \cdot \mathbf{B}(t)$ , where  $A$  is the hyperfine structure constant,  $\mathbf{I}$  and  $\mathbf{J}$  are the nuclear and electronic angular momenta, respectively,  $\mu_B$  and  $\mu_N$  are the Bohr and the nuclear magnetons, respectively, which are multiplied by the corresponding  $g$  factors. We solve the unperturbed Schrödinger equation for  $I = J = 1/2$  and obtain the four eigenvectors that represent a basis of the system. Next we express any quantum state in this basis and solve the perturbed Schrödinger equation, i.e.

$$|\psi(t)\rangle = \sum_{i=1}^4 c_i(t) e^{-iE_i t/\hbar} |i\rangle \quad \text{and} \quad i\hbar \frac{\partial |\psi(t)\rangle}{\partial t} = H(t) |\psi(t)\rangle$$

Figure 2: Relative occupation numbers as function of coil current.

This yields a system of four coupled first order differential equations, of the following form.

$$i\hbar \frac{\partial c_k(t)}{\partial t} = \sum_{j=1}^4 c_j(t) e^{-i(E_j - E_k)t/\hbar} \langle k|V(t)|j\rangle$$

They are solved numerically using Mathematica. The relative occupation numbers as a function of the coil current, assuming that the hydrogen atoms are initially in the  $\alpha_1$  state and undergo the magnetic field structure of Fig. 1, are shown in Fig. 2. The  $\alpha_1$  and  $\alpha_2$  occupation numbers have been measured [4] and agree with the simulations.

## References

- [1] P. G. Sona, *Energia Nucleare* **14** (1967) 295.
  - [2] P. Buske, B. S. Thesis, RWTH Aachen University (2016).
  - [3] Y. Gan, B. S. Thesis, Fachhochschule Aachen (2017).
  - [4] R. Engels et al., arXiv:2010.13690 (2020).
- <sup>a</sup> Institute for Nuclear Physics, FZ Jülich, Germany  
<sup>b</sup> III. Physikalisches Institut B, RWTH Aachen University, Germany  
<sup>c</sup> Peter Grünberg Institut (PGI-6), FZ Jülich, Germany  
<sup>d</sup> Institut für Laser- und Plasmaphysik, HHU Düsseldorf, Germany  
<sup>e</sup> Zentralinstitut für Engineering, Elektronik und Analytik (ZEA), FZ Jülich, Germany

## Status of the ExB Deflector Development

J. Böker<sup>1</sup>, N. Demary, U. Giesen<sup>2</sup>, K. Grigoryev\*, J. Hetzel, C. Käseberg<sup>3</sup>, G. Langenberg, F. Scheiba

A new JEDI prototype ring[1] requires development of unique electromagnetic bending elements. The electric field strength in the order of  $7 \text{ MV m}^{-1}$  has to be achievable at the gap distances of 60 mm between the plates. For testing the electrodes of this size a new experimental area inside the COSY storage ring was organized. An existing ANKE D2 dipole magnet was picked to provide necessary magnetic field. It was already equipped with a 1400 mm large vacuum chamber suitable for the installation of 1080 mm long electrodes. Two Heinzinger ultra precise high voltage power converters will be used to reach 200 kV at each electrode. The mechanical design of the assembly with deflector prototypes (shown in Fig. 1) was made at IKP design buro.

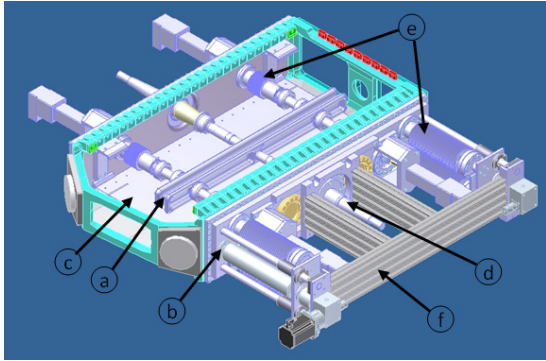


Figure 1: CAD drawing of the electrodes in the vacuum chamber with infrastructure. Labeling of individual parts described in the text.

The setup for the measurements in the vacuum chamber consist of two rogowski-shaped TiN coated aluminum electrodes (a) mounted on the flanges (b) of the vacuum chamber, protected from the discharge by set of 0.5 mm Ti-foils (c). The high-voltage feedthroughs (d), positioning devices (e) and mounting support (f) were designed for testing the electrodes at the gaps between 20 and 120 mm. The flat area of each electrode is 984 mm long and 54 mm high. It should be sufficient to produce a good-field region  $20_{\text{hor}} \times 60_{\text{vert}} \text{ mm}^2$  at the nominal distance between the electrodes.

Production, polishing and TiN coating of the electrodes was performed by external companies. After UHV cleaning all parts were assembled in the dust-free conditions of the flow-box at the COSY building. It allows mounting all vacuum elements together in the clean air without time pressure. The electrodes were fixed on the flanges, unique for each side of the vacuum chamber, using linear actuators with ceramic isolators. The high-voltage feedthroughs were attached to the center of the electrodes.

After individual components assembly, the adjustment campaign was conducted using FARO 3D portable coordinate measurement tool. Due to the different geometry of the vacuum flanges the distance from the flange to the flat area of the electrode has to be different. The inner and outer electrodes were aligned parallel to the flanges and positioned at 337.90 mm and 311.20 mm correspondingly within the measurement accuracy of  $50 \mu\text{m}$ . The mounting position of the electrodes corresponds approximately to the gap distance of 90 mm.

The installation into the vacuum chamber was coupled with some technical issues. Unremovable supporting bars of the upper part of the magnet were on the way of one of the linear drives of the inner flange. To overcome this a special arm to keep the electrode at place during mounting was developed. The linear drive was reattached to the isolator after fixing the flange. The insertion of the outer flange has to be done in parallel with tightening of the Titanium foils. They were few centimeters apart of the electrodes and should not touch it. The final assembly in the vacuum chamber is shown in Fig. 2.

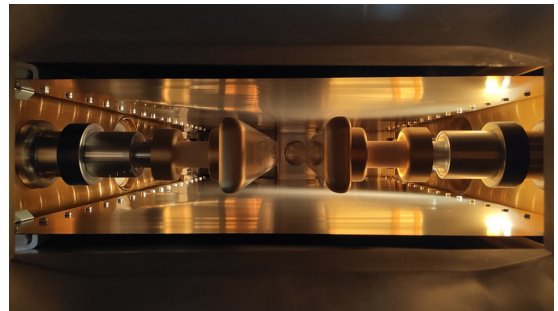


Figure 2: The electrodes inside the vacuum chamber.

The ultra-high vacuum conditions are mandatory for tests. For this, a turbomolecular and two cryopumps wer mounted on the vacuum chamber for initial pumping and an ion getter pump to maintain vibration-free vacuum conditions. After all installations no significant leaks larger than  $10^{-9} \text{ mbar} \cdot \text{l/s}$  were found at the vacuum conditions of  $10^{-7} \text{ mbar}$ . This allows in the near future to implement it in the common safety system and perform electrical tests.

## References

[1] F. Abusaif, et.al., arXiv:1812.08535 (2019).

<sup>1</sup> Currently at Deutsches Zentrum für Luft-und Raumfahrt e.V.

<sup>2</sup> Institut für Engineering und Technologie (ZEA-1)

<sup>3</sup> Currently at I. Physikalisches Institut, RWTH Aachen

## Preparation for Single Bunch Extraction from the Cyclotron JULIC

Nils-Oliver Fröhlich, Ralf Gebel, and Yury Valdau

The Juelich Light Ion Cyclotron (JULIC) is used as injector for the Cooler Synchrotron (COSY) and for irradiations at the two target stations Industriebe- strahlungsplatz (IBP) in the cyclotron bunker and Niederenergiestrahlsplatz (NESP) in the Big Karl ex- perimental hall. As injector for COSY JULIC deliv- ers 20 ms long pulses  $H^-$  or  $D^-$ -ions at a maximum repetition rate of 0.5 Hz. For irradiations pulses with minimum width of  $50 \mu s$  can be generated by an electrostatic chopper in the source beam line (QBL). For time-of-flight-measurements (nToF) during the LOEWE-NP experiment beam pulses with a length of 50 ns and a repetition rate up to 4 MHz were re- quested [1]. During preparations for this experiment a new approach to generate short pulses using the cyclotron buncher system was developed.

A buncher is an rf cavity which is usually used to "match" the unbunched beam delivered by the ion sources to the phase acceptance of the cyclotron RF accelerating voltage. An RF voltage applied to the buncher leads to an energy and velocity modulation of the beam in front of the cyclotron. Those velocity modulation matches a particle distribution in the beam to the phase acceptance of the RF voltage at the first acceleration gap of the cyclotron.

The JULIC buncher system consists of two resonance and one broadband double-gap buncher installed in the QBL in front of the cyclotron. A fundamental harmonic resonance buncher is used for routine operation of the cyclotron in a frequency range of 20-30 MHz. The second resonance buncher is operated at the second harmonic of the accelerating frequency. The broadband buncher is operated with an 100 W broadband amplifier in the frequency range of 100-500 MHz [2]. The buncher system of JULIC allows to increase extracted beam intensity up to a factor of 3 [3].

To generate the pulsing scheme requested by the LOEWE-NP-experiment, one can operate the fun- damental buncher at a frequency  $(n - 1)/n * f_{RF}$  different from the acceleration frequency  $f_{RF}$ . This should match one bunch to the JULIC phase ac- ceptance of  $40^\circ$  [4] and shift subsequent bunches out of it.

A *Mathematica* code was written to simulate the combined operation of the three bunchers. In Fig. 1 a simulation for operating the fundamental buncher with a frequency of  $9/10 * f_{RF} = 26.64$  MHz is shown. After 330 ns every ninth bunch is matched to the phase acceptance of the accelerating voltage. When a bunch is matched to the phase acceptance, the number of ions available for further acceleration is eight times higher than when the bunch is shifted out of phase acceptance. Hence, operation of only

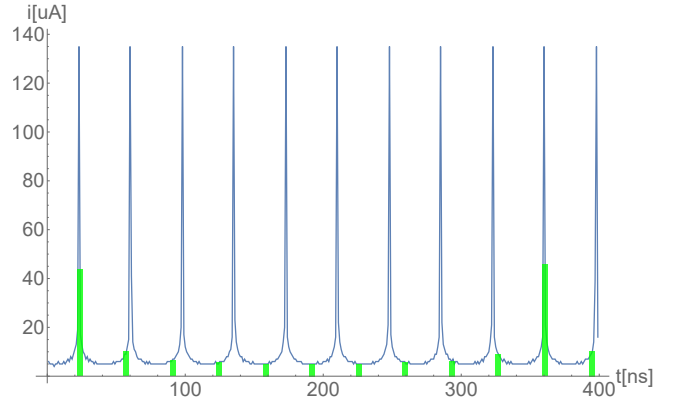


Figure 1: Simulation of a  $10 \mu A$  bunched beam delivered by the ion source arriving at the first accel- erating gap of the cyclotron. The green bars indi- cates the phase acceptance of the cyclotron RF and the estimate average beam current during the phase acceptance. The fundamental resonance buncher is operated with a frequency of  $0.9 * f_{RF}$ .

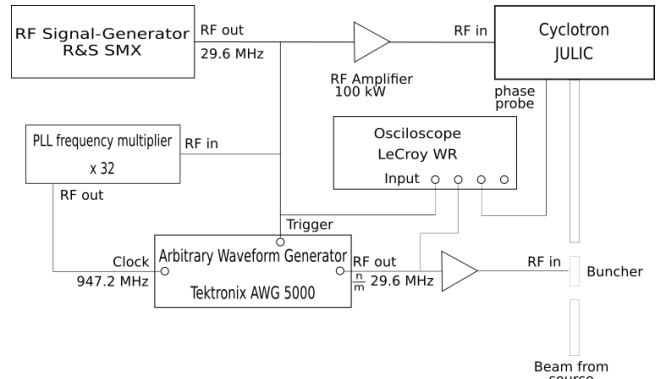


Figure 2: Experimental Setup during tests in Octo- ber 2020

the fundamental buncher at the selected frequency will allow to make every ninth bunch accelerated in the cyclotron factor eight more intense.

The experimental setup is shown in Fig. 2. For this studies the fundamental double-gap buncher was used. The RF signal for the buncher is generated by an Tektronix arbitrary waveform generator (AWG 5000). The AWG is synchronised with the cyclotron RF by an Phase-locked-loop (PLL) frequency mul- tiplier, which generates a clock signal with a thirty- twofold of the cyclotron RF frequency. The phase relation between the cyclotron and buncher RF is ad- justed triggering on the cyclotron RF. Signals from phase probes at different positions in the cyclotron are readout using a digital oscilloscope for diagnostic purposes.

The proposed approach was tested during three days of LOEWE-NP beamtime in October 2020. Desired bunch length and separation was not achieved, due to issues with amplifiers in front of the buncher and difficulties in bunch diagnostics. Further investigation are needed, to demonstrate possibility of single bunch extraction from the cyclotron.

## References

- [1] B. Schmitz, A017.1, 11th CBAC (2020)
- [2] W. Bräutigam et al., Investigation of bunchers for injection into the cyclotron, IKP Annual Report (1997).
- [3] W. Bräutigam et al., Operation of a double-gaped buncher with complex waveforms, IKP Annual Report (1998).
- [4] V.S. Pandit, P. Wucherer, Numerical Calculation of beam Buncher, Internal report (1982).

## Tests with multiplexed proton beam from JULIC

M. Rimmler, F. Dahmen, O. Felden, N.-O. Fröhlich, M. Retzlaff, U. Rucker, Y. Valdau, R. Gebel

The High-Brilliance neutron Source project (HBS) aims at developing a medium-flux accelerator-driven neutron source based on a 70 MeV, 100 mA proton accelerator [1, 2]. The concept intends to optimize the facility such that it provides high-brilliance neutron beams for instruments operating at different time structures. This can be realized by generating an interlaced proton pulse structure, i.e. called multiplexed proton beam, which is unraveled and sent to three different target stations by a multiplexer system [3]. A balance between wavelength bandwidth and resolution of the time-resolved neutron spectrum extracted from the thermal or cold neutron moderator can be obtained by multiplexing short pulse components with high repetition rate and long pulse components with low repetition rate. Parts of the multiplexer system intended for HBS are tested at the JULIC accelerator. In this report, we summarize first tests of a kicker magnet being synchronized to the micropulsing of JULIC which show the generation of a multiplexed proton beam consisting of two different pulse sequences and subsequent spatial separation of the individual pulse components.

The experimental setup for the tests of the kicker magnet synchronized to the proton pulse generation of JULIC is shown in Figure 1. 800 mm downstream the kicker magnet an aluminum collimator with two electrically insulated plates is installed and combined with a tantalum beam cup which is positioned behind the collimator. The cup and the two collimator plates are wired individually to a multi-channel picoammeter such that a destructive current measurement of the proton beam can be carried out at three different horizontal positions. With this setup three potential target stations are mimicked. Between the collimator and the kicker magnet, a movable multi wire proportional chamber (MWPC) is installed at variable distance  $d_{MWPC}$  which allows to monitor the transversal beam position and beam size.

The pulse components for the multiplexed proton beam are chosen to be  $t_{p1} = 5$  ms,  $T_{p1} = 50$  ms for the short pulse components and  $t_{p2} = 15$  ms,  $T_{p2} = 5$  s for the long pulse components with a delay of  $t_d = 5$  ms with respect to the short pulse component. The pulse and period lengths are chosen such that the timing provided by the kicker magnet power supply is maxed out. The kicker magnet is controlled by a pulse generator which in parallel operates the pulsing of the proton beam. The corresponding logics are presented in Figure 2. Here, a multiplexed proton pulsing scheme

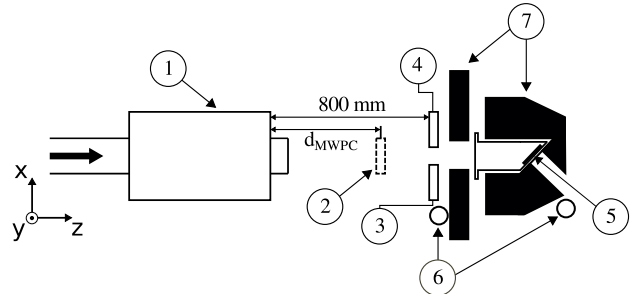


Figure 1: Schematic drawing of the experimental setup for tests of the kicker magnet (1) synchronized to the proton beam pulsing of the JULIC accelerator. The scheme shows the  $xz$ -plane with the proton beam passing from the left side as indicated by the black arrow. The experimental setup comprises a movable multi wire proportional chamber (2), a collimator system with an electrically insulated right and left side (3 + 4), a tantalum target used as beam cup (5),  $^3\text{He}$  detectors (6) and a polyethylene moderator (7).

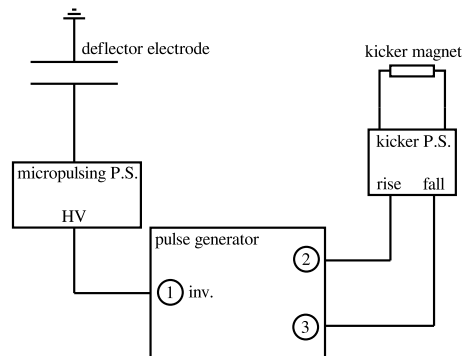


Figure 2: Logics for tests of the kicker magnet synchronized to the micropulsing of the JULIC accelerator. A pulse generator controls the proton beam pulse structure by setting the HV applied from the micropulsing power supply to a deflector electrode in the source beam line of JULIC. The proton pulse structure is dictated by the pulse generator as inverted TTL sequence of the actual pulse structure (1). Simultaneously, the kicker magnet's rise (2) and fall (3) sequences of the magnet current are controlled by the pulse generator.

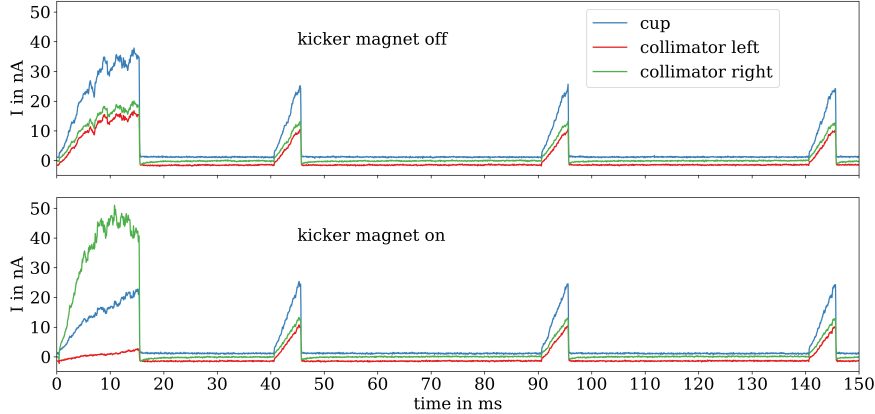


Figure 3: Proton beam current measurement at the beam cup and collimator plates shown in Figure 1 for a multiplexed proton beam with  $t_{p1} = 5$  ms,  $T_{p1} = 50$  ms,  $t_{p2} = 15$  ms,  $T_{p2} = 5$  s and  $t_d = 5$  ms. The measurement is triggered by the long pulse components. With the kicker magnet being switched on, the long pulse components are deflected towards the right collimator plate while the short pulse components pass unperturbed. The measurements are averaged over ten times occurrence of the long 0.2 Hz pulse components, i.e. 50 s.

is generated through the micropulsing of the JULIC accelerator. The pulse scheme is realized through a deflector electrode in the source beam line of JULIC. For this reason, the pulse scheme intended for the proton beam needs to be inverted as HV on at the micropulsing results in beam off. The rising of the kicker magnet current is triggered to deflect the long pulse components and adjusted to take into account the time of flight of protons from the pulse generation to the kicker magnet. The time of flight of protons  $t_{TOF}$  from the deflector electrode in the source beam line to the kicker magnet is dominated by the acceleration inside the cyclotron and approximated with  $t_{TOF} \approx 100$   $\mu$ s.

It can be seen from the beam current measurements at the collimator plates and the beam cup in Figure 3 that the proton beam goes straight through the collimator for all pulse components when the kicker magnet is off as indicated by the left and right collimator signal being almost equal. When switching on the kicker magnet which is synchronized to deflect the long pulse components, these pulse components exhibit a larger beam current signal on the right collimator plate and a smaller signal on the left collimator plate, thus indicating that the long proton pulses are deflected to the right while the short proton pulses pass the kicker magnet unperturbed. Note that the proton pulses experience a linear increase of the beam current on a time scale of  $\approx 10$  ms which is attributed to non-optimized injection into the cyclotron.

In addition to the beam current measurements in Figure 3, an MWPC is used to determine the deflection angle of the long pulse components by measuring

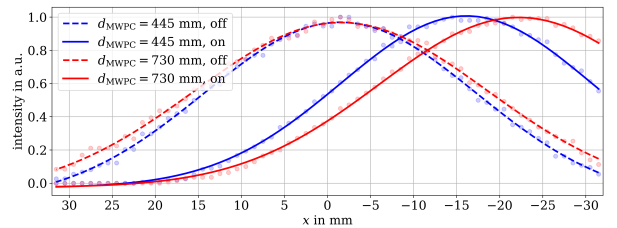


Figure 4: MWPC measurement of the horizontal proton beam profile at  $d_{MWPC} = 445$  mm, 730 mm in Figure 1 triggered by the long pulse component in Figure 3 with the kicker magnet being off and on, i.e. powered with 250 A. A gaussian fit is performed individually for all measurements with kicker magnet being off (dotted line) and on (solid line).

the proton beam position at two different distances  $d_{MWPC} = 445$  mm, 730 mm in Figure 1. The results are given in Figure 4. From the fit results in Figure 4, one obtains the average beam position for the different MWPC positions and kicker settings which allows to derive the deflection angle from the kicker magnet to be

$$\alpha = -21.0(7) \text{ mrad.} \quad (1)$$

The kicker magnet provides a maximum dipole field of 35 mT at 250 A. With an effective length of 610 mm, this yields 21.8 mrad deflection angle for 45 MeV protons, i.e.  $B(\rho) = 0.98$  Tm, which is consistent with the result obtained in Equation 1.

With the synchronization of the kicker magnet to the micropulsing of JULIC being set up, further devel-

opments of the multiplexer system at JULIC intend to implement a newly developed performant kicker magnet power supply which allows to generate multiplexed pulse sequences with higher repetition rate of the deflected pulse components, up to 100 Hz. Furthermore, the setup will be extended by a septum magnet. The kicker magnet is then operated such that the different proton pulse components are sent to different magnetic field regions of the septum magnet.

## References

- [1] U. Rücker et al., The Jülich high-brilliance neutron source project, *The European Physical Journal Plus*, 131 (2016) 19. <https://doi.org/10.1140/epjp/i2016-16019-5>.
- [2] P. Zakalek et al., High-brilliance neutron source project, *J. Phys.: Conf. Ser.*, 1401 (2020) 012010. <https://doi.org/10.1088/1742-6596/1401/1/012010>.
- [3] M. Rimmner et al., Proton Beam Multiplexer Developments for Multi-Target Operation at the High-Brilliance Neutron Source HBS, *EPJ Web Conf.*, 231 (2020) 02002. <https://doi.org/10.1051/epjconf/202023102002>.

# Automatic Position Shift of the Magnet 3MDBE32

D. Büngener, M. Krstic, G. Mirau, D. Wituchnowski (BK GuT)  
 J. Böker, N. Bongers, C. Ehrlich, O. Felden, M. Küven, M. Schmühl, H. Zens (IKP-4)  
 27 November 2020



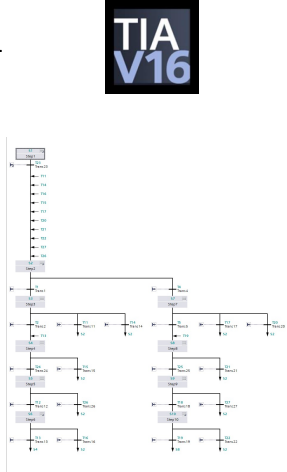
### Magnet 3MDBE32



- Weight: 8.4 t
- Dimensions:
  - Length: 2100mm
  - Width: 900mm
  - Height: 600mm
- Bending angle: 6.9 °

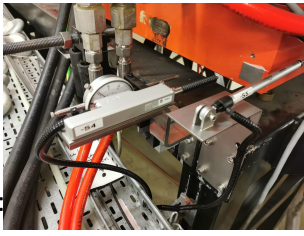
### Software – TIA Portal

- TIA V16
- Calculation with SCL
- Sequence control with Grafcet
- If there is a deviation from the target value, the probe value is evaluated
- Correction value is calculated and passed on to the converter



### Hardware - Keyence

- 0.5 µm resolution
- 50 mm measuring range
- Communication via Profinet
- Measuring principle: differential transformer method

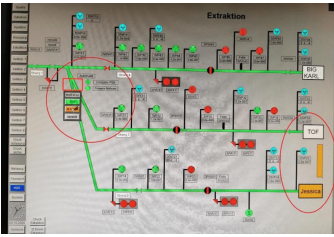


### Hardware – SEW Motor

- Maximum force: 21.6 kN
- 3000 - 6000 min<sup>-1</sup>
- Connection to the PLC via the converter
- SEW converter for the motor

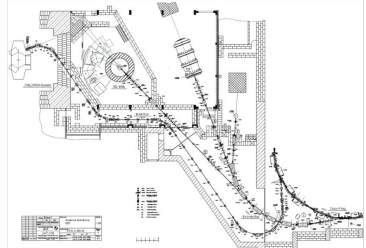


### Visualization @ COSY control room



- The process is triggered by selecting the required position
- The bar on the right illustrates the movement of the magnet
- The current position is shown in yellow and green

### Extraction beamline



### Outlook

The project can be applied to any position of magnets, regardless of their size and weight. Only the servo motor has to be adapted.

## Redetermination of the strong-interaction width in pionic hydrogen

A. Hirtl<sup>1</sup>, D.F. Anagnostopoulos<sup>2</sup>, D.S. Covita<sup>3,4</sup>, H. Fuhrmann<sup>1</sup>, H. Gorke, D. Gotta, A. Gruber<sup>1</sup>, M. Hennebach, P. Indelicato<sup>5</sup>, Th.S. Jensen<sup>3,6</sup>, E.-O. Le Bigot<sup>5</sup>, Y.-W. Liu<sup>3</sup>, V.E. Markushin<sup>3</sup>, J. Marton<sup>1</sup>, M. Nekipelov, J.M.F. dos Santos<sup>4</sup>, L.M. Simons<sup>3</sup>, Th. Strauch, M. Trassinelli<sup>7</sup>, J.F.C.A. Veloso<sup>8</sup>, J. Zmeskal<sup>1</sup>

Pionic hydrogen is formed when pions are slowed down to few eV kinetic energy and captured into high-lying atomic states. In a last de-excitation step the atomic ground state  $1s$  is reached by  $np - 1s$  X-ray transitions. The strong interaction manifests in a shift  $\epsilon_{1s}$  and a broadening  $\Gamma_{1s}$  of the  $1s$  state.

Shift  $\epsilon_{1s}^{\pi H}$  and broadening  $\Gamma_{1s}^{\pi H}$  in pionic hydrogen ( $\pi H$ ) and, after applying 3-body corrections, also the hadronic shift  $\epsilon_{1s}^{\pi D}$  in pionic deuterium ( $\pi D$ ) are related to  $\pi N$  scattering lengths. In the limit of isospin conservation, the scattering lengths of all  $\pi N$  reactions can be expressed by two quantities only, the isoscalar and isovector  $s$ -wave scattering lengths  $a^+$  and  $a^-$ . In view of the theoretical achievements for the isospin violating corrections within the framework of an effective field theory, *Chiral Perturbation Theory* ( $\chi$ PT), the extraction of  $\pi N$  scattering lengths from experiment is desirable at a level of a few% or better (for recent reviews see [1, 2, 3]).

The new result for  $\Gamma_{1s}^{\pi H}$  completes a series of experiments performed at PSI aiming at an improved determination of the strong-interaction effects both in  $\pi H$  and  $\pi D$ . A specifically developed cyclotron trap was used together with a Johann-type spectrometer equipped with spherically bent Bragg crystals as well as a large-area array of charge-coupled devices, and an especially tailored concrete shielding.

The measured X-ray line shape is a convolution of the hadronic width  $\Gamma_{1s}^{\pi H}$ , the spectrometer response, and a Doppler broadening, which originates from acceleration of the  $\pi H$  atom in collisional processes during the atomic de-excitation cascade and which constitutes the main difficulty in the extraction of  $\Gamma_{1s}^{\pi H}$ . The kinetic energy of the  $\pi H$  atoms and with that the Doppler-induced broadening changes during the atomic cascade and depends on the hydrogen density and on the initial state  $np$ . Therefore, the three most intense X-ray lines  $\pi H(2p - 1s)$ ,  $\pi H(3p - 1s)$ , and  $\pi H(4p - 1s)$  have been studied at various hydrogen densities between 3.9 bar and liquid  $H_2$  in order to ensure sufficient knowledge for a consistent correction of the Doppler broadening.

For this experiment, a new calibration method was introduced. The spectrometer resolution function was measured precisely with narrow fluorescence X-rays emitted from helium-like ions. In this way, the uncertainty of the spectrometer response does not contribute in the analysis of the line shape. Fig. 1 shows as an example the  $\pi H(2 - 1)$  transition measured at 10 bar equivalent hydrogen density as well as the spectrometer resolution measured by means of helium-like sulphur.

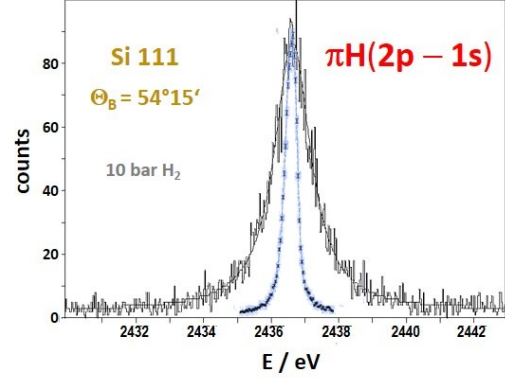


Figure 1: Spectrum of the  $\pi H(2p - 1s)$  transition measured using the silicon 111 Bragg reflection (adapted from [6]). The narrow peak displays the spectrometer response.

The complete set of strong-interaction effects,

$$\begin{aligned} \epsilon_{1s}^{\pi H} &\propto (a^+ + a^-) + \dots = (7.0858 \pm 0.0096) \text{ eV [4]}, \\ \epsilon_{1s}^{\pi D} &\propto 2a^+ + \dots = (-2.356 \pm 0.031) \text{ eV [5]}, \\ \Gamma_{1s}^{\pi H} &\propto (a^-)^2 + \dots = (0.856 \pm 0.027) \text{ eV [6]}, \end{aligned}$$

onefold constrains the determination of the scattering length yielding the most precise values for  $a^+$  and  $a^-$  [6]. Ellipses denote the corrections as obtained within the framework of  $\chi$ PT and multi-body corrections [1, 2, 3].

In conclusion, the recent experimental results obtained for the scattering lengths from pionic-atom and  $\pi N$  scattering data are highly consistent when analysed within the framework of  $\chi$ PT [3, 6].

## References

- [1] J. Gasser et al., Phys. Rep. 456 (2008) 167.
- [2] V. Baru et al., Nucl. Phys. A 872 (2011) 118.
- [3] M. Hoferichter et al., Phys. Rep. 625 (2016) 1.
- [4] M. Hennebach et al., Eur. Phys. J. A 50 (2014) 190; Eur. Phys. J. A 55 (2019) 24(E).
- [5] Th. Strauch et al., Eur. Phys. J. A 47 (2011) 88.
- [6] A. Hirtl et al., Eur. Phys. J. A 57 (2019) 70.

<sup>1</sup> SMI, Österr. Akademie d. Wiss., Vienna

<sup>2</sup> Dept. of Mat. Sci., Univ. Ioannina, Greece

<sup>3</sup> PSI, Switzerland

<sup>4</sup> Dept. of Phys., Univ. Coimbra, Portugal

<sup>5</sup> Lab. Kastler-Brossel, Univ. P. et M. Curie, Paris

<sup>6</sup> PI, Univ. Zürich, Switzerland

<sup>7</sup> INSP, CNRS, Sorbonne Univ., Paris, France

<sup>8</sup> I3N, Dept. of Phys., Aveiro University, Portugal

# Measurement of the Radiative Decay $\Sigma(1385) \rightarrow \Lambda\gamma$ in the Reaction $\gamma p \rightarrow K^+\Lambda\gamma$ at GlueX

K. Luckas, J. Ritman and S. Schadmand

Measurements of the radiative decays of hyperons can discriminate between different theoretical models of their wave functions and the underlying SU(3) structure. So far only a few such measurements have been published. This work presents the ongoing analysis of the decay of  $\Sigma(1385) \rightarrow \Lambda\gamma$ , where the excited hyperon is produced in photoproduction. The branching ratio of this particular decay has previously been measured [1].

The GlueX experiment at Jefferson Lab provides excellent opportunities to study hyperon decays in general and the reaction discussed here in particular. A detailed description of the detector system can be found in [2]. In the experiment a photon beam ranging from 6.0–11.6 GeV incident on a liquid hydrogen target is used to produce the reaction of interest.

For the analysis in this work, a kinematic fit with an energy-momentum constraint and geometric constraints for the production vertex and the detached decay vertex of the  $\Lambda$ -baryon is applied to the raw data. Only events, where this fit converges are considered for the following analysis steps.

After this preprocessing of the experimental data, different cuts are performed, in order to apply an event selection. First of all, a cut on the confidence level of the kinematic fit is applied with the requirement  $\chi^2 > 10^{-4}$ . Additionally, a cut on the squared missing mass of the full final state with  $|\text{MM}^2| < 0.08 \text{ GeV}^2$  is used. A cut is placed such that the production vertex lies within the physical volume of the target. To select  $\Lambda$ -baryons, the invariant mass of the proton and  $\pi^-$  (see fig. 1) is selected with a total width of 18 MeV centered around the physical mass of the  $\Lambda$ -baryon, which corresponds to a  $\pm 2 \sigma$ -region. Finally, the shower quality [3] is used to suppress background in the photon sample.

With these selection criteria applied, it was found,

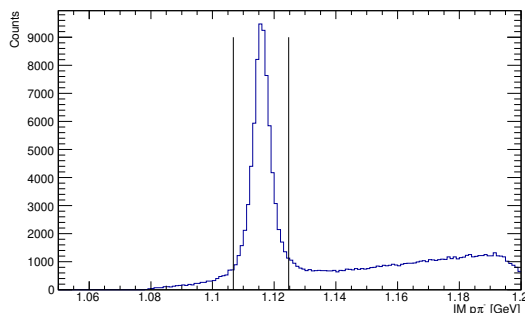


Figure 1: Distribution of the invariant mass of the proton and  $\pi^-$ . The cut region is indicated by the black lines.

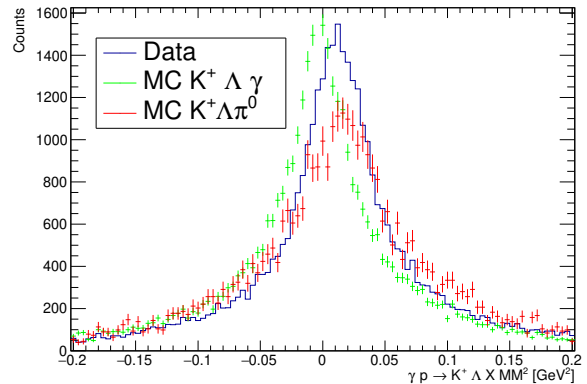


Figure 2: Distribution of the  $K^+\Lambda$  - squared Missing Mass for Data and MC simulations of the signal, and the main background contribution. The MC distributions have been scaled to the same integral as the data.

that the sample contains background from two reactions, namely  $\gamma p \rightarrow K^+\Sigma(1385) \rightarrow K^+\Lambda\pi^0$  and  $\gamma p \rightarrow K^+\Lambda$ . In the first case, one of the decay photons of the  $\pi^0$  is lost in the reconstruction, usually due to its low energy. Whereas in the second case noise from the calorimeter is reconstructed as a photon. The latter can be significantly suppressed by requiring the polar angle of the photon in the helicity frame to be  $\cos \Theta_{\text{HF}} > -0.95$ .

So far no means of distinguishing the remaining background reaction from the signal could be identified. As can be seen in the missing mass distributions in fig. 2, the data distribution is not reproduced in the Monte Carlo (MC) simulations. Nonetheless, it can be concluded, that the data is dominated by misidentified events of the reaction  $\gamma p \rightarrow K^+\Sigma(1385) \rightarrow K^+\Lambda\pi^0$ , as the missing mass is shifted towards the squared mass of  $\pi^0$ . Further investigation is needed to select a clean sample of the signal reaction  $\gamma p \rightarrow K^+\Sigma(1385) \rightarrow K^+\Lambda\gamma$ .

## References

- [1] Electromagnetic Decay of  $\Sigma^0(1385)$  to  $\Lambda\gamma$ , D. Keller et. al (The CLAS collaboration), Phys. Rev. D 83, 072004, 2011.
- [2] S. Adhikari et al. (GlueX Collaboration), The GlueX beamline and detector, Nucl. Instrum. Meth. A987, 2021.
- [3] Rebecca Barsotti and Matthew R. Shepherd, Using machine learning to separate hadronic and electromagnetic interactions in the GlueX forward calorimeter, JINST Vol. 15 No. 05, 2020.

# Search for $c\bar{c}s\bar{s}$ States in the $J/\psi\phi$ Invariant Mass Distribution

Ashish Thampi, Elisabetta Prencipe and James Ritman

The  $J/\psi\phi$  invariant mass distribution is suitable to search for  $c\bar{c}s\bar{s}$  exotic states. We propose to study this by investigating two different production mechanisms:

- the rare  $B^{\pm,0} \rightarrow J/\psi\phi K^{\pm,0}$  decay channel, using the whole Belle data set collected at the centre of mass energy of the  $\Upsilon(4S)$ , corresponding to 772 million  $B\bar{B}$  pairs
- $e^+e^- \rightarrow J/\psi\phi X$  in the continuum, where  $X$  is anything else.

The  $J/\psi$  is reconstructed from  $e^+e^-$  or  $\mu^+\mu^-$  within the mass range of  $2.95 < M_{ee} < 3.16$   $\text{GeV}/c^2$  or  $3.06 < M_{\mu\mu} < 3.13$   $\text{GeV}/c^2$ . The  $\phi$  is reconstructed from  $K^+K^-$  in the mass window  $1.0045 < M_{KK} < 1.0390$   $\text{GeV}/c^2$ . The  $K_S^0$  is reconstructed from  $\pi^+\pi^-$  in the mass window  $0.477 < M_{\pi\pi} < 0.517$   $\text{GeV}/c^2$ . The  $B$  mesons are selected by selecting on the beam constrained mass ( $M_{bc} > 5.27$   $\text{GeV}/c^2$ ) and energy difference ( $|\Delta E| < 0.03$   $\text{GeV}$ ). All selection cuts of this analysis have been optimized by maximizing the Punzi figure of merit. In this report we present the study on  $B^{\pm,0} \rightarrow J/\psi\phi K^{\pm,0}$ .

We have studied the generic Monte Carlo (MC) sample to reproduce the branching fraction ( $\mathcal{BF}$ ) of the decay modes. A  $M_{bc}$  fit is performed on generic MC sample to obtain the signal yield, and measure the  $\mathcal{BF}(B^{\pm,0} \rightarrow J/\psi\phi K^{\pm,0})$ . The results validated our analysis procedure (see table 1). We have evaluated the background to the main figures of interest by using the  $M_{bc}$  or  $\Delta E$  sidebands (see Fig 1). In these plots, one can see that with  $M_{bc}$  sidebands evaluated in the interval (5.250, 5.265)  $\text{GeV}/c^2$ , the  $\Delta E$  distribution in the  $J/\psi$ -inclusive MC sample match the estimated background. The evaluation of the  $M_{bc}$  background using the  $\Delta E$  sidebands, evaluated in the interval (0.04, 0.075)  $\text{GeV}$  also matches the background expectation.

We performed a comparison of data to MC. We have checked the  $M_{bc}$  distribution in the allowed region, i.e.  $M_{bc} < 5.27$   $\text{GeV}/c^2$  and  $|\Delta E| > 0.03$   $\text{GeV}$ , and found a reasonable agreement. Several new MC samples have been produced, simulating the presence of the 4 enhancements which LHCb has observed in the same invariant mass distribution:  $X(4140)$ ,  $X(4274)$ ,  $X(4500)$ ,  $X(4700)$ . LHCb has looked at data only through the charged  $B$  channel.

Table 1: Branching fraction of  $B \rightarrow J/\psi\phi K$ .

Mode	Efficiency, $\epsilon$ (%)	Reconstructed $\mathcal{BF}$ ( $\times 10^{-5}$ )	Generated $\mathcal{BF}$ ( $\times 10^{-5}$ )
$B^\pm \rightarrow J/\psi\phi K^\pm$	$17.87 \pm 0.04$	$5.3 \pm 0.1$	5.2
$B^0 \rightarrow J/\psi\phi K_S^0$	$8.94 \pm 0.03$	$4.8 \pm 0.1$	4.7

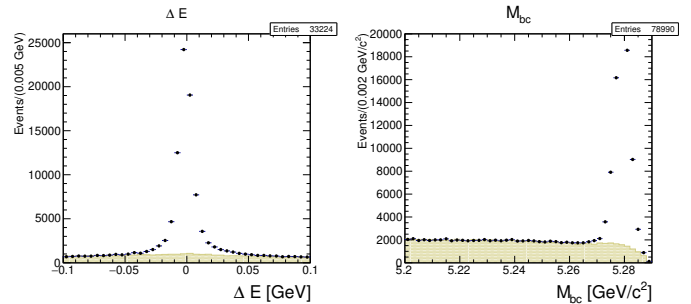


Fig. 1:  $\Delta E$  (left) and  $M_{bc}$  (right) plots for signal region(black dots) and sidebands(yellow) using the  $J/\psi$ -inclusive MC sample.

Our simulations of Belle indicate that we can perform the analysis of the neutral  $B$  channel with a reasonably high reconstruction efficiency compared to the charged  $B$  channels. It allows to verify the presence of such enhancements through the  $B^+$  and  $B^0$  channels.

Our MC simulations, based on a PHSP model only, can well reproduce these new resonant states. Of course, since  $J/\psi$  and  $\phi$  are 2 vector mesons, the poor knowledge of the  $J/\psi\phi$  dynamics does not allow us to perform more realistic simulations, therefore a study on real data is needed. This analysis is a blind analysis, and after review it will be applied to real data. In the meantime, we have evaluated the systematic error, including the model systematic uncertainties: two extreme cases, 100%  $J/\psi$  and  $\phi$  longitudinally polarized and 100%  $J/\psi$  and  $\phi$  transversely polarized have been considered. Other sources of systematic effects are due to the  $B\bar{B}$  counting, tracking, particle identification, limited MC sample events. The total systematic errors on the final  $\mathcal{BF}$  calculation are 4.29% (charged mode) and 3.56% (neutral mode). Our MC fitted values are in very good agreement with the MC input parameters. A summary of the reconstruction efficiency of the newly simulated resonances can be found in table 2.

Table 2: Reconstruction efficiency of  $B \rightarrow XK$ .

Decay mode	Efficiency(%)	
	$K^\pm$	$K_S^0$
$B \rightarrow X(4140)K$	$8.49 \pm 0.03$	$4.69 \pm 0.02$
$B \rightarrow X(4274)K$	$14.57 \pm 0.04$	$7.72 \pm 0.03$
$B \rightarrow X(4500)K$	$20.45 \pm 0.04$	$9.71 \pm 0.03$
$B \rightarrow X(4700)K$	$18.38 \pm 0.04$	$9.09 \pm 0.03$

After the study in data, the branching fraction can be calculated and the presence existence of the resonant states can be investigated. This analysis is partially supported by the DFG project no. 389090153.

## P349 Antiproton Polarization Experiment: Results and Monte Carlo Simulations of Elastic $\bar{p}p$ -Scattering

D. Alfs, D. Grzonka, K. Kilian, T. Sefzick, J. Ritman

**The Experiment.** The goal of the P349 antiproton polarization experiment is to investigate if antiprotons produced in a high energy proton beam collision with an unpolarized solid target are polarized [1]. The experiment was performed at the T11 beamline of the CERN/PS complex. A transverse polarization  $P$  of antiprotons is going to be extracted from the left-right asymmetry in  $\bar{p}p$ -scattering in the Coulomb-Nuclear Interference (CNI) region:  $PA_y = \frac{N_L - N_R}{N_L + N_R}$ , where  $A_y$  is analyzing power and  $N_{L/R}$  is the number of events scattered to the left/right. For further details of the experiment and analysis methods see [2].

**Results.** There were in total 21 days of data taking during the 2014/15 measurements resulting in  $7.7 \times 10^5$  antiproton candidates in contrast to about  $3.4 \times 10^8$  antiproton events expected [3]. The main reasons for the event loss are pile-up and low efficiency of the drift chambers. Pile-up events are not analyzable in the drift chambers due to undefined drift times. Therefore, pile-up events were removed from the sample by requesting single START and STOP detector signals. This resulted in a rejection of about 70% of the data sample, however, the distribution of remaining events is broad compared to the expected beam size (see Fig. 1, left). For track reconstruction in the drift chambers only hits from a selected range of cells in the beam region are taken into account. Less than 5% of the initial data sample fulfills minimum conditions for the scattered track reconstruction (see Fig. 1, right) which can be attributed to a low efficiency of the drift chambers under a too high particle flux. The combined efficiency of track finding and track fitting in D1D2 drift chambers is equal to about 70%. For successfully reconstructed tracks a particle identification was performed with a Plexiglas DIRC by a Monte Carlo supported analysis of the photon distribution. The detection efficiency of the DIRC was about 95%.

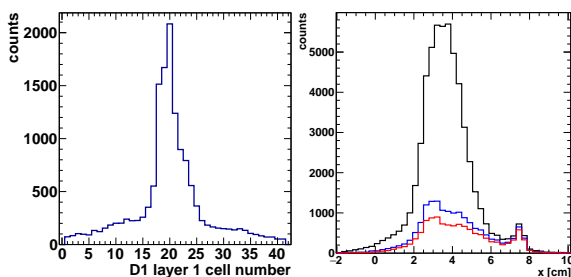


Figure 1: Left: Hit distribution in a vertical wire plane of the D1 drift chamber. Each bin corresponds to a drift cell (4 cm wide). The expected beam size at this plane is about 1.5 cm ( $\sigma$ ). Right: Horizontal beam profile reconstructed in the fiber hodoscope. Black: single-particle events. Blue: Events selected for track finding and reconstruction. Red: Successfully reconstructed events.

### Monte Carlo simulations of elastic $\bar{p}p$ scattering.

According to existing cross section data, about one per thousand antiprotons is expected to be elastically scattered within the target volume in the interesting angular range (the CNI range). Therefore, only about 1000 events useful for polarization analysis would result from the measurements. In order to quantitatively check if this amount of statistics is sufficient to set a useful upper limit for polarization, Monte Carlo simulations were prepared. The detector was implemented using Geant4 and a sample of events was simulated assuming realistic beam parameters and using a polarization of 100%. The analysis scheme for the simulated sample was the same as for the experimental data. With only 1000 events it is not possible to observe any conclusive asymmetry, see Fig. 2. Furthermore, the minimum

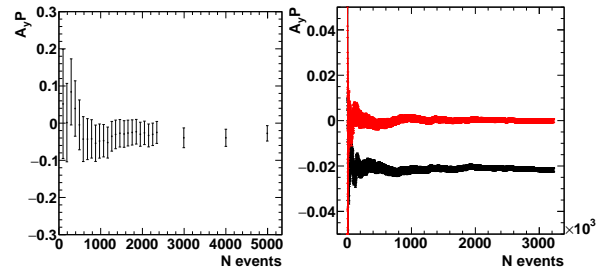


Figure 2: Left-right asymmetry as a function of statistics for scattered track directions relative to the mean beam direction with 100% polarization for small event samples (left) and high statistics samples (right) with up-down asymmetry (plotted in red) to check systematic errors.

amount of statistics needed to observe a polarization at a level useful for a polarized antiproton beam preparation was estimated.  $4.6 \times 10^6$  unpolarized antiproton-proton scattering events (double the statistics assumed in the proposal) allow to determine a polarization of 12% (7%) with a precision of  $5 \sigma$  ( $3 \sigma$ ).

**Summary and outlook.** The achieved statistics is not sufficient to extract an upper limit for the polarization in the antiproton production process. But the analysis and simulation studies have shown that a measurement of the antiproton polarization via elastic antiproton-proton scattering in the CNI region under the conditions at the T11 beam line at CERN is achievable with sufficient statistics. Currently the focus is on preparation and tests of an improved detector setup which would be better suited for the measurement.

### References

- [1] D. Grzonka, et al., Acta Phys. Polon. B 46 191 (2015).
- [2] D. Alfs, et al., Annual Reports 2017 - 2019, IKP/COSY and references therein.
- [3] D. Grzonka, CERN-SPSC-2014-016/SPSC-P349 (2014).

## Study of SiPM Irradiation with COSY Beam

D. Alfs, D. Grzonka, J. Ritman, T. Sefzick, T. Tolba<sup>1</sup>

Studies of the behavior of SiPMs under irradiation with the JULIC cyclotron beam have shown that a very low radiation dose has a strong effect on the performance of the SiPMs under investigation. In order to study this behavior under conditions which are more relevant for hadron physics experiments, irradiation studies have been performed with a COSY proton beam. The measurements were done with beam momenta of 0.85, 1.3 and 2.74 GeV/c extracted into the JESSICA area. As for the cyclotron measurements [1] SiPMs with an area of  $3 \times 3 \text{ mm}^2$  from AdvanSid, Hamamatsu, KETEK and SensL were used. In Fig.1 the installation at the JESSICA beam line is shown. The SiPMs were mounted in a vacuum chamber operated at a pressure below  $10^{-5}$  mbar which was separated by a stainless steel foil from the beam line vacuum. The beam was adjusted to the center with wire chambers in front of and behind the SiPM arrangement which also measured the beam current and allowed to monitor the beam position. In addition a radiation sensitive foil was placed close to the SiPMs which gives the integrated beam current distribution. In Fig.2 the SiPM arrangement is shown with 4 SiPMs placed in a distance of about 5 mm from the beam center

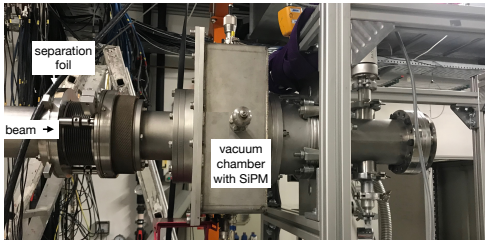


Figure 1: Setup for the SiPM irradiation study installed. The wire chambers are located 1.4 m upstream and 3.5 m downstream the SiPM chamber.

The measurement procedure starts with an adjustment of the beam concerning position and intensity without SiPMs. After the adjustment the vacuum

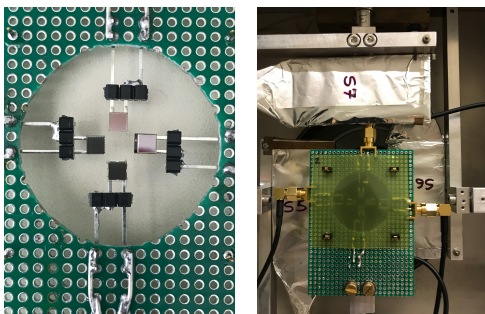


Figure 2: SiPM arrangement (left) mounted for irradiation covered with an irradiation foil (right).

chamber was opened and the SiPM board was installed. For the measurements the SiPM outputs were amplified and connected to a 4-channel CAEN DT5720B digitizer unit<sup>1</sup> with 12 bit resolution, 2 V dynamic range, and a maximum sampling rate of 250 MHz. The SiPM signals were registered during the whole irradiation period in separate 60 s long runs. The beam intensity was set to  $2.5 \cdot 10^8$  particles per spill with an extraction time of 50 s. The beam size at the SiPM position was in the order of 30 mm (FWHM). The SiPMs were irradiated until a drastic increase of the noise level was observed. Then the SiPM board was removed and the beam was prepared for the next momentum setting. For each beam momentum a new set of SiPMs was used. The results are comparable to the studies with cyclotron beam. A change in the SiPM performance starts already at a rather low dose. In Fig.3 the spectra of the SiPM output charge for increasing irradiation is shown. Starting with well separated single photon peaks a rather low dose is sufficient to remove the separation due to an increased noise width. A detailed analysis of the data is in process.

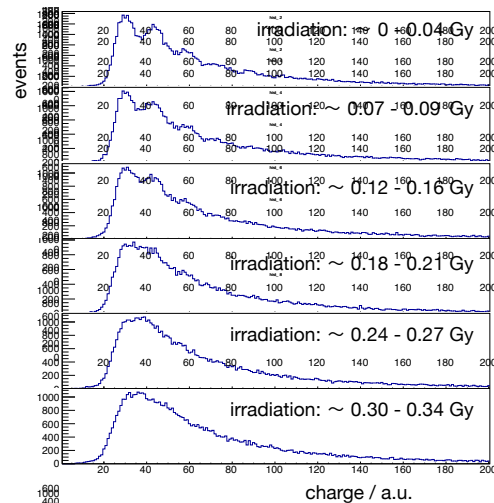


Figure 3: Distribution of the signal charge for increasing irradiation as example for the AdvanSid SiPM. At the irradiation start the single photoelectron peaks are separable and the peak structure is mostly removed after a rather low radiation dose.

## References

- [1] IKP Annual report 2019, Jül-4423, p73.

<sup>1</sup> current address: Universität Hamburg, Institut für Experimentalphysik, Luruper Chaussee 149, 22761 Hamburg

<sup>1</sup>CAEN, "DT5720B Digitizer Data Sheet." <http://www.caen.it>

## Cold moderator tests with liquid hydrogen at Big Karl

A. Schwab, P. Zakalek, M. Strothmann, S. Eisenhut, M. Rimmler, J. Baggemann, U. Rucker, T. Gutberlet, Th. Brückel

Liquid hydrogen ( $\text{LH}_2$ ) is a commonly used and highly effective cold neutron moderator material due to its high hydrogen density and its low-lying vibrational modes [1]. At temperatures necessary to liquify hydrogen (below 22 K), it mainly comprises its para spin isomer ( $\text{p-H}_2$ ), converted from its normal form ( $\text{n-H}_2$ , 75%/25% ortho to para ratio) either by a natural or catalyzed reaction. The neutron scattering cross section of  $\text{p-H}_2$  shows a large drop below 50 meV with a minimum value at approximately 15 meV [2] resulting in nearly no interaction with cold neutrons. This prevents further thermalization and results in a large mean free path for cold neutrons crossing a volume of liquid  $\text{p-H}_2$ . A large moderator would be necessary to further cool down the neutrons, but this is undesirable due to the relatively high neutron absorption cross section of hydrogen.

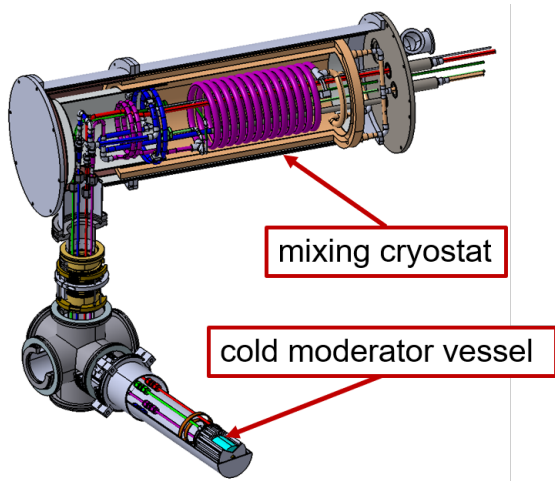


Figure 1: Mixing cryostat with cold finger for the production of different ortho-para-hydrogen ratios

A way to counteract this problem lies in realizing a higher orthohydrogen ( $\text{o-H}_2$ ) fraction inside the liquid hydrogen (e. g. 5 – 10%  $\text{o-H}_2$ ) to increase the probability of collisions at thermal and cold neutron energies. To achieve this, a novel concept was applied at the Jülich Centre for Neutron Science (JCNS) that consists of mixing a mass flow of cold, almost pure  $\text{p-H}_2$  gas with different flow rates of cold  $\text{n-H}_2$  gas as shown in Figure 1 [3]. By adjusting the flow rates of the respective hydrogen flow, one can realize any composition between normal and 100%-parahydrogen, depending mainly on the accuracy of the flow measurement and control.

In January 2020, a cryostat to produce such hydro-

gen mixtures was installed at the Big Karl experimental area at IKP. As previously reported for measurements using solid mesitylene as a cold moderator, a pulsed 45 MeV, 10 nA proton beam from the cyclotron JULIC was used to produce neutrons from a target made of tantalum.

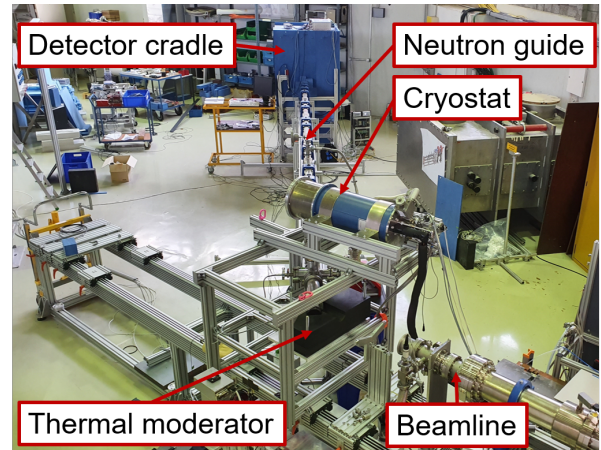


Figure 2: Measurement setup

The neutrons were then thermalized inside a polyethylene block and subsequently entered a cylindrical cold moderator vessel filled with  $\text{LH}_2$  (Figure 2). From this vessel, the neutrons were led to a  $^3\text{He}$  detector assembly via a 7 m long neutron guide. The ortho-para-hydrogen ratio was continuously monitored by using a speed-of-sound measurement device, which was thoroughly investigated before at TU Dresden. This device proved to be suitable for the task, provided that it was frequently re-calibrated.

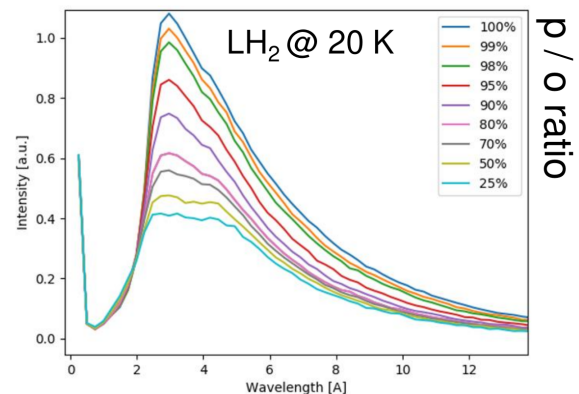


Figure 3: Neutron spectrum from time of flight measurements with different ortho-para-hydrogen ratios

Time-of-flight measurements were done using liquid

hydrogen with different ortho-para ratios ranging from n-H<sub>2</sub> to approximately 100% p-H<sub>2</sub>. The results of these measurements are presented in Figure 3 showing an increase in cold neutron intensity with increasing pH<sub>2</sub> ratio.

Furthermore, some transient measurements were performed on the process of filling the moderator vessel, changing the ortho-para ratio and freezing the hydrogen inside the vessel.

Thanks to the support of the IKP staff in setting up the test stand and running the measurements, the beam time was successfully carried out and it was shown that it is feasible to employ liquid hydrogen with different spin isomer ratios as a cold neutron moderator by using the aforementioned procedure. Furthermore, the results indicated that p-H<sub>2</sub> produces a higher cold neutron yield by up to one order of magnitude compared to solid mesitylene using almost the same setup and similar compact cold moderator dimension [4].

## References

- [1] G. S. Bauer, Proceedings of the International Workshop on Cold Moderators for Pulsed Neutron Sources, Argonne National Laboratory, 1997
- [2] W. D. Seiffert et al., Z. Naturforsch. 25 a, 967—972, 1970
- [3] S. Eisenhut et al., EPJ Web Conf., Volume 231, 8th International Meeting of Union for Compact Accelerator-Driven Neutron Sources (UCANS-8), 2020
- [4] M. Strothmann, Efficiency of a mesitylene based cold moderator system for a compact accelerator driven neutron source, Master Thesis, RWTH Aachen, 2020